DOCTORAL THESIS

POLARIZATION SWITCHING KINETICS IN FERROELECTRIC CERAMICS

AUTHOR:
RUBEN KHACHATURYAN

Referent:
Apl. Prof. Dr. Yuri Genenko
Technische Universit Darmstadt

Co-referent:
Prof. Dr. Hongbin Zhang
Technische Universit Darmstadt

A thesis submitted in fulfillment of the requirements
for the degree of Doctor rerum naturalium

Department of Materials- and Earth Sciences
Technische Universität Darmstadt
D17

Tag der Einreichnung:

Darmstadt
March 30, 2019

Polarization switching kinetics in ferroelectric ceramics.

1. Referent: Apl. Prof. Dr. Yuri Genenko
2. Co-referent: Prof. Dr. Hongbin Zhang
Tag der Einreichung: 17.10.2018
Tag der Prüfung: 17.12.2018
Darmstadt - D17

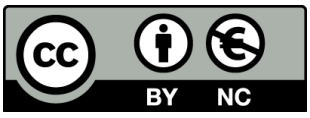

Hiermit versichere ich, die vorliegende Dissertation ohne Hilfe Dritter nur mit den angegebenen Quellen und Hilfsmitteln angefertigt zu haben. Alle Stellen, die aus Quellen entnommen wurden, sind als solche kenntlich gemacht. Diese Arbeit hat in gleicher oder ähnlicher Form noch keiner Prüfungsbehörde vorgelegen.

Approved: _____

R. Khachaturyan

Contents

Acknowledgements

Working on this project was a great adventure for me; jumping up to the sky when nice results were obtained and rolling down to the hell when all I have calculated appeared to be incorrect. Maybe I can compare the feelings from a newly derived formula to the first moments of love. The feeling is awesome. And these three years have more to do with the pursuit of this feeling rather than doing some work in common understanding. That always brings about enthusiasm, however as a person in love you become vulnerable in front of stupid mistakes. Hope to become more concentrated with time and hope not to lose the enthusiasm on that way.

Sometimes the work was challenging: it took me a while to get used to work in the field of materials modelling, and to look at problems from a machine′s point of view from time to time. However, that was very useful, as simulations play a crucial role in contemporary research and development. I learned a lot, and the implementation of this knowledge was always enjoyable. Furthermore, I want to mention that such a collaborative work, as ours was, where theory, experiment and simulations meet each other to solve problems, always opens new horizons for any scientist.

First and foremost, I would like to express my sincere gratitude to my supervisor Prof. Yuri Genenko for accepting me into the project. This position became a great step in my scientific career and I am immensely grateful for this opportunity. Thank you for introducing me into the subject of ferroelectrics, and for always being available to discuss any problem. I especially appreciated that you always found the time and patience to consider my ideas. Despite the fact that most of them were not very successful, I learned a lot while discussing them with you. It is my great fortune to have you as my Doktorvater!

I am thankful to our collaborators in our joint work, especially Dr. Koruza and Dr. Schultheiß for the experimental results and fruitful discussions. You always reminded me that there are real materials behind our theories and simulations and how we should deal with that.

Many thanks to my colleagues. I enjoyed the atmosphere you have created in our group. There was always time for science and for fun, and sometimes it could overlap. Thank you for introducing me to alternative simulation methods, it always helps to look at problems from different sides. Particularly, it was important to know that Dr. Jochen Rohrer′s and Constanze Kalcher′s doors are always open for questions and discussions. Thank you Prof. Karsten Albe for the lectures and your teaching approach. I strongly believe that the science I learned there will accompany my future research.

It is my pleasure to thank my family for supporting me. Thanks to my parents David and Ganna for raising me, I know that was not the easiest task. I want to express my deep gratitude to my father David for his advice, you are my voice of reason; warm thanks to my aunt Nina who put many efforts to help me to enter the University. Special thanks to Christoph and Inna Leifers, you continuously supported me starting from my first visit to Germany; it was so important to

know that I have family nearby.
I would especially like to thank my friends! You always motivated me to move, no matter how difficult it might be. It was essential for me that we stay in touch nonetheless the huge distances and times gap separated us. Thank you dear Nerses Simonyan for never stopping to dream, thus inspiring me to do the same!
Dear Vahram Mekhitarian, I am so happy and grateful to life that I met you. Thank you for introducing me into the world of physics; you have shown how me beautiful it is! I can dare to set up any problem, because I know that I can always count on you. I am indebted to you for very long conversations both in person and via Skype, no matter what time it is. Thank you for being always available and answering any question that was spontaneously generated in my head. This work would not have been possible without the financial support of the Deutsche Physikalische Gesellschaft, so that it is warmly acknowledged. Last but not least, I am grateful to all of those people who has read the manuscript, I know that my grammar is painful to read, so I am indebted to you: Prof. Genenko, Prof. Albe, Dr. Shahnazaryan, Dr. Ayrikyan, and Prof. Rödel, Prof. Lupascu, Prof. Zhang, for your efforts!

Abstract

The classical Kolmogorov-Avrami-Ishibashi (KAI) model [1–3] successfully describes polarization switching kinetics of single crystals. Later on, Tagantsev *et al.* [4] introduced a statistical distribution of switching time (SwT) in the KAI model; the improved statistical model is known as the nucleation limited switching(NLS) model and became suitable for thin films. Based on a robust dependence of SwT on an electric field, Lupascu *et al.* [5] have proposed that the nature of the SwT statistical distribution can be attributed to a corresponding distribution of local electric fields inside a material. Using this assumption, the inhomogeneous field mechanism (IFM) model [6] was developed.

Although the NLS and IFM are able to describe experimental measurements with high accuracy they neglect several crucial physical aspects of the poling problem. A disordered granular structure in a polarized state is unavoidably accompanied by charge formation on grain boundaries (GB), therefore giving rise to additional electric fields. Charges on grain boundaries should vary depending on polarization, therefore depolarization fields should be also time dependent. The latter fact, however, is omitted in the NLS as well as in the IFM models. Another questionable assumption, included in all statistical models, is the statistical independence of switching regions, which is doubtful since the huge depolarization fields have to produce grain correlations. Statistical independence of switching events disable accounting for non-180° switching events because these events are sequential processes rather than independent. Hence an independent switching mechanism is not suitable for this process. All these factors make the aforementioned statistical models and the reliability of extracted parameters questionable.

This work aims to shed some light on the reliability of statistical models by investigation of charge formation on grain boundaries during a poling process as well as produced depolarization fields and their evolution. Correlations of polarization and electric field components are analyzed. All studies are carried out for tetragonal, rhombohedral and orthorhombic symmetries and are in good agreement with previous theoretical results [7] and experimental measurements [8]. A new statistical model which involves non-180° switching events is presented and successfully applied to the recent polarization-time and strain-time measurements [9]. A statistical distribution of electric fields is additionally studied for the case of porous ceramics as they are materials where the distribution can be controlled by modifications to the structure.

Abbreviations

α	dimension of domain growth (Avrami index)
ε_0	dielectric permittivity of vacuum
τ_0	characteristic SwT (SwT at extremely high fields)
θ	polar angle between a *c*-axis and applied field
θ_{max}	maximal polar angle between a *c*-axis and applied field direction
ϕ	azimuthal angle of a *c*-axis around applied field
ρ	charge density
σ	surface charge density
χ_{ij}	tensor of electric susceptibility
BT	$BaTiO_3$
$\mathbf{d}_{ijk}$	third-rank piezoelectric coefficient tensor
DFT	density functional theory
DW	domain wall
$\vec{E}$	electric field vector
E_A	activation field
E_a	applied field
E_c	coercive field
E_d	depolarization field
E_{max}	field corresponding to a peak position of the logarithmic derivatives in the IFM model
E_{th}	threshold field
$f(\theta, \varphi)$	*c*-axes distribution function
FeRAM	ferroelectric random access memories
g	statistical distribution of SwT
GB	grain boundary
i	switching current
i_0	switching current at extremely high fields

IFM	inhomogeneous field mechanism model
KAI	Kolmogorov-Avrami-Ishibashi model
LGD	Landau-Ginzburg-Devonshire theory
MSM	multistep stochastic mechanism (model)
$\vec{n}$	unit vector normal to a plane
NLS	nucleation limited switching model
ΔP	total polarization variation
ΔP^k	total polarization variation according to the KAI model
$\vec{P}$	vector of spontaneous polarization
$\vec{p}$	polarization vector
P	spontaneous polarization
P_r	remanent polarization
P_s	saturation polarization
PDM	polarization difference map
PT	$PbTiO_3$
PZT	$Pb(Ti_x,Zn_{1-x})O_3$, where $0 \leq x \leq 1$
$\mathbf{Q}_{ijkl}$	fourth-rank electrostriction coefficient tensor
R	nucleation rate per unit volume
S_{ij}^p	piezoelectric strain
$\mathbf{S}_{ij}$	second-rank strain tensor
SMS	self-consistent mesoscopic switching (model)
SwT	switching time
T_c	Curie temperature
v	DW velocity
w	DW thickness
$\mathbf{X}_{ij}$	second-rank mechanical stress tensor
XRD	X-ray diffraction

List of Figures

1. Introduction

1.1 History and applications

Ferroelectrics are polar solid (single- or polycrystalline or polymeric) or liquid crystals, in which spontaneously emerging electric polarization can be switched by applying electric or mechanical fields [11]. Having various phases, a ferroelectric can experience dramatic structural changes when passing from one phase to another, which gives rise to new physical properties or their modification. Therefore ferroelectrics have been a hot topic of condensed-matter science for a long-time.

By analogy to ferromagnets which possess a spontaneous magnetic moment, ferroelectrics pertain to a class of materials which exhibit spontaneous electric moment below some temperature. The ability to switch an electric moment under an applied electric field makes ferroelectrics an indispensable part of many electronic devices, such as sensors and ferroelectric random access memories (FeRAM). Though polar properties of magnetic materials are also related to a materials structural geometry (magnetostriction), this relation is much more pronounced in ferroelectrics (electrostriction) making them an irreplaceable part of electro-mechanical devices, such as sonars [32; 33] and energy harvesting devices [34].

Being first discovered in 1920 in Rochelle salt [35] ferroelectricity was primarily of purely scientific interest until 1943 when application demand had arisen [36]. First, it was believed that ferroelectricity is based on hydrogen bonds, causing a high water solubility and fragility. The discovery of $BaTiO_3$ (BT), with its simple and stable structure, encouraged further theoretical investigations and enabled modelling of ferroelectric-based devices. BT–based materials are a very interesting research platform, as their phase diagrams involve phase transitions at relatively low temperatures, making them attractive for probing mechanisms of enhanced piezoelectricity [37]. In the present day, electroceramics are 6.0 % of the total ceramic and glass industry market share by product type, and piezoceramics are predicted to become the major industry within electroceramics by 2021 [38].

Initially, understanding of a polarization switching in ferroelectrics was limited by experimental [13; 39] and theoretical [3] studies of single crystals. Due to their switchable polarization, ferroelectric thin films are promising materials for non-volatile FeRAM [40; 41], while bulk ferroelectric ceramics are widely implemented for actuators.

1.2 Polarization and strain

In most cases, polarization of a material exhibits linear field dependence if the field amplitude is small in comparison to inner electric fields related to a material structure formation, Eq. (1.1).

Some typical exceptions are high-intensity fields, for example, generated by lasers, or polarization of ferroelectric materials. Beyond these exceptions, materials exhibit a linear dielectric response

$$p_i = \varepsilon_0 \chi_{ij} E_j, \tag{1.1}$$

where p_i, E_i are components of polarization and electric field vectors, χ_{ij} is a component of an electric susceptibility tensor. Here and below the Einstein convention on summation over the repeated indices is adopted.
A general property of any polarized solid body is electrostriction, which couples strain tensor (S) components with polarization vector components as

$$S_{ij} = Q_{ijkl} p_k p_l, \tag{1.2}$$

where Q_{ijkl} is a component of fourth–rank tensor of the electrostriction coefficient.
Considering dielectric materials with regard to their poling properties, the following subgroups can be discerned: piezoelectrics, pyroelectrics, ferroelectrics. As is shown in Fig. 1.1 each group in this list is a subgroup of the previous one.

According to a crystallographic structure, materials can be classified into 32 crystallographic point groups. Among these groups there exist 21 non-centrosymmetric groups. In all of them, except for the group 432, a linear relationship between an electric field and mechanical deformation exists. This property is called the converse piezoelectric effect and is a fundamental feature of piezoelectrics. Their relation can be expressed as follows

$$S^p_{ij} = d^T_{ijk} E_k, \tag{1.3}$$

where S^p_{ij} is piezoelectric strain, d^T_{ijk} is a component of a transposed third–rank tensor of a piezoelectric coefficient.
The direct piezoelectric effect relates polarization to a mechanical stress X [42]

$$p_j = d_{jkl} X_{kl}. \tag{1.4}$$

From these 21 point groups there exist 10 where spontaneous polarization may appear in a certain temperature range. Materials belonging to this sub-group is referred to as pyroelectrics.
Pyroelectrics, where a spontaneous polarization can be switched by applying an electric field, are called ferroelectrics and were first discovered by Valasek in 1920 [35].
A transition temperature between a polar and non-polar phases is known as the Curie temperature (T_c) [43] by analogy with a transition temperature in ferromagnets discovered by Pierre Curie. It can vary over a broad range depending on composition and defects [44], or external conditions, such as pressure. The size of a sample itself plays an important role [45] for a transition between ferroelectric and paraelectric states [46]. For instance, reduction of a film thickness usually decreases its ferroelectric properties [47; 48].
Under an external electric field, the polarization of a ferroelectric can be considered as a sum of the spontaneous polarization ($\vec{P}$) (induced by a symmetry breaking below a phase transition temperature) and an additional polarization part which is proportional to an electric field [49]

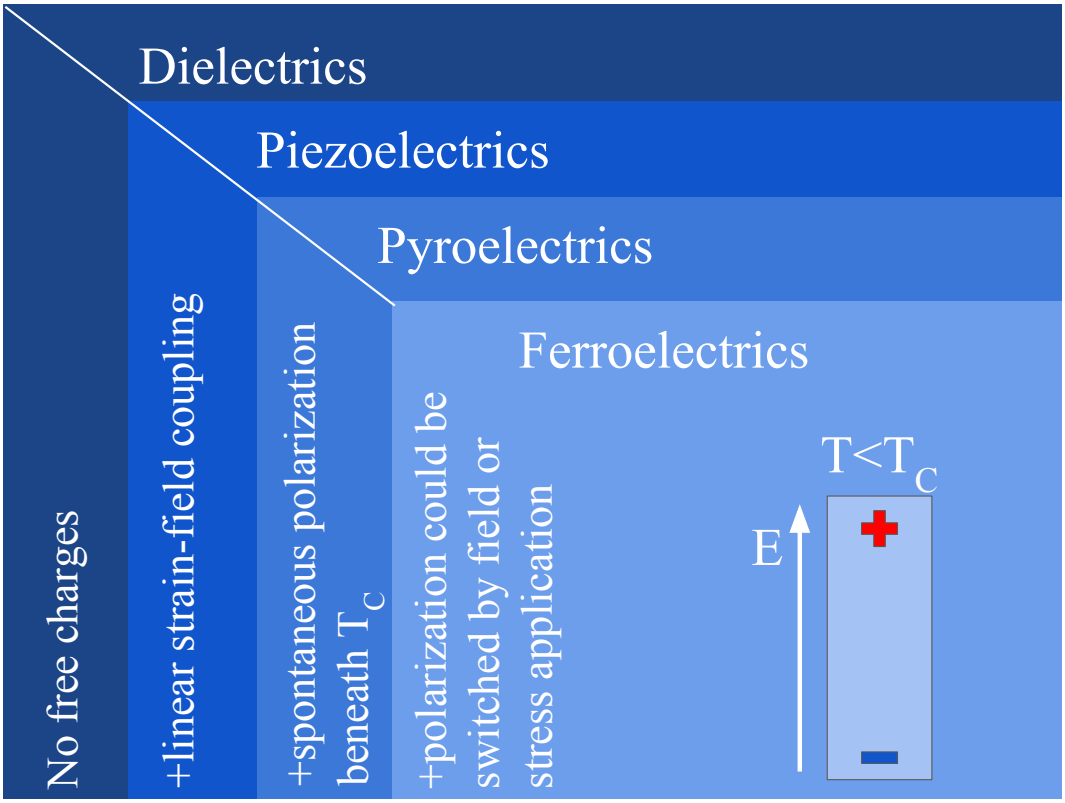

Figure 1.1: Dielectrics' subgroups.

$$p_i = P_i + \varepsilon_0 \varepsilon_{ij} E_j. \tag{1.5}$$

If now Eq. (1.5) is substituted into Eq. (1.2) then the strain tensor modifies as follows [49; 50]

$$S_{ij} = Q_{ijkl} P_k P_l + d_{ijk} E_k, \tag{1.6}$$

where $d_{ijk} = 2\varepsilon_0 \varepsilon_{km} Q_{ijml} P_l$ is a component of a third–rank tensor of a piezoelectric coefficient (a small contribution (quadratic in field) is neglected here). Thus, even centrosymmetric materials with no piezoelectric properties in a parent phase become piezoelectric in a ferroelectric phase with a piezoelectric coefficient proportional to a spontaneous polarization.
In addition to a non-linear polarization-field dependence, ferroelectrics are characterized by hysteretic behaviour (Fig. 1.2) when a cyclical electric field is applied. In a polar state, each ferroelectric lattice has several possible polarization directions. An applied field causes some polarization directions to become energetically more favourable. However, to change its direction from an unfavourable to a favourable one an energetic barrier has to be overcome. Therefore, polarization is changed only after a sufficiently large field is applied. This leads to the presence of a hysteresis in the polarization response. Though a barrier between two polarization states is a characteristic of a material itself, the field required to overcome this barrier depends on a time

interval over which the field was applied, in other words even at comparatively low fields but long poling time a switching probability exists [51]. An area which is covered by a hysteresis loop is associated with energy losses as most of the energy is being released as heat [37].

Polarization switching in a ferroelectric may be accompanied by a change of the lattice shape.

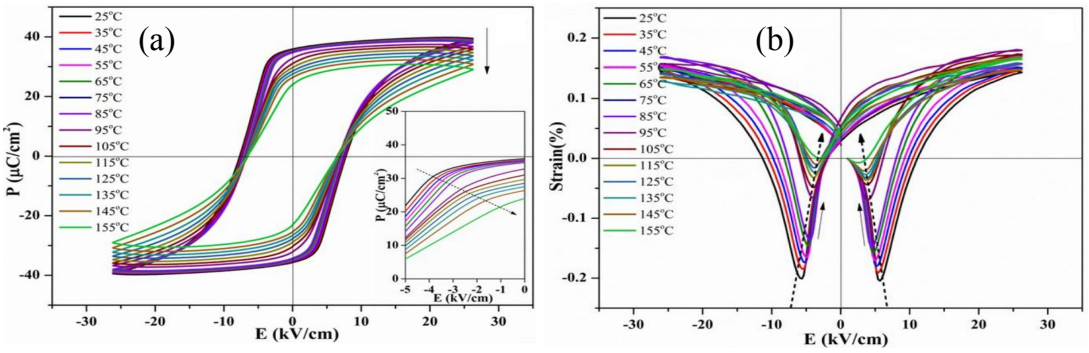

Figure 1.2: (a) A polarization–electric field and (b) a strain–electric field loops for a PT single crystal measured at different temperatures. Arrows on the graphs point a direction of increasing temperature (Reprinted by permission from MDPI: Crystals [10])

.

In a simple tetragonal unit cell, for example BT, such a switching produces a strain variation of the order of 1%, and 6% for $PbTiO_3$ (PT). That is easily seen by comparing *a* and *c* sites of the cells, which exchange after a non-180° rotation. *a* and *c* sides for BT are 3.99Å and 4.03Å, respectively, and for PT they are 3.9Å and 4.15Å, respectively [28]. Analogous to the polarization response, the strain-electric field dependence also demonstrates hysteretic behaviour, and is referred to as a butterfly loop. Hysteresis loops both for polarization-field and strain-field dependencies for a PT single crystal are shown in Fig. 1.2, and exhibit macroscopic strain of approximately one order of magnitude smaller than the above unit cell estimations.

2. Single crystals

2.1 Perovskites

Currently more than 700 organic and inorganic ferroelectric materials are known. Their state varies from solids and polymers [52] to liquid crystals [53]. Different exemplary types of structures where ferroelectricity is observed are shown in Fig. 2.1.

The most important feature for the appearance of ferroelectricity is the presence of a sponta-

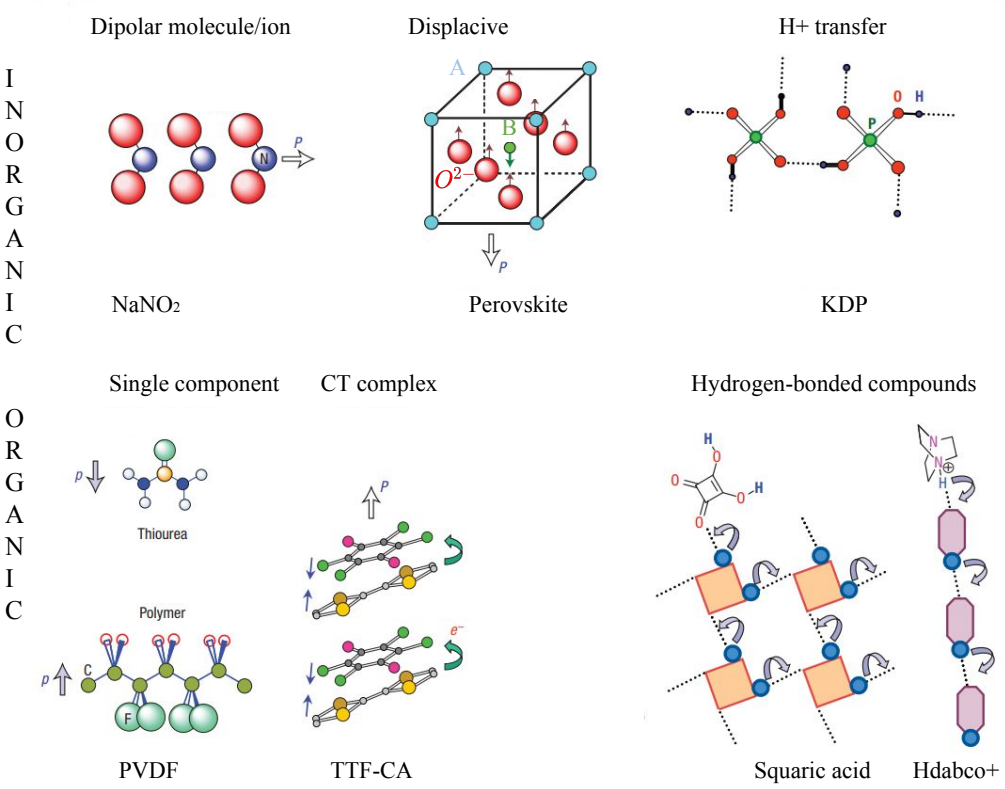

Figure 2.1: Conventional designs of typical ferroelectric materials and dipole moment origination: the first row inorganic, the second row organic ferroelectrics, adopted from [11].

neous polarization, the origin of which strongly depends on the material's structure, see Fig. 2.1. It might be polar molecules/ions, for instance, a sodium nitrite or thiourea, which under some conditions orient in such a way that non-zero net polarization is generated. Another mechanism

is triggered by dynamic protons on hydrogen bonds, as is the case in case of KH_2PO_4.
Among all these ferroelectrics, perovskite ferroelectrics are most often used in applications [54] because they allow a versatile control of the material's properties. In perovskite ferroelectrics, a spontaneous polarization occurs as a result of displacement of an ion in a lattice cell, known as the displacive mechanism. Further on, we will focus on these materials.
A perovskite crystal is described by the chemical formula ABO_3 and in a parent phase has a cubic structure as represented in Fig. 2.2.

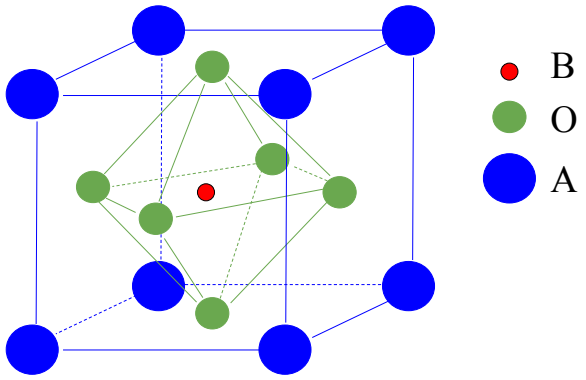

Figure 2.2: An exemplary structure of a cubic perovskite.

The A site can be occupied by a metal ion typically with valence +1 or +2, such as Li or Ba, respectively; the B site may have valence +4 or +5, as Ti or Nb have, respectively, O is the oxygen ion with valence -2. Atoms in the lattice could be substituted to modify properties or to enhance the stability of a material [55–57]. The substituted atom can have a different size and hence distorts the lattice affecting ferroelectric properties [58], or even inducing ferroelectricity [59]. Below T_c a ferroelectric undergoes a phase transition; the cell elongates giving rise to a polar phase. Elongation might occur in different directions depending on the symmetry to which a system is expected to transform. The most common symmetries are: tetragonal, rhombohedral, and orthorhombic; those are the only possibilities for materials of a cubic symmetry in a high–temperature parent phase. In the first case, a system can elongate in six possible directions equivalent to $\langle 001 \rangle$, in the rhombohedral phase there are 8 possible directions equivalent to $\langle 111 \rangle$, and in orthorhombic case, there are twelve possible directions equivalent to $\langle 101 \rangle$, see Fig. 2.3.
In an elongated cell, a central atom shifts along an elongation axis separating centres of mass of positive and negative charges. Thus, a phase transition induces a polarization and strain response simultaneously, see Fig. 2.3.
One of the most notable features of ferroelectrics is polarization switching under an applied field (E_a). As is known, if a field is applied an electric dipole tends to orient in a direction of the applied field to minimize the system's energy. However, a ferroelectric cell can be poled only in one of the possible polar directions. The simplest case is a switching in a tetragonal symmetry

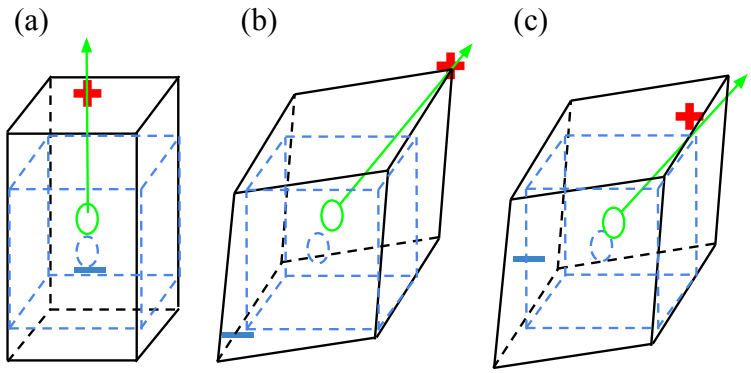

Figure 2.3: Schematic illustration of (a) tetragonal, (b) rhombohedral, (c) orthorhombic symmetries. The plus and minus signs denote positive and negative charge formation.

where only 90° and 180° rotations exist, see Fig. 2.4.
Angles between polarization directions in other symmetries differ from 90°: they can be 71° or 109° in the rhombohedral case. Thus, in general, we distinguish between 180° and non-180° switching.

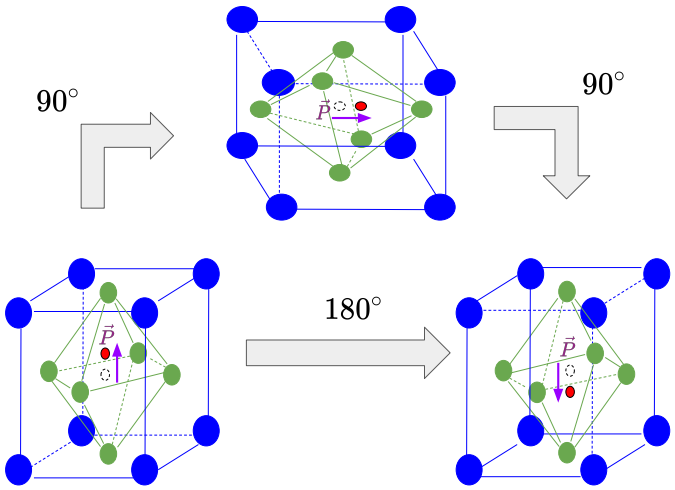

Figure 2.4: A schematic illustration of 90° and 180° domain switchings.

It is important to note that a system can come to a final state in experiencing different combinations of 180° and non-180° switchings, depending on crystal structure, and external conditions such as an applied electric field. Among all switchings, 180° ones are of particular interest because they do not produce strain variation as the cell does not undergo change of its form.

2.2 Single crystal

Let us consider a ferroelectric crystal which goes beneath T_c from a paraelectric into a polar state. In a polar state, polarization can be distributed either homogeneously or inhomogeneously. A region with homogeneous polarization is called a domain [28].
Variation of spontaneous polarization in space is a source of charge density (ρ)

$$\rho = -\vec{\nabla}\vec{P}. \tag{2.1}$$

Such a charge might occur between adjacent regions (cells) with different polarizations, for instance, on a surface of a polarized object where it meets a non-polarized surrounding. A field produced by these charges is known as a depolarization field (E_d), which can reach high values (of the order of 10 kV/mm) [7; 28]. Such enormous fields are not observed in experiments, because they are immediately suppressed by different mechanisms such as screening on an open surface/electrodes, *inter alia* [60; 61].
A depolarization field increases the free energy of a material. If the free energy increases too much, then it renders the single-domain state unfavourable and the material splits into domains to reduce the surface charges, thereby quenches a depolarization field [62]. The domain size may vary from nanometers to microns in a bulk ceramic [63] and depends on many parameters, such as structure symmetry or grain size [64; 65].
Let us consider two regions of different polarizations, see Fig. 2.5 (a).

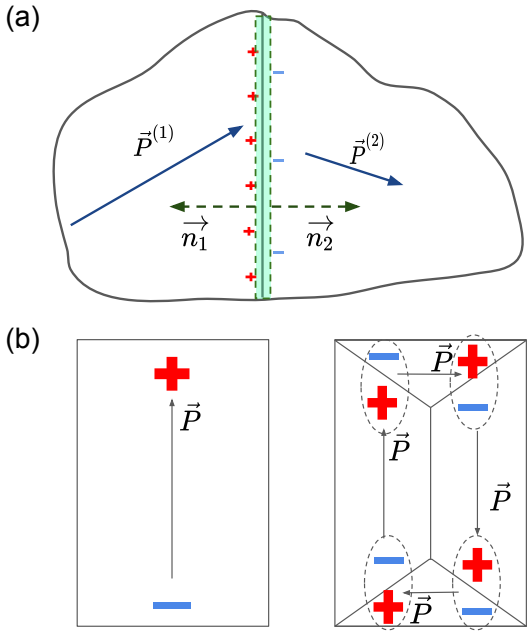

Figure 2.5: (a) Surface charge formation on the boundary of regions with different polarization components normal to the surface ($\vec{P}_n^1 \neq \vec{P}_n^2$), (b) multidomain state formation out of a single domain state (vortex-like structure).

Referring to Eq. (2.1) we can conclude that the surface will be charged due to polarization variation between the regions. A surface charge could be related to a polarization by integration of Eq. (2.1) over a small region in a vicinity of a surface and applying the Gauss theorem

$$\int \rho(\vec{r})dr^3 = -\int \vec{\nabla}\vec{P}(\vec{r})dr^3 = -\oint \vec{P}\vec{n}ds, \tag{2.2}$$

where $\vec{n}$ is a vector normal to the surface which points outside a volume at an each point of a surface.
Assuming the region to be infinitesimally thin, an integration over a surface reduces to

$$\oint \vec{P}d\vec{s} = ((\vec{P}\cdot\vec{n}_1) + (\vec{P}\cdot\vec{n}_2))\cdot s, \tag{2.3}$$

where $\vec{n}_1$ and $\vec{n}_2$ are normal to a surface vectors pointing inside the first and the second regions correspondingly, see Fig. 2.5 (a), and s is surface area of the considered small region.
By introducing notations for polarization projections on the $\vec{n}_i$ direction as $P_i = \vec{P}\cdot\vec{n}_i$ for a surface charge (σ) we finaly get

$$\sigma = -(P_1 + P_2). \tag{2.4}$$

It is seen from Eq. (2.4) that a surface is charged when $P_1 + P_2 \neq 0$ and is neutral when $P_1 + P_2 = 0$.
Any structure tends to minimize its surface charge density, which means it lines up according to a head-to-tail configuration. As a result, polarization in adjacent domains could be parallel or lay within some angle (which, depends on crystallographic symmetry) with a tendency to minimize a charge on surfaces. A simplified schema of domain splitting is shown in Fig. 2.5 (b).
A region between two domains is called a domain wall (DW). It represents a transition layer wherein polarization monotonically changes its direction from one domain to another. Polarization within a DW is inhomogeneous. Such an inhomogeneous structure as a DW may be a place of non-zero charge density and a stress formation. Consequently, energy density inside a DW is always higher than energy density of a domain itself. A DW, which separates domains with an antiparallel orientation of polarizations is called 180° DW, others are non-180° DWs. DWs which experience stress from non-uniform strain tensor between adjacent domains are called ferroelastic DWs, such DWs separate regions where both a polarization vector and a spontaneous strain change across the boundary [66]. Important to note that 180° DWs are only ferroelectric, whereas non-180° DWs might be ferroelectric and ferroelastic. It means that both 180° and non-180° DWs reduce depolarization fields but the only formation of non-180° DWs leads to stress reduction. Consequently, both 180° and non-180° DWs can be changed by an electric field, whilst external stresses affect only non-180° DWs.
Considering Eq. (1.2) we can see that domain formation may create strain inhomogeneity which results in stress formation over domains. A condition for a stress-free DW is [12]

$$\sum \langle S_{ij}(2) - S_{ji}(1)\rangle n_i n_j = 0, \tag{2.5}$$

where $S_{ij}(1)$ and $S_{ji}(2)$ are strain tensor components from regions (1) and (2), respectively and a $\vec{n}$ is a normal unit vector to a DW plane.
Using the criteria from Eqs. (2.3,2.5) several types of stress free DWs were identified by Marton

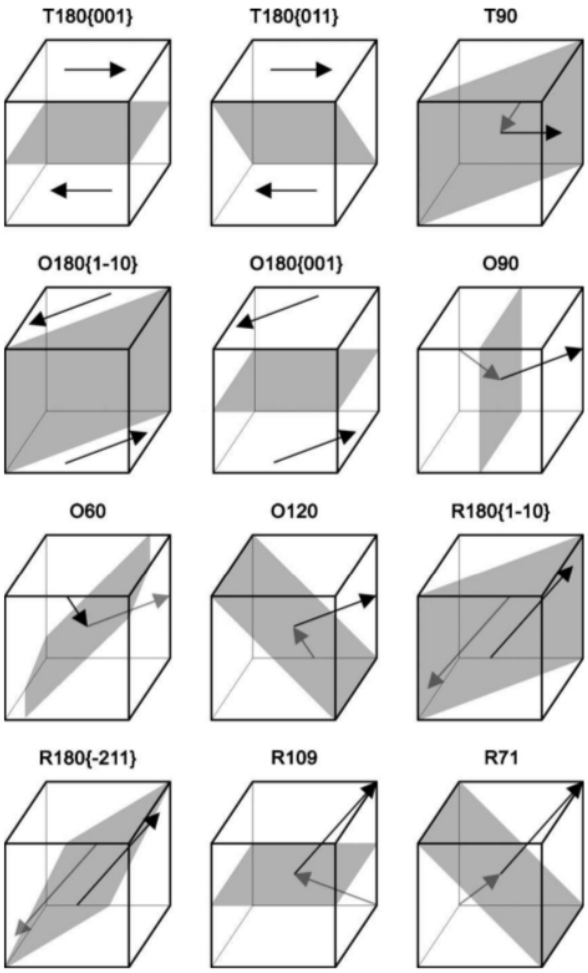

Figure 2.6: Set of mechanically compatible and electrically neutral DWs in the three ferroelectric phases of a BT (Reprinted by permission of APS: Phys.Rev.B [12]).

et al. [12] using the LGD approach; a list of stress- and charge-free DWs is given in Fig. 2.6. Their calculations revealed that DWs with the lowest-energy in an orthorhombic phase of BT are 90° and 60° DWs, for a rhombohedral phase they are 71° and 109° DWs. All these ferroelastic DWs have thickness below 1 nm except for the 90° DW in a tetragonal phase and the 60° DW in an orthorhombic phase, for which a larger thickness on the order of 5 nm was found. The calculation indicates that the lowest-energy structure of the 109° DW and few other DWs in orthorhombic and rhombohedral phases resemble Bloch DWs known from magnetism.
If possible to neglect compensation of a bound charge on DWs by free carriers and if a domain pair is non-ferroelastic, then electrical neutrality plays the key role for a wall orientation [63]. Two typical situations for a mutual orientation of a planar DW and polarization vectors in neighbouring domains are shown in Fig. 2.7 [13] and are applicable, for instance, for a tetragonal phase of BT [63].

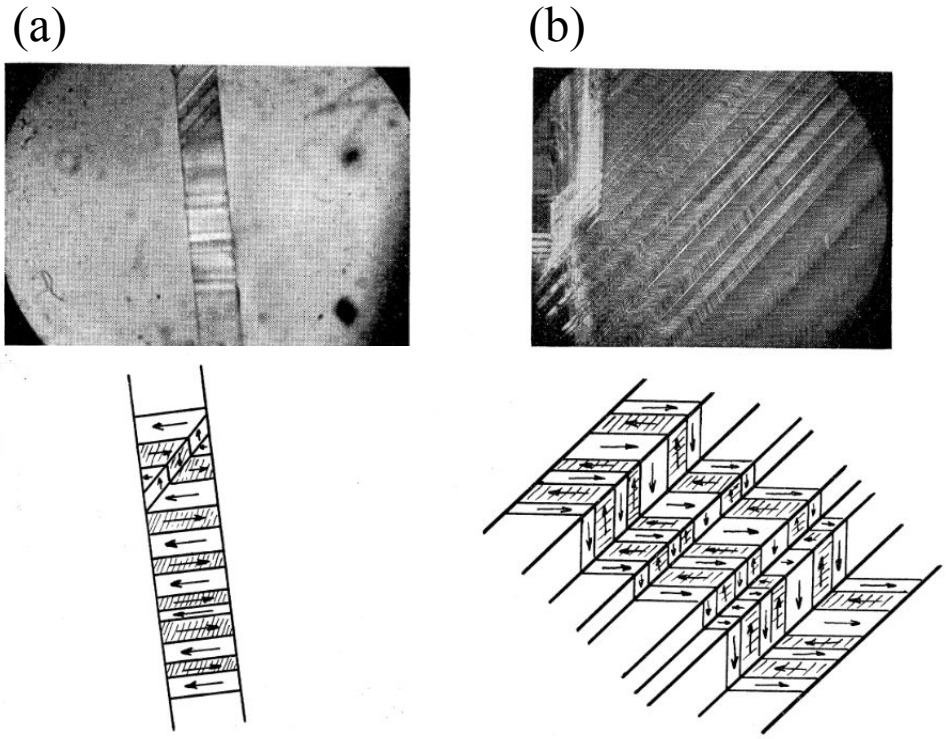

Figure 2.7: Optical observation of DW arrangement: (a) view on an edge, (b) view on a surface of a crystal (Reprinted by permission of APS: Phys.Rev [13]).

A shape and a size of DWs depend not only on the pure physical interactions like depolarization and stress fields, but on many other factors [37] such as crystal growth, the process of phase transformation from a parent phase or presence of dopants [67].

2.3 Polarization kinetics of single crystals

Polarization reversal is the main property which distinguishes ferroelectrics from other dielectrics. Based on earlier works [16; 19; 68; 69] the main stages of a poling process are summarized in the following steps [14]:

1. Formation of new domains (nucleation);
2. Forward growth of domains through the sample
3. Sideways motion of DWs and coalescence of residual domains.

Representations of these stages is given in Fig. 2.8.

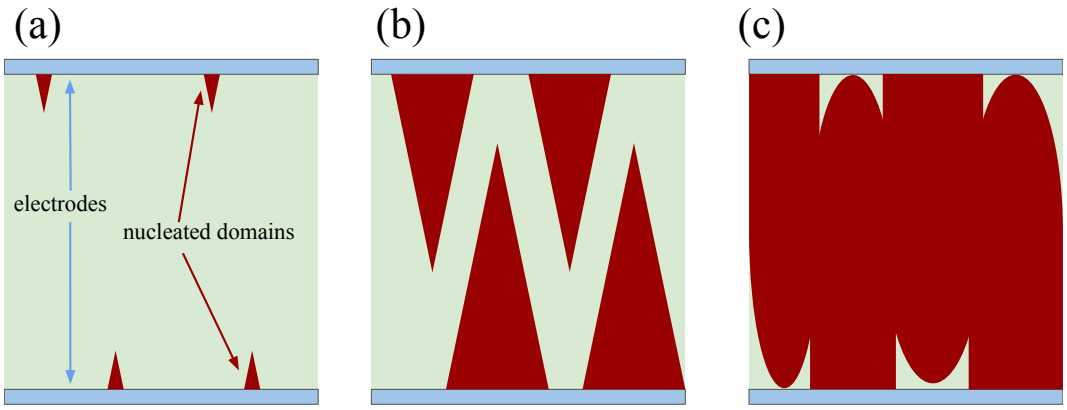

Figure 2.8: Stages of polarization reversal in a single crystal: (a) reversed domain nucleation at the surface of electrodes, (b) the nucleated domains grow (mostly forward motion) through the crystal, (c) sidewise motion and coalescence of domains, based on works [13; 14].

All nucleation centres are located on surfaces attached to the electrodes. The stages listed above are most typical for thin films. However, the triangle-like domain nucleation is expected to demand high energy, which only a big domain can exhibit [70]. Different mechanisms which could decrease the nucleation energy were proposed, for instance crystal inhomogeneities, lattice defects, a surface layer, and a small residual nuclei [70; 71]. However, experimental observation by Jiang *et al.* demonstrated nuclei with a sizes around 4.5 nm in a 300 nm thick in a $Pb(Ti,Zn)O_3$ (PZT) film [72] claiming that the high depolarization energy of the nuclei has to be mitigated by electrons from the electrodes. Actually, a shape of domains can also vary depending on the applied field, having not only a circular, but also a quadratic cross-section [18].
The way domains grow affects a polarization–time dependence to the same degree as an applied field. Microscopically, a polarization rate can be characterized by the SwT, which is a value reciprocal to a switching current (i) measured during a switching process. In most cases the SwT dependence on electric field can be described by an exponential law [16; 19]. An exponential behaviour of SwT was observed by Merz [73] on ferroelectric BT, where, a switching current

measurement was well fitted by an exponential dependence

$$i_{max} = i_0 \exp(-E_A/E), \tag{2.6}$$

where i_0 is current at extremely high field values, E_A is a so called activation field, or equivalently for the SwT

$$\frac{1}{\tau_s} = \frac{1}{\tau_0} \exp(-E_A/E), \tag{2.7}$$

where τ_0 is switching time at extremely high field values.
However, it occurs that at high fields SwT might change its field dependence from an exponential to a power law ($E^{-1.4}$) [74].
One of the possible explanations of this phenomena is as follows: DWs propagate according to the Merz law. However, at high fields, a nucleation starts to dominate over DW motion. Provided that the nucleation rate has a $E^{1.4}$ dependence [19], the SwT dependence also starts to obey the power law. A direct observation of domain formation and growth was reported by Stadler *at el.* and demonstrated that the latter concept likely the case. Sidewise growth of domains with a velocity proportional to the switching current at high fields was confirmed [19] and depends on the nucleation rate. The velocity of the sidewise motion is one order of magnitude smaller than the forward velocity [18], which mostly has exponential field dependence. The SwT dependence, in cases where a sidewise motion is a primary mechanism, also follows a power law [19],

$$\tau = (4v^2R)^{-\frac{3}{2}}, \tag{2.8}$$

where $R \sim E^{1.4}$ is a nucleation rate.
An alternative idea was to use an exponential dependence of DW velocity and introduce a DW thickness dependence [17],

$$v = v_{\text{inf}} \sum e^{-(E_A/E)w^{1.5}}, \tag{2.9}$$

where w is DW thickness in interatomic distances units. Assuming that at high fields DWs may have a thickness of more than one or two interatomic distances the series Eq. (2.9) tends to a power law E^{β} where β may vary from 1.36 to 1.45.
The DW velocity also depends on sample geometry, for instance on crystal thickness. It was shown by Landauer *et al.* that the characteristic SwT decreases exponentially with increasing thickness [13; 75]. A DWs velocity for BT dependence on an applied field is shown in Fig. 2.9, based on data from the works [19; 73].
DW sidewise motion in a single crystal of a BT was studied by Merz using optical microscopy. It was found that the poling process is mostly due to nucleation of new domains and their needle-like growth from one electrode to another. It was also proposed that there is an effect from 180° DWs sidewise motion, but the effect is comparatively small. A reason for privileged forward domain growth was assumed to be a field of dipoles that tends to reorient neighbours in front of them and "does not care much about neighbours on the sides" [13; 73]. A similar picture was observed by Leschhorn *et al.*, where a single crystal was simulated using a scheme of dipole flipping. Simulations showed that nucleation can occur in a dead layer on an electrode, as well as on defects which are not able to switch. The model takes into account the field induced by polarized regions. It was shown that the first domains grow along the applied field and then

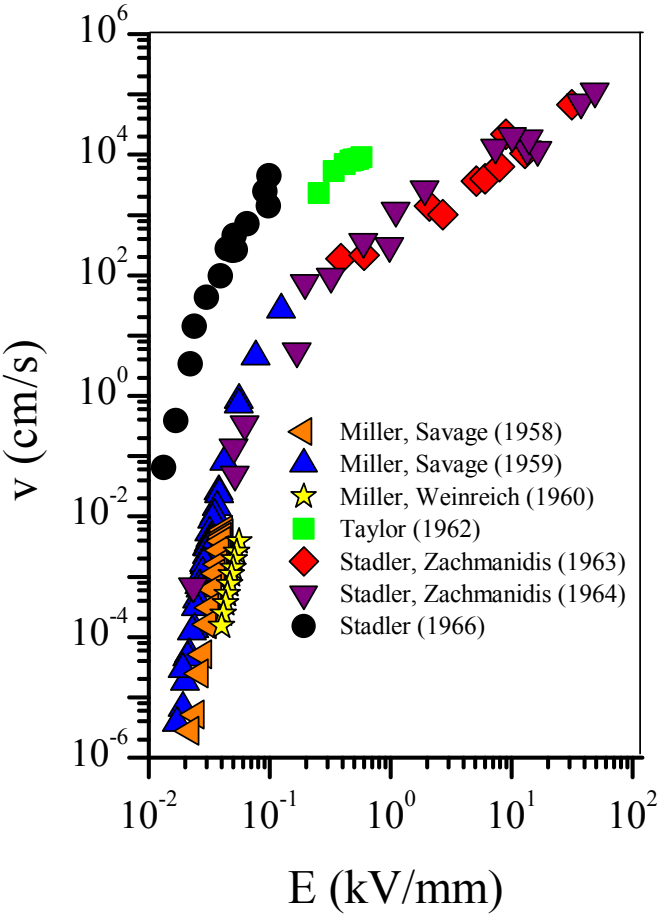

Figure 2.9: Field-dependent DW velocity, v, of 180° DWs in BT, the data was taken from Ref. [15–21], adopted after [22]

expand to the sides [76].
As is well-established, a ferroelectric lattice can switch either by 180° or by non-180° domain reorientation. The latter comprises two sequential switching steps and produces strain variation due to lattice distortion, see Fig. 2.4. Different switching events require different amounts of energy. Therefore each of them can dominate at different conditions. The observations of Merz demonstrated predominantly non-180° DWs sidewise motion [13; 73]. On the contrary, in the work of Stadler and Zachmanidis, it was shown that 180° DWs sidewise motion provides a substantial contribution to BT polarization over a broad field range (2-14 kV/cm) [19].
Another mechanism of domain growth was suggested by Miller and Weinreich [17]. Their work states that a 180° DW does not move sidewise in a continuous manner. It was assumed that the most probable scenario for polarization evolution is a growth of new domains over the DWs, as is schematically shown in Fig. 2.10.

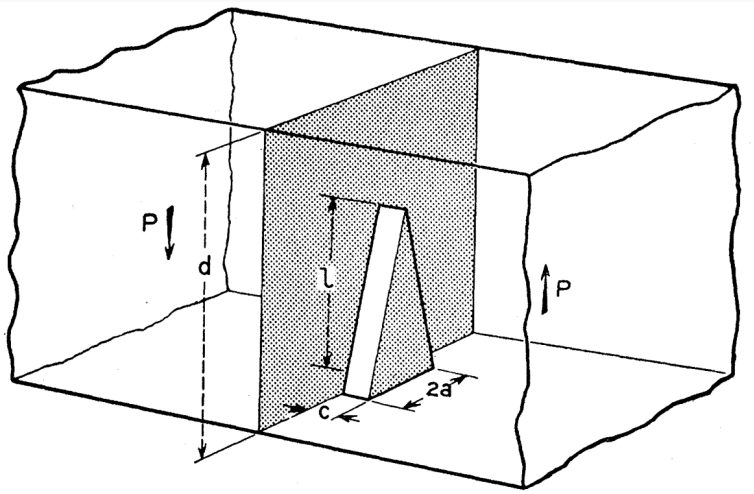

Figure 2.10: Polarization due to formation of triangle domain on the DW (Reprinted by permission of APS: Phys.Rev.B [17]).

A local electric field plays a part in DW motion. Being initially electrically neutral, after the DW movement, a surface charge appears over the domain. The surface charge generates a depolarization field, whose direction is opposite to the applied field. The depolarization field affect the DW velocity. The local field is a superposition of an applied field and depolarization field. As the DW velocity depends on a local field, a DW would therefore undergo retardation until the induced charge is compensated [77].
Parallel to the investigation of 180° switching, many works reported non-180° switching [78–80]. Particularly, in the work of Jiang *et al.* the full single crystal was switched by non-180° processes, specifically for a tetragonal symmetry so-called 90° switching DW motion as is shown in Fig. 2.11 [23].
While 90° switching in the work of Jiang *et al.* happens coherently, so that no strain or charge is induced on domain boundaries, Cross *et al.* reported 1% strain variation, while the strain vari-

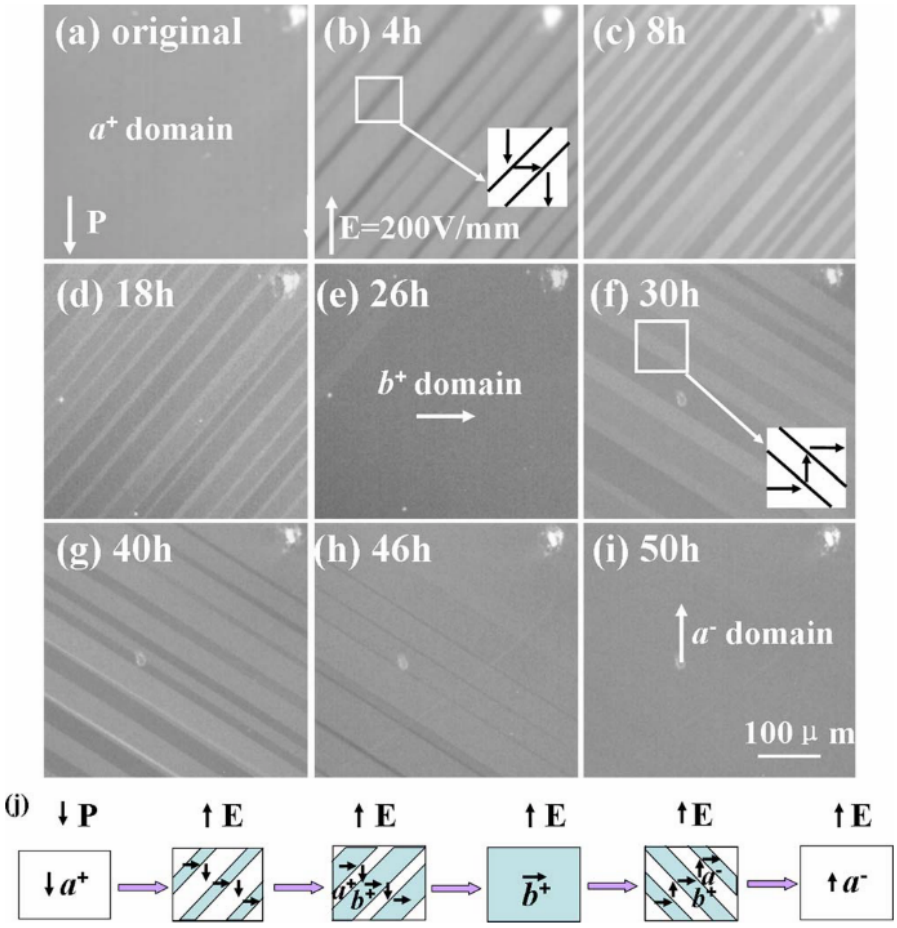

Figure 2.11: *In situ* optical observation of polarization due to 90° switching in a BT thin film (Reprinted by permission of AIP: Appl.Phys.Lett. [23]).

ation due to piezoeffect is typically one order of the magnitude smaller; such a strain variation was explained by electrostriction because of non-180° polarization switching [78].

3. Ceramics

3.1 Structure of ceramics

Most ferroelectric applications utilize ceramic materials [81]. Ceramic consists of a number of grains, which in turn contain one or more domains. Ferroelectric ceramics are characterized by at least three sorts of randomness: a random form of grains, a random position of grains and random orientation of the crystal lattice inside the grains [7]. A typical granular PZT ceramic is shown in Fig. 3.1, which consists of grains with irregular forms. Stripes inside the grains reveal a domain system.

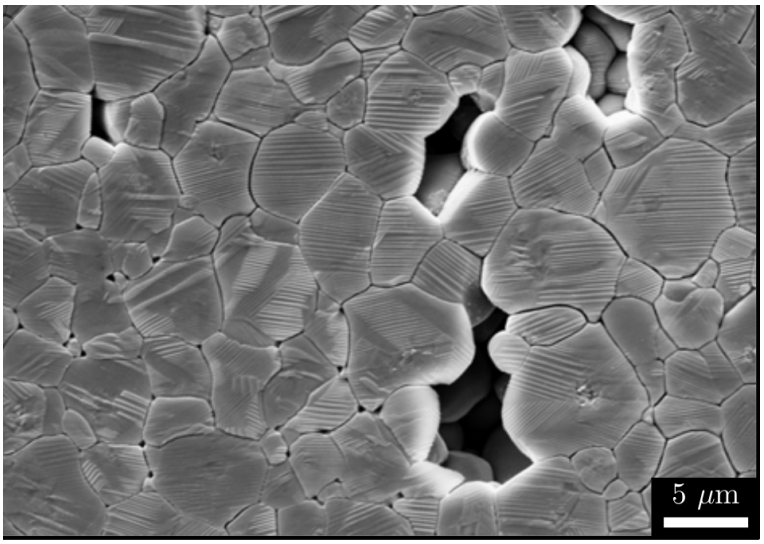

Figure 3.1: SEM image of a granular polycrystalline PZT (Reprinted by permission of Materials Forum [24]).

A granular ceramic, if it was not intentionally textured, can be equally polarized in any direction. However, the maximum available polarization is always smaller than that of a single crystal of the same materials. The reason is a spacial distribution of c-axes inside a ceramic so that there is no direction which coincides with the c-axis of all grains, see Fig. 3.2.

Let us now assume that we have a ceramic with single crystalline grains. If a strong enough field is applied to the system it polarizes in the field direction. If the polarization of each grain is equal to a saturation polarization (P_s), then the polarization of the system as a whole is averaged

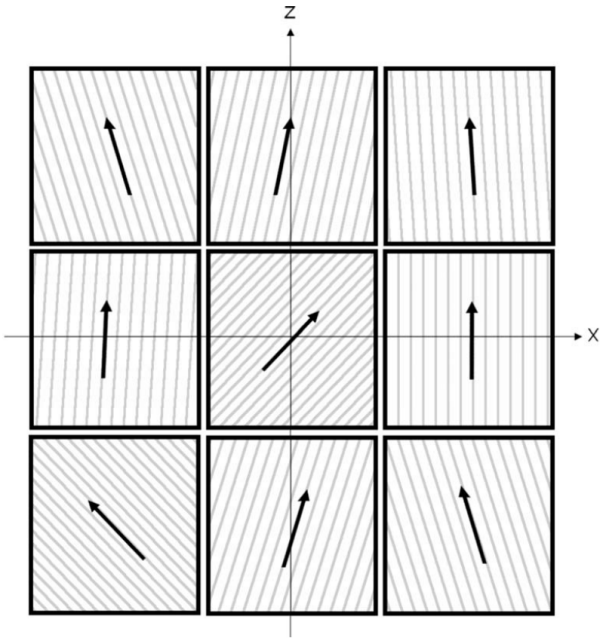

Figure 3.2: Two-dimensional projection of polarization distribution in a fully polarized ferroelectric ceramic. Hatching pattern shows schematically the orientation of the crystal lattice (Reprinted by permission of APS: Phys.Rev.B [7]).

over all grains and amounts to $\langle P_s \rangle = P_s \langle \cos\theta \rangle$, where θ is the angle between the c-axis of a grain and the applied field.
The mean cosine was calculated for three symmetries by Uchida and Ikeda and Baerwald: 0.83, 0.87, 0.91 for tetragonal, rhombohedral, and orthorhombic symmetries, respectively [82; 83].
A granular ceramic is a very complicated structure. Being less sensitive to effects on interfaces than thin films are, it possesses a rather complicated intrinsic structure. In a multigranular ceramic properties may strongly vary between grain interiors and a grain boundaries, where the former is a crystal and the latter one violates crystal structure and is prone to defects accumulation. GBs itself may be considered planar defects due to violation of an ordered crystal structure. Grain size has a profound effect on dielectric and piezoelectric properties of ferroelectrics [37]. Furthermore, it was recently demonstrated that grain size may affect the emergence of ferroelectricity, for instance providing a long-range net polarization in $NaNbO_3$ [84]. At an ultra-fine grain size an orthorhombic-tetragonal phase transition was observed in BT depending on the grain size [85]. There is a critical size of grains below which ferroelectricity disappears. The general reason is a charge formation of GBs which suppresses the polarization [37]. Such a critical size of grains for a BT granular ceramic was experimentally observed in the range of 30-40 nm [86]. An enlargement of grain size from around 0.4 μm to above 20 μm enhances the electromechanical properties [87]; for instance, Hao *et al.* [25] observed an increase of saturation polarization of 40% and about five-fold strain enhancement in $BaZnO_3$-50$BaCaO_3$. Kamel and de With observed a dramatic decrease of polarization with decreasing grain size from 10 μm to

2 μm on donor-doped ferroelectric PZT, see Fig. 3.3. Depending on its size, a grain contains

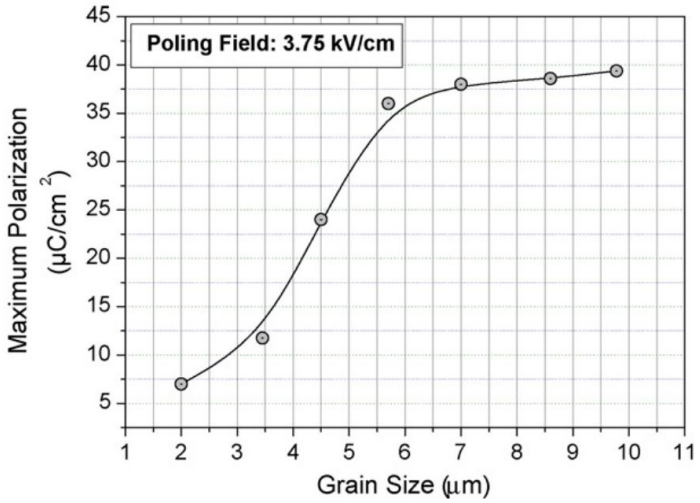

Figure 3.3: The maximum polarization as a function of grain size for a donor-doped PZT subjected to a 3.75 kV/cm electric field (Reprinted by permission of ECERS: J.Europ.Cer.Soc. [25]).

different amounts of domains [65; 88]. Furthermore, the dielectric permittivity, coercive field (Ec) and remnant polarization (P_r) have been found to be strongly grain size dependent quantities [89; 90]. GBs have also an impact on the switching kinetics of ceramics [91–93].
While dipoles in a single crystal can accommodate each other by compensating charges and stresses on domain boundaries, the same does not necessarily occur between grains, as different grains have a different crystallographic orientation. A crystallographic mismatch always leads to a polarization mismatch between neighbouring grains, thereby resulting in the appearance of internal charges and stress. It was found out that piling up of charges on GBs during a poling process plays a significant role in intergranular fracture, due to repulsive forces between the accumulated charges [94].
Charge formation on GBs in ceramics with crystals of tetragonal symmetry was estimated by Genenko *et al.* [7]. In their work, a ceramic was exemplarily considered as a tight array of cubic boxes as shown in Fig. 3.2, each box representing a fully polarized grain. The crystal structure of neighbouring grains was assumed to be independent because it forms at temperatures much higher than T_c. Fields induced by charge densities on the GBs were assumed to trigger charge-defect migration leading to material aging.
A *c*-axis mismatch in neighbouring grains produces substantial stresses when a ceramic is cooled down to T_c. This internal mechanical stress can be released by domain twinning, or by forming a martensite structure [95]. However, that is not always possible and highly stressed regions may occur. In Ref. [96] an anomalously high dielectric permittivity (up to 6000) in a fine-grained BT ceramic was explained by the absence of 90° twinning within grains, giving rise to internal stresses (up to 800 kg/cm^2) as the ceramic cools below T_c. The thickness of 90° DWs was measured by Little to be approximately 0.4 μm [39]. In contrast to coarse-grained ceramics,

where grain sizes are about 10-50 μm [97], in a fine-grain ceramics with grain sizes of about 1 μm, the existence of a DW of 0.4 μm size is very unlikely. Therefore, in fine-grain ceramics, the amount of 90° twinning within the grains is quite low, giving rise to internal stresses as the ceramic is cooled below T_c. The work of Kelman and McIntyre [98] provides observations of 90° DW motion to accommodate inner strains in $Pb(Zr_{0.35}Ti_{0.65})O_3$ thin films.
In contrast to a single crystal, ceramics may have GBs where domains are cut off. However, by means of electric and/or elastic interactions, domains can proceed from one grain to another. This was observed experimentally for BT [99] and for PZT [100]. Arlt and Calderwood proposed that the electric field of one grain triggers the evolution of a neighbor [101].
Internal stresses participate in domain reorientation in a similar manner to external stress. Uniaxial compressive stress causes domains to orient in the plane perpendicular to an applied stress. On the other hand, tensile stress causes a domain to orient along the lateral direction. Such an influence was observed in Ref. [102], where remanent polarization increased under compressive strain and decreased under tensile strain.
Configurational averaging of local angle-dependent variables, such as polarization or electric field, is equal to the averaging over a sample volume and can be performed by using a distribution function $f(\theta,\varphi)$ of possible polarization directions compatible with an applied field direction. Derivation of this function is a non-trivial task which involves cumbersome calculations. For the case of tetragonal symmetry, the appropriate distribution function, $f(\theta,\varphi)$, was derived in Ref.[7]

$$f(\theta,\varphi)=\begin{cases}\dfrac{3}{2\pi}, & 0\le\theta\le\dfrac{\pi}{4}\\ \dfrac{6}{\pi^2}\left[\dfrac{\pi}{4}-\arccos\left(\cot\theta\right)\right], & \dfrac{\pi}{4}\le\theta\le\theta_{max},\end{cases} \tag{3.1}$$

for $0\le\varphi<2\pi$ where φ, θ and θ_{max} are, respectively, the azimuthal, polar angle and maximum possible polar angle in spherical coordinates associated with the above introduced Cartesian coordinates, see in Fig. 3.2, and centered in the center of the chosen grain.

3.2 Polarization kinetics in ceramics

A substantial part of this section is based on the review of Damjanovic [28].
Starting with pioneering studies by Berlincourt and Kruger it was established that both 180° and non-180° switching events contribute in poling process of ceramics [82; 103–105].
Applying *in situ* high-energy X-ray diffraction (XRD) J. Daniels *et al.* identified relative intensities I_{002} and I_{200} of the (002) and (200) tetragonal doublet, respectively, to characterize the evolution of a non-180° switching event. The higher the relation I_{002}/I_{200} the more domains have *c*-axis oriented parallel to the applied field. As is seen in Fig. 3.4, the I_{002}/I_{200} ratio changes during the poling time, providing evidence for non-180° switching events [26].
In situ 3D-XRD of a polycrystalline PZT ceramic revealed that nearly 80% of domains have switched by consecutive 90° reorientations. It was also observed that XRD peaks change depending on the applied electric field [79]. Bowman *et al.* used the polarization difference maps

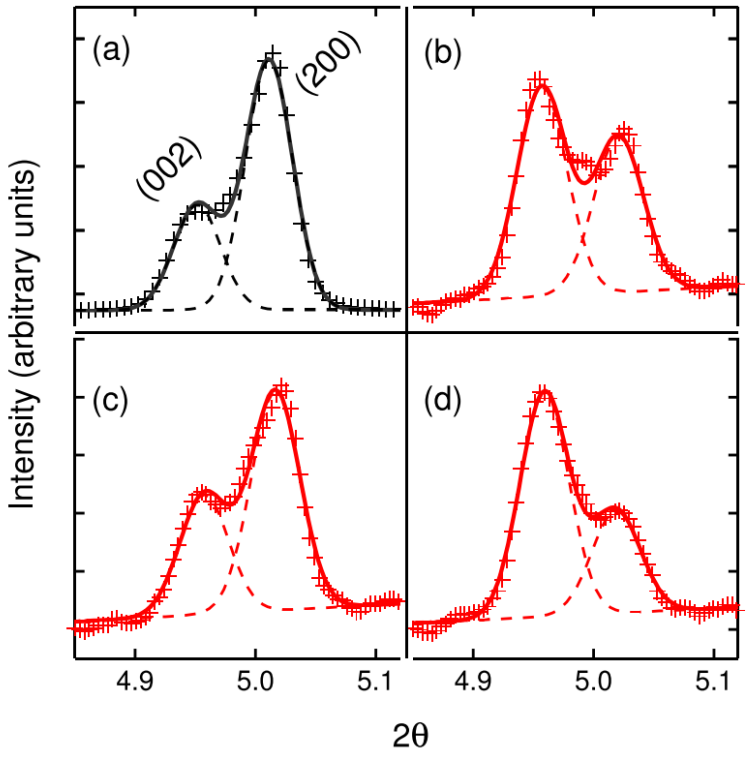

Figure 3.4: (a) Initial diffraction profile of the unpoled sample, (b) remanent state after initial poling, (c) after 1 ms, i.e., intermediate state during polarization reversal, and (d) after 1000 ms. The solid lines represent the total fit profile, while the dashed lines are the individual peak component profiles (Reproduced from [26], with the permission of AIP Publishing).

(PDM)s technique to visualize the polarization map of 180° switching and non-180° in 100 nm thick polycrystalline $PbZr_{0.2}Ti_{0.8}$ thin film [27]. As is seen in Fig. 3.5 most of the sample was switched by 90° events.

Contrary to previous results, Fancher *et al.* [106] had performed polarization measurements of a commercial soft polycrystalline bulk PZT ceramic (K350) and concluded that the largest contribution in polarization originates from 180° switching events (near 80% of the total polarization). Analogous results were also reported for a BT polycrystalline material, where 180° switching events reach up to 70% of the total polarization. Polarization switching in tetragonal ferroelectric ceramics can be achieved by generating new 90° DWs at the boundary of each grain and their migration through the grain driven by an electric field. This transient DW is perpendicular to the regular 90° DWs. Then the polarization is rotated by 90° and the average polarization of the grain is rotated by 180° [23; 107].

As was discussed, due to complex elastic and electrostatic interactions a ferroelectric tends to split into domains to minimize its free energy, hence having zero net polarization. One way to bring it to a polar state is to subject it to an electric field. Then one preferable direction appears and domains tend to align along this direction.

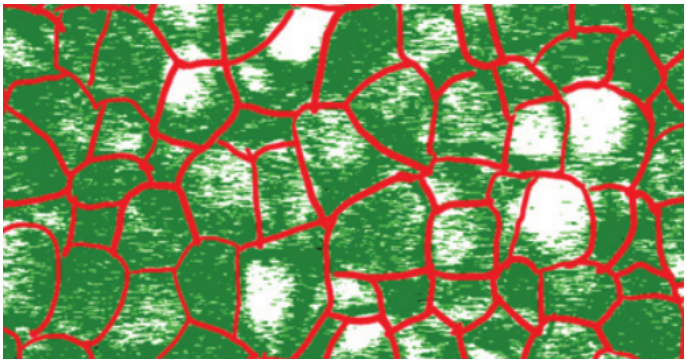

Figure 3.5: A map of fully polarized $PbZr_{0.2}Ti_{0.8}O_3$ created by PDMs. Regions switched by 90° and 180° are colored in green and white colours respectively (Reproduced from [27], with the permission of AIP Publishing).

Let us consider the poling process of $Pb(Zr_{0.45}Ti_{0.55})O_3$ with 1.3 μm thickness. Point A in Fig. 3.6 corresponds to a virgin state. While the applied field is comparatively small we can observe a linear polarization–field dependence, which is a general phenomenon described by Eq. (1.1). On the segment A–B no domain reorientation is expected. However, as the field gets stronger, orientation along the field requires significantly smaller energy. This triggers domain reorientation which is as avalanche-like process characterized by a strong non-linearity of the P–E curve, corresponding to the segment B–C. Once most of the domains are aligned, the materials again demonstrates linear P–E behaviour (segment C–D). This is due to several processes, one of which is an elongation of already oriented domains, described by the second term in Eq. (1.5), another is partial reorientation of polarization, which was not switched on the segment B–C.
It is important to note that in contrast to the idealized situation of a single crystal, not all domains (cells) can be switched. Some of them may be pinned on defects or substantial fields which arise because of insurmountable interaction with already switched neighbours.
If the field strength starts to decrease, some domains switch back, but when the field decreases to zero, the net polarization remains (point E). This polarized state is known as remanent polarization (denoted above as P_r). Obviously $P_r \leq P_s$, where P_s is the saturation polarization. P_r depends on many factors, such as the crystal symmetry, sample geometry, crystal structure, and the presence of defects.
The field necessary to bring the polarization to zero is called the coercive field (E_c). Strictly speaking, the coercive field is not a rigorous value for a given material; if a smaller field is applied for a substantially long time, the material starts to switch, approaching a zero polarization value. The poling process could therefore be referred as a relaxation-like process rather then threshold-like behaviour process, when the process simply takes a longer time to transpire if correspondingly strong forces are not applied.

If the field periodically changes its direction, and a material reaches maximum polarization during each poling cycle, a hysteresis loop appears as shown in Fig. 3.6.
Ideally, a hysteresis loop should possess a symmetrical form relative to the P and E axes. However, a symmetry violation is sometimes observed [108–110]; for instance, thin films are quite

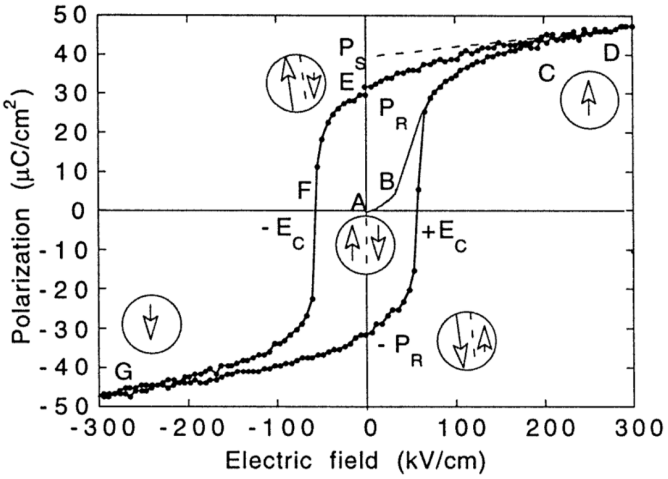

Figure 3.6: Ferroelectric (P–E) hysteresis loop. Circles with arrows represent the polarization state of the material at the indicated fields. The symbols are explained in the text. The actual loop is measured on a (111)-oriented 1.3 μm thick sol-gel $Pb(Zr_{0.45}Ti_{0.55})O_3$ film (Reprinted by permission of Rep.Prog.Phys. [28])

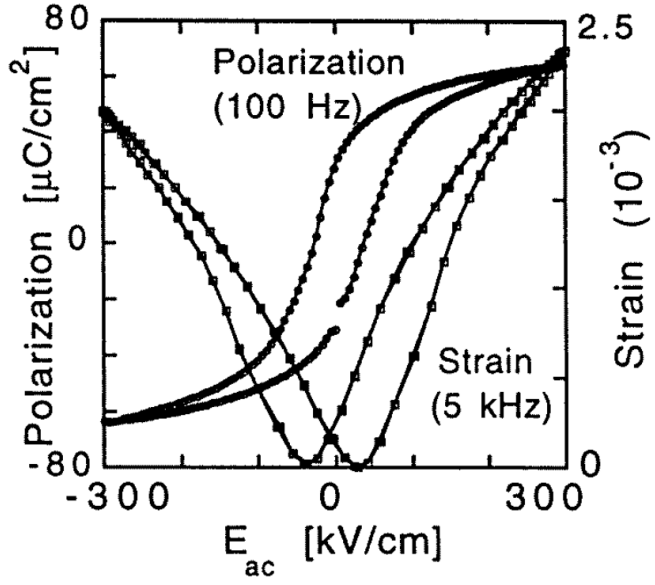

Figure 3.7: Polarization and strain loops measured on (111)-oriented, 322 nm thick, sol-gel $Pb(Zr_{0.53}Ti_{0.47})O_3$ (Reprinted by permission of Rep.Prog.Phys. [28]).

sensitive to electrode-ferroelectric interface [111] and a spacial charge formation [112]. Hysteresis asymmetry normally emerges as a result of fatigue owing to a charge migration to the GBs [67] or to other pinning sites.
Another characteristic hysteretic loop for ferroelectrics is a strain-field loop, the form of which resembles a butterfly. This loop accompanies electric hysteresis loop and it makes sense to explore them together, as shown in Fig. 3.7.
It is well established that, solids can change their size under an electric field, the common example thereof being electrostriction, see Eq. (1.2). Less common is the converse piezoeffect, see Eq. (1.3). Both effects are present in ferroelectrics, where the quadratic term of the electrostriction, see Eq. (1.6) plays a noticeable role due to non-180° rotations.
If at this point a strain-field loop is compared to polarization-field loop, we can see that coming from the $-P_s$ state to zero, we have strain reduction, as initially stretched sample shrinks, due to non-180° switching events. A minimum value of strain can be observed at the coercive field where most part of the material is switched and the average polarization is zero. As the applied field continuously increases, the material polarizes in the field direction by domain reorientation. We can observe a rapid increase in strain, which slows down with time because most of the domains were reoriented. At this point, the piezoeffect starts to dominate, as further polarization is predominantly due to unit cell elongation.

3.3 Models to describe polarization kinetics

In most of the cases such complex systems as ferroelectrics cannot be described by models in a closed analytic form, therefore computer simulations are of great importance. Most atomic calculations are based on a solution of the Schrödinger equation. Such a compelling approach provides direct information about the physical properties of an object of interest. However, the significant complexity of such an approach makes it difficult to apply to complex structures as solid solutions, which most of ferroelectrics are. The close analogue to the direct Hamiltonian approach is the density functional theory (DFT) utilization, which implies a density functional instead of direct referring to a wave function of a system. This method is used to investigate thermodynamic and kinetic properties of ferroelectrics [113]. However, ideally, the DFT has to be applied at 0 K with a regular structure. Molecular dynamics and Monte Carlo simulations are powerful means based on a statistical approach [76; 114; 115]. They allow materials investigation on an atomistic level and are useful for describing effects on the corresponding scale [116; 117]. But being also resource demanding, these approaches hardly allow kinetic investigations on a macroscopic scale. Probably, the most widely used simulation approach to describe polarization and mechanical evolution in ferroelectrics are methods based on the Landau-Ginzburg-Devonshire (LGD) theory [118], where an order parameter is introduced and its distribution within a material is defined by minimization of the system energy. An order parameter can be any quantity, which affects the energy of a system, for example, polarization or stress. While polarization-field or stress-field dependencies for ceramics could be obtained as solutions of a static problem [119], kinetic problems in ceramics are more complicated, therefore are not considered by the LGD approach. This approach is, however, typically applied to

well-ordered systems.
The only analytical approach which is widely used for an investigation of disordered systems is a macroscopic statistical approach. Such an approach is the classical KAI model based on the concept developed to describe solidification [1] and assumes random and statistically independent nucleation and growth of reversed polarized domains in an uniform medium [2; 3].
The model assumes an infinite crystal and recognizes motion of DWs after a nucleation as the primary process for switching. The DW velocity v is also assumed to be constant for a given applied field E.

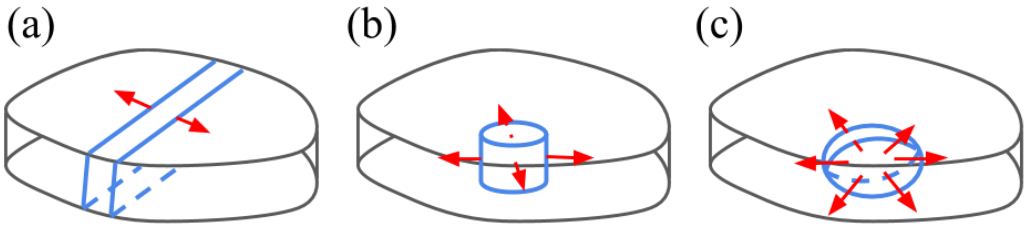

Figure 3.8: Shape of the growing domains of reversed polarization. (a), (b), (c) correspond to one, two an three dimensional growth, respectively.

The growth of a domain may either be one, two, or three-dimensional (Fig. 3.8): (a) stripe-like domain expanding in width, or (b) cylindrical expanding radially, or (c) bubble-like expanding spherically.
The main idea of the KAI model is to estimate probability of a particular point to be inside of a switched region during a time period $t-t'$, where t' is an initial moment of a nucleation. The probability depends on domain geometry which is represented by the Avrami index α, and domain growth velocity v in the following way

$$S(t,t') = C[r_c + v(t-t')]^{\alpha}, \tag{3.2}$$

where α is a dimensionality of a domain growth.
If the nucleation rate per unit volume and time is $R(t)$ then a probability of a particular point not to be covered by a switched region at the time moment t is

$$\Xi(t) = \exp\left(-\int_0^t R(t')S(t,t')dt'\right). \tag{3.3}$$

Then the total polarization variation is

$$\Delta P^k(t,\tau) = 2P_s[1-\exp(-(t/\tau)^{\alpha})], \tag{3.4}$$

where τ is the characteristic time assumed to be given by the Merz law Eq. (2.7), and the α represents an effective dimensionality of a domain growth.
The original relation Eq. (3.4) does not hold for more complicated structures than a single crystal, such as thin films [4; 29; 120], organic-ferroelectric composites, or bulk polycrystalline

samples [121; 122]. The KAI function yields, when plotted on a logarithmic time scale, a nearly symmetric curve with respect to its inflection point. This is not reproduced by experiments, for instance on ceramics, as polarization reversal curves are mostly non-symmetric with a quasi-linear tail on a logarithmic time scale in the end of a process.
The assumptions made about domain growth in the KAI model are reasonably justified for bulk single crystals, but hold no longer in thin ferroelectric films and ceramics. There, other polarization processes with a broad distribution of relaxation times contribute noticeably [29].
Furthermore, the KAI model assumption of unrestricted domain growth after a nucleation is unfounded for real materials which are not defect-free. These defects effectively pin DWs and thus limit a region the domain can maximally occupy. The NLS model [4] addresses these issues by dividing a sample into elementary regions, which have different sizes and switching kinetics. Basically an i^{th} elementary region is characterized by its volume fraction ς_i and its waiting time τ_i. The NLS model additionally assumes, that once a nucleation centre in an elementary region is formed, the region is basically switched. The waiting time τ_i, consequently, is assumed to be much bigger than the time it takes to let the nucleus of opposite polarization grow to its maximum extent restricted by defects.
The equation for $P(t)$ then gives

$$P(t) = 1 - \langle \varsigma_i \exp(-t/\tau_i) \rangle, \tag{3.5}$$

where $\langle ... \rangle$ denotes volume averaging.
If now the sample is divided into many regions the continuum approach is justified

$$\langle \exp(-t/\tau_i) \rangle = \int_0^\infty \exp(-t/\tau) g(\ln(\tau)) d\ln(\tau), \tag{3.6}$$

with g being a distribution function for waiting times which and obeying to the normalization condition

$$\int_0^\infty g(z) dz = 1. \tag{3.7}$$

Comparison of the two models is shown in Fig. 3.9 where experimental results on PZT film were fitted by Gruverman *et al.* [29]. It is clearly seen from the graph that the introduction of SwT distribution noticeably improves the fitting.
However, the reason for such a SwT distribution remained unclear. Lupascu *et al.* [5] suggested that a field distribution inside a ferroelectric matrix is responsible for a SwT distribution: "In a polycrystalline material the local projections of the external field onto the permitted polarization directions in each grain cover a wide range of local fields and thus time constants.". It was motivated by the strong $\tau(E)$ dependence described by the Merz law Eq. (2.7).
Based on this assumption Genenko *et al.* [6] conceived the IFM model. It reconstructs polarization kinetics based on statistical field distribution. The model assumes the existence of a threshold field $E_{th}(t)$ at which reversal switching occurs, important to highlight that the threshold field is time-dependent value. That means ideally polarization-time behaviour of the region which is subjected to a field $E = E_{th}(t)$ should be described by a step-like function. The time-dependent total polarization can be expressed in a form

$$\Delta P(t) = 2P_s \int_{E_{th}(t)/E_a}^\infty f(s) ds, \tag{3.8}$$

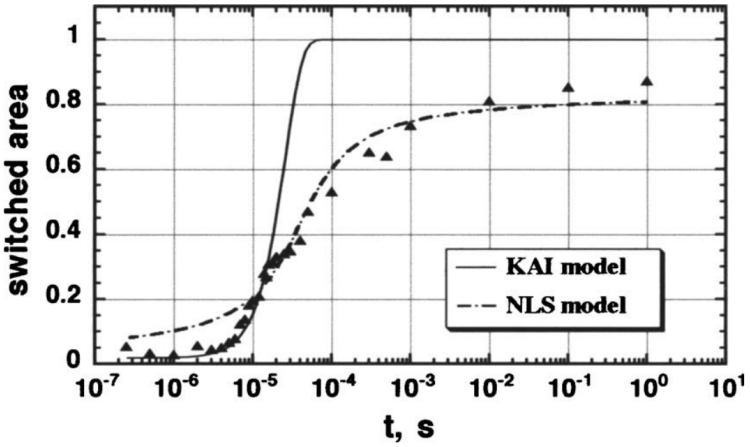

Figure 3.9: Fitting of the time dependence of the switched area of PZT/Pt capacitor (triangle dots) of 180 nm thickness for the 1.2 V bias by the KAI function (solid line) and the NLS model (dashed line) (Reproduced from [29], with the permission of AIP Publishing).

where $\Delta P(t)$ is polarization variation, f(s) is an electric field amplitude distribution function, with $s = E/E_a$, and E_a is an applied field.
The applicability of the IFM model can be judged from a function presenting a derivative of the local polarization response with respect to the applied electric field

$$D(s) = \frac{E_a}{2P_s}\left(\frac{\partial \Delta P^k}{\partial \tau}\frac{\partial \tau}{\partial E}\right), \tag{3.9}$$

where ΔP^k is polarization variation which changes according to the KAI model Eq. 3.4 at a field value E. The IFM model works well in case when $D(s)$ is much more narrow then $f(s)$ [6; 8], that is physically identical to the Heaviside-Function behaviour assumed previously. If the condition is met then logarithmic derivative $\frac{1}{2P_s}\frac{\partial \Delta P}{\partial \ln(E)}$ would scale to the same function which represents a fingerprint of the system, see Fig. 3.10. Polarization-field curves were measured at different poling times, Fig. 3.11 (a). Obviously, the longer the poling time in the given field is the higher polarization is achieved. The logarithmic derivative were calculated from these curves, Fig. 3.11 (b). As is seen, all peaks are approximately at the same height, which meets the scaling criteria. A peak position of the logarithmic derivatives corresponds to E_{max}, using which the fingerprint function can be found, Fig. 3.11 (c). It was found that E_{max} can be well fitted by $E_0/\ln(\frac{t}{\tau_0})^{\frac{1}{\alpha}}$ function, Fig. 3.11 (d).

Having the fingerprint of the system, the field distribution function was found out, Fig. 3.11 (e). Having the statistical field distribution function, polarization-time curves were reconstructed and compared to experimental measurements, Fig. 3.11 (f). The model reproduces experimental measurements with high accuracy.
A common drawback of the statistical models [2–4; 123; 124] is the assumption of independent nucleation regions and uncorrelated growth of reversed domains, thus virtually neglecting the

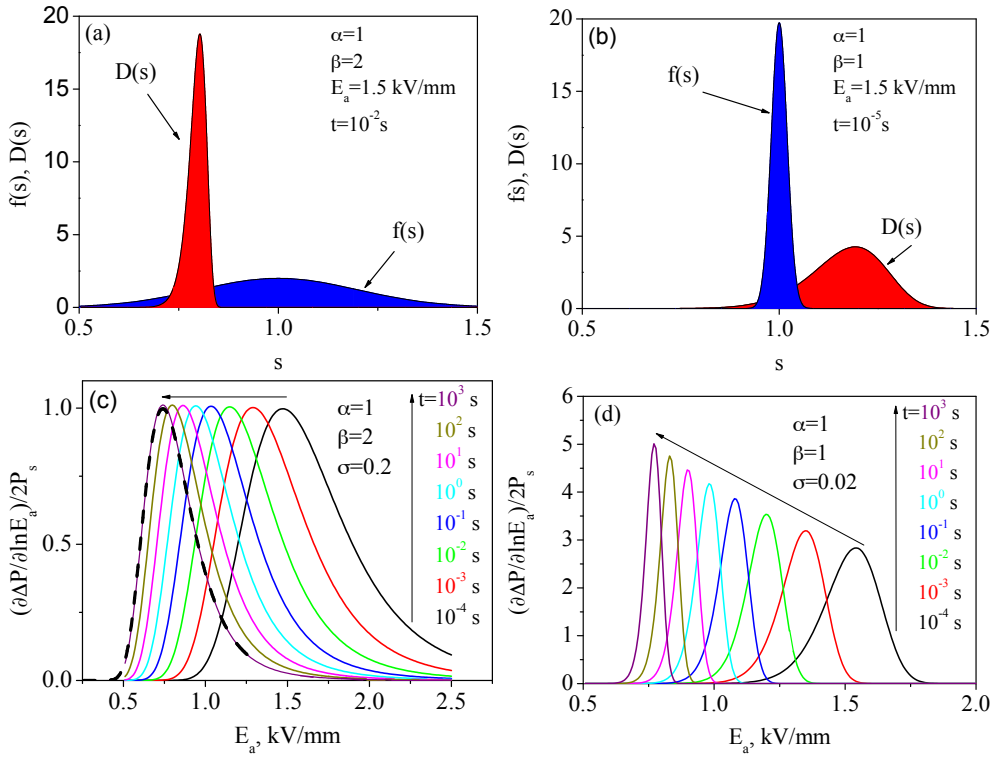

Figure 3.10: Model field derivative of the local polarization $D(s)$ and the distribution function $f(s)$ for the case when this distribution is (a) much wider and (b) much more narrow than the derivative peak. (c) Model calculations of the logarithmic field derivative for the case described in (a), (d) the same calculations for the case described in (b), adopted after [6].

feedback of a depolarization field during polarization reversal. However, in many cases they can successfully describe experimental results, for instance the IFM model [7; 125] also assuming independent polarization switching in individual regions describes the time-dependent response of various ferroelectric ceramics of different chemical compositions and phase symmetries [7; 8; 125–128] as well as of semicrystalline polymers [129] with high accuracy.

There are a number of piezoelectric systems which are interesting with regard to the influence of texturing of crystalline anisotropy and its symmetry on their functional properties. For example, polycrystalline ceramics incorporating increasingly complex crystal systems (e.g., those with monoclinic symmetry or monoclinic distortions of a unit cell) [130; 131]. Field distribution begins to play an even more essential role in textured materials, where an additional inhomogeneity is incorporated [130]. Texturing plays an important role in enhancement of different properties of polycrystalline ceramics, for instance, piezoelectric properties [132], or temperature stability [133], and introduces a difference in poling directions [127; 134]. A notable example of textured materials are ceramics with oriented pores. Pores are hollow inclusions with a low relative dielectric permittivity. As most of the properties reveal on the pore/host interface a shape and a size of pores play an important role.

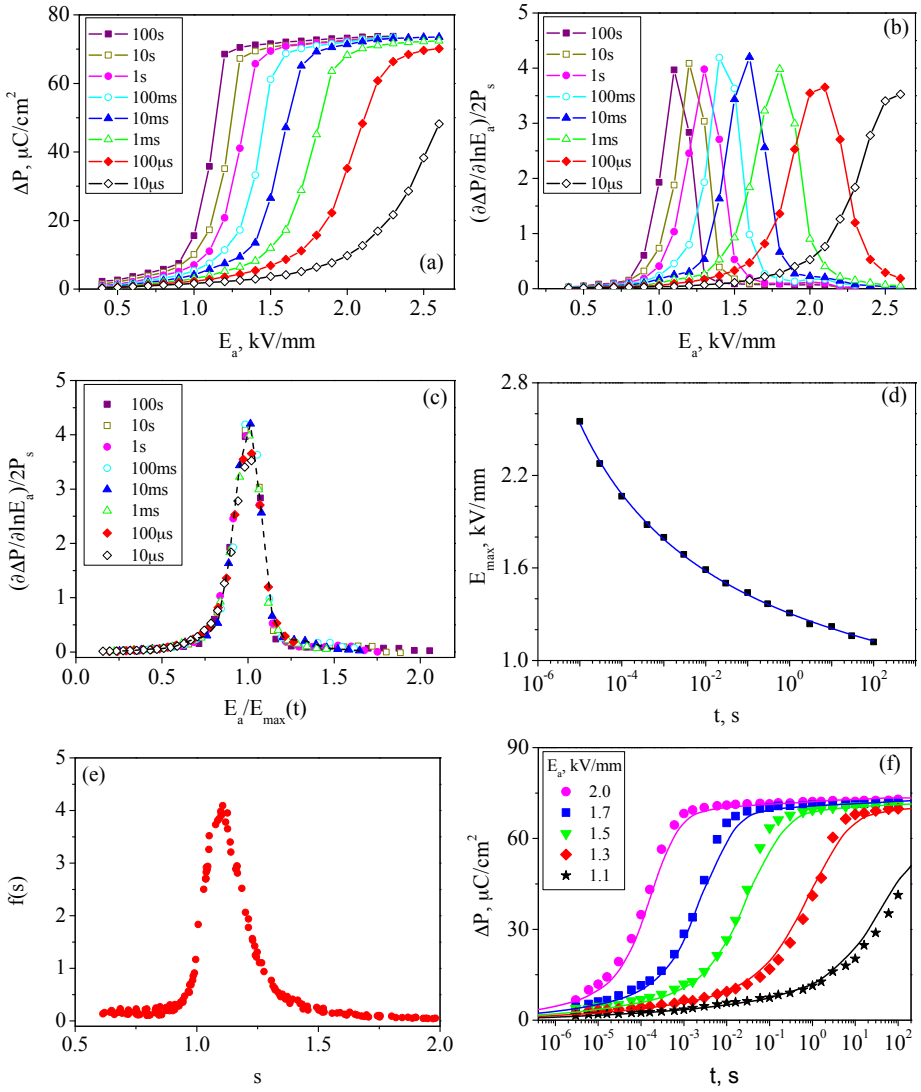

Figure 3.11: (a) Switched polarization of PZT ceramic ΔP as a function of applied field E_a at different poling times t as indicated, (b) its logarithmic derivatives versus applied field, (c) the same derivatives scaled to their maximum positions $E_{max}(t)$, (d) fitting of $E_{max}(t)$ with an inverse logarithmic function, (e) the weighted statistical distribution of the local field values $f(E/E_a)$ in PZT as extracted, (f) representation of the time-dependent polarization reversal in PZT for different applied fields E_a and respective experimental data shown by symbols, adopted after [6].

Ferroelectric materials are utilized in various applications exhibiting several functional properties, such as large permittivity, switchable spontaneous polarization, large electromechanical coupling, pyroelectricity, electro-optic effects, and others [135]. Besides, through the compositional and microstructural engineering, the properties of these materials can be additionally tailored by the formation of composites, whereby the second phase of low permittivity, such as polymer or air, is introduced into the structure [136]. For example, porosity results in increase in the ratio between the longitudinal and transverse piezoelectric coefficients, which in turn increases the hydrostatic piezoelectric coefficient [137]. Such parameters as porosity, pores size and shape may tailor properties of a material, for instance, dielectric, piezoelectric [138; 139], or pyroelectric response [140].

An inhomogeneous field distribution attributed to pores inclusions is a key to various functional properties, as shown by computer simulations compared with experiments on porous PZT and BT ceramics [141–144]. Particularly, dielectric permittivity and voltage-driven tunability can be engineered by using anisotropic porosity (pore shape and orientation) as a tailoring factor. Related studies [142–144] were mostly focused on nonlinear dielectric properties and the impact of porosity on the effective macroscopic permittivity. Two-dimensional (2D) field simulations [142] have shown ways to increase tunability whilst reducing permittivity for small porosity levels. More advanced 3D modelling of porous [143] and other composite [144] materials allow consideration of high porosity where the effective-medium approach fails. A comprehensive thermodynamic and micromechanical approach was developed by Jayendiran *et al.*, which was able to describe the viscoelastic behaviour and nonlinear electromechanical response of regular idealized piezocomposite structures [145–147].

While structural and functional properties are well studied [148], an influence of porosity, pores shape and orientation on a field statistical distribution and the corresponding SwT distribution are less understood, although a switching of a spontaneous polarization is a basic feature of ferroelectric materials, distinguishing them from other dielectrics. Analysis of ferroelectric switching in a similar system of sodium nitrite: poly(vinyl alcohol) composite films has shown the great effect of composition on polarization-switching kinetics [149; 150].

Obviously, introducing a statistical field distribution provides a better description of the experimental results. However, both the NLS and the IFM assume a static field distribution, which does not take into account the feedback of depolarization fields. According to Eq. (2.4) this field is produced by charge densities on the GBs which should change in time with polarization evolution. Furthermore, the produced field should yield a long-range correlation. Long-range correlations are supposed to condition coherent switchings of grains which is not captured in the above statistical models as all switching events are assumed to be independent.

In principle, in the case of long-range correlations, a specially and temporally coherent switching may keep the depolarization fields small. This would explain, on the one hand, a weak effect of the depolarization field, but also means, on the other hand, that switchings in different regions cannot be considered as independent.

The importance of collective domain dynamics was recognized and studied in thin ferroelectric films for more than a decade by various methods. Strong correlations of domain structures extending across the GBs have been observed by piezoelectric scanning probe microscopy in polycrystalline thin films [151] and by transmission electron microscopy and piezoresponse force

microscopy in model single-grain structures [152–154]. Polarization response exhibited clustering ranging from few grains [151] to agglomerations of near 100 grains [155; 156].
Extremely long-range electrostatic correlations were predicted for uniform media by phase-field simulations [157] and by a microscopic model describing self-consistently the polarization reversal randomized by thermal vibrations [76]. However, the role of long-range electrostatic interactions in the switching dynamics of bulk ferroelectric ceramics still remains unclear. Thus, a paradoxical ability of the statistical concepts, which neglect the feedback of depolarization fields, to accurately describe polarization switching kinetics in a variety of inorganic ferroelectric ceramics [4; 6; 8; 123; 125–128; 158], organic ferroelectrics [23; 129; 159–163], and organic-inorganic ferroelectric composites [149; 164] needs to be comprehended.
Viola *et al.*[165] introduced a model to simulate polarization kinetics, taking into account such mechanisms as nucleation and domain growth. Coming from Ref. [166] authors assumed that a switching rate controlling mechanism is domain expansion rather than a nucleation, because the growth is calculated to be extremely fast compared to the nucleation rate. Each polarization variation either by nucleation or DW motion contributed to the total energy of the system by means of depolarization and stress fields generation. An impact of all switched regions was averaged over the sample and summarized into some effective field. This field provided an impact on the polarization kinetics together with an applied permanent electric field. The model allows to study influence of two mechanisms on polarization retardation with time: one is an evolution of internal fields (depolarization and stress fields), another is exhaustion of nucleation centres. To enlighten polarization rate-time dependence a PZT ceramic was experimentally investigated. Comparison of the experimental measurements of the polarization kinetics with simulations allows suggesting that internal field monotonically increases with polarization evolution and is a major mechanism of polarization retardation.
Lou [30] developed an elaborate model to take into account a feedback of a field from each polarized grain in thin film-like granular structures, see Fig. 3.12. It is assumed that a thin dielectric layer exists between a film and electrodes, so the field on the surface of the film is not screened by the electrodes. Introducing a dielectric layer between film and electrodes seems to be a little artificial, but it has been experimentally shown, that thin dielectric layers emerge due to the contact with the electrodes [167].

The depolarization field in poled Pt/PZT/Pt capacitor with interface layers has been taken in accordance with [168]

$$E_d(t) = -\frac{d_i P(t)}{d\varepsilon_i \varepsilon_0}, \tag{3.10}$$

where d is a film thickness, d_i is a dielectric layer thickness, ε_i the relative dielectric permittivity, P_s is a spontaneous polarization, ε_0 is dielectric susceptibility in vacuum.
Obviously, the depolarization field depends on polarization and thus is time-dependent, so that a total field is also time-dependent and now can be expressed as

$$E_{tot}(t) = E_a + E_d(t) = E_a - \frac{d_i P(t)}{d\varepsilon_i \varepsilon_0}, \tag{3.11}$$

where E_a is the applied field.
It is seen from Eq. (3.11) that depolarization increases the field of the system while $P < 0$, and

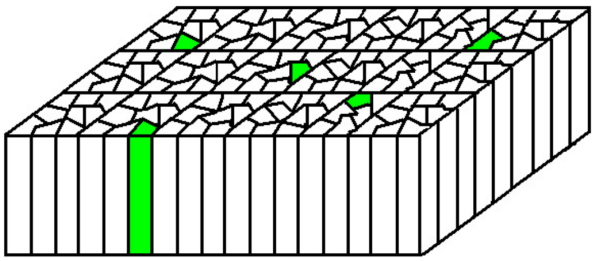

Figure 3.12: Diagram of the polarization reversal according to Lou's model. The green regions denote areas which have already been switched, e.g. polarization pointing downwards, whereas white regions indicate non-switched parts with polarization pointing upwards. The electrodes on the top and bottom and the thin dielectric layer inducing the depolarization field are not drawn (Reprinted by permission of Journal of Physics: Cond.Matt. [30]).

decreases while $P > 0$.
Taking d=200 nm, d_i=2 nm, and values for ε_i=40, and $P_s = 30\mu C/cm^2$ adopted from [169], a value of the maximum depolarization field was estimated up to 85 kV/cm.
We assume that the probability $1/\xi$ of a retained part to switch until time t is described by the Merz law Eq. (2.7)

$$\frac{1}{\xi(t)} = \frac{t}{\tau_s} = \frac{t}{\tau_0 \exp(\frac{E_A}{E_{tot}(t)})}. \tag{3.12}$$

By dividing the ferroelectric into M_0 equally sized domains, see Fig. 3.12, and using Eq. (3.11) in Eq. (3.13), Lou obtained a system of equations to describe a probability of the domain switching [30]

$$\begin{aligned}
\frac{M_0 - 1}{M_0} &= \exp\left(-\frac{t_1}{t_0}\left(-\frac{E_A}{E_a - \frac{d_i P_{M_0}}{d\varepsilon_i\varepsilon_0}}\right)\right) \\
&\vdots \\
\frac{M_0 - N - 1}{M_0 - N} &= \exp\left(-\frac{t_{N-1}}{t_0}\left(-\frac{E_A}{E_a - \frac{d_i P_{M_0}}{d\varepsilon_i\varepsilon_0}}\right)\right) \\
&\vdots \\
\frac{M_0 - M_0}{M_0 - M_0 + 1} &= \exp\left(-\frac{t_{M_0}}{t_0}\left(-\frac{E_A}{E_a - \frac{d_i P_1}{d\varepsilon_i\varepsilon_0}}\right)\right) = 0,
\end{aligned} \tag{3.13}$$

where t_N is the time interval between the switching of the (N-1)-th and N-th domain. The complete switching time t then follows as

$$t = \sum_i^N t_i. \tag{3.14}$$

The corresponding polarization change is just the fraction of switched domains

$$\frac{\Delta P(t)}{2P_{M_0}} = \frac{N}{M_0}. \tag{3.15}$$

The obtained switching curves (Fig. 3.13) show the retardation behaviour at later stages in the switching process which cannot be described in the KAI-model with neglecting of the depolarization field. Later on, Genenko *et al.*, have introduced the self-consistent mesoscopic polariza-

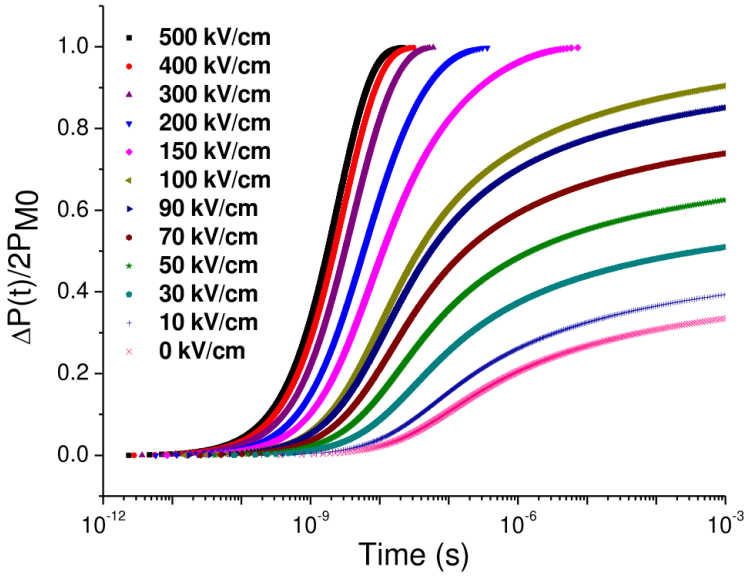

Figure 3.13: Polarization kinetics curves calculated by Lou for different applied fields (Reprinted by permission of Journal of Physics: Cond.Matt. [30]).

tion switching (SMS) model [31] which in 1D case solves the problem stated by Lou but in a much simpler way. The analogous to Lou's structure was considered: two electrodes separated by ferroelectric films with thickness d, and thin insulating layers between electrodes and ferroelectric with thickness d_i, see Fig. 3.14. In contrast to Lou, no granular structure was specified, considering only mean polarization of the ferroelectric and not each grain separately. That allowed the authors to solve one differential equation for the global polarization instead of solving 100-500 equations as Lou did [30].

Assuming polarization of the ferroelectric at the beginning $-P_s$, a voltage is applied to polarize it in the opposite direction. If charge density on the electrodes at the moment of time t is $\sigma(t)$ and polarization of ferroelectric is $p(t)$ then field in the insulating layers equals $E_i(t) = \sigma(t)/\varepsilon_i\varepsilon_0$, and the field in ferroelectric equals $E(t) = (\sigma(t) - p(t))/\varepsilon_f\varepsilon_0$, where $\varepsilon_i, \varepsilon_f$ are the dielectric constants of the insulating and the ferroelectric materials, respectively, and ε_0 is the permittivity of vacuum.

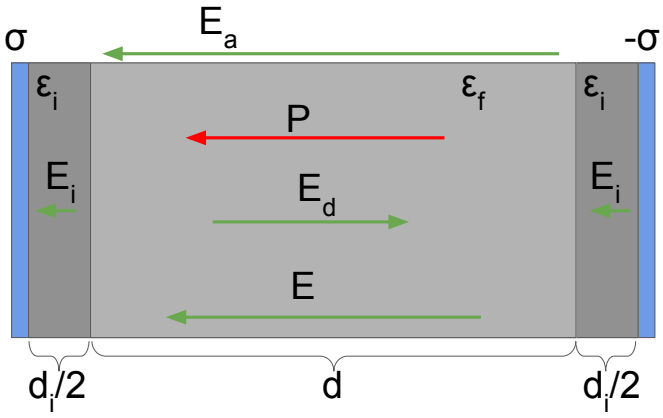

Figure 3.14: 1D-scheme of the field and polarization distribution in the initial state of the capacitor, adopted after [31].

The voltage between electrodes amounts as $V = E_i d_i + Ed$. It follows then:

$$\sigma = \frac{\varepsilon_0 \cdot V}{d_i/\varepsilon_i + d/\varepsilon_f} - \frac{p(t)}{1 + \varepsilon_f d_i/\varepsilon_i d} \tag{3.16}$$

and

$$E(t) = \frac{V}{d\,(1 + \varepsilon_f d_i/\varepsilon_i d)} - \frac{p(t) \cdot d_i}{\varepsilon_0 \varepsilon_i d\,(1 + \varepsilon_f d_i/\varepsilon_i d)}. \tag{3.17}$$

Eq. (3.4) was differentiated with respect to time to obtain an equation which describes polarization-time evolution. Taking into account the Merz law Eq. (2.7), with a single value τ inside the ferroelectric, a differential form of Eq. (3.4) has the form:

$$\frac{dp(t)}{dt} = \frac{P_s \mathrm{sgn}(E) - p(t)}{\tau} \alpha \left(\frac{t}{\tau}\right)^{\alpha - 1}. \tag{3.18}$$

Eq. (3.18) was solved for small time steps, and at each time step the depolarization field Eq. (3.17) was recalculated for actual values of polarization.
To compare results, all parameters were taken as in the work [30]. The comparison is shown in Fig. 3.15. The perfect coincidence of the results pointed out that the consideration of local polarizations by Lou gives no additional information above that obtained in the self -consistent mean-field treatment of the total polarization.
Attempts made so far to account for the feedback of depolarization fields remained mostly within the mean-field approximation which assumes emergence of a time-dependent specially uniform electric field due to averaging of multiple switching events [30; 165; 170]. The assumption of a uniform medium, however, is not applicable to a granular ceramic, where each grain can have unique structure thus providing inhomogeneity in form and principal axes orientation. The later brings an inhomogeneous distribution of a dielectric tensor which together with a polarization plays an important role in an electric field scattering. This fact makes the recourse to the mean

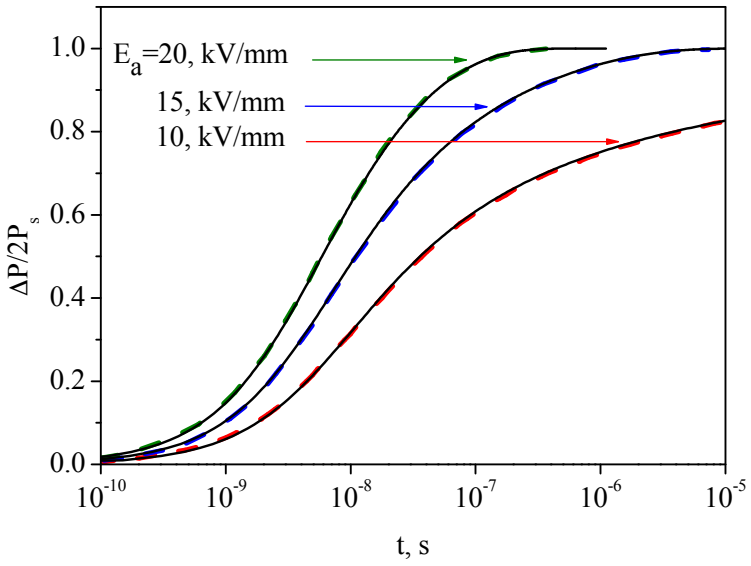

Figure 3.15: Polarization reversal with time for different magnitudes of the applied electric field as calculated by Lou [30] is shown by coloured dashed lines. The same quantity calculated using Eq. (3.18) is shown by thin solid lines for corresponding field values, adopted after [31].

field approximation strongly disputable for a granular ceramic. To study multi-granular structure the SMS model was extended to 2D [31].

A granular structure with a linear size L=20μm, which contains 400 grains(20×20 grains, $1 \times 1 \mu m^2$ each) Fig. 3.16, was generated using the Voronoi tessellation [171]. Then the direction of c-axes was randomly assigned according to the crystal symmetry. Authors considered 40/60 PZT with tetragonal symmetry, so Eq. (3.1) was used. Each grain was characterized by an activation field E_A, and a two-dimensional tensor $\varepsilon_{ij} = \varepsilon_0 K_{ij}$ with principal values of dielectric constants $K_\alpha = 499, K_c = 198$ [172; 173], with $P_s = 0.57$ Cm^{-2}. The system was placed between two electrodes and voltage assumed to be applied by stating a permanent potential difference (V) between electrodes. The electric field, induced by the potential difference inside the system, was evaluated by solving the Laplace equation using the finite element method (FEM). Because of an inhomogeneity of a dielectric tensor in the system, the electric field strays, which results in an inhomogeneous field map. Then field was averaged in each grain, thereby the electric field within each grain was substituted by its spacial average $\langle E \rangle_i$.

Two important approximations were used: polarization within each grain was supposed to be homogeneous, and only 180° switching events might occur.

Eq. (3.18) was generalized for the 2D case

$$\frac{dp_i(t)}{dt} = \frac{P_s \mathrm{sgn}(\langle \vec{E} \rangle_i \cdot \vec{n}_i) - p_i(t)}{\tau_i} \alpha \left(\frac{t}{\tau_i} \right)^{\alpha - 1}, \tag{3.19}$$

where p_i is polarization amplitude, and $\vec{n}_i$ is the unit vector along c-axis of an i^{th} grain. A c-axis which is assigned to each grain in the initial state.

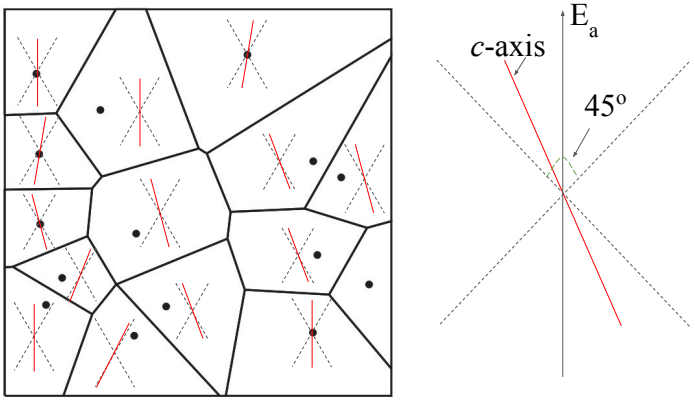

Figure 3.16: 2D scheme of randomly arranged and oriented grains of a polycrystalline ferroelectric (left). A c-axis lies within a cone of 45° (right), adopted after [31].

Eq. (3.19) is virtually one dimensional along the direction $\vec{n}_i$ within each grain while the two-dimensional coupling between grain enters this equation through the local field-dependent SwT

$$\tau_i = \tau_0 \exp(E_A/|\langle\vec{E}\rangle_i \cdot \vec{n}_i|). \tag{3.20}$$

Therefore, the rate of a local polarization switching is determined by the projection of the averaged local field onto the local polarization direction.
Eq. (3.19) was integrated using following parameters: $E_A = 25.3$ kV/mm, $\beta = 1$, $\tau_0 = 5 \cdot 10^{-11}$. Integration was performed by multiple time steps, evaluating actual field values between steps to take into account the field map evolution in the integration process. This results in polarization curves, which are shown in Fig. 3.17 (solid lines) for different applied fields. The curves are compared with those calculated with isotropic dielectric tensor with dielectric constant $\sqrt{K_a \cdot K_c}$ (dotted lines), and curves calculated by the KAI model (dashed lines).

The difference between curves can be explained by the field distribution. In the case of an anisotropic tensor a field inside a material is homogeneous, however, its value is smaller than V/L which results in the difference with the KAI, where a process is driven by V/L, that causes substantial retardation in the poling process. In the case with anisotropic tensor, the field is inhomogeneous, being at some places higher than V/L causing acceleration of the poling process, while at some places smaller than V/L causing polarization retardation, thus providing bigger spreading of the polarization-time curve compared to an isotropic tensor case.
To capture the electrostatic picture of ceramics another important modification of the model is taking into account discontinuous of the spontaneous polarization on the GBs, which forms charge densities and produces additional stray fields. Following the calculations in the work [7], a depolarization field produced by charge densities due to polarization mismatch is around one order of magnitude bigger than the typical coercive field for PZT. So, polarization was artificially reduced to $P_s = 0.02$ Cm^{-2} to depress local fields below the coercive field $E_c = 1.5$ kV/mm. Results are presented in Fig. 3.18 and compared to those where surface charge formation was neglected.

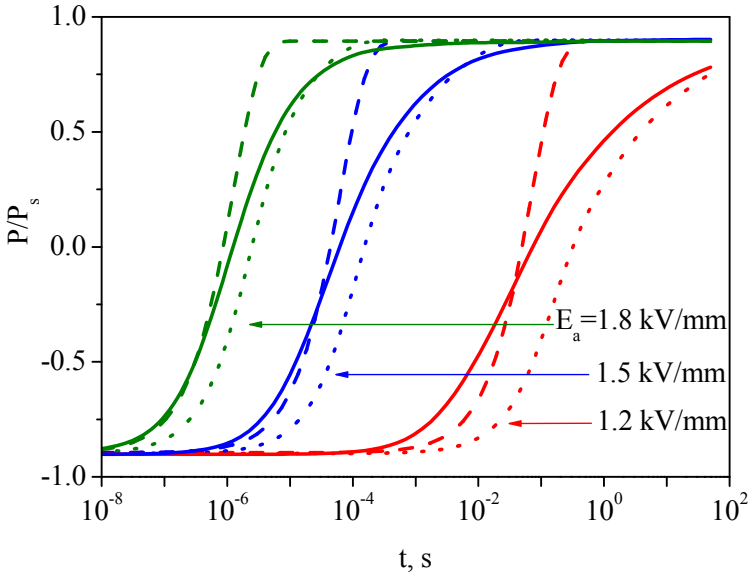

Figure 3.17: Polarization switching according to the KAI-law (dashed lines) compared to the response of systems with spacially disordered polarization directions and either isotropic (dotted lines) or anisotropic (solid lines) dielectric tensor for three different values of the applied fields ($E_a = V/L$), adopted after [31].

The difference between the curves can be explained by the normalized logarithmic field derivatives of the reversed polarization with respect to the applied electric field, introduced by Genenko *et al.* [6]. The logarithmic field derivatives evolution is shown in Fig. 3.19 for both cases with charge formation and without. The logarithmic field derivatives with charge densities taken into account are not so dispersed, thus the corresponding polarization curves are not so smeared, while curves without charge densities are experienced bigger retardation at a long time.

The Ref. [31] revealed the importance of field distribution for the poling process, as well as the influence of depolarization fields and charge formation, which is attributed to polarization mismatch and is unavoidable in granular ceramics.

Macroscopic and local measurements of nonlinear behaviour in mechanically clamped and released polycrystalline films revealed the dominant role of collective long-range strain interactions mediated by the local and global mechanical boundary conditions, possibly by elastic coupling through the substrate [174; 175]. The latest *in situ* high-energy x-ray diffraction advances allowed for the time resolution of different switching processes in bulk ferroelectric ceramics [26; 176; 177]. Furthermore, the grain resolved 3D-XRD was used to trace the non-180° switching events within polycrystalline bulk media [178; 179]. The collective dynamics in bulk materials was found to be correlated over approximately 10–20 grains, a scale presumably resulting from the complicated and still not understood interplay between the electrostatic field [180] and the elastic strain field.

Elastic interaction due to strain variation is conditioned by non-180° switching. Important to note is that polarization by consequent non-180° switching events cannot be described by inde-

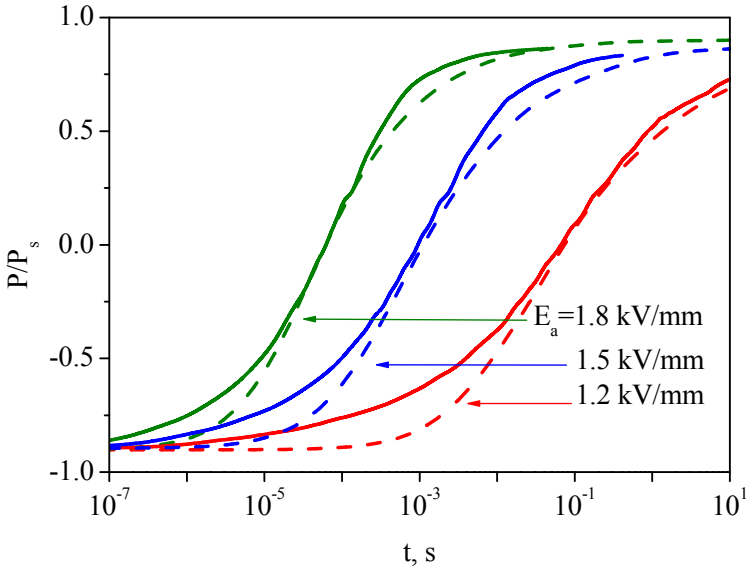

Figure 3.18: Normalized switching curves for various applied fields with substantial (solid lines) and a negligible (dashed lines) spontaneous polarization, adopted after [31].

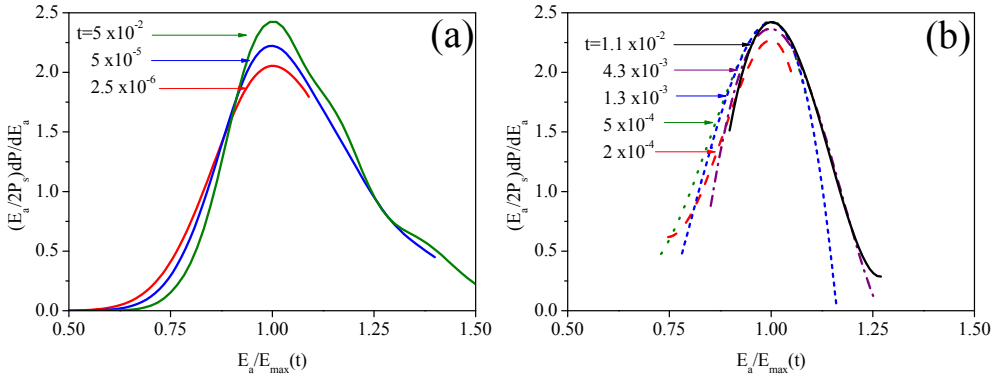

Figure 3.19: Normalized logarithmic field derivatives of the reversed polarization with respect to the applied electric field in the case of an isotropic dielectric tensor with (a) omitted charge formation, (b) charge formation, adopted after [31].

pendent switching mechanism as a second non-180° event might occur only after a first non-180° event had occurred. Thus, such switchings and consequently elastic interactions are not included in the current statistical models.
Consideration of non-180° is crucial for multiaxial ferroelectrics, which are the most widely used group of ferroelectric materials. Such two-step polarization reversals were observed by in situ x-ray diffraction measurements [79] and ultrasonic investigations [80]. Respective characteristic times for two distinct and sequential domain reorientation steps were determined [26]. Furthermore, some reports suggest that contributions from 180° switching events during the reversal process cannot be excluded [106; 181]. In order to distinguish between both contributions, the macroscopic strain of the polycrystalline sample should be measured simultaneously with the switched polarization.

4. Results

4.1 Review of objectives and results

The present chapter summarizes the problems considered in this dissertation and presents a review of the four publications which cover these problems.
Continuously developing techniques provide essential experimental data which has to be analyzed to describe materials behaviour and to design new materials with desired properties. Both static (activation fields, maximum polarization and strain, etc.) and kinetic (polarization and strain variations, depolarization fields evolution) properties has to be considered using different modeling and simulation approaches. Regarding the simplicity and performance the NLS and the IFM models are the most widely used statistical approaches for describing and analyzing disordered ferroelectric systems behaviour. However, both models suffer from an assumption placed in the core of the KAI model - the statistical independence of switching regions. Another significant drawback is the assumption of steady statistical distributions of SwT and electric field values, while the latter are expected to vary depending on a poling state of a material.
In this work new models are developed. The aim of the models is to shed light on the role of depolarization fields and correlations in switching kinetics. All existing simulation models, which also highlighted an impact of depolarization fields, operate within the mean-field approach, that prevents an investigation of either spacial or statistical field distributions. The later, however, is very important as is evident by the IFM model, especially for textured materials.
By means of computer simulations, we investigated correlations during a poling process and consequent charge formations. In its turn, charge formations are additional sources of depolarization fields, therefore a corresponding field-map in real-time is studied together with a statistical field distribution. All these studies are performed for different symmetries: tetragonal, rhombohedral, and orthorhombic, to illustrate an impact of crystal symmetry on switching kinetics and the concomitant effects listed above.
While simulations allow investigation of local processes in ceramics, analytical models provide statistical data regarding the macroscopic effects; particularly a c-axes distribution function, which has been calculated only for a tetragonal symmetry, now is presented for a rhombohedral and an orthorhombic symmetries as well. This function plays an important role in the analytical estimation of average values in ceramics such as variance of charges on grain faces, or maximal possible polarization which can be achieved at a given symmetry [7]. A new analytical model discriminates between 180° and non-180° switchings, enabling the description of polarization kinetics and simultaneous strain variation. The model was implemented to describe recent measurements where polarization-time dependence was measured simultaneously with a strain variation [182]. Fitting of the experimental results provided a set of parameters such as amount of 180° and non-180° switching events, their characteristic activation energies and many

others, which are in a good agreement with the experimentally measured values.
The global objectives of the current work are

1. Understanding of a role of a depolarization field, its magnitude and evolution
2. Understanding of a role of electrostatic correlations
3. Development of a new model to describe sequential switching events and to account for non-180° switchings.

A two-dimensional model to study local electric field evolution during a poling process was advanced by Genenko *et al.* [31]. This model, however, has to be further elaborated to account for correlations and include consideration of a 3D structure necessary to describe all relevant symmetries.
According to the covered problems the publications are categorized in the following way

1. Influence of porosity, pores size and anisotropy on switching kinetics, theory and experiment 4.2.
2. 2D/3D models and investigation of spacial field distribution, charge density formation and electric field/polarization correlations during poling ceramics for different crystalline symmetries 4.3.
3. Stochastic model to involve non-180° switching in description of simultaneous polarization and strain kinetics, theory and experiment 4.4.

4.2 Porosity influence on switching kinetics

The electric field distribution plays a crucial role in field-driven polarization switching. It leads to an accelerated switching of some regions, whereas retardation or pinning of others is also observed. Additionally, regions of high field intensity strongly affect donor/acceptor migration, leading to a bias field formation, and causing ageing and fatigue of ceramics [183].
Having comparatively low values of a relative dielectric permittivity, pores are centres of an electric field distortion [142; 144]. Control over a pore's size, their form and orientation makes porous materials promising objects for a new materials design. However, it is important to predict an influence of each geometrical parameter on switching kinetics of materials. PAPER I (sec. 6.2.1) considers various porous structures (Fig. 4.1) to disclose their impact on a poling process.
First, we considered effects of size and porosity for pores of an isometric form (circles). Samples of the same porosity but with a different pore size or a pore size distribution were compared. The simulation revealed that a statistical field distribution does not depend on pore size or their size distribution if porosity is kept the same. Afterwards, we kept the same size, but changed porosity. As was expected, the higher porosity brings a broader field distribution.

In the next step, we changed isometric pores to anisometric (elliptic) ones. An anisometry introduces a new degree of freedom – pore orientation relative to an applied field. Elliptic pores

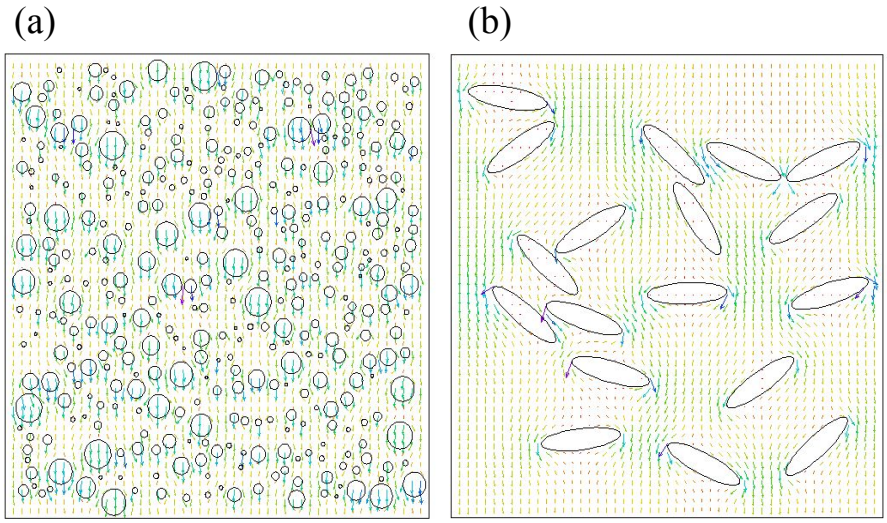

Figure 4.1: Electric field strays around (a) pores with sized distribution, (b) around elliptical pores with a random distribution of major elliptical axis.

having 45° angle with an applied electric field were compared to circle pores, demonstrating how electric field distribution shifts towards lower field values. After that, samples with the same porosity and the pore shape, however with different inclination angles $(0, \pi/6, \pi/3, \pi/2)$ were compared, by this way illustrating how an electric field distribution is broadening with the angle increasing. Finally, a sample with randomly oriented anisometric pores was compared with the sample of the same porosity but stuffed with isometric pores. The simulation result exhibited no difference in a field distribution picture.

For each simulated case a mean cosine of a local field deviation was calculated. It is well known that porosity dramatically reduces maximum polarization of a system. There was an assumption that a reason of low polarizability is hidden in the field deviation around pores which polarizes a part of a material in arbitrary directions. Our calculation exclude this explanation due to comparatively small mean cosine variation; secondly, a mean cosine depends on porosity monotonically, wheres a non-monotonic decreasing of polarization was observed.

According to the Merz law Eq. (2.7) the field distributions were converted into the distributions of SwT for all cases in order to see an influence of porosity on a poling process. Calculated SwT allows one to reconstruct polarization-time curves using the IFM model.

4.3 Spacial field distribution and correlations during a switching kinetics

Present topic is covered by two articles based on the SMS model. PAPER II (sec. 6.2.2) presents 2D simulations and considers a tetragonal symmetry, PAPER IV (sec. 6.2.4) deals with 3D simulations and considers tetragonal, rhombohedral, and orthorhombic symmetries. The 2D simulations are based on a model proposed in the work [31]. The Laplace equation is being solved for a granular structure to describe an electric field map induced by applied voltage and surface charges. A KAI-based kinetic equation is solved to describe an evolution of polarization taking into account actual values of an electric field. Examples of polarization and field maps are presented in Fig. 4.2.

Main assumptions adopted in the model are

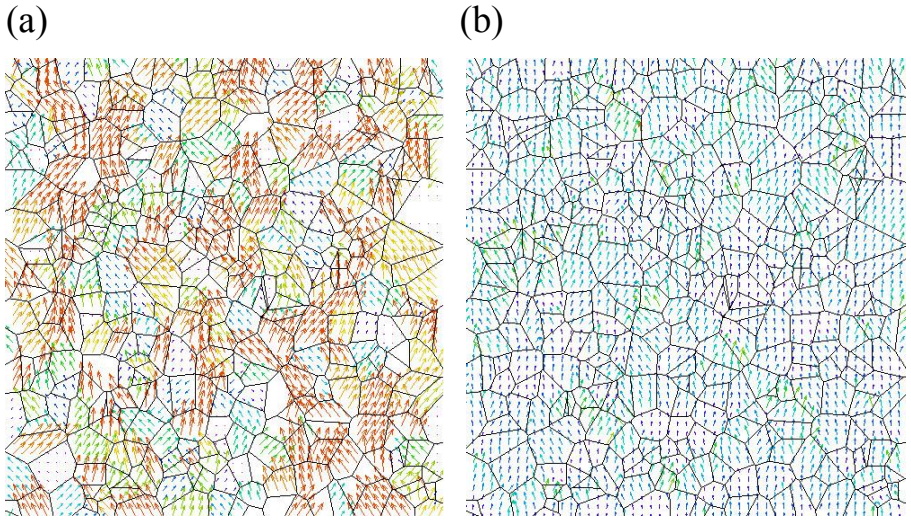

Figure 4.2: Examples of polarization (left) and the corresponding field (right) maps at the intermediate poling stage.

1. polarization within each grain is supposed to be uniform
2. GBs are infinitesimally thin
3. only 180° switchings are considered
4. spontaneous polarization of a unit cell is artificially reduced to diminish produced depolarization fields.

The reason for the last assumption is based on an electronic band structure of a material. Produced depolarization field bend energetic bands of a material. If a depolarization field is sufficiently large then electrons will be provided to a conduction band and later flow through grains

to suppress these fields. Therefore polarization was intentionally reduced to correspond to a band gap of a studied material.
The model provides information to study a field distribution and correlations in a system. It was found that a statistical field distribution changes while a material is being polarized. More detailed analysis of the depolarization field revealed two sources of the depolarization fields dispersion: a dielectric tensor inhomogeneity, and a charge formation on grain boundaries. The behaviour of both mechanisms was discussed; the statistical distribution of fields due to the tensor inhomogeneity monotonically broadens, whereas statistical distribution of a charge-induced field scales with polarization magnitude and thereby has a non-monotonic behaviour. The variance anisotropy (VA) factor, which is a new characteristic introduced in PAPER II, revealed finite correlations of electric and polarization components in a system. However, all variables (except at the beginning of a poling process) exhibited only short-range aoutocorrelations.
The 2D model has been extended to a 3D, which allows consideration of other symmetries as well. A grain structure in the 3D cases was intentionally simplified to a cubic grain array. That provided an easier estimation of surface charges on the boundaries of the grains and gave a possibility of a direct reference to the theoretical calculations [7] where the same cubic structure has been considered. The main assumption for the model was kept the same as in the 2D model except for the reduced polarization values, which in the 3D work corresponds to real polarization values of studied materials. That provided a more realistic picture of depolarization field magnitude and evolution. Assuming that depolarization field has to be cut off by some critical value based on physical mechanisms such as band bending or polarization inhomogeneity within the grain, this critical field was also found for different symmetries, using a comparison of polarization-time curves with experimental measurements [8]. The 3D simulations revealed an evolution of a statistical distribution of electric field, however, the distributions do not change much, that supports assumptions contained in the NLS and the KAI models. The contradiction with the 2D simulated system might arise because of artificially suppressed depolarization fields and the form of the grains, i.e. 2D grains correspond to pipes;field can turn around Pipes worse than the around cubes. None of three symmetries revealed long-range correlations. The absence of correlations was related to a Debay's screening effect which directly relates to a charge formation density. Charge density evolution was estimated using mean square deviation. It was found that the charge density obeys a symmetry of the studied system and can provide a screening length of the order of a grain size, which maintains the idea of the screening mechanism of the correlation suppression, first stated in PAPER II (sec. 6.2.2).
The simulations demonstrated that a poling process does not happen coherently in ceramic materials, as it might occur in single crystals [23]. However, correlations are of short-range, that allows the assumption of independent switching regions which is the core of the statistical models. Evolution of a field distribution found to be negligible, which supports the next assumption to use a steady statistical distribution of SwT/electric field.

4.4 A model to describe polarization and strain kinetics

PAPER III (sec. 6.2.3) presents the mulstistep stochastic mechanism (MSM) model. It is formulated in the spirit of the KAI model, so that contains a similar set of parameters, such as the

characteristic switching time and the Avrami index. However, the core of the model is substantially extended, so that non-180° also taken into account. This gives a possibility to connect polarization evolution with strain variation.
Together with strain the MSM model comprises many important physical parameters: SwTs for different switching mechanisms, share of non-180° and 180° switchings, electrostriction coefficients, and relative dielectric permittivity, by this way providing an opportunity to decouple contributions of non-180° and 180° events, as well as extrinsic and intrinsic contributions into a strain variation (the first and the second terms in the Eq. (1.6), see Fig. 4.3.
The MSM model was successfully applied to the recently performed unique experiment where

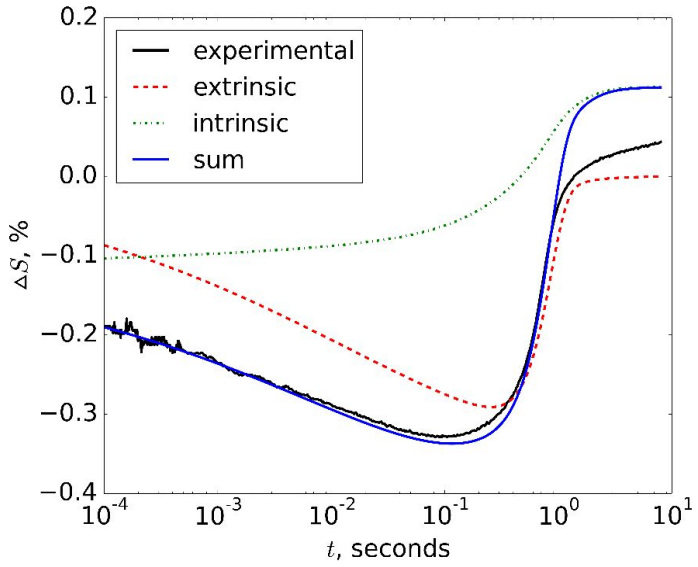

Figure 4.3: Decoupled extrinsic and intrinsic contributions to the strain variation curve, where experiment (black solid line), fitting curve (blue solid line), extrinsic contribution (red dashed line), and intrinsic contribution (red dots).

polarization kinetics was measured simultaneously with strain variation [9] for different fields. As the model contains a large set of parameters, first only strain curves were fitted. Then, the extracted parameters were kept unchanged while Polarization curves were fitted. A good fitting of both the strain- and polarization-time curves provided a set of parameters, which had a good coincidence with independently experimentally measured quantities. Fitting of SwT values established at different fields by the Merz law gave information about an activation fields. The activation field for 180° process was in a perfect agreement with an activation field extracted in the experimental work on the same PZT material [8]. Activation fields for the first non-180° and the second non-180° switching events are attainable from the experiment, however, were extracted from the fitting.

5. Outlook

In the present serious of works a statistical model (MSM) to describe non-180° switching events was for the first time introduced in PAPER III (sec. 6.2.3). The model contains several simplifications at the moment: an electric field is assumed to be uniform and steady during a poling process, correlations between grains are absent, all grains experience either 90° or 180° switchings, no spacial distribution of *c*-axes is taken into account. The model, however, successfully described experimental measurements for a tetragonal PZT proving its applicability, but demonstrating only fair agreement with the experimental data at a later switching stage. Further modifications are important for describing other symmetries and more accurate estimation of the results in the whole time window. Simulations performed in the works PAPER II (sec. 6.2.2) and PAPER IV (sec. 6.2.4) have clearly demonstrated the absence of long-range electrostatic correlations, hence there is no need to introduce the correlations in the MSM model, but a statistical field distribution plays a role in polarization kinetics. Uniform field approximation does not allow to describe the retardation at the later stage of poling process, thus leading to some deviation from experimental results. In the PAPER IV (sec. 6.2.4) it was demonstrated, however, that a statistical field distribution varies in time slightly. This means that a statistical distribution can improve the model, providing a more accurate estimation of activation fields for all switching events and more precise description of the time-dependent data, however, a steady distribution approximation may still be introduced which is essential to keep the simplicity of the model. In PAPER IV (sec. 6.2.4) different symmetries were investigated. It is seen that a distribution of *c*-axes also affects a statistical field distribution and a polarization process, therefore another reasonable modification of the MSM model is an incorporation of *c*-axes distribution according to a system symmetry. That would allow a direct incorporation of such a parameter as a maximum possible strain which can be directly measured experimentally and more accurate estimation of 180° and non-180° switchings amount.

Recently Roscow *et al.* [184] investigated porous "sandwich" structures for energy harvesting applications to see the relationship between the geometry of porous structure and poling characteristics. Pores incorporation into the SMS model will permit extending the simulations carried out by Roscow *et al.* by incorporation of a materials symmetry feedback and fields produced by charges on GBs. Therefore the next modification of the SMS model can be a pore structure incorporation which provides a good opportunity to study kinetics of porous materials.

The 3D SMS model is a good tool to explore a charge formation, correlations and local fields. The model, however, suffers from an assumption of the only 180° switchings, which prevents its application over a wide range of fields as well as description of strain. The next step of the model modification is an introduction of non-180° switchings. It is important that a dielectric tensor has to experience rotation together with a *c*-axis after each non-180° switching. This fact is mostly being omitted in simulations, though it plays an important role in depolarization

field formation. Such a modification as non-180° switchings would permit an investigation of local strains as the latter are directly related to a polarization. The model promises to distinguish between the 180° and two coherent non-180° events which are not resolvable by the current experimental methods or the MSM model. These modifications together with a more elaborated random grain shape will provide an opportunity to add mechanical interaction between grains, which gives an impact on a switching processes, in some cases even preventing them [185].

6. Publications

6.1 Author's contribution

In all works in this thesis, I personally performed all computer calculations and was responsible for the development of python codes and algorithms for the calculations, structure generations, result visualizations. I contributed in all manuscripts preparation, particularly the calculated results analysis and description of the results.
In PAPER I (sec. 6.2.1) I was the first author. The work was initiated by Dr. Genenko and Dr. Zhukov with an idea of field control via a porous structure. Among my duties were an algorithm for porous structure generation construction, writing original scripts which imported the structures into the commercial software FlexPDE program where the Laplace equation was solved to evaluate an electric field map. I also developed an original python script which takes field values, calculated by the FlexPDE, and derives a statistical distribution of the field. I also introduced the idea to study concentration and size-dependent effects. For this work I've wrote the most part of the manuscript.
In PAPER II (sec. 6.2.2) I was the first author as well. The work had to continue the work proposed by Dr. Genenko where the 2D-SMS model was advanced by Dr. Genenko and Dr. Wehner [31]. My duties were to extend Python script earlier developed in the work [31], to investigate statistical field distributions, and to estimate correlations in a system. To that end, I have used the script from PAPER I for a field distribution calculation. However, I had to write an original algorithm and a script for correlations calculation; an extensive work was done for better visualization of the correlation functions. I invented the variance anisotropy (VA) factor which allows an estimation of coherence of a system evolution and correlations spacial anisotropy much faster than it can be done by means of the correlation coefficient calculations. The parts of the model description, calculations and results were prepared by me for the manuscript.
In PAPER III (sec. 6.2.3) I was the second author. The origin of the work owes to the unique experiment conducted by Dr. Koruza and Dr. Schultheiß [182]. There was a need in a model which can take into account non-180° switchings and relate polarization-time measurements to a corresponding strain variation. Dr. Genenko developed a mathematical model of consequent switchings which allows one to include non-180° switchings into polarization kinetics. My contribution were an implementation of this model to fit the experimental data, to extract valuable parameters and to analyze them. The main obstacle was a large number of parameters and their dependence from each other. I had to simplify and modify the formulas in such a way to use as few fitting parameters as possible and to utilize parameters measured independently in direct experiments. I also developed a Python script which is capable to fit experimental data by the formulas for polarization and strain variations which was the main tool for calculations in the work. This manuscript was written together with the experimental group, among my duties was

preparation of the calculated results and their description.
In PAPER IV (sec. 6.2.4) my idea was to simulate a regular cubic structure, which Dr. Genenko suggested to compare to the theoretical studies [7]. I extensively modified the previous SMS model. First, the structure was extended from 2D to 3D. That made simulations much more time-consuming (instead of 400 2D grains, now 1000 3D grains were simulated). Therefore a new calculation algorithm was developed. Previously the FlexPDE provided a field map, and an equation responsible for polarization evolution was solved within Python using the Runge-Kutta method. In the present work, the whole computational process was carried out by the FlexPDE solver which works much faster than the self-written python script. I had modified boundary conditions in the problem to separate field fluctuation caused by a dielectric tensor inhomogeneity and those caused by charges on grain boundaries. That simplified a way of charge density estimation. I was also responsible for writing a script to calculate a standard deviation of electrical field components and charge densities on grain boundaries as well as visualization of their evolution. The manuscript of this work contains massive theoretical calculations, which were described by Prof. Genenko. The manuscript was mostly prepared by him, while I had to contribute to the part regarding the model, calculations and results.

6.2 Papers

6.2.1 PAPER I

Polarization-switching dynamics in bulk ferroelectrics with isometric and oriented anisometric pores

R Khachaturyan, S Zhukov, J Schultheiß, C Galassi, C Reimuth, J Koruza, H von Seggern and Y A Genenko, *Journal of Physics D.*, **50(4)**, 045303 (2017).
DOI: 10.1088/1361-6463/aa519c

IOP Publishing Journal of Physics D: Applied Physics

J. Phys. D: Appl. Phys. **50** (2017) 045303 (14pp) doi:10.1088/1361-6463/aa519c

Polarization-switching dynamics in bulk ferroelectrics with isometric and oriented anisometric pores

R Khachaturyan[1], S Zhukov[2], J Schultheiß[2], C Galassi[3], C Reimuth[1], J Koruza[2], H von Seggern[2] and Y A Genenko[1]

[1] Institute of Materials Science, Technische Universität Darmstadt, Jovanka-Bontschits-Straße 2, 64287 Darmstadt, Germany
[2] Institute of Materials Science, Technische Universität Darmstadt, Alarich-Weiss-Straße 2, 64287 Darmstadt, Germany
[3] CNR-ISTEC National Research Council of Italy, Institute of Science and Technology for Ceramics, Via Granarolo 64, I-48018 Faenza RA, Italy

E-mail: genenko@mm.tu-darmstadt.de

Received 7 August 2016, revised 30 November 2016
Accepted for publication 5 December 2016
Published 29 December 2016

Abstract

Highly porous ferroelectric ceramics possess remarkably less polarizability than dense ceramics; instead they display high tunability of various physical properties. Particularly, the shape and orientation of pores as well as the total porosity exhibit a great effect on the polarization-switching dynamics. In the present work, finite-element simulations of the electric-field distributions and related statistical distributions of local switching times are analysed and compared with the switching characteristics of porous lead zirconate titanate ceramics, extracted from the experiment by means of the inhomogeneous field mechanism model of polarization switching. Surprisingly, the simulated statistical field-distributions turn out to be virtually independent of the pore-size distribution; however, they are sensitive to the anisometric shape and orientation of the pores. Additionally, they exhibit notable broadening with increasing porosity; an effect confirmed by experimental observations.

Keywords: porous ferroelectrics, polarization-switching dynamics, oriented anisometric pores, statistical field-distributions

(Some figures may appear in colour only in the online journal)

1. Introduction

Ferroelectric materials are utilized in various applications due to several functional properties, such as large permittivity, switchable spontaneous polarization, large electromechanical coupling, pyroelectricity, electro-optic effects, and others [1]. Besides through the compositional and microstructural engineering, the properties of these materials can be additionally tailored by the formation of composites, whereby a second phase of low permittivity, such as polymer or air, is introduced into the structure [2]. For example, increased porosity results in an increase of the ratio between the longitudinal and transverse piezoelectric coefficients, which in turn increases the hydrostatic piezoelectric coefficient [3]. Furthermore, porosity was demonstrated to considerably improve piezoelectric sensitivity, acoustical energy transfer, and pyroelectric energy conversion. These characteristics make porous piezoelectrics and their composites useful for underwater acoustics, medical diagnostics, non-destructive testing and others [3–6].

While the functional properties of porous ferroelectrics with isometric pores have been investigated by several authors [7], the influence of the shape, orientation, and distribution of the pores is less well understood. Tailoring these parameters, for example by pore alignment, was recently reported to considerably improve the piezoelectric [8, 9] and pyroelectric conversion response [10] of piezoelectric materials.

Inhomogeneous field distribution due to the pores is key to various functional properties of the investigated materials, as shown by computer simulations compared with experiments on porous lead zirconate titanate- and barium titanate-based ceramics [11–14]. Particularly, dielectric permittivity and voltage-driven tunability can be engineered by using anisotropic porosity (pore shape and orientation) as a tailoring factor. Related studies [12–14] have mostly focused on nonlinear dielectric properties and the impact of porosity on the effective macroscopic permittivity. Two-dimensional (2D) field simulations [12] have shown ways to increase tunability while reducing permittivity for small porosity levels. More advanced three-dimensional (3D) modelling of porous [13] and general composite [14] materials allows consideration of high porosity where the effective-medium approach fails. A comprehensive thermodynamic and micromechanical approach was developed by Jayendiran and Arockiarajan, which was able to describe the viscoelastic behavior and nonlinear electromechanical response of regular idealized piezocomposite structures [15–17].

Although the switching of spontaneous polarization is a basic feature of ferroelectric materials, distinguishing them from other dielectrics, little information is available on the influence of porosity on the switching process. Analysis of ferroelectric switching in a similar system of sodium nitrite: poly(vinyl alcohol) composite films has shown the great effect of composition on polarization-switching kinetics [18, 19]. The publication by Stoleriu *et al* [11] was devoted to the description of polarization-switching loops in porous ferroelectric ceramics by a Preisach-like, first-order reversal-curve analysis. However, this formal approach does not allow attribution of a physical entity to an elementary switching unit and, particularly, a dynamic description of the time-dependent polarization reversal. The latter problem presents the main task of this work, which is focused, on the one hand, on the finite-element electric-field simulations in model porous ferroelectrics and, on the other hand, on the statistical analysis of the time-dependent polarization-switching response in porous lead zirconate titanate.

2. Statistical electric field and switching-time distributions in porous dielectric ceramics: a statistical model approach

The polarization response of ferroelectric ceramics exhibits dispersive features and is characterized by wide statistical switching-time distributions [20]. Considering the strong electric-field dependence of the switching time [21], the inhomogeneous-field-mechanism (IFM) model of polarization response explains these broad distributions by a statistical distribution of the local electric-field values over a random polycrystalline media [22, 23]. This concept, suggested by the authors of the current study, was successfully confirmed using different ferroelectric ceramics [23–26] and even ferroelectric polymers [27, 28], and presents an alternative to the statistical description in terms of Preisach-like models [11, 29]. Application of this approach to analysis of the response of porous ferroelectrics is presented below.

According to the concept of nucleation-limited switching (NLS) suggested for ferroelectric films, the total reversed polarization of a polycrystalline ceramic sample exposed to an applied step-like voltage results from superimposing contributions of different sample regions characterized by individual switching times τ [20]. In the 3D case of a bulk ceramic such a response is described by the formula [23]

$$\Delta P(E_{\mathrm{m}}, t) = \langle \cos\theta \rangle \int_0^\infty \mathrm{d}\tau \; Q(\tau)\, p(t, \tau) \tag{1}$$

where local polarization reversals in each region are assumed to follow the classical Kolmogorov–Avrami–Ishibashi (KAI) $p(t, \tau)$ dependence [30] with time t elapsing after application of the external field E_{m}. $\langle \cos\theta \rangle$ denotes the mean cosine of the polar angle θ between the direction of the local electric field and the direction of the applied field, while $Q(\tau)$ denotes the weighted statistical switching-time distribution [23].

The main hypothesis of the IFM model is that the statistical switching-time distribution follows from the statistical distribution of the local electric-field values E due to the strong field-dependence of the local switching times $\tau(E)$. For strongly heterogeneous media, such as polycrystalline ceramics, which exhibit pronounced non-uniform spatial distributions of the electric field, this hypothesis entails a scaling property of the total polarization [22]:

$$\frac{E_{\mathrm{m}}}{\Delta P_{\mathrm{max},0}} \frac{\partial \Delta P}{\partial E_{\mathrm{m}}} = \Phi\left(\frac{E_{\mathrm{m}}}{E_{\mathrm{max}}(t)} \right) \tag{2}$$

where $\Delta P_{\mathrm{max},0}$ is the maximum total polarization of a dense ceramic consisting of a single composition, $E_{\mathrm{max}}(t)$ is the maximum position of the normalized field derivative with respect to field and $\Phi(u)$ is a function presenting a fingerprint of a specific medium. The relation (2) shows that the field derivative of the polarization, depending on the field and time, may be presented as a function of a single combined variable depending on the field and time. In other words, the derivatives in equation (2), evaluated at different times, are expected to fall onto the same master curve, characteristic of a certain material. This property, confirmed so far for all investigated polycrystalline ceramics [22–28], is not trivial; it fails, as expected, in the case of uniform media such as single crystals [23, 31] where the KAI model applies to the total polarization response.

We note also that the IFM model, as well as the NLS model, is still not self-consistent since it does not account for generation of depolarization fields due to switching of individual regions and their mutual influence in the course of polarization reversal. The fact that the IFM model nevertheless successfully explains experiments may be related to the fact that the depolarization fields might be kept low due to coherent polarization reversal, an understanding supported by the self-consistent 2D simulations [32]. Another point worth noting is that the statistical distribution of local switching times might alternatively result from random activation barriers in heterogeneous pinning media or random local electric fields due to various defects, as suggested in some previous models [33, 34]. The problem of these models is that, in contrast to the IFM approach, they are unable to explain the field-time

scaling of reversed polarization (equation (2)) observed in many ferroelectric ceramics [22–28, 31] since the activation barriers in these models are not dependent on the applied field.

If the property (2) is confirmed experimentally and the two characteristic functions $E_{max}(t)$ and $\Phi(u)$ are established, the switching polarization (1) can be represented for any applied field magnitude E_m in terms of these functions as

$$\Delta P(E_m, t) = \Delta P_{max,0} \int_0^{E_m/E_{max}(t)} \frac{du}{u} \Phi(u), \tag{3}$$

without using any fitting parameter [23].

The field dependence of the local polarization-switching time $\tau(E)$ can also be obtained from the solution of the equation $E_{max}(t)/\gamma = E$ with respect to E, where the constant γ can be derived from the shape of the master curve and is typically around unity [22–26, 31].

The master curve $\Phi(u)$ is directly related to a weighted statistical distribution of the electric-field values in a system $f(E/E_m)$ by the expression [35]

$$f(s) = \frac{\langle \cos\theta \rangle_0}{\langle \cos\theta \rangle} \frac{1}{s} \Phi\left(\frac{1}{\gamma s}\right), \tag{4}$$

where $\langle \cos\theta \rangle_0$ and $\langle \cos\theta \rangle$ denote the mean cosine of the polar angle θ for the local electric field in the dense and porous ceramics, respectively. Considering the dense ceramic as a much more homogeneous medium in comparison with porous ones, for simplicity, the value $\langle \cos\theta \rangle_0$ will be set to unity in the following analysis.

The field distribution $f(E/E_m)$, in turn, determines the weighted statistical distribution of the local switching times

$$Q(\tau) = \left|\frac{d\tau}{dE}\right|^{-1} \frac{1}{E_m} f\left(\frac{E}{E_m}\right). \tag{5}$$

In composites or fatigued systems, consisting of switchable and non-switchable regions, both statistical distributions $f(s)$ and $Q(\tau)$ obey the following normalization:

$$\int_0^\infty ds f(s) = 1 - \nu \text{ and } \int_0^\infty d\tau Q(\tau) = 1 - \nu, \tag{6}$$

where $\nu < 1$ describes the non-switchable part of the sample volume [35]. When comparing the maximum total polarization of a porous ceramic ΔP_{max} with that of the compositionally identical dense ceramic, $\Delta P_{max,0}$, this part can be determined as [35]

$$\nu = 1 - \frac{\Delta P_{max}}{\Delta P_{max,0}} \frac{\langle \cos\theta \rangle_0}{\langle \cos\theta \rangle}. \tag{7}$$

The relation (5) shows that the homogeneity of a system plays a crucial role in the dynamic polarization response. For a uniform system like a single crystal the distributions (4) and (5) are both reduced to δ-function-like peaks, transforming the total response (1) to the local response $p(t, \tau)$ with a single switching time $\tau(E)$. Common non-textured polycrystalline ceramics are characterized by non-uniform spatial field distributions followed by wide statistical field-distributions (4), which result in a wide switching-time dispersion in (5). Textured ceramics exhibit less scattered electric-field values and subsequently more concentrated distributions than compositionally identical non-textured ones [31]. It is anticipated, therefore, that the choice of size, shape and spatial orientation of the pores, which all affect the electric-field distributions in porous ferroelectric ceramics, may have a crucial effect on their polarization dynamics. In the next section we simulate the effects of structural properties of porous systems on the field and switching-time distributions in them.

3. Statistical electric-field distributions in porous dielectric ceramics: finite element simulations

Different 2D porous structures are simulated using a finite element method (FEM) program FlexPDE (version 6.38, PDE Solutions Inc.). To this end, a box of size $3 \times 3\,mm^2$ was created with non-overlapping inserted regions with a material of dielectric permittivity ε_p, randomly distributed over the complete area. The centres of these regions were generated using a random number generator. To adapt this structure to a typical ferroelectric material such as lead zirconate titanate (PZT) the relative dielectric permittivity of the background area was set to $\varepsilon_r = 2000$, while the dielectric permittivity of the incorporated regions was set to $\varepsilon_p = 1$, as for air-containing pores. Constant electrostatic potentials were prescribed to the top and bottom boundaries of the box with a potential difference of $4.5 \cdot 10^3$ V generating an electric field equal to 1.5 kV mm^{-1} in the vertical y-direction. Note that this is comparable to a typical coercive field in PZT. A map of spatial electric-field distribution was then calculated and analysed.

The collected data of the electric-field distributions in the matrix with different pore configurations were converted into statistical distributions of the field amplitude (referred to as 'field distributions' in the following) normalized to the value of the applied field. The statistical switching-time distributions were subsequently calculated from the field distributions using the formula (5) and (exemplarily) the Merz law [21] $\tau = \tau_0 \exp(E_a/E)$ and presented at a logarithmic timescale. The evaluations were carried out for the following set of parameters: the activation field $E_a = 25.28$ kV mm^{-1} and characteristic switching time $\tau_0 = 3.91 \cdot 10^{-11}$ s, corresponding to a porous PZT ceramic with isometric pores (experimentally confirmed in section 4).

3.1. Samples with isometric pores of different fixed sizes

Because of the very different dielectric permittivity values of the ceramic matrix and the pores, the electric field tries to surpass the pores resulting in a field-amplitude variation, as is well known from previous simulations [12] and is shown here exemplarily in figure 1(a). This generates a statistical distribution of field amplitudes in the box around the pore (figure 1(b)). It can be seen that the distribution is shifted towards the values smaller than the mean field ($E < E_m$).

To investigate the influence of pore sizes on the field and switching-time distributions the samples with round pores of different fixed radii r (from 20 μm to 120 μm) were simulated (figure 2). The total porosity of all samples was 22%.

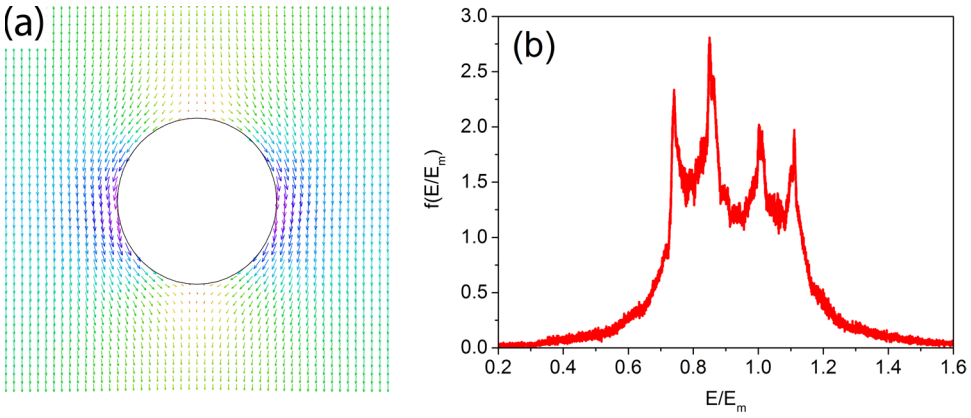

Figure 1. (a) Electric-field-line distribution surrounding a round air pore in a high-permittivity dielectric matrix and (b) the resulting statistical field-amplitude distribution.

The corresponding field distributions are presented in figure 3(a). Switching-time distributions calculated by equation (5) are shown in a more convenient form $G(\ln(\tau/\tau_0)) = \tau Q(\tau)$ in figure 3(b). For implementation of the formula (5), here and in the following, the true statistical distributions of the field values obtained from the FEM field maps are identified with weighted distributions [23], which result from averaging over spherical angles with a factor of cosine of the polar angle. This does not lead to large errors since a narrow distribution of polar angles in all configurations is confirmed by the respective values of mean cosines close to unity, namely $\langle\cos\theta\rangle$ =0.946 (*A*1), 0.945 (*A*2), 0.945 (*A*3), and 0.944 (*A*4).

As can be seen from figure 3, the shapes of the field and time distributions converge to limiting shapes when the pore size decreases. These limiting shapes can only be dependent on the total porosity, being a common characteristic for all configurations *A*1–*A*4. Particular features of the curves *A*3 and *A*4 are more sensitive to a certain realization of the random pore configuration that can be explained by a small amount of comparatively big pores where a pore distribution in the matrix still plays a role.

3.2. Samples with different size distributions of isometric pores

Porous ceramics usually do not exhibit a constant pore size, but a distribution of sizes, which may be mono-, bi-, or multimodal. Therefore, samples with different size distributions in the range of 10–160 μm (*B*1–*B*3), but with approximately equal porosity (19.5–20.5%) were simulated to trace the size-distribution effect on the field and switching-time distributions. One sample (*B*4) with a fixed pore size of 60 μm and approximately the same porosity was also simulated, to compare this with variable sizes in *B*1–*B*3. For samples *B*1–*B*2 a log-normal distribution was used, while for *B*3 a bimodal distribution was created. All size-distribution functions $v(r)$ are presented in figure 4(a). The procedure for stochastic pore generation with sizes according to a selected size distribution was as follows. First, the probability for a random pore to have a radius r smaller than a was found by integration as $W(a) = \int_0^a v(r)\,\mathrm{d}r \leqslant 1$.

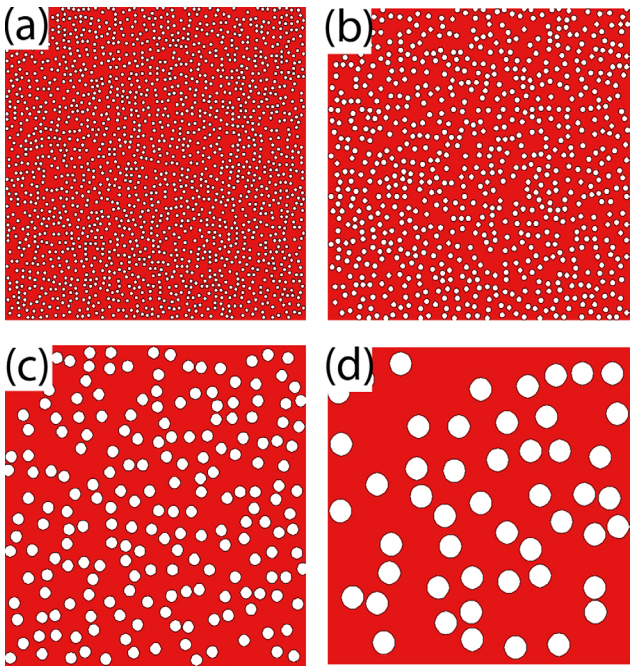

Figure 2. Samples with the same total porosity (22%), but different pore radii r (μm): (a) 20 (*A*1), (b) 30 (*A*2), (c) 60 (*A*3), (d) 120 (*A*4).

Then, a random number q in the range from 0 to 1 was generated for each pore. Subsequently, a size a corresponding to the probability $W(a) = q$ was assigned to the pore. This procedure of pore generation was carried out until a predetermined porosity was reached. The structures of samples *B*1–*B*4 are displayed in figure 4(b). The statistical distributions of field values for samples *B*1–*B*4 and the corresponding switching times, calculated by equation (5), are presented in figure 5.

As can be seen, all distributions are similar to each other, except for random point-like fluctuation peaks as well as minor deviations related to the porosity variations of about ~1%. The similarity of the graphs in figure 5 reveals that size distributions at the same total porosity have no substantial effect on field and switching-time distributions. This applies as well to the mean cosines, which amount to $\langle\cos\theta\rangle$ = 0.954 (*B*1), 0.950 (*B*2), 0.948 (*B*3), and 0.950 (*B*4). This also means that, concerning the field and switching-time distributions, a sample with a pore-size distribution can be effectively

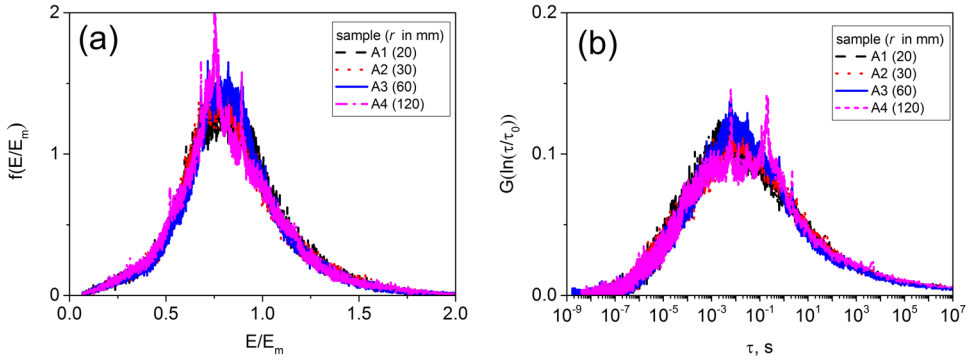

Figure 3. Statistical distributions of (a) field values and (b) switching times for the samples *A*1–*A*4.

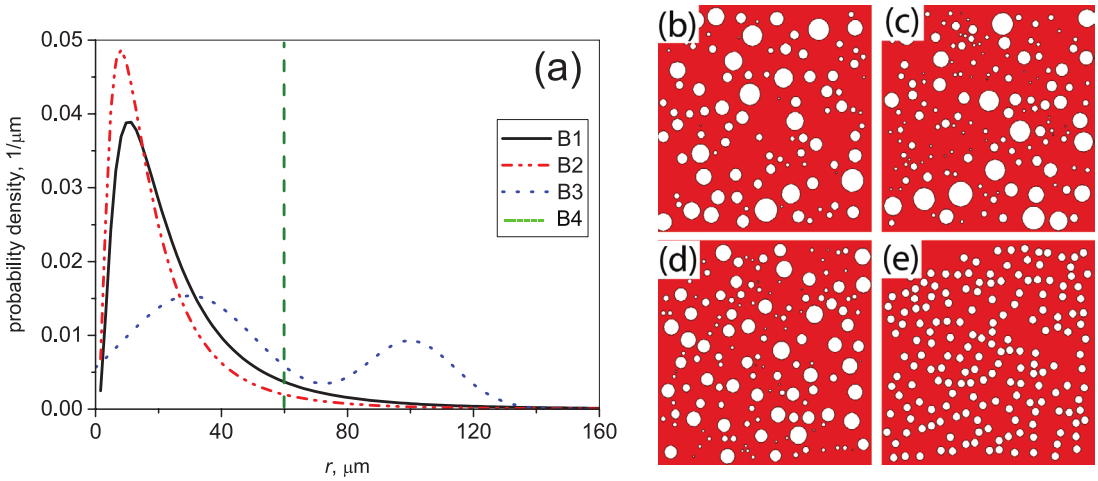

Figure 4. (a) Pore-size distributions of samples *B*1–*B*4. Structures of samples with different size distributions: (b) *B*1, (c) *B*2, (d) *B*3 according to the distribution functions in (a). Sample *B*4 (e) presents a random spatial distribution of equal pores with a radius of 60 μm for the same total porosity as in *B*1–*B*3.

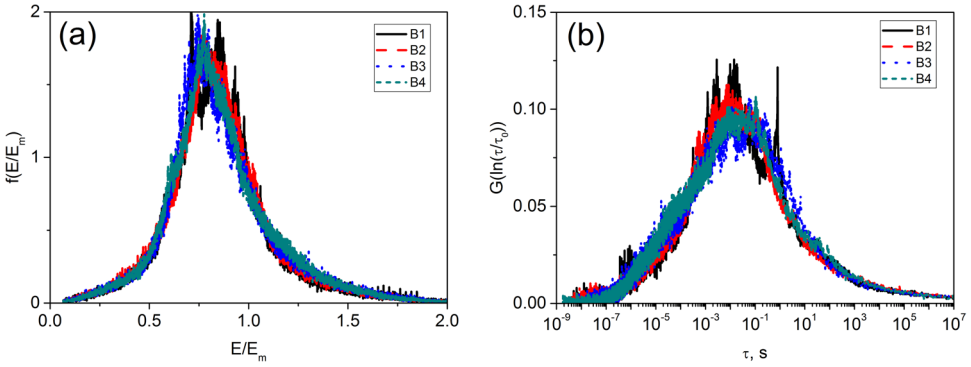

Figure 5. Statistical distributions of (a) field values and (b) switching times for samples *B*1–*B*4.

replaced in simulations by a sample with a fixed pore size and the same total porosity. The pore radius itself can be selected arbitrarily because, as seen from the results in figures 2 and 3, the field and switching-time distributions are weakly size-dependent at the same total porosity.

3.3. Samples with equal pores, but different total porosities

To observe the influence of porosity on field and switching-time distributions, simulations of structures with different total porosity were performed. The radius of pores was kept equal to 30 μm in all simulations. Pictures of spatial pore distributions in samples *C*1–*C*4 are shown in figure 6. Electric-field and time distributions for these samples are presented in figure 7.

As can be seen from figure 7, field and switching-time distributions are notably dependent on the porosity of the material: the higher the porosity, the wider the field and switching-time distributions. Field distributions are thereby shifted towards smaller fields and consequently time distributions towards longer times. Mean cosine magnitudes are progressively reduced with the porosity, so that $\langle \cos\theta \rangle = 0.987$ (*C*1), 0.971 (*C*2), 0.957 (*C*3), and 0.931 (*C*4).

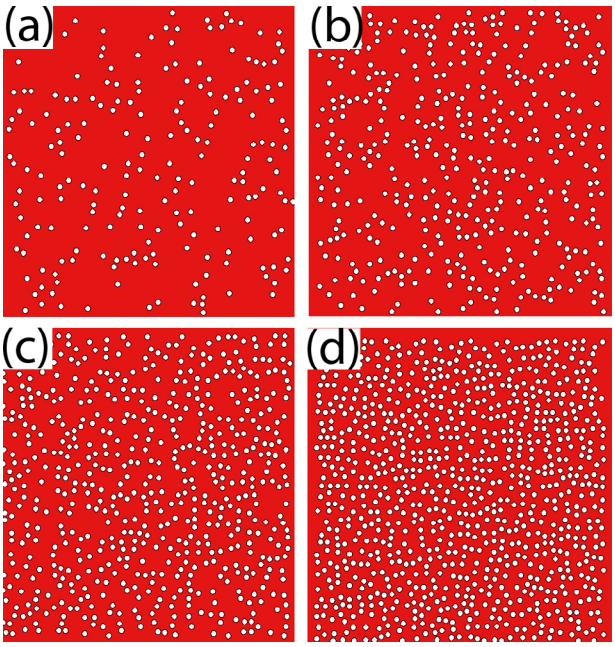

Figure 6. Structures of samples with different total porosity: (a) 5.5% (*C*1), (b) 11% (*C*2), (c) 16.5% (*C*3), and (d) 27.5% (*C*4).

These trends can be explained by the fact that the higher porosity content corresponds to a larger number of field-straying centres. Contribution to the statistical distribution function of strayed field components is proportional to the part of the sample volume subjected to a substantial field variation. Thus the higher number of scattering centres leads to the wider field distribution.

3.4. Samples with differently oriented pores of anisometric shapes

In contrast to a round pore, an elliptical one is anisometric in form, which affects the electric-field distortion (see figure 8(a)). Field distributions due to round and elliptical pores are different, as can be seen in figure 8(b), in spite of the equal areas of the pores providing equal porosities.

Simulations with elliptical pores of the same aspect ratio 1:4, but different tilt angles χ with respect to the applied electric-field direction were performed to observe the influence of the shape anisotropy and pore orientation. Structures of the simulated samples *D*1–*D*4 with the same porosity of 15% and pore size of $r = 80$ μm are shown in figure 9.

Here, and in the following, the terms 'longitudinal' and 'transverse' refer to the orientation of the major axis (with length defined as $2r$) of the pores with respect to the applied field. The field and switching-time distributions for samples *D*1–*D*4 are shown in figure 10. As expected, the larger the pore tilt angle the wider the field and switching-time distributions become. The widest field distribution corresponds to sample *D*4 because of the largest depolarization effect in this configuration. The narrowest one corresponds to the case *D*1 where the depolarization effect is the smallest. As expected, the mean cosine is reduced the most for the sample with the strongest depolarization effect: $\langle\cos\theta\rangle = 0.992$ (*D*1), 0.962 (*D*2), 0.884 (*D*3), and 0.845 (*D*4).

3.5. Samples with elliptical pores of different sizes and orientations

Here, the combined influence of the size and orientation of pores with anisometric shape on field and switching-time distributions is investigated. Simulations of elliptical pores with a different tilt angle χ with respect to the applied field were performed for different sizes and compared with each other and with the isometric case (round pores). The total porosity was kept at 15% in all cases. Pictures of samples *E*1–*E*5 are presented in figure 11. Field and switching-time distributions for samples *E*1 and *E*2, *E*3, and *E*4 are presented pairwise in figure 12, together with the results for round pores (*E*5). As previously observed in the case of round pores (figure 2), the field and switching-time distributions are virtually independent of the size of the elliptical pores (figure 12). The distributions for equally tilted elliptical pores are wider than those for round pores and are shifted towards smaller fields and larger times, respectively. On the other hand, samples with a random orientation of elliptical pores display narrower distributions than those with equally tilted pores and turn out to be very similar to those for isometric pores with the same porosity. The mean cosine reveals similar features, virtually coinciding pairwise for tilted (*E*1, *E*2) and randomly oriented (*E*3, *E*4) pores: $\langle\cos\theta\rangle = 0.945$ (*E*1), 0.945 (*E*2), 0.966 (*E*3), 0.965 (*E*4) and 0.966 (*E*5). In conclusion, we can state that both anisotropy and orientation of the pores play an important role in field and switching-time distributions, whereas their size is irrelevant.

As expected, the mean cosines of the local-field orientation decrease with increasing total porosity for pores of both isometric and anisometric shapes, as displayed in figure 13(a). The dependencies turn out to be virtually linear in a wide porosity range. The mean cosines for isometric pores are larger than those for elliptical pores, tilted by an angle of $\pi/4$, which in turn are larger than those for transverse elliptical pores, exhibiting the largest depolarization effect. In the case of an anisometric pore shape the mean cosine strongly depends on the tilt angle, as is seen in figure 13(b). In spite of the equal changes of the tilt angle (by $\pi/6$) from sample *D*1 to sample *D*2, to sample *D*3, and to sample *D*4 it is visible in figure 10 that field and switching-time distributions change non-uniformly. This is confirmed by the nonlinear dependence of the mean cosine on tilt angle in figure 13(b).

Summarizing the results of section 3 it can be concluded that individual sizes of pores randomly distributed in space have no significant effect on statistical field and switching-time distributions when the total porosity of the material is fixed. Particularly, this applies to statistically distributed pore sizes and to anisometric pore shapes. For the latter, however, their shape and orientation in space remarkably affect the field and time distributions. These facts can be explained in the following way: each pore notably distorts the field around it in an area comparable to the pore size (figures 1(a) and 8(a)) because the stray field is of dipole nature and behaves at a large distance ρ like $\sim (r/\rho)^2$, where r is a characteristic size of the pore. Each pore can be surrounded by an imaginary frame

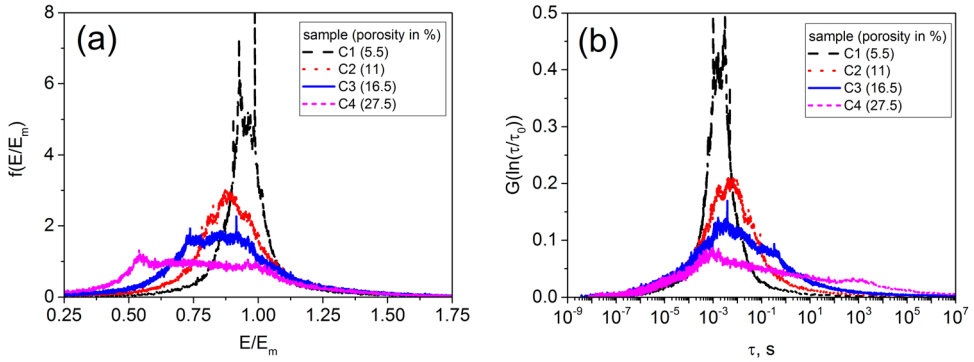

Figure 7. Statistical distributions of (a) electric-field values and (b) switching times for samples with different total porosity $C1$–$C4$, as indicated.

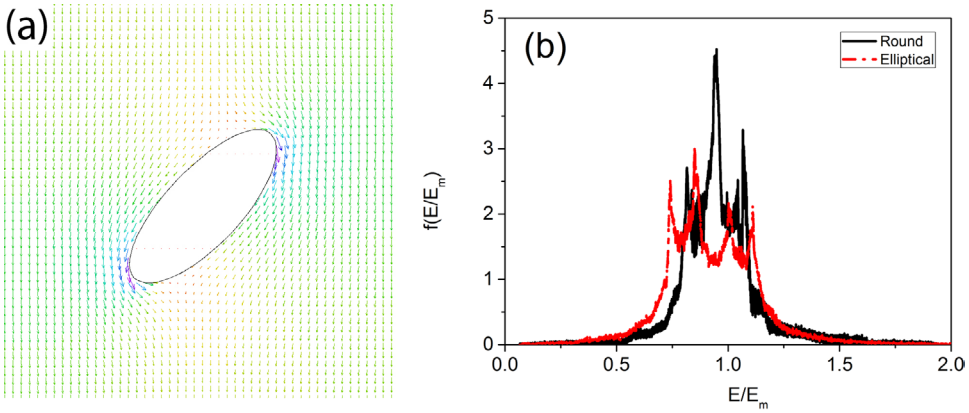

Figure 8. (a) Electric-field-line distribution around an elliptical air pore in a high-permittivity dielectric matrix and (b) statistical field-amplitude distributions for an elliptical and a round pore.

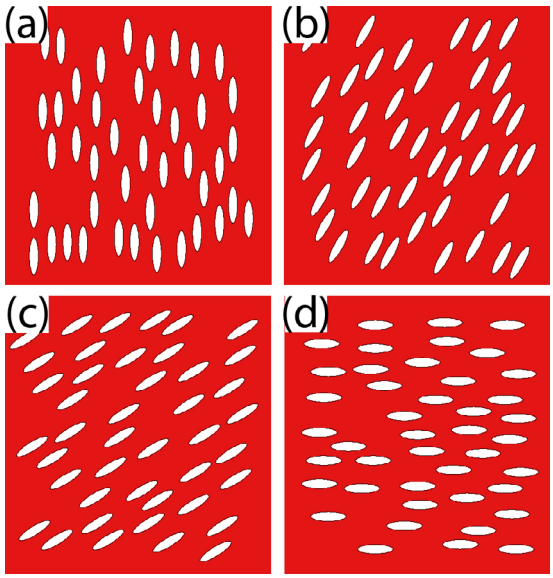

Figure 9. Elliptical pores with different tilt angles χ with respect to the vertically applied electric field: (a) $\chi = 0$ ($D1$), (b) $\chi = \pi/6$ ($D2$), (c) $\chi = \pi/3$ ($D3$), and $\chi = \pi/2$ ($D4$).

outside of which the field distortion is negligible with a given accuracy. The area where the total field deviates substantially from the applied field also depends on the shape and orientation of the pore (see figure 8(a)). The statistical distribution of the field components is apparently dependent on the share of the frame area where the field is substantially distorted, but not on the absolute size of the pore. The same total share of such randomly distributed frames with respect to the total matrix area means the same porosity and results in the same statistical distribution of field values, irrespective of the pore size. The higher porosity means the higher share of areas with a strayed field and, therefore, leads to spreading of the field and time distributions.

4. Analysis of the experimental polarization response of porous ceramics

4.1. Experiment: materials preparation and characterization

Ceramic powders with a pure perovskite phase of the composition $Pb_{0.988}(Zr_{0.52}Ti_{0.48})_{0.976}Nb_{0.024}O_3$ were produced by solid-state synthesis. Fine lamellar graphite powder and modified potato starch were used as pore formers in order to obtain pores with anisometric and isometric shapes, respectively. Disc-shaped samples with 2 mm thickness and 25 mm in diameter were produced by die pressing, orienting the lamellar graphite powder with their main axis perpendicular to the pressing direction. All PZT samples were sintered at 1150° C for 2 h using a heating rate of 100 °C h^{-1} to ensure the complete burn-out of the organic pore formers before the onset of densification. A detailed description of the processing conditions and sample characterization can be found

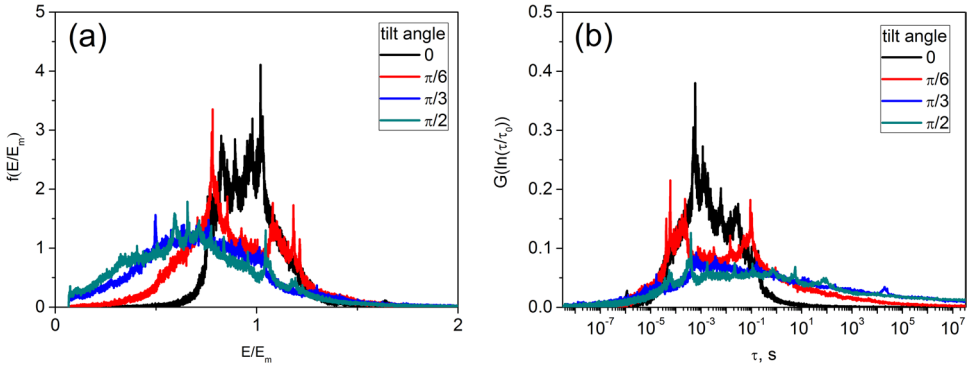

Figure 10. Statistical field and switching-time distribution for samples *D*1–*D*4.

elsewhere [36]. Both porous PZT samples had a total porosity of 37%, whereas the reference sample, prepared conventionally without the pore former, had a porosity of 3.3% (hereafter it is referred to as the 'dense sample').

For microstructural analysis the samples were cut parallel to the pressing direction and embedded into a resin. The samples were ground, polished to a 1 μm finish, and investigated by scanning electron microscopy (SEM; XL 30 FEG, Philips, the Netherlands). Characteristic features of the microstructure of the samples are shown in figure 14. Note that the direction of the applied electric field (marked by an arrow) was the same as the pressure direction used for compaction. Both porous samples contain different types of porosity: large pores, created by the pore former, and small pores, intrinsic to the PZT ceramics. A detailed characterization of the different pores is given in previous work [37]. Comparing figures 14(b) and (c) reveals the different shape and orientation of the pores obtained by the different pore formers, which will be characterized in more detail below.

The porosity was analysed by the ellipsoid method using the ImageJ software (v. 1.50i, National Institutes of Health, USA), whereby about 1500 pores per sample were taken into account. For further analysis, only pores with an equivalent diameter larger than 6 μm and 11 μm for the isometric and anisometric case, respectively, were considered, since the contribution of the smaller ones to the total porosity was less than 1.5%. The results of the porosity analysis are shown in figure 15. While the total porosity of both porous samples was the same (37%), sample *N*2 prepared by using lamellar graphite exhibited pores with larger aspect ratios (anisometric shape), as compared to sample *N*1 prepared using potato starch (isometric shape) (figure 15(a)). Moreover, the elongated pores in the former sample were found to be predominantly oriented in the plane parallel to the sample's circular surfaces (perpendicular to the pressing and electric-field direction), whereas the pores in the latter sample did not show any preferred orientation (figure 15(b)). In addition, it should be noted that the median pore size of the pores in the sample with anisometric pore shape was larger than in the sample with isometric pore shapes (80 μm and 30 μm, respectively), as determined from area distributions.

Polarization loops shown in figure 16, measured by a conventional Sawyer-Tower circuit, demonstrate the ferroelectric

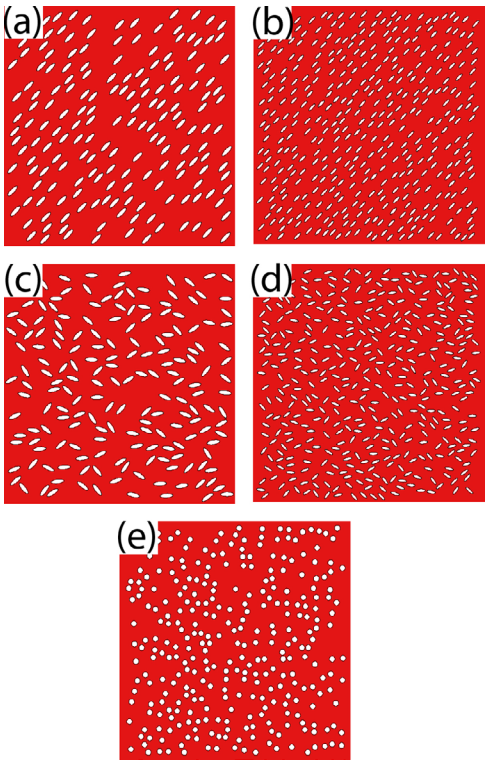

Figure 11. Structures of samples: (a) elliptical pores of size $r = 90$ μm with $\chi = \pi/4$ (*E*1), (b) elliptical pores of size $r = 60$ μm with $\chi = \pi/4$ (*E*2), (c) randomly oriented elliptical pores of size $r = 90$ μm (*E*3), (d) randomly oriented elliptical pores of size $r = 60$ μm (*E*4), (e) round pores of size $r = 40$ μm.

nature of the dense and porous samples. The remanent polarization of the dense sample ($P_{rem} = 40$ μC cm^{-2}) is much higher compared to the porous samples ($P_{rem} = 5$ μC cm^{-2}). This decrease can be explained by the reduced amount of the ceramic phase and increased pinning of the domain walls in the porous samples. The latter can occur due to the pore morphology, residual carbon at the pore surfaces, residual thermal stresses, or stresses induced by the ferroelastically switched regions.

The coercive field of the dense PZT ($E_c = 1.4$ kV mm^{-1}) is lower compared to the PZT with oriented anisometrically shaped pores ($E_c = 1.6$ kV mm^{-1}), but higher compared to the PZT with isometrically shaped pores ($E_c = 1.1$ kV mm^{-1}).

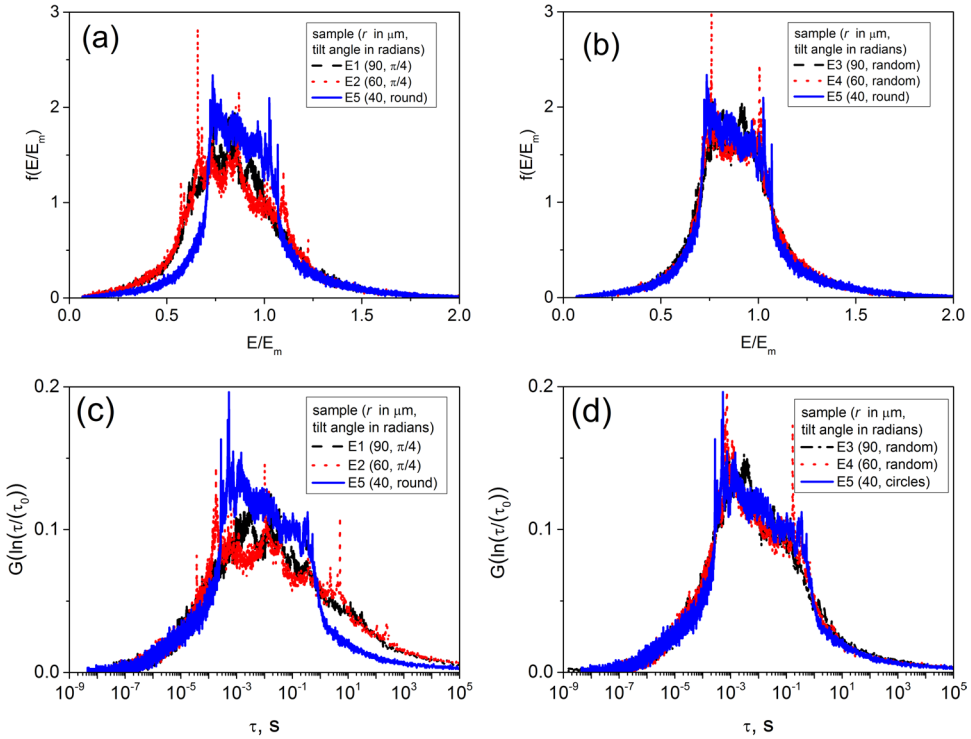

Figure 12. Comparison of field distributions for (a) samples *E*1, *E*2, and *E*5, (b) samples *E*3, *E*4 and *E*5, and of switching-time distributions for (c) samples *E*1, *E*2, and *E*5, (d) samples *E*3, *E*4, and *E*5.

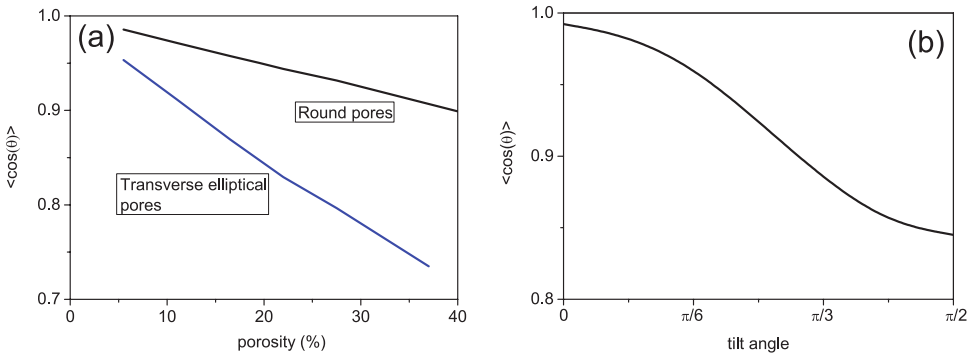

Figure 13. Mean cosine of the local spatial field directions with respect to the applied field direction as a function of (a) porosity for round pores and transverse elliptical pores, as indicated on the plot, (b) tilt angle of the elliptical pores with respect to the applied field for a porosity of 15%.

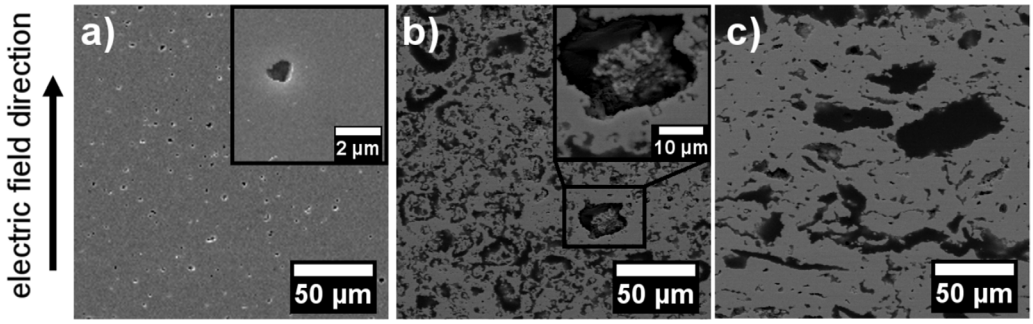

Figure 14. SEM images of microstructures of the investigated PZT samples: (a) dense (*N*0), (b) porous with isometric pore shape (*N*1), and (c) porous with anisometric pore shape (*N*2).

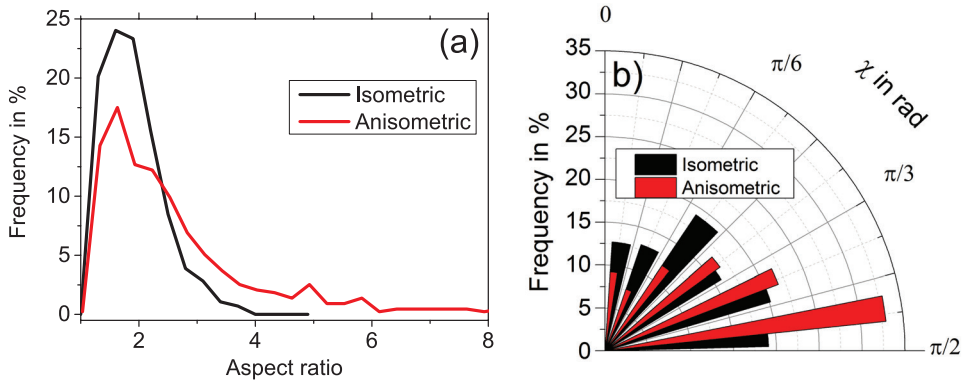

Figure 15. Distribution of the (a) aspect ratio, and (b) the tilt angle (χ) between the main pore axis and the applied field direction.

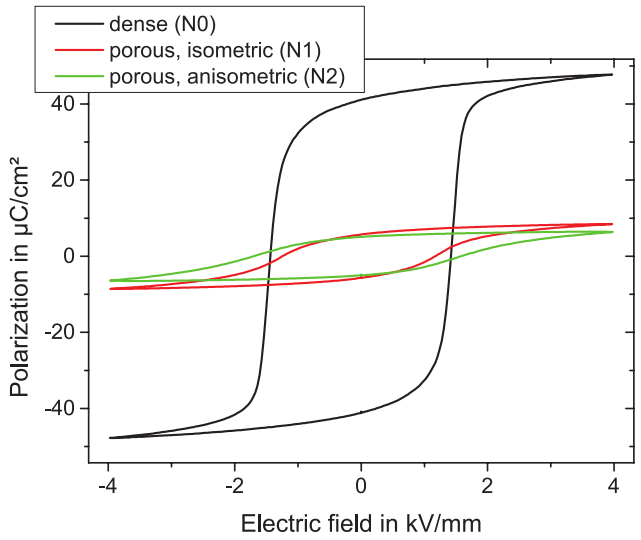

Figure 16. Polarization loops of dense ($N0$) and porous samples with isometric ($N1$) and anisometric ($N2$) shape of the pores (measured at 1 Hz).

4.2. Polarization-switching measurements and the IFM model analysis

In this section, experimental data on time-dependent polarization switching in dense and various porous PZT ceramics are presented and treated by means of the IFM model. For measurements of the switched polarization ΔP as a function of the applied electric field E_m and time t, a pulse-switching method was implemented using the electrical circuit and procedure described in [38]. A high-voltage/high-current push-pull switch from Behlke (Germany), which included a buffer 1 μF capacitor C_B as a voltage source, was used to provide the voltage step U_0 up to 3 kV. The pulse duration from 1 μs to 10^3 s was controlled by a programmable signal source (Model 8165A from Hewlett Packard). The temporal evolution of the electric displacement in sample C_s was detected by a sensing capacitor $C_m = 4.4$ μF connected in series with the current limiting resistor R_s of 100 Ω. The voltage drop U_m across the series capacitor was registered by means of a digital oscilloscope (Tektronix TDS 510 A) connected via a high-impedance amplifier. The RC time constant of the experimental setup of about 100 ns was shorter than the actual ferroelectric switching time of the investigated ferroelectric materials and shorter than the shortest voltage pulse (1 μs) applied in this study.

To investigate the polarization-switching phenomenon, the samples were first poled by applying the negative DC field of $E_o = 2E_c$ for 300 s, ensuring that the maximum negative saturated polarization was reached after the poling procedure. After complete poling in the negative-field direction, the positively directed switching field E_m was applied to the sample for a certain time t. After the switching experiment the sample was conditioned again, to restore its positive saturated state by applying a positive field $E_o = 2E_c$ for 300 s. At the fourth step, forward poling was performed by applying the field E_m to the conditioned sample in the same direction for the time t. Since the sample was already polarized to its positive saturation, the apparent displacement during forward poling contains all those components which exist in the switching experiment except for the switched ferroelectric polarization ΔP. Therefore, the switched polarization ΔP was determined as the difference between the displacement values of switching and forward poling taken at time t after application of the step voltage pulse. A number of applied-field values E_m covered the range from $0.5E_c$ to $2E_c$.

The data for the dense PZT reference (sample $N0$) are displayed in figure 17(a), exhibiting the coercive field in agreement with figure 16. The symbols show experimental points for different applied-field magnitudes, while solid lines represent theoretical calculations for corresponding field values, as explained below. Switching experiments were performed at 25–30 different values of the applied field E_m (more than the number of points shown in the graphs), which allows calculation of the field derivatives and further treatment according to the IFM approach [22]. From the latter data, the positions of maxima of derivatives (2) for different times, $E_{max}(t)$, can be evaluated. When the field values for each derivative plot are normalized by the respective maximum position, all the curves may be represented as functions of the dimensionless reduced field $E/E_{max}(t)$, as shown in figure 17(b). A satisfactory match of different curves with respect to distinct times t proves the applicability of the IFM concept to the material studied [23] and simultaneously presents its master curve $\Phi(u)$. Using $\Phi(u)$ and $E_{max}(t)$ the theoretical response (3) can be calculated resulting in solid lines in figure 17(a).

Now, we consider dynamic polarization data for the porous material with pores of isometric shape and a total porosity

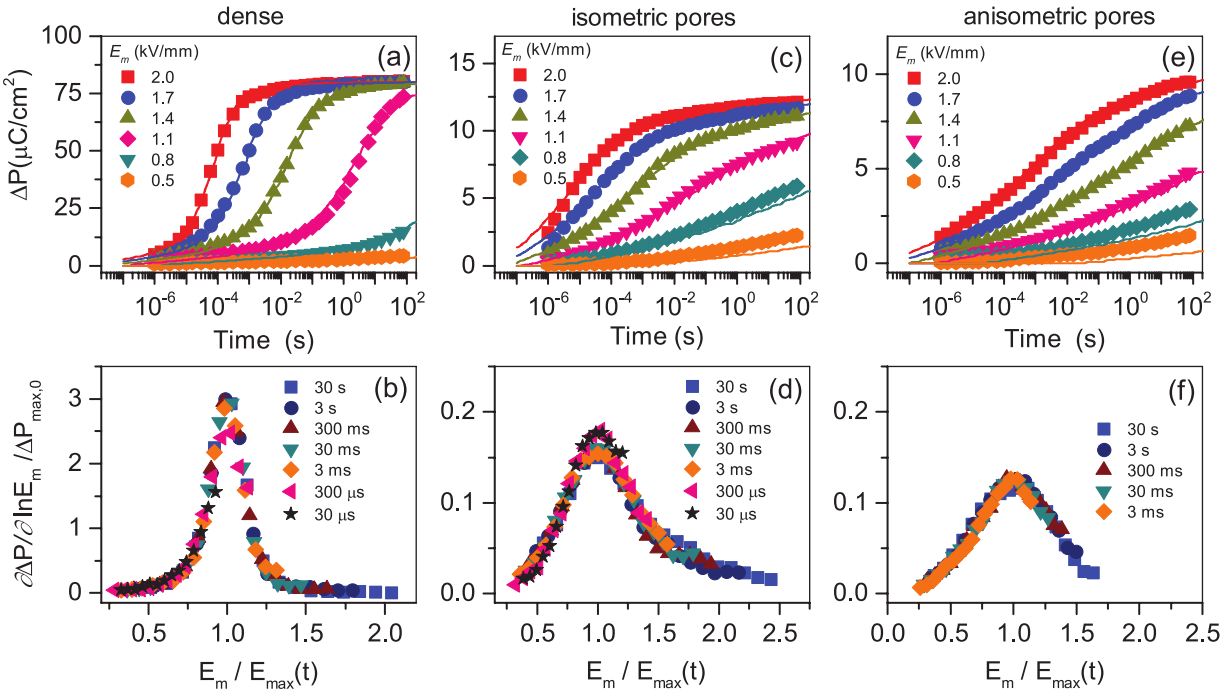

Figure 17. Switched polarization ΔP versus poling time for the (a) dense PZT sample *N*0, (c) porous PZT sample *N*1, and (e) porous PZT sample *N*2. Symbols correspond to the experimental results measured at different fields E_m, as indicated. Solid curves represent the field-related IFM model calculations. Normalized logarithmic field derivative of the polarization response scaled to its respective maximum position $E_{max}(t)$ and thus displaying master curves, equation (2), for the (b) dense PZT sample *N*0, (d) porous PZT *N*1 sample, and (f) porous PZT *N*2 sample.

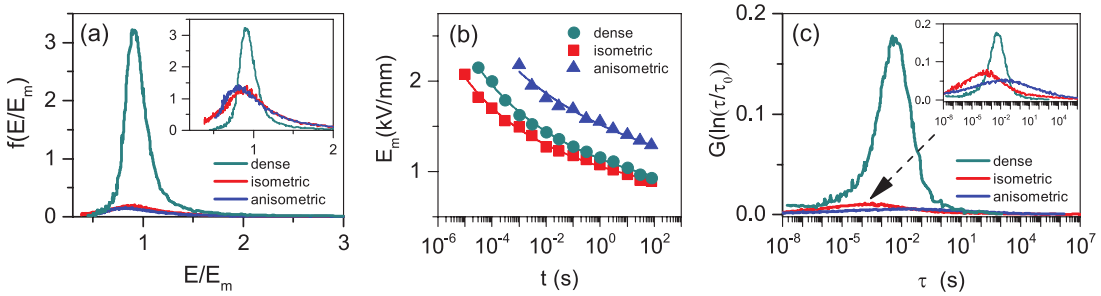

Figure 18. (a) statistical field-magnitude distributions for different porous and dense PZT, as indicated. (b) Positions of the maximum of the field derivative (2) on the field scale as a function of time in the mentioned materials (symbols) and their fitting with the Merz function (solid lines). (c) Statistical switching-time distributions for the same materials derived from equation (5) at $E_m = 1.5\,\mathrm{kV\ mm^{-1}}$.

of 37% (sample *N*1). The polarization-switching behaviour shown in figure 17(c) is apparently more dispersive than that of the dense material displayed in figure 17(a). This is accompanied by broader field derivatives in figure 17(d) and finally by a wider master curve. Coincidence of the scaled field derivatives at different times for sample *N*1 is inferior to that for the dense sample *N*0 (figure 17(b)); therefore, the theoretical description of dynamic polarization data (solid lines in figure 17(c)) is fair at low-field values. The reason might be that the microscopic polarization-switching mechanism in the porous material is not unique anymore. In particular, the parameters of the local-field dependence of the switching time $\tau(E)$(e.g. the activation field E_a) may become different at different locations. In fact, even in dense materials, different polarization-switching mechanisms are observed, such as 90° and 180° rotations [39, 40], which might result in different activation fields E_a [41]. Nevertheless, as is seen in figure 17(a), the IFM model describes the response perfectly using a unique value of E_a that implies domination of one switching mechanism. Additionally, in the case of porous ceramics, figures 17(c) and (e), the performance of the IFM model with only one value of the parameter E_a is remarkably better than the best possible fitting of these data with the KAI model. Note the strongly dispersive character of the polarization response, which is comprehensible in view of the field-distribution simulations of highly porous samples in section 3.

Even more dispersive behaviour is revealed for the polarization-switching dynamics of sample *N*2 with elongated pores and a total porosity of 37%, displayed in figure 17(e). Switching dynamics for this system could only be measured for the field direction normal to the preferred pore orientation. Despite the fact that the IFM analysis presented in figure 17(f) exhibits a well-defined master curve, the theoretical fitting by means of formula (3), shown by solid lines in figure 17(e), is

Table 1. IFM-model parameters.

Sample	ΔP_{max} (μC cm^{-2})	E_a (kV mm^{-1})	τ_0(s)	Υ	$\langle\cos\theta\rangle$
*N*0 dense PZT	80.00	25.24	2.55×10^{-10}	1.086	1
*N*1 isometric	12.40	25.28	3.91×10^{-11}	1.083	0.909
*N*2 anisometric	9.75	37.78	1.60×10^{-11}	1.140	0.725

only fair for lower-field values, doing well for medium- and high-field strengths.

From the master curves $\Phi(u)$ obtained for different materials and displayed in figures 17(b), (d) and (f), the corresponding weighted statistical field and switching-time distributions are derived using formulas (4) and (5) and presented in figure 18. The distributions for porous samples are strongly reduced in magnitude with respect to the dense material. It can be seen that the two field distributions for porous materials are strongly broadened and shifted to lower fields, in agreement with simulations displayed in figures 7 and 12. To better recognize the width and maximum positions of the field distributions for porous materials they are shown in the insert on figure 18(a) when normalized to unity (i.e. divided by the factor $1 - \nu$) as in case of the distribution for the dense material. The maximum for the elongated pores is, however, shifted only slightly more strongly than for the isometric pores in contrast to expectations when considering figure 10(a). The reason for this discrepancy can be seen in the difference between the simulations in 2D and the experiment in 3D. In the 2D case, electric-field lines have to bend around the transversely oriented elliptical pores with a much lower dielectric constant, thus contributing to a wide distribution of the field values as is seen in figure 8(a). From the 3D point of view, this sort of behaviour corresponds to the disk-shaped pores oriented transversely to the field direction, which can be compared in a cross-sectional view with the ellipses shown in figures 9 and 11. Sample PZT *N*2, investigated here experimentally, however, possesses pores of a more complicated shape than simple disk-shaped structures. Though they are mostly flat and show a tendency to orient preferably in the plane perpendicular to the field direction (see figure 15(b)) they have random irregular configurations, as may be recognized in figure 14(c). When going around such an obstacle, electric-field lines find the shortest curvature radius of each pore and thus stray less than around an ideal transverse disk-shaped cavity of the same size. That is why the statistical field-distributions for isometric and transverse elongated pores in figure 18(a) appear closer to each other than in the simulated cases in figures 10(a) and 12(a).

Having established the field distributions for each system, the statistical switching-time distributions can be derived by equation (5). To this end, however, the knowledge of the field dependence of the local switching time $\tau(E)$ is required. This can be obtained by solving the equation $E_{max}(t)/\gamma = E$ with respect to E. This task can be performed analytically if the numerically extracted dependences $E_{max}(t)$ are approximated by a suitable ansatz-function. The function $E_{max}(t) = \gamma E_a/\ln(t/\tau_0)$ appears to be appropriate for all three PZT systems, as is seen in figure 18(b) with the fitting parameters E_a and τ_0 listed in table 1. This kind of approximation results in the well-known field dependence of the switching time $\tau = \tau_0 \exp(E_a/E)$, first introduced by Merz [21].

We note that the parameters τ_0 and E_a in the three studied PZT compounds are different despite having the same chemical composition. To comprehend this fact we should take into account the effect of the different microstructures of the samples on the local polarization-switching mechanism. Since the preparation routes of the two porous materials are different and involve different organic constituents (see the beginning of section 4.1), the residual content of conducting carbon, particularly, in closed pores, may be different. This may provide different local-screening effects on the applied field, which prevent domain switching. Another feature that may differ in the two porous materials is the pore-surface morphology, providing different domain-pinning strength on the boundaries of pores. On the other hand, introducing porosity in PZT films makes switching conditions easier, at least at low porosities, due to stress relief [42]. These contradictory trends make it difficult to predict the changes in the parameters of Merz's law in porous ceramics that have been prepared differently. It does not preclude, however, the possibility of consistently describing each material by the individual set of model parameters.

Using equation (5) the statistical switching-time distributions are now calculated and displayed in figure 18(c) in the convenient logarithmic form [20] $G(\ln(\tau/\tau_0)) = \tau\, Q(\tau)$. The insert in figure 18(c) shows all distributions when normalized to unity and the distribution for the dense material, which allows one to better recognize and compare their width and maximum position. The switching-time spectrum for elongated pores appears to be the most spread out and considerably shifted towards longer times. Considering the field distributions for both porous systems in figure 18(a) it is clear that they are not the reason for such a big difference in switching-time spectra. The reason appears to be rather a much larger activation field E_a in the case of the elongated pores, as is seen from table 1, which might be related to difficult material-specific conditions for the reversed domain nucleation.

Using the mean cosine magnitude for isometric samples with a porosity of 37%, as shown in figure 13, and the maximum polarization values from table 1, the non-switchable part of these samples may be estimated by the formula (7) as $\nu_{is} = 0.829$ and $\nu_{anis} = 0.866$, respectively. Both values by far exceed the nominal porosity of the samples of 0.37. This means that, beyond the volume of pores, a substantial part of the sample is prevented from polarization switching by physical reasons described in the previous section. Note that a similar reduction was observed in heavily fatigued ferroelectrics [43]. In this respect, the enhanced microporosity, observed in figure 14, may play a role, particularly due to polarization compensation by local partial-discharge events [44].

5. Conclusions

Controlling the porosity of ferroelectric ceramics allows tailoring of their physical properties, such as piezoelectric sensitivity, hydrostatic piezoelectric coefficients, pyroelectric energy conversion, and others. Particularly, the concept of the IFM of polarization switching predicts, on the one hand, the broadening of the switching-time distribution in porous materials but, on the other hand, also the possibility of affecting the polarization dynamics by orientation of pores and choosing the direction of an applied field with respect to the major direction of pore orientation.

FEM simulations of the statistical field-distributions in ferroelectric ceramics with pores of different size, shape, and orientation predict the following traits of the switching-time distributions:

- In systems with isometric pores, statistical distributions of the switching times are smeared out with increasing porosity, while being virtually independent of the particular pore size or size distribution. Polarization switching becomes more dispersive and is retarded with increasing porosity.
- In systems with pores of anisometric shapes (exemplarily, elliptical ones), statistical distributions of the switching times become dependent on the aspect ratio and orientation of pores. The larger the depolarization effects due to the pore shape and orientation are, the wider the statistical distributions of both field and time will be. Thus, they are the most broadened for elliptical pores oriented transversely to the applied field. Similarly as to the isometric pores, the size of the pores is irrelevant, while the distributions become progressively broadened with an increasing in the total porosity.
- Polarization dynamics of a system with randomly oriented pores of anisometric shapes are expected to be quite similar to those of the system with isometric pores of the same total porosity.

In qualitative agreement with the above predictions, measurements of the polarization switching in the available PZT ceramics with either isometric or anisometric porosity reveal that switching-time spectra become substantially wider in comparison to that of the dense ceramic of the same composition. The spectrum of the system with pores elongated perpendicular to the applied-field direction appears, as expected, wider than that of the system of the same porosity, but with isometric pores. The latter difference is, however, not substantial because of the incomplete transverse orientation and irregular pore shapes.

Acknowledgments

This work was supported by the Deutsche Forschungsgemeinschaft (DFG) within the grants SE 941/19-1 and GE 1171/7-1. The authors thank C Capiani (CNR-ISTEC) for the skillful preparation of the samples.

References

[1] Moulson A J and Herbert J M 2003 *Electroceramics: Materials, Properties, Applications* 2nd edn (San Francisco, CA: Wiley)
[2] Topolov V Y and Bowen C R 2009 *Electromechanical Properties in Composites Based on Ferroelectrics* (London: Springer)
[3] Akdogan E K, Allahverdi M and Safari A 2005 Piezoelectric composites for sensor and actuator applications *IEEE Trans. Ultrason. Ferroelectr. Freq. Control* **52** 746
[4] Galassi C 2006 Processing of porous ceramics: piezoelectric materials *J. Eur. Ceram. Soc.* **26** 2951
[5] Zhang H L, Li J F and Zhang B P 2007 Microstructure and electrical properties of porous PZT ceramics derived from different pore-forming agents *Acta Mater.* **55** 171
[6] McLachlan M A, McComb D W, Ryan M P, Morozovska A N, Eliseev E A, Payzant E A, Jesse S, Seal K, Baddorf A P and Kalinin S V 2011 Probing local and global ferroelectric phase stability and polarization switching in ordered macroporous PZT *Adv. Funct. Mater.* **21** 941
[7] Wersing W, Lubitz K and Mohaupt J 1986 Dielectric, elastic and piezoelectric properties of porous PZT ceramics *Ferroelectrics* **68** 77
[8] Guo R, Wang C A and Yang A K 2011 Effects of pore size and orientation on dielectric and piezoelectric properties of 1–3 type porous PZT ceramics *J. Eur. Ceram. Soc.* **31** 605
[9] Xu T T and Wang C A 2016 Control of pore size and wall thickness of 3–1 type porous PZT ceramics during freeze-casting process *Mater. Des.* **91** 242
[10] Zhang Y, Bao Y X, Zhang D and Bowen C R 2015 Porous PZT ceramics with aligned pore channels for energy harvesting application *J. Am. Ceram. Soc.* **98** 2980
[11] Stoleriu L, Stancu A, Mitoseriu L, Piazza D and Galassi C 2006 Analysis of the switching properties of porous ferroelectric ceramics by means of the first-order reversal curves (FORC) diagrams *Phys. Rev.* B **74** 174107
[12] Padurariu L, Curecheriu L, Galassi C and Mitoseriu L 2012 Tailoring non-linear dielectric properties by local field engineering in anisotropic porous ferroelectric structures *Appl. Phys. Lett.* **100** 252905
[13] Stanculescu R, Ciomaga C E, Padurariu L, Galizia P, Horchidan N, Capiani C, Galassi C and Mitoseriu L 2015 Study of the role of porosity on the functional properties of (Ba,Sr)TiO_3 ceramics *J. Alloy. Compd.* **643** 79
[14] Padurariu L, Curecheriu L P and Mitoseriu L 2016 Nonlinear dielectric properties of paraelectric-dielectric composites described by a 3D finite element method based on Landau–Devonshire theory *Acta Mater.* **103** 724
[15] Jayendiran R and Arockiarajan A 2012 Modeling of dielectric and piezoelectric response of 1–3 type piezocomposites *J. Appl. Phys.* **112** 044107
[16] Jayendiran R and Arockiarajan A 2014 Viscoelastic modeling and experimental characterization of thermo-electromechanical response of 1–3 piezocomposites *J. Appl. Phys.* **116** 214103
[17] Jayendiran R and Arockiarajan A 2015 Effect of viscoelastic and dielectric relaxing matrix on ferroelastic behaviour of 1–3 piezocomposites *AIP Adv.* **5** 027103
[18] Sekhar K C, Nautiyal A and Nath R 2009 Analysis of ferroelectric switching in sodium nitrite:poly(vinylalcohol) nanocomposite films *Appl. Phys.* A **95** 415
[19] Mishra N, Dabra N, Nautiyal A, Hundal J S, Varma G D, Pathak N P and Nath R 2015 Ferroelectric and switching properties of spray deposited $NaNO_2$: PVA composite films on porous silicon *Ferroelectr. Lett.* **42** 75

[20] Tagantsev A K, Stolichnov I, Setter N, Cross J S and Tsukada M 2002 Non-Kolmogorov–Avrami switching kinetics in ferroelectric thin films *Phys. Rev.* B **66** 214109
[21] Merz W J 1954 Domain formation and domain wall motion in ferroelectric $BaTiO_3$ single crystal *Phys. Rev.* **95** 690
[22] Zhukov S, Genenko Y A, Hirsch O, Glaum J, Granzow T and von Seggern H 2010 Dynamics of polarization reversal in virgin and fatigued ferroelectric ceramics by inhomogeneous field mechanism *Phys. Rev.* B **82** 014109
[23] Genenko Y A, Zhukov S, Yampolskii S V, Schütrumpf J, Dittmer R, Jo W, Kungl H, Hoffmann M J and von Seggern H 2012 Universal polarization switching behavior of disordered ferroelectrics *Adv. Funct. Mater.* **22** 2058
[24] Zhukov S, Genenko Y A, Acosta M, Humburg H, Jo W, Rödel J and von Seggern H 2013 Polarization dynamics across the morphotropic phase boundary in $Ba(Zr_{0.2}Ti_{0.8})O_{3-x}(Ba_{0.7}Ca_{0.3})TiO_3$ ferroelectrics *Appl. Phys. Lett.* **103** 152904
[25] Zhukov S, Kungl H, Genenko Y A and von Seggern H 2014 Statistical electric field and switching time distributions in PZT 1Nb2Sr ceramics: crystal- and microstructure effects *J. Appl. Phys.* **115** 014103
[26] Zhukov S, Acosta M, Genenko Y A and von Seggern H 2015 Polarization dynamics variation across the temperature- and composition-driven phase transitions in the lead-free $Ba(Zr_{0.2}Ti_{0.8})O_{3-x}(Ba_{0.7}Ca_{0.3})TiO_3$ ferroelectrics *J. Appl. Phys.* **118** 134104
[27] Schütrumpf J, Zhukov S, Genenko Y A and von Seggern H 2012 Polarization switching dynamics by inhomogeneous field mechanism in ferroelectric polymers *J. Phys. D: Appl. Phys.* **45** 165301
[28] Lee J, van Breemen A J J M, Khikhlovskyi V, Kemerink M, Janssen R A J and Gelincket G H 2016 Pulse-modulated multilevel data storage in an organic ferroelectric resistive memory diode *Sci. Rep.* **6** 24407
[29] Robert G, Damjanovic D, Setter N and Turik A V 2001 Preisach modeling of piezoelectric nonlinearity in ferroelectric ceramics *J. Appl. Phys.* **89** 5067
[30] Ishibashi Y and Takagi Y 1971 Superstructure in the ferroelectric phase of ammonium Rochelle salt *J. Phys. Soc. Japan* **31** 506
[31] Zhukov S, Genenko Y A, Koruza J, Schultheiß J, von Seggern H, Sakamoto W, Ichikawa H, Murata T, Hayashi K and Yogo T 2016 Effect of texturing on polarization switching dynamics in ferroelectric ceramics *Appl. Phys. Lett.* **108** 012907
[32] Genenko Y A, Wehner J and von Seggern H 2013 Self-consistent model of polarization switching kinetics in disordered ferroelectrics *J. Appl. Phys.* **114** 084101
[33] Jo J Y, Han H S, Yoon J G, Song T K, Kim S H and Noh T W 2007 Domain switching kinetics in disordered ferroelectric thin films *Phys. Rev. Lett.* **99** 267602
[34] Kedzierski D, Kirichenko E V and Stephanovich V A 2011 On the theory of domain switching kinetics in ferroelectrics *Phys. Lett.* A **375** 685
[35] Zhukov S, Glaum J, Kungl H, Sapper E, Dittmer R, Genenko Y A and von Seggern H 2016 Fatigue effect on polarization switching dynamics in polycrystalline bulk ferroelectrics *J. Appl. Phys.* **120** 064103
[36] Piazza D, Capiani C and Galassi C 2005 Piezoceramic material with anisotropic graded porosity *J. Eur. Ceram. Soc.* **25** 3075
[37] Piazza D, Galassi C, Barzegar A and Damjanovic D 2010 *J. Electroceram.* **24** 1706
[38] Zhukov S, Fedosov S, Glaum J, Genenko Y A and von Seggern H 2010 Effect of bipolar electric fatigue on polarization switching in lead-zirconate-titanate ceramics *J. Appl. Phys.* **108** 014105
[39] Pramanick A, Prewitt A D, Forrester J S and Jones J L 2012 Domains, domain walls and defects in perovskite ferroelectric oxide: a review of present understanding and recent contributions *Crit. Rev. Solid State Mater. Sci.* **37** 243
[40] Daniels J E, Cozzan C, Ukritnukun S, Tutuncu G, Andrieux J, Glaum J, Dosch C, Jo W and Jones J L 2014 Two-step polarization reversal in biased ferroelectrics *J. Appl. Phys.* **115** 224104
[41] Liu S, Grinberg I and Rappe A M 2016 Intrinsic ferroelectric switching from first principles *Nature* **534** 360
[42] Johnson-Wilke R J, Wilke R H T, Wallace M, Rajashekhar A, Esteves G, Merrit Z, Jones J L and Troiler-McKinstry S 2015 Ferroelectric/ferroelastic domain wall motion in dense and porous tetragonal lead zirconate titanate films *IEEE Trans. Ultrason. Ferroelectr. Freq. Control* **62** 46
[43] Genenko Y A, Glaum J, Hoffmann M J and Albe K 2015 Mechanisms of aging and fatigue in ferroelectrics *Mater. Sci. Eng.* **192** 52
[44] Hang T, Glaum J, Genenko Y A, Phung T and Hoffman M 2016 Investigation of partial discharge in piezoelectric ceramics *Acta Mater.* **102** 284

6.2.2 PAPER II

Correlated polarization-switching kinetics in bulk polycrystalline ferroelectrics: A self-consistent mesoscopic switching model
R. Khachaturyan, J. Wehner, Y.A. Genenko, *Physical Review B.*, **96(5)**, 054113 (2017).
DOI: 10.1103/PhysRevB.96.054113

Correlated polarization-switching kinetics in bulk polycrystalline ferroelectrics: A self-consistent mesoscopic switching model

Ruben Khachaturyan,[1,*] Jens Wehner,[2] and Yuri A. Genenko[1,†]

[1]*Institut of Materials Science, Technische Universität Darmstadt, Jovanka-Bontschits-Str. 2, D-64287 Darmstadt, Germany*

[2]*Max Planck Institute for Polymer Research, Ackermannweg 10, 55128 Mainz, Germany*

(Received 28 April 2017; revised manuscript received 28 July 2017; published 17 August 2017)

Analysis of statistical distributions and auto- and cross correlations of polarization and electric field during the field-driven polarization reversal in a bulk polycrystalline ferroelectric is performed. A mesoscopic switching model is used which accounts self-consistently for the development of depolarization fields. Correlations mediated by electrostatic fields are shown to be mostly isotropic and short range at the typical scale of the grain size which is explained by an effective screening via adapting bound charges. The short-range screening clarifies the paradoxical ability of common statistical concepts neglecting the feedback effect of depolarization fields to adequately describe the polarization switching kinetics. The statistical distribution of the local electric field magnitudes is continuously spreading in the course of the global polarization reversal due to mismatching of both dielectric tensor and spontaneous polarization at grain boundaries. The increasing field dispersion substantially contributes to the well-known deceleration of the polarization reversal at long times.

DOI: 10.1103/PhysRevB.96.054113

I. INTRODUCTION

Electric field-driven switching of spontaneous polarization is a fundamental process in ferroelectric materials relevant to many applications, for example digital data storage. Despite the great significance of polarization dynamics for applications, switching mechanisms remain poorly understood even for well-studied ferroelectrics in single crystal or polycrystalline forms. Indeed, the classical picture of polarization switching developed in works by Landauer [1], Miller *et al.* [2], and Ishibashi *et al.* [3] suggests spontaneous nucleation and growth of domains of the opposite polarization within a previously homogeneously polarized medium. Polarization reversal inevitably creates local bound charges due to polarization mismatch at the domain boundaries which, in turn, generate electric depolarization fields. In nonconducting media these large and long-range fields are not expected to be screened. Thus, depolarization fields have to play an essential role in the switching process by providing mutual influence of different switching regions. However, widely used statistical concepts of the polarization switching [3–8] assume independent and uncorrelated nucleation and growth of reversed domains and thus virtually neglect the feedback effect of the depolarization fields during the polarization reversal. Furthermore, the inhomogeneous field mechanism (IFM) model, recently advanced by the authors [9,10] and also assuming independent polarization switching in individual regions, describes the time-dependent response of various ferroelectric ceramics of different chemical compositions and phase symmetries [10–16] as well as of semicrystalline polymers [17] with high accuracy.

Whereas in single-crystalline media the polarization switching may, in principle, occur by moving charge-free 90°-domain walls without generating local bound charges [18,19], avoiding local charges in polycrystalline media, such as bulk ferroelectric ceramics, is impossible because of inevitable mismatches of different crystalline orientation in adjacent grains. A paradoxical ability of statistical concepts, which neglect the feedback of depolarization fields, to accurately describe polarization switching kinetics in a variety of inorganic ferroelectric ceramics [6,7,9–16,20,21], organic ferroelectrics [17,22–27], and organic-inorganic ferroelectric composites [28,29] needs to be comprehended.

Attempts made so far to account for the feedback of depolarization fields remained mostly within the mean-field approximation which assumes emergence of a time-dependent spatially uniform electric field due to averaging of multiple switching events [30–32]. Being an important step towards the understanding of the polarization switching in disordered media such an approach still misses the intrinsically stochastic nature of emerging depolarization fields which are possibly correlated at a finite scale. Particularly, in the case of long-range correlations a spatially and temporally coherent switching could, in principle, keep the depolarization fields small. This would explain, on the one hand, a weak effect of the depolarization field, but mean, on the other hand, that switching in different regions cannot be considered as being independent.

The importance of collective domain dynamics was recognized and studied in thin ferroelectric films for more than a decade by various methods. Strong correlations of domain structures extending across the grain boundaries have been observed by piezoelectric scanning probe microscopy (SPM) in polycrystalline thin films [33] and by transmission electron microscopy (TEM) and piezoresponse force microscopy (PFM) in model single-grain structures [34–36]. Polarization response exhibited clustering ranging from few grains [33] to agglomerations of 10^2–10^3 grains [37,38]. Macroscopic and local measurements of nonlinear behavior in mechanically clamped and released polycrystalline films revealed the dominant role of collective long-range strain interactions mediated by the local and global mechanical boundary conditions, possibly by elastic coupling through the substrate [39,40].

*rubenftf@gmail.com

†genenko@mm.tu-darmstadt.de

Latest *in situ* high-energy x-ray diffraction advances allowed for time resolution of different switching processes in bulk ferroelectric ceramics [41–43]. Furthermore, the grain-resolved three-dimensional x-ray diffraction (3D-XRD) was used to trace the non-180° ferroelectric domain switching within polycrystalline bulk media [44,45]. The collective dynamics in bulk materials was found to be correlated over approximately 10–20 grains, a scale presumably resulting from the complicated and still not understood interplay between the electrostatic field [46] and the elastic strain energy. This moderate characteristic length disagrees with extremely long-range electrostatic correlations predicted for uniform media by phase-field simulations [47] and by a microscopic model describing self-consistently the polarization reversal randomized by thermal vibrations [48]. Thus, the role of long-range electrostatic interactions in the switching dynamics of bulk ferroelectric ceramics still remains unclear.

Recently a self-consistent mesoscopic switching (SMS) model [49] was suggested by the authors which accounts in a self-consistent way for the local depolarization fields. These arise in a random polycrystalline medium leading to the interaction of different regions during the field-driven polarization switching. In the current study, the auto- and cross correlations of random polarization and electric fields and evolution of their statistical distributions are investigated in a polycrystalline ferroelectric by extension of the SMS model. The paper is organized as follows. The model is introduced in Sec. II. Investigation of spatial correlations of electric field and polarization components including their evolution in the course of the total polarization reversal is presented in Sec. III. Associated development of the statistical distribution of the electric field is described in Sec. IV. The results are discussed and concluded in Sec. V.

II. TWO-DIMENSIONAL SELF-CONSISTENT MODEL OF POLARIZATION SWITCHING

An advanced SMS model combines a numerical solution of coarse-grained local equations for polarization development in individual grains with the global calculation of the electric field by the finite-element method (FEM). In the following, the description of a ferroelectric ceramic and the evolution equations are introduced.

A. Creation of a random structure

We consider a polycrystalline bulk ferroelectric placed between two—top and bottom—plain electrodes. The material is assumed to consist of many single-crystalline grains of random shape and position. A representative two-dimensional (2D) structure is created using the Voronoi tessellation around randomly distributed seed points (see an example of the structure in Fig. 1).

Each grain possesses tetragonal phase symmetry and a random crystal orientation uncorrelated with neighbor grains. An initial polarization state is assumed to be created by a very strong electric field applied in positive z direction given by the vertical axis in Fig. 1. In this case, polarization directions in individual grains are arbitrarily chosen from the appropriate three-dimensional angle distribution function for a nonoriented

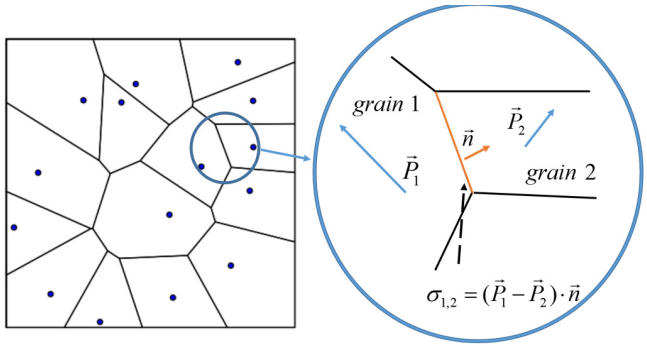

FIG. 1. Voronoi tessellation diagram around 15 randomly located seeds; appearance of a surface bound charge at a grain boundary as a result of mismatching polarizations is shown in the inset.

ferroelectric bulk ceramic of tetragonal symmetry [50]:

$$f(\theta,\varphi) = \begin{cases} \frac{3}{2\pi}, & 0 \leqslant \theta \leqslant \frac{\pi}{4} \\ \frac{6}{\pi^2}\left[\frac{\pi}{4} - \arccos(\cot\theta)\right], & \frac{\pi}{4} < \theta < \theta_{\max} \end{cases} \quad (1)$$

with $\theta_{\max} = \arcsin\sqrt{2/3}$ the threshold angle introduced by Uchida and Ikeda [51]. According to the chosen polarization (c-axis) direction, each grain is characterized by the two-dimensional dielectric tensor $\varepsilon_{ij} = \varepsilon_0 K_{ij}$, with principal values of the relative permittivity K_a and K_c.

Polarization within each grain is substituted by its mean value, $\mathbf{p}_i$, in the hard ferroelectric approximation which entails discontinuities at grain boundaries where surface charge densities arise equal to an abrupt variation of the normal component of the polarization when traversing the boundary (see inset in Fig. 1). The electric field, in contrast, varies within the grains according to the Laplace equation and natural boundary conditions at the grain boundaries which comprise continuity of the tangential electric field and discontinuity of the normal component of the electric displacement equal to the surface charge density. To apply an external electric field of either direction to the system, the top and the bottom lines of the computation box in Fig. 1 are held at constant potentials, whereas periodic boundary conditions are applied to the left and the right side of the box.

B. Evolution equations

The change in the polarization of individual grains is assumed to obey the Kolmogorov-Avrami-Ishibashi (KAI) model of domain nucleation and growth [3–5]:

$$\triangle p(t) = 2P_s\{1 - \exp[-(t/\tau)^\beta]\}, \quad (2)$$

where P_s is the saturation polarization, β is the Avrami index depending on the reversal domain dimensionality, t is the time elapsed after the voltage application, and τ is the switching time. It is well known that τ is strongly dependent on the electric field value E, for example, according to the empiric Merz law $\tau(E) = \tau_0 \exp(E_a/E)$ [52], where E_a is the so-called activation field and τ_0 is the switching time at very high fields.

In the original KAI approach the field E is assumed to be uniform in the whole system and constant in time. In such heterogeneous systems as ferroelectric ceramics the field is of course distributed nonuniformly, at least, due to complying

with the boundary conditions at the grain boundaries. In the spirit of the IFM model [9,10] we suppose that the local switching time $\tau(E)$ is determined by the local value of the electric field E. Over and above, we account for the fact that local switching time values are also time dependent together with the field E. To be able to capture this dependence we substitute the global time dependence of the polarization (2) by the instantaneous rate of the polarization change derived by differentiation of Eq. (2) with respect to the time t:

$$\frac{dp}{dt} = \frac{P_s\,\mathrm{sgn}(E) - p}{\tau}\beta\left(\frac{t}{\tau}\right)^{\beta-1}. \tag{3}$$

Here, the signum function $\mathrm{sgn}(\cdot)$ determines the direction to which the saturation of the polarization proceeds.

Furthermore, the polarization reversal is assumed to be dominated by 180°-switching events, so that the polarization only changes along the chosen c direction within each grain given by a unit vector $\mathbf{n}_i$. This means that the local dielectric tensor remains unchanged during this process. Thus Eq. (3) can be generalized to the vectorial form

$$\frac{d\mathbf{p}_i}{dt} = \frac{\mathbf{n}_i P_s\,\mathrm{sgn}(\langle\mathbf{E}\rangle\cdot\mathbf{n}_i) - \mathbf{p}_i}{\tau(|\langle\mathbf{E}\rangle\cdot\mathbf{n}_i|)}\beta\left[\frac{t}{\tau(|\langle\mathbf{E}\rangle\cdot\mathbf{n}_i|)}\right]^{\beta-1}, \tag{4}$$

where $\langle\mathbf{E}\rangle$ is the value of the electric field averaged over the area of each grain. Equation (4) takes into account that only the field projection on the local c axis promotes switching.

C. Simulation procedure

Simulations include the following steps:

(1) generation of a random geometry (grain forms, c-axes choice)

(2) assignment of material parameters (saturation polarization, activation field, and dielectric permittivity values)

(3) evaluation of the spatial field distribution and average field magnitudes inside each grain using a commercial finite element software FlexPDE from PDE Solutions, Inc.

(4) evaluation of the polarization change during the time step $\triangle t$ by integration of Eq. (4) over $\triangle t$ using the above calculated local average field values and employing the Fehlberg-Cash-Karp method based on the Runge-Kutta approach; consequent updating of polarizations in each grain

(5) calculation of the total polarization by adding up the local modified polarizations weighted by the volume fraction of each grain

(6) transfer of the structure with new polarization values to FlexPDE and repetition of steps 3–5 until the total polarization reaches a saturated value.

A simulation box of the size $20 \times 20\ \mu\mathrm{m}^2$ comprising 400 grains was chosen, which makes up an average linear size of the grain $R \simeq 1\ \mu$m. Material parameters of the tetragonal lead zirconate titanate (PZT) were taken [12] with the activation field $E_a = 35$ kV/mm, $\tau_0 = 5 \times 10^{-11}$ s, and the principal values of the relative dielectric permittivity $K_a = 499$ and $K_c = 198$ as for the tetragonal 40/60 PZT composition [53,54]. The parameter β was set to unity; the choice that does not have a significant effect on the statistical and correlation properties studied below.

Local values of the depolarization field scale with the magnitude of the saturation polarization P_s. When calculated directly from a typical saturation polarization for PZT of $0.45\ \mathrm{C/m^2}$ the field values appear to be unphysically large and therefore should be reduced by various physical mechanisms. A characteristic magnitude of the fluctuation depolarization field ΔE_d due to random charged grain boundaries [50] is as high as $\Delta E_d \simeq 3.5 P_s/4\pi\varepsilon_0\sqrt{K_a K_c} \simeq 50$ kV/mm with the vacuum permittivity ε_0 which is much larger than typical coercive fields for PZT. For low total polarization this high field can be depressed by splitting in domains which leads to low mean polarizations of grains. In a highly polarized state of the ceramic, too high local fields may be depressed due to semiconductor properties of the material. Indeed, the fluctuation field ΔE_d provides a variation of the electrostatic potential across a grain about $\Delta\varphi = \Delta E_d R \simeq 50$ V. Being much larger than the typical band gap in PZT of $E_g \simeq 3.5$ eV such a potential sweep causes strong band bending and produces electron and hole spatial pockets which effectively reduce the mismatch bound charges at grain boundaries. Due to this internal screening effect the local fields cannot exceed a typical value of E_g/qR, with the elementary charge q, so that the potential sweep remains below $E_g/2q$ [55,56]. To account for the internal screening in the calculation of the depolarization fields an effective value of the local saturation polarization $P_s^* = 0.01\ \mathrm{C/m^2}$ is introduced that limits too high charges which may occur at grain boundaries. When delivering the results of solution of Eqs. (4) to the FEM program for evaluation of the spatial field distribution the polarization values are scaled down by a factor of P_s^*/P_s providing the said limitation of the local fields and reasonable switching kinetics.

Polarization reversal was simulated at three applied fields of 3, 4 and 5 kV/mm. The initial state of the system with maximum polarization value P_s in each grain (which results in the total polarization of $0.831 P_s$ [51]) is unphysical since it occasionally includes very unlikely local configurations with highly charged grain boundaries. To start simulations from a physically reasonable initial state the system was first polarized to a saturation value from the initial zero polarization state and then fully re-polarized two times by the change of the voltage

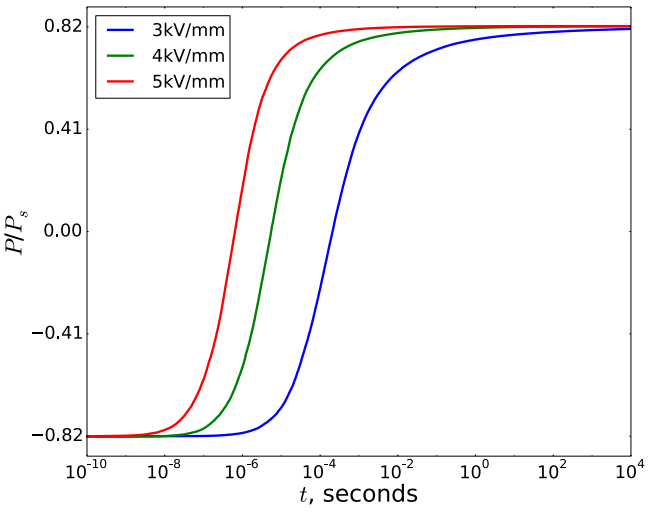

FIG. 2. Time evolution of the total polarization $P = \langle p_z\rangle$ for the Avrami index $\beta = 1$ and different applied voltages as indicated in the plot.

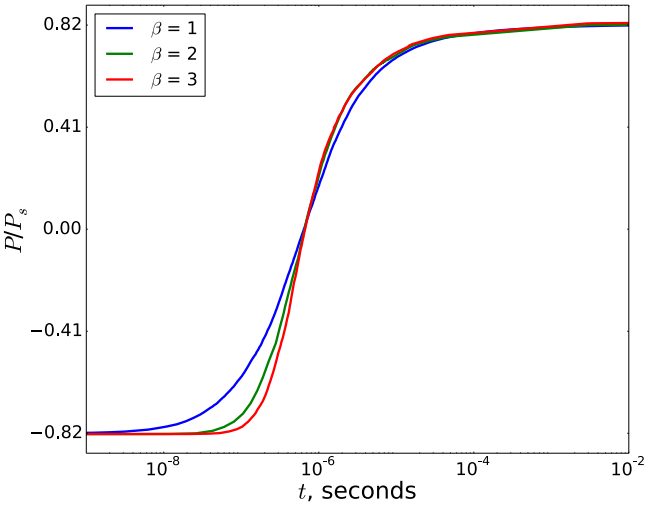

FIG. 3. Time evolution of the total polarization $P = \langle p_z \rangle$ for the applied field of 5 kV/mm and different values of the Avrami index β as indicated in the plot.

sign. These three steps proved to be sufficient to represent a physically valid initial configuration because further full polarization reversals reproduced each other. Time evolution of the total polarization at different applied voltages is presented in Fig. 2.

The choice of the Avrami parameter β has an influence on the kinetics of switching as exemplary calculations for $\beta = 1$, 2, and 3 show in Fig. 3. However, the variation with β vanishes for higher values of β as is expected from the analysis within the IFM model [10] and is confirmed by comparison between curves for $\beta = 2$ and $\beta = 3$ in the latter figure. Since the tests have shown no remarkable changes in statistical and correlation functions for different β, the value $\beta = 1$ was used for simplicity in further simulations.

A polarization map in the saturated state obtained at the applied field of 5 kV/mm is shown in Fig. 4, which reveals that not all grains achieve the saturation state. Local depolarization fields prevent the full polarization reversal thus demonstrating the importance of the local fields for the polarization switching.

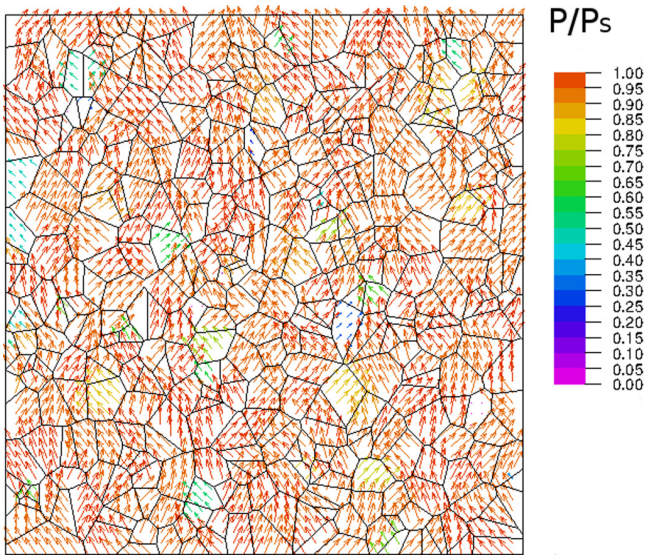

FIG. 4. Polarization map at $P \simeq 0.79 P_s$.

III. CORRELATIONS

To take a closer look into coarse-grained spatial fluctuations of polarization and field we introduce the variance anisotropy factor (VA-factor) as

$$\mathrm{VA(C)} = \frac{\sum_i \sum_j (C_{ij} - \langle C_{\updownarrow j} \rangle)^2}{\sum_i \sum_j (C_{ij} - \langle C_{\leftrightarrow i} \rangle)^2}. \tag{5}$$

Here the values of a spatially dependent variable C_{ij} are evaluated at certain nodes on a quadratic grid of 60×60 points (approximately 9 points per grain) using FlexPDE at different time steps. The values $\langle C_{\updownarrow j} \rangle$ and $\langle C_{\leftrightarrow i} \rangle$ denote the mean values of the variable along the jth column and ith row, respectively. Thus, the VA-factor (5) represents a ratio of mean variances of a physical quantity along and across the applied field direction as is shown in Fig. 5.

In terms of this approach a value of VA close to 1 means that a physical quantity fluctuates similarly in both x- and z-directions, while VA deviation from 1 means that the quantity develops more coherently along (if VA is smaller than 1) or across the field (if VA is larger than 1). The closest analog to the VA factor is the so-called F test in statistics which estimates the ratio of variances of two variables [57]. The absence of correlations of a physical quantity is equivalent to the so-called null hypothesis assuming the VA-factor equal to unity. Disproving the null hypothesis reveals the correlation itself and the correlation anisotropy.

In Fig. 6 the evolution of the VA factor for the variables p_x, p_z, E_x, and E_z is shown during the development of the total polarization value $P = \langle p_z \rangle$ from the maximum negative to the maximum positive value when the field $E_0 = 3$ kV/mm is maintained in the ferroelectric. Here and

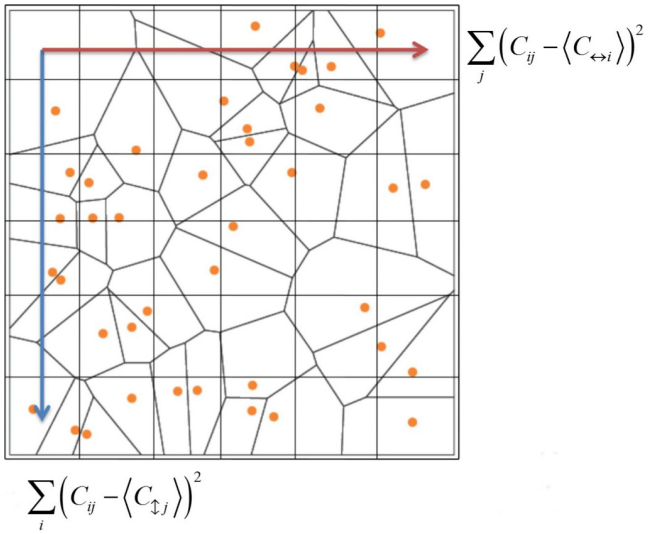

FIG. 5. Scheme of the coarse-grained calculation of the VA factor for a variable C on a quadratic grid. Indexes i and j numerate nodes of the grid.

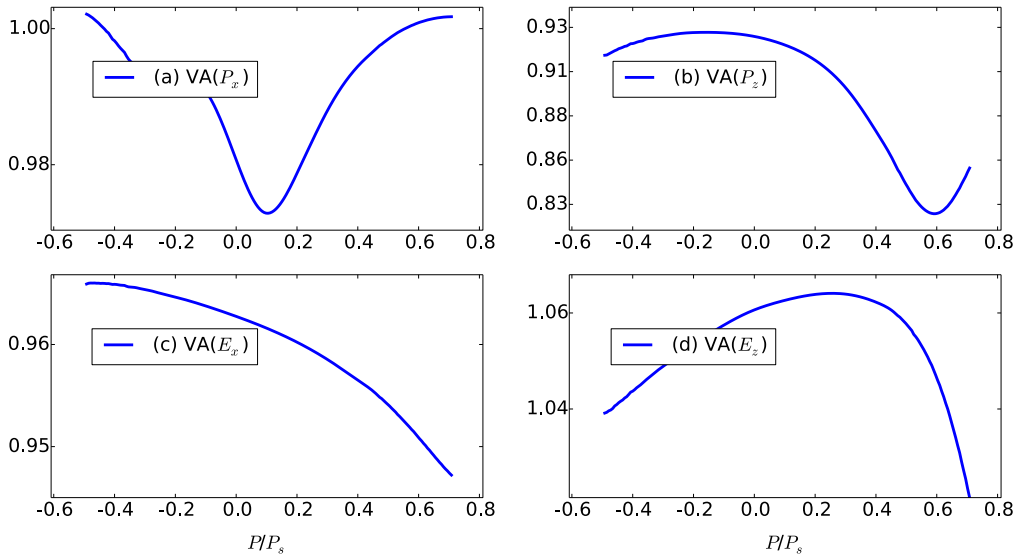

FIG. 6. The VA-factor evolution for (a) p_x, (b) p_z, (c) E_x, (d) E_z components when the total polarization P varies from $-0.7P_s$ to $0.7P_s$.

below the notation of the mean value $\langle ... \rangle$ means averaging over the above introduced 60×60 points grid. It is seen that both components of polarization and electrical field do not obey the null hypothesis exhibiting deviations of the VA factor from unity. The most striking violation of the null hypothesis is observed for p_z component where the VA factor deviates by 20% from unity which is by one order of magnitude larger than for the other variables. This variation of the VA factor is in favor of anisotropic correlations and their evolution during the sample poling. Asymmetric shape of the curves is well reproduced for simulations with different realizations of the random grain structure keeping the same mean grain size. We note that, when poling in the opposite direction the curves in Fig. 6 will be mirrored with respect to $P = 0$.

Based on the results presented in Fig. 6 it is advisable to study spatial autocorrelations of the polarization components, of the electric field components, and cross correlations of the polarization and electric field components at various distances. To this end we use the Pearson two-point correlation

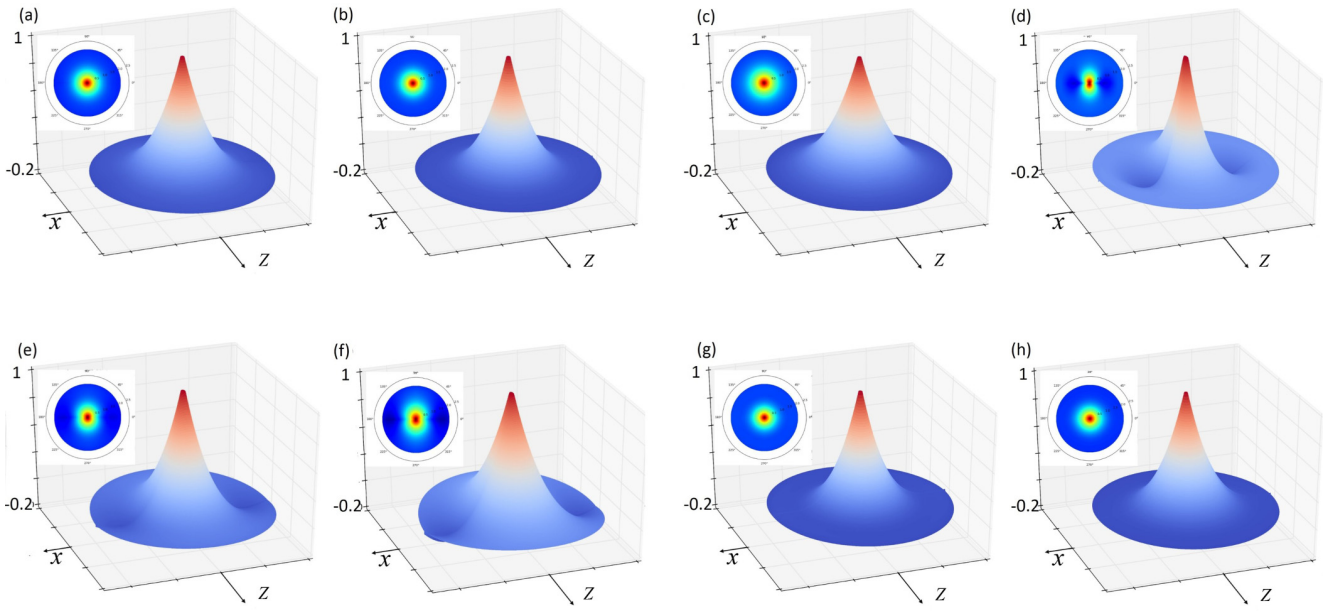

FIG. 7. Correlation coefficients $R(P)$ shown over the area of 2×2 μm^2 at different polarization states $P = \langle p_z \rangle$ when switching from $P = -0.7P_s$ to $0.7P_s$: (a) $R_{p_x,p_x}(0)$, (b) $R_{p_x,p_x}(0.7)$, (c) $R_{p_z,p_z}(0)$, (d) $R_{p_z,p_z}(0.7)$, (e) $R_{E_x,E_x}(0)$, (f) $R_{E_x,E_x}(0.7)$, (g) $R_{E_z,E_z}(0)$, (h) $R_{E_z,E_z}(0.7)$. Electrical field is applied in the negative z direction. The insets in each graph correspond to the view in polar coordinates with colors changing from red to blue when the amplitude of correlation coefficients decreases from 1 to 0.

coefficients defined as

$$R_{E_x,E_x}(\rho) = \frac{\langle E_x(\mathbf{r}+\rho)E_x(\mathbf{r})\rangle}{\langle E_x^2\rangle}, \quad (6)$$

$$R_{E_z,E_z}(\rho) = \frac{\langle E_z(\mathbf{r}+\rho)[E_z(\mathbf{r})-E_0]\rangle}{\langle E_z(\mathbf{r})[E_z(\mathbf{r})-E_0]\rangle}, \quad (7)$$

$$R_{p_x,p_x}(\rho) = \frac{\langle p_x(\mathbf{r}+\rho)p_x(\mathbf{r})\rangle}{\langle p_x^2\rangle}, \quad (8)$$

$$R_{p_z,p_z}(\rho) = \frac{\langle p_z(\mathbf{r}+\rho)[p_z(\mathbf{r})-P]\rangle}{\langle p_z(\mathbf{r})[p_z(\mathbf{r})-P]\rangle}, \quad (9)$$

where the magnitude of the correlation coefficients is bounded by $-1 \leqslant R \leqslant 1$. For strongly correlated quantities $|R| = 1$, while for uncorrelated quantities $R = 0$. The other, non-diagonal autocorrelation coefficients R_{E_x,E_z}, R_{p_x,p_z}, and all cross-correlation coefficients R_{p_α,E_β} appear to be negligible within the calculation error.

Owing to the spatial direction given by the applied electric field the system exhibits macroscopic anisotropy so that a two-point correlation coefficient may depend on the distance vector ρ in the plane (x,z), or on both polar coordinates (ρ,ϕ) in this plane. Correlation coefficients as functions of the distance ρ and angle ϕ are presented in Fig. 7.

The polarization-polarization correlations, as well as field-field correlations, change during the field-driven switching. However, they remain notable only within the range of $\rho \leqslant 1$ μm that corresponds to a neighbor grain distance. An exception is exhibited only by the longitudinal polarization autocorrelations R_{p_z,p_z} which stretch over several μm when $P = -0.6P_s$, see Fig. 8. This polarization stage corresponds to the deepest minimum in the variance anisotropy VA(p_z), as is seen in Fig. 9.

Correlations of the transverse polarization R_{p_x,p_x} [Figs. 7(a) and 7(b)] and of the longitudinal field R_{E_z,E_z} components [Figs. 7(g) and 7(h)] are isotropic in both zero- and high-polarization states. The correlation coefficient for the longitudinal polarization components R_{p_z,p_z} develops from isotropic behavior in the zero-polarization state [Fig. 7(c)] to anisotropic one in the high-polarization state [Fig. 7(d)]. The

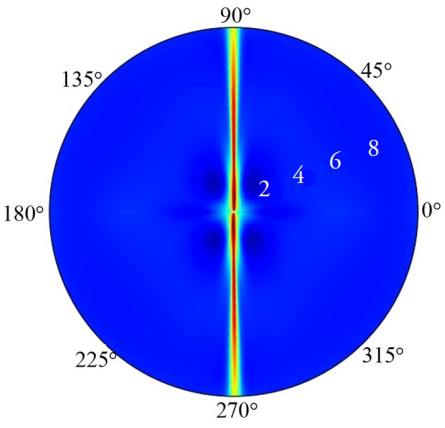

FIG. 8. The correlation coefficient R_{p_z,p_z} in polar coordinates for the total polarization $P = -0.6P_s$ with an electric field applied in the positive z direction. The numbers along the radius ρ indicate distance in μm. The color legend used is the same as in Fig. 7.

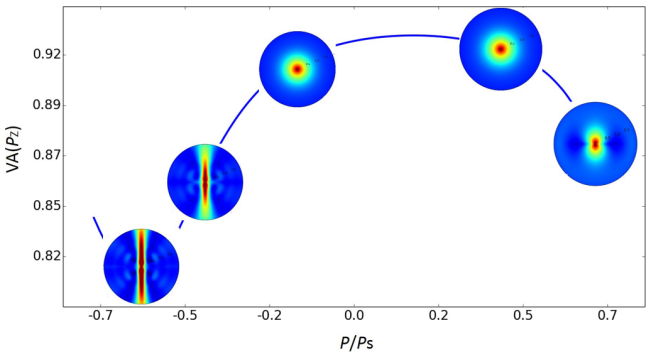

FIG. 9. Evolution of the VA(p_z) factor when the total polarization P varies from $-0.7P_s$ to $0.7P_s$ is shown together with polar plots of the correlation coefficient R_{p_z,p_z} for corresponding polarization stages. The color legend used is the same as in Fig. 7.

correspondence between the VA(p_z) factor and the correlation coefficient R_{p_z,p_z} is displayed in Fig. 9 exhibiting the highest anisotropy in the intermediate stage with $P = -0.6P_s$, as mentioned above. In contrast, correlations of the transverse field components, R_{E_x,E_x}, exhibit remarkable anisotropic features in both zero-polarization and high-polarization state [Figs. 7(e) and 7(f)]. We note here that zero-polarization states result from the field-driven development starting from the high-polarization state and hence retain anisotropic properties. Generally, polarization reversal does not reveal a concerted avalanchelike switching behavior involving hundreds of grains which was sometimes observed in polycrystalline ferroelectric films [37–39]. Consequently this phenomenon cannot be facilitated by electrostatic interactions but is rather provided by long-range elastic interactions as suggested in Refs. [37,40].

IV. ELECTRIC FIELD DISTRIBUTIONS

The spatial distributions of the electric field play an important role in the polarization switching dynamics of polycrystalline systems. Due to the well-known strong field dependence of the switching time [52] different field magnitudes at different locations may provide a substantially retarded or accelerated local switching. Thus, the statistical distributions of switching times may be directly related to the statistical distributions of local electric field magnitudes using the IFM model [9–16]. In this section we analyze the development of the statistical distribution of the local field values $f(E)$ in the course of the polarization reversal.

The electric field is distributed randomly within a polycrystalline ferroelectric for two reasons: random variations in orientation of principal axes of the dielectric tensor in different grains, on the one hand, and random bound charges at grain boundaries due to mismatches of the polarizations in adjacent grains, on the other hand. An example of the spatial field distribution is shown in Fig. 10. Both mentioned factors substantially and independently contribute to the dispersion of the statistical field distribution which is remarkably modified in the course of polarization reversal and the subsequent voltage switching. This can be observed in the following example.

The statistical field distribution for a highly polarized sample was evaluated and compared with the distribution

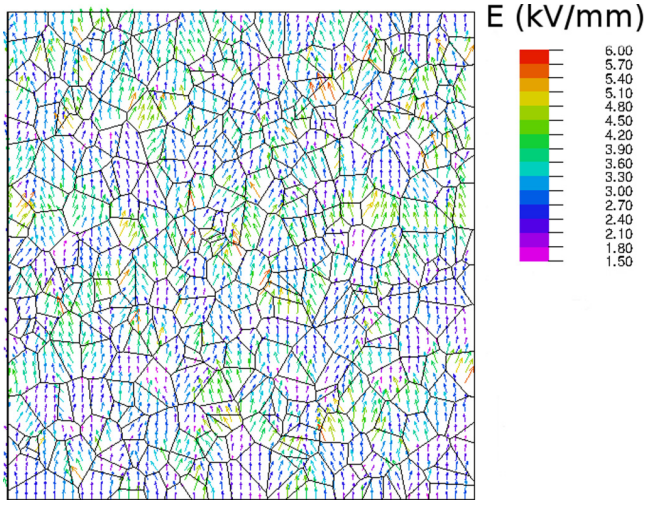

FIG. 10. Field map at an applied field of $E_0 = 3$ kV/mm and the total polarization $P \simeq 0.71P_s$.

immediately after the voltage polarity switching so that the polarization map had not changed yet, see Fig. 11. Though the spatial distributions of both spontaneous polarization and dielectric tensor in a system remain the same the spatial and statistical distributions of the electric field changed remarkably and instantaneously. To comprehend this phenomenon a deeper insight into the nature of the depolarization field is required. For detailed analysis the whole set of field values at all FEM mesh points (10^6) was used.

By the superposition principle, the local electric field at any point of the material can be presented as

$$\mathbf{E} = \mathbf{E}_{\text{ext}} + \Delta_K \mathbf{E} + \langle \mathbf{E}_p \rangle + \Delta_P \mathbf{E}. \tag{10}$$

The first two terms result from the spatial redistribution of the external field applied to the ferroelectric by the charged

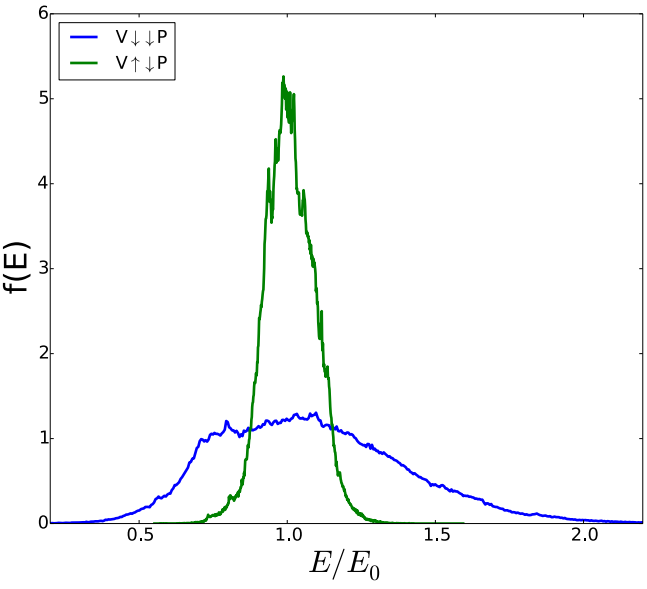

FIG. 11. Statistical field distribution for the saturated highly polarized state before (wider distribution) and after (narrower distribution) the voltage polarity switching.

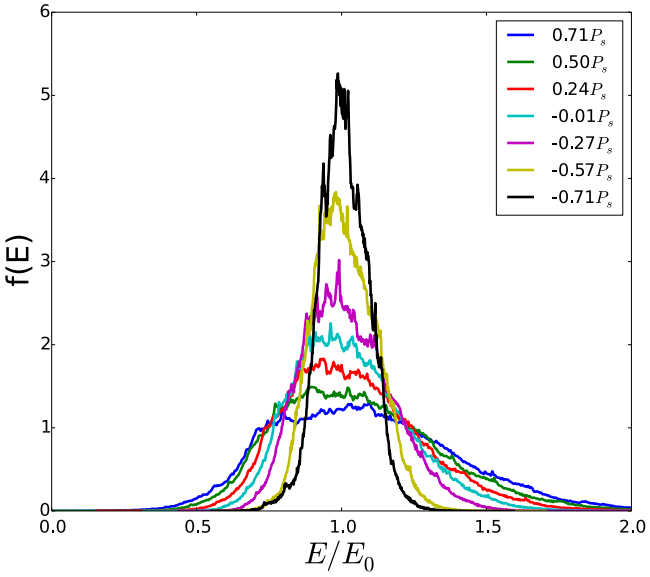

FIG. 12. Evolution of the statistical field distribution with increasing P.

electrodes, whereby $\mathbf{E}_{\text{ext}}$ represents the uniform mean value of the external field in ferroelectric and the spatial fluctuation part obeys the condition $\langle \Delta_K \mathbf{E} \rangle = 0$. Due to linearity of the potential problem the amplitudes of the local spatial field fluctuations $\Delta_K \mathbf{E}$ scale with the magnitude of the external field $\mathbf{E}_{\text{ext}}$. The second two terms in Eq. (10) result from the polarization bound charges and both scale approximately with the total polarization value $P = \langle p_z \rangle$, particularly, the mean value $E_P \simeq -P/\varepsilon_0 \varepsilon_f$ where $\varepsilon_f = \sqrt{K_a K_c}$.

During the polarization reversal the voltage is kept constant together with the mean field in the ferroelectric

$$\frac{V}{L} = E_{\text{ext}} + E_P. \tag{11}$$

Since the total polarization P is changing continuously and eventually changes its sign, the two fields in the right-hand side of Eq. (11) have to change synchronously. This means that with the change of the total polarization from $-P_{\max}$ to $P_{\max}$ the external field E_{ext} should monotonically rise. As the local fluctuation fields $\Delta_K \mathbf{E}$ are scaled together with E_{ext} the field distribution $f(E)$ should increasingly spread due to increasing fluctuation contributions $\Delta_K \mathbf{E}$. Note that at the saturated polarization values both fields E_{ext} and E_P are at their maximum magnitudes so that the dispersion of the field distribution $f(E)$ is a maximum due to both fluctuation fields $\Delta_K \mathbf{E}$ and $\Delta_P \mathbf{E}$. In Fig. 12 such a spreading evolution is observed when the total polarization varies from $-0.71P_s$ to $0.71P_s$.

As soon as the voltage polarity is changed, after reaching the maximum polarization value, Eq. (11) changes to

$$-\frac{V}{L} = E_{\text{ext}} + E_P. \tag{12}$$

Since the value E_P remains unchanged together with the spatial polarization distribution in the system, the external field E_{ext} must be adjusted, thus abruptly reducing its magnitude. This explains the abrupt reduction of the dispersion of the field distribution in Fig. 11. Note that at the end of the polarization

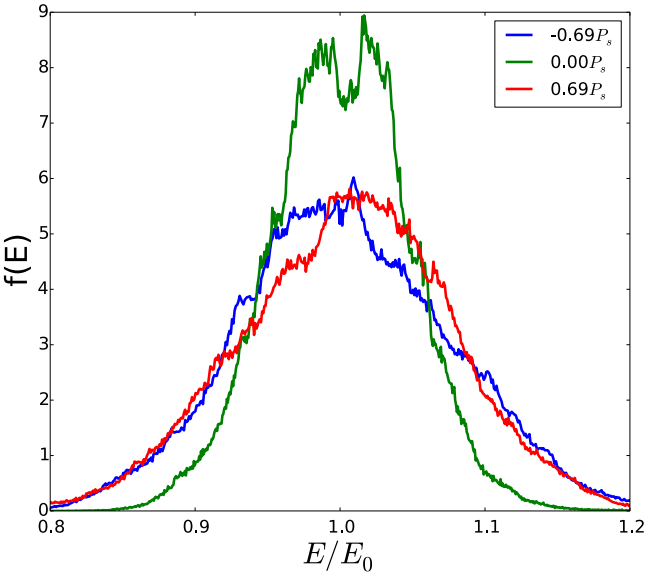

FIG. 13. Statistical field distributions in an isotropic system with $K_a = K_c$.

switching the field E_P is of opposite sign to the external field, while at the onset of the polarization reversal they are of the same sign.

In contrast to the fluctuation field $\Delta_K \mathbf{E}$ the field $\Delta_P \mathbf{E}$ evolves nonmonotonically during the polarization reversal. Since the latter field roughly scales with the total polarization P its dispersion is expected to be at minimum when $P = 0$ and at maximum when polarization reaches its maximum magnitude. Such behavior should be explicitly observed if we neglect the spatial variation of the dielectric tensor. With $\Delta_K \mathbf{E} = 0$ the field fluctuations are caused solely by the polarization variations. Thus the width of the distribution $f(E)$ is minimal when $P = 0$ as is apparent in Fig. 13. The statistical field distributions here roughly exhibit the mirror symmetry with respect to the vertical line $E/E_0 = 1$ indicating the mean field value. This occurs due to local depolarization fields changing their sign together with the total polarization. The symmetry of these distributions is not perfectly bilateral because of the finite size of the random system.

V. DISCUSSION AND CONCLUSIONS

Using the self-consistent mesoscopic switching (SMS) model the correlations of the polarization and the electric field and the statistical distributions of the electric field were studied in the course of the global polarization reversal in a ferroelectric ceramic. Correlation analysis throws some light on the paradoxical ability of statistical concepts neglecting the feedback of depolarization fields to adequately describe polarization switching kinetics.

Two alternative scenarios of depolarization field reduction in disordered polar media are conceivable: highly coherent switching with depolarization fields correlated at a long range, on the one hand, and very short-range correlations of both local polarizations and fields which make switching at different locations effectively independent, on the other hand. The results of the correlation analysis presented in Fig. 7 are clearly in favor of the second scenario. Nevertheless, a question remains as to how the long-range electrostatic interaction is impeded in a nonconducting medium.

The answer seems to hide in the peculiar properties of disordered ferroelectrics. Though these materials are not conducting, local bound charges due to polarization mismatches at grain boundaries are randomly distributed all over the system and possess a considerable mean density. These charges cannot move but are variable. They change in time in order to screen any charge and thus are able to perform the effective Debye screening of the long-range fields. Indeed, a typical surface bound charge resulting from the mean squared fluctuations of the polarization disparity at grain boundaries [50] amounts to $\sigma_P \simeq 0.1 P_s$ which leads to the effective volume density of charge carriers $n_P \simeq \sigma_P / qR \simeq 6 \times 10^{21}$ m^{-3}. Such a high density results in the effective Debye screening length $\lambda_P = \sqrt{\varepsilon_0 \varepsilon_f k_B T / q^2 n_P} \simeq 0.3$ μm comparable to the mean size of grains. This explains the absence of long-range electrostatic field correlations.

Autocorrelations of both polarization and electric field components are mostly isotropic and do not vary essentially during the global polarization switching, while cross correlations of all components remain generally negligible. The only exception from this behavior is given by the autocorrelations of the longitudinal polarization components which occasionally stretch over a dozen grains and undergo remarkable variations in its anisotropy during the polarization reversal. This typical spatial scale of the response appears to be comparable to that observed by 3D-XRD in bulk ferroelectric ceramics [44,45]. Much larger correlation radii are expected for electrostatic reasons in thin ferroelectric films [58]. However, considerably larger clusters of coherent response revealed by PFM and TEM in ferroelectric films [33,37,38] suggest a significant role of the long-range elastic interactions which are not included in the current simulations. We note a substantial difference in correlation behavior between the considered polycrystalline systems and uniform media where long-range electrostatic correlations appear to be dominant as phase-field simulations have demonstrated [47].

Generally, the external electric field remains the original driving force of the global polarization reversal which triggers and dominates the polarization switching at the local and the macroscopic scales. Depolarization fields arising because of mismatches of the local dielectric tensors and spontaneous polarizations in adjacent grains are relevant and not small. They develop in the course of the global polarization switching in a nontrivial way. On the one hand, the dispersion of the statistical distribution of the local electric field values is monotonically increasing during the whole polarization reversal process. On the other hand, the dispersion decreases abruptly after the change of the voltage polarity. An increasing part of locations with substantially reduced electric field magnitudes during the polarization reversal leads to even further retardation of the global switching process with respect to the statistical field distribution alone [9,10] as is already known from the self-consistent quasi-one-dimensional [30] and two-dimensional [49] simulations. However, local switching events may still be considered as independent from each other because of the effective screening of the long-range electrostatic fields.

The obtained results are representative for a wide class of polycrystalline perovskite ferroelectrics. In the presented simulations the material parameters of PZT were used in the calculations. Some of them, such as the saturation polarization and the activation field are not critical for the main conclusions of the paper. In contrast, the anisotropy of the dielectric tensor have a remarkable effect on the statistical field distributions as is seen from the comparison between Fig. 12 (anisotropic case) and Fig. 13 (isotropic case). Anisotropy of the dielectric tensor contributes to the width of the statistical field distributions as discussed in Sec. IV. Thus in more anisotropic materials like $BaTiO_3$ these distributions will be wider. Different realizations of the random grain structure and their initial polarization states do not have a significant effect on the evolution of the VA factor (Fig. 6), correlation functions (Fig. 7–9), and statistical field distributions as long as the mean grain size is kept constant and much smaller than the computation box size, that is important for the quality of the statistical data. The parameter β has a notable effect on the kinetic polarization curves in Fig. 3 making them steeper when higher β is assumed, the effect saturating with increasing β. Different β values have, however, no significant effect on the statistical and correlation functions and the main conclusion on the short-range correlations of the electric field.

Concluding, extremely short spatial correlations of the random electric field and polarization in ferroelectric ceramics explain the apparent absence of the electric interaction between different switching regions. This supports statistical concepts assuming an independent region by region switching in ceramics. This does not mean, however, that the effect of the emerging depolarization fields is negligible. They appear to be comparable in amplitude to the applied field and very much dispersive. This results in the substantial retardation of the global polarization reversal since local polarization switching events are driven by the local fields.

ACKNOWLEDGMENTS

R.K. gratefully acknowledges support from the Deutsche Forschungsgemeinschaft (DFG) through Grant No. GE 1171/7-1.

[1] R. Landauer, J. Appl. Phys. **28**, 227 (1957).
[2] R. C. Miller and G. Weinreich, Phys. Rev. **117**, 1460 (1960).
[3] Y. Ishibashi and Y. Takagi, J. Phys. Soc. Jpn. **31**, 506 (1971).
[4] A. N. Kolmogoroff, Izvestiya Akad. Nauk USSR, Ser. Math. **1**, 355 (1937).
[5] M. Avrami, J. Chem. Phys. **8**, 212 (1940).
[6] A. K. Tagantsev, I. Stolichnov, N. Setter, J. S. Cross, and M. Tsukada, Phys. Rev. B **66**, 214109 (2002).
[7] J. Y. Jo, H. S. Han, J.-G. Yoon, T. K. Song, S.-H. Kim, and T. W. Noh, Phys. Rev. Lett. **99**, 267602 (2007).
[8] D. Kedzierski, E. V. Kirichenko, and V. A. Stephanovich, Phys. Lett. A **375**, 685 (2011).
[9] S. Zhukov, Y. A. Genenko, O. Hirsch, J. Glaum, T. Granzow, and H. von Seggern, Phys. Rev. B **82**, 014109 (2010).
[10] Y. A. Genenko, S. Zhukov, S. V. Yampolskii, J. Schütrumpf, R. Dittmer, W. Jo, H. Kungl, M. J. Hoffmann, and H. von Seggern, Adv. Funct. Mater. **22**, 2058 (2012).
[11] S. Zhukov, Y. A. Genenko, M. Acosta, H. Humburg, W. Jo, J. Rödel, and H. von Seggern, Appl. Phys. Lett. **103**, 152904 (2013).
[12] S. Zhukov, H. Kungl, Y. A. Genenko, and H. von Seggern, J. Appl. Phys. **115**, 014103 (2014).
[13] S. Zhukov, M. Acosta, Y. A. Genenko, and H. von Seggern, J. Appl. Phys. **118**, 134104 (2015).
[14] S. Zhukov, Y. A. Genenko, J. Koruza, J. Schultheiß, H. von Seggern, W. Sakamoto, H. Ichikawa, T. Murata, K. Hayashi, and T. Yogo, Appl. Phys. Lett. **108**, 012907 (2016).
[15] S. Zhukov, J. Glaum, H. Kungl, E. Sapper, R. Dittmer, Y. A. Genenko, and H. von Seggern, J. Appl. Phys. **120**, 064103 (2016).
[16] R. Khachaturyan, S. Zhukov, J. Schultheiß, C. Galassi, C. Reimuth, J. Koruza, H. von Seggern, and Y. A. Genenko, J. Phys. D: Appl. Phys. **50**, 045303 (2017).
[17] J. Schütrumpf, S. Zhukov, Y. A. Genenko, and H. von Seggern, J. Phys. D: Appl. Phys. **45**, 165301 (2012).
[18] B. Jiang, Y. Bai, W. Chu, Y. Su, and L. Qiao, Appl. Phys. Lett. **93**, 152905 (2008).
[19] S. Liu, I. Grinberg, and A. M. Rappe, Nature (London) **534**, 360 (2016).
[20] A. Gruverman, B. J. Rodriguez, C. Dehoff, J. D. Waldrep, A. I. Kingon, and R. J. Nemanich, Appl. Phys. Lett. **87**, 082902 (2005).
[21] J. Y. Jo, S. M. Yang, H. S. Han, D. J. Kim, W. S. Choi, T. W. Noh, T. K. Song, J.-G. Yoon, C.-Y. Koo, J.-H. Cheon, and S.-H. Kim, Appl. Phys. Lett. **92**, 012917 (2008).
[22] A. Nautiyal, K. C. Sekhar, N. P. Pathak, N. Dabra, J. S. Hundal, and R. Nath, Appl. Phys. A **99**, 941 (2010).
[23] N. Dabra, J. S. Hundal, A. Nautiyal, K. C. Sekhar, and R. Nath, J. Appl. Phys. **108**, 024108 (2010).
[24] D. Zhao, I. Katsouras, K. Asadi, P. W. M. Blom, and D. M. de Leeuw, Phys. Rev. B **92**, 214115 (2015).
[25] J. Lee, A. J. J. M. van Breemen, V. Khikhlovskyi, M. Kemerink, R. A. J. Janssen, and G. H. Gelinck, Sci. Rep. **6**, 24407 (2016).
[26] D. Zhao, I. Katsouras, K. Asadi, W. A. Groen, P. W. M. Blom, and D. M. de Leeuw, Appl. Phys. Lett. **108**, 232907 (2016).
[27] A. V. Gorbunov, T. Putzeys, I. Urbanavičiūtė, R. A. J. Janssen, M. Wübbenhorst, R. P. Sijbesma, and M. Kemerink, Phys. Chem. Chem. Phys. **18**, 23663 (2016).
[28] K. C. Sekhar, A. Nautiyal, and R. Nath, Appl. Phys. A **95**, 415 (2009).
[29] N. Mishra, N. Dabra, A. Nautiyal, J. S. Hundal, G. D. Varma, N. P. Pathak, and R. Nath, Ferroelectr. Lett. **42**, 75 (2015).
[30] X. J. Lou, J. Phys.: Condens. Matter **21**, 012207 (2009).
[31] G. Viola, K. B. Chong, F. Guiu, and M. J. Reece, J. Appl. Phys. **115**, 034106 (2014).
[32] K. Auluck and E. C. Kan, IEEE Trans. Electron Devices **63**, 631 (2016).
[33] I. Stolichnov, L. Malin, E. Colla, A. K. Tagantsev, and N. Setter, Appl. Phys. Lett. **86**, 012902 (2005).

[34] D. M. Marincel, H. Zhang, A. Kumar, S. Jesse, S. V. Kalinin, W. M. Rainforth, I. M. Reaney, C. A. Randall, and S. Trolier-McKinstry, Adv. Funct. Mater. **24**, 1409 (2014).
[35] D. M. Marincel, H. R. Zhang, J. Britson, A. Belianinov, S. Jesse, S. V. Kalinin, L. Q. Chen, W. M. Rainforth, I. M. Reaney, C. A. Randall, and S. Trolier-McKinstry, Phys. Rev. B **91**, 134113 (2015).
[36] D. M. Marincel, H. Zhang, S. Jesse, A. Belianinov, M. B. Okatan, S. V. Kalinin, W. M. Rainforth, I. M. Reaney, C. A. Randall, and S. Trolier-McKinstry, J. Am. Ceram. Soc. **98**, 1848 (2015).
[37] P. Bintachitt, S. Trolier-McKinstry, K. Seal, S. Jesse, and S. V. Kalinin, Appl. Phys. Lett. **94**, 042906 (2009).
[38] K. Seal, S. Jesse, M. P. Nikiforov, S. V. Kalinin, I. Fujii, P. Bintachitt, and S. Trolier-McKinstry, Phys. Rev. Lett. **103**, 057601 (2009).
[39] P. Bintachitt, S. Jesse, D. Damjanovic, Y. Han, I. M. Reaney, S. Trolier-McKinstry, and S. V. Kalinin, Proc. Natl. Acad. Sci. USA **107**, 7219 (2010).
[40] F. Griggio, S. Jesse, A. Kumar, O. Ovchinnikov, H. Kim, T. N. Jackson, D. Damjanovic, S. V. Kalinin, and S. Trolier-McKinstry, Phys. Rev. Lett. **108**, 157604 (2012).
[41] J. E. Daniels, C. Cozzan, S. Ukritnukun, G. Tutuncu, J. Andrieux, J. Glaum, C. Dosch, W. Jo, and J. L. Jones, J. Appl. Phys. **115**, 224104 (2014).
[42] S. Gorfman, Crystallogr. Rev. **20**, 210 (2014).
[43] G. Esteves, C. M. Fancher, and J. L. Jones, J. Mater. Res. **30**, 340 (2015).
[44] J. E. Daniels, M. Majkut, Q. Cao, S. Schmidt, J. Wright, W. Jo, and J. Oddershede, Sci. Rep. **6**, 22820 (2016).
[45] M. Majkut, J. E. Daniels, J. P. Wright, S. Schmidt, and J. Oddershede, J. Amer. Ceram. Soc. **100**, 393 (2017).
[46] S. Mantri, J. Oddershede, D. Damjanovic, and J. E. Daniels, Acta Mater. **128**, 400 (2017).
[47] J. E. Zhou, T.-L. Cheng, and Y. U. Wang, J. Appl. Phys. **111**, 024105 (2012).
[48] A. Leschhorn and H. Kliem, J. Appl. Phys. **121**, 014103 (2017).
[49] Y. A. Genenko, J. Wehner, and H. von Seggern, J. Appl. Phys. **114**, 084101 (2013).
[50] Y. A. Genenko, J. Glaum, O. Hirsch, H. Kungl, M. J. Hoffmann, and T. Granzow, Phys. Rev. B **80**, 224109 (2009).
[51] N. Uchida and T. Ikeda, Jpn. J. Appl. Phys., Part 1 **6**, 1079 (1967).
[52] W. J. Merz, Phys. Rev. **95**, 690 (1954).
[53] M. J. Haun, E. Furman, S. J. Jang, and L. E. Cross, Ferroelectrics **99**, 63 (1989).
[54] X. H. Du, U. Belegundu, and K. Uchino, Jpn. J. Appl. Phys., Part 1 **36**, 5580 (1997).
[55] M. Y. Gureev, A. K. Tagantsev, and N. Setter, Phys. Rev. B **83**, 184104 (2011).
[56] Y. A. Genenko, O. Hirsch, and P. Erhart, J. Appl. Phys. **115**, 104102 (2014).
[57] R. G. Lomax and D. L. Hahs-Vaughn, *Statistical Concepts: A Second Course* (Taylor & Francis, New York, 2007).
[58] M. D. Glinchuk, A. N. Morozovska, and E. A. Eliseev, Ferroelectrics **400**, 243 (2010).

6.2.3 PAPER III

Stochastic multi-step polarization switching in ferroelectrics
Y.A. Genenko, R. Khachaturyan, J. Schultheiß, A. Ossipov, J. E. Daniels, and J. Koruza, *Physical Review B.*, **97(14)**, 144101 (2018).
DOI: 10.1103/PhysRevB.97.144101

Stochastic multistep polarization switching in ferroelectrics

Y. A. Genenko,[1,*] R. Khachaturyan,[1] J. Schultheiß,[2] A. Ossipov,[3] J. E. Daniels,[4] and J. Koruza[2]
[1]*Institute of Materials Science, Technische Universität Darmstadt, Otto-Berndt-Straße 3, 64287 Darmstadt, Germany*
[2]*Institute of Materials Science, Technische Universität Darmstadt, Alarich-Weiss-Straße 2, 64287 Darmstadt, Germany*
[3]*School of Mathematical Sciences, University of Nottingham, University Park, Nottingham NG7 2RD, United Kingdom*
[4]*School of Materials Science and Engineering, UNSW Sydney, NSW, 2052, Australia*

(Received 9 January 2018; published 4 April 2018)

Consecutive stochastic 90° polarization switching events, clearly resolved in recent experiments, are described by a nucleation and growth multistep model. It extends the classical Kolmogorov-Avrami-Ishibashi approach and includes possible consecutive 90°- and parallel 180° switching events. The model predicts the results of simultaneous time-resolved macroscopic measurements of polarization and strain, performed on a tetragonal $Pb(Zr,Ti)O_3$ ceramic in a wide range of electric fields over a time domain of seven orders of magnitude. It allows the determination of the fractions of individual switching processes, their characteristic switching times, activation fields, and respective Avrami indices.

DOI: 10.1103/PhysRevB.97.144101

I. INTRODUCTION

Polarization switching driven by an applied electric field is a fundamental process in ferroelectrics involving thermally activated nucleation and growth of reversed polarization domains. Understanding the kinetics of this process is important for many applications, particularly for ferroelectric memories [1]. Previously, macroscopic polarization switching kinetics was described by stochastic models, such as the classical Kolmogorov-Avrami-Ishibashi (KAI) model based on the concept developed to describe melt solidification [2] and assuming random and statistically independent nucleation and growth of reversed polarized domains in a uniform medium [3,4]. This stochastic model works well for some single crystals [5–7] but performs unsatisfactorily when applied to polycrystalline ferroelectric films [8–10] or bulk polycrystalline ceramics [11,12]. A range of intrinsic physical features of ferroelectrics are missing in the KAI approach.

The KAI model assumes only a single characteristic switching time for the whole macroscopic system. Introducing a statistical distribution of switching times, characterizing different regions of such a nonuniform system as a polycrystalline solid, helped to improve the characterization of switching kinetics in ferroelectric films [8,13–14] and bulk ceramics [15,16]. The regions are distinguished based on different local electric-field amplitudes, originating from the random crystallographic orientations of the grains [16]. Although this model extension provided rather accurate description of polarization response in a range of ferroelectric materials [7,13,14,16–20] another important feature still remained missing, namely the feedback due to depolarization fields emerging during the polarization reversal of individual regions [21–26]. In model simulations [27,28] interaction of different switching regions via the depolarization fields was shown to play an important role in uniform systems providing highly coherent switching in single crystals at long spatial ranges. In contrast, in polycrystalline media the emerging depolarization fields appear to be effectively screened by adapting local bound charges, as disclosed by recent simulations using the self-consistent mesoscopic switching model [29]. Thus, the switching of different regions in a ceramic can still be considered as statistically independent with regard to electrical interactions. Correlations in polarization switching, observed between tens of grains in bulk samples [30,31] or up to thousand grains in films [32–34], seem to be related to the elastic rather than to the electric interactions. Therefore, the original definition of different regions has to be extended to take elastic interactions into account. Beyond the deficiencies listed above, a common shortcoming of all mentioned statistical concepts of polarization switching [2–4,8,13–17,24,26] is that individual random switching events are assumed to occur statistically independent and parallel to each other. In reality, however, some events occur in succession as, for example, consecutive 90°- or, generally, non-180° switching events. This consideration is crucial for multiaxial ferroelectrics, which are the most widely used group of ferroelectric materials. Such two-step polarization reversals were observed by *in situ* x-ray diffraction measurements [35] and ultrasonic investigations [36]. Respective characteristic times for two distinct and sequential domain reorientation steps were determined [37]. Furthermore, some reports suggest that contributions from 180° switching events during the reversal process cannot be excluded [38,39]. In order to distinguish between both contributions, the macroscopic strain of the polycrystalline sample should be measured simultaneously with the switched polarization.

The present work is devoted to the development of a model to describe polarization and strain switching dynamics with consecutive stochastic switching events and its implementation for fitting of macroscopic measurements of a bulk ferroelectric ceramic. In Sec. II, the classical KAI model is extended by including two sequential non-180° polarization reorientation

*Corresponding author: genenko@mm.tu-darmstadt.de

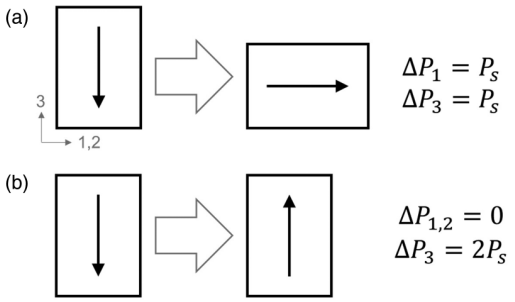

FIG. 1. Changes in polarization due to an idealized (a) 90° and a (b) 180° switching event.

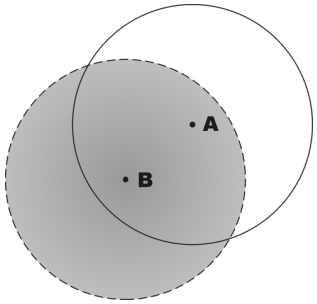

FIG. 2. Scheme of probability calculation in the KAI model. Dark area presents a growing reversed domain nucleated at point B and covering point A.

steps and a parallel 180° switching event which we call a multistep stochastic mechanism (MSM) model. Additionally, a relation between the time-dependent strain and polarization is derived. In Sec. III, polarization and strain switching experiments over a time domain from 10^{-6} to 10^{1} s are presented for a range of applied electric-field values. The experimental results are analyzed and discussed in Sec. IV based on the concepts from Sec. II. Finally, the results are concluded in Sec. V.

II. THEORY OF CONSECUTIVE STOCHASTIC POLARIZATION SWITCHING PROCESSES

A. Extension of the KAI model to consecutive switching events

Let us first consider a consecutive 90° switching process in a polycrystalline ferroelectric in the spirit of the KAI model [2–4]. It is assumed, for simplicity, that polarization may adopt only directions parallel or perpendicular to the electric field, which is applied along the z axis of the Cartesian coordinate system (x,y,z); see Fig. 1.

In the initial state, the system is assumed to be uniformly polarized downward, exhibiting a saturation polarization $-P_s$. When a reversed (positive) field is applied, the local polarization may experience two sequential 90° switching events with respective nucleation rates per unit time and unit volume R_1 and R_2. We first consider the nucleation of switched domains according to the first process after the application of the electric field upward at time $t > 0$.

When an unconstrained domain emerges at some point B at a time $\tau > 0$ it is supposed to grow with a constant (field-dependent) velocity v_1 so that its "spherical" volume reaches the value

$$\Omega_1(t,\tau) = C_1[v_1(t-\tau)]^{n_1} \tag{1}$$

by the time $t > \tau$, where n_1 is the spatial dimensionality of the domain and C_1 is an appropriate numerical coefficient. Here, a possible initial nucleus size is neglected. Let us evaluate the probability $q_1(t)$ for a point A to be not covered by a switched area of some domain. To this end, following Ishibashi and Takagi [4], let us construct a spherical volume $\Omega_1(t,\tau)$ around the point A (see Fig. 2). If the nucleation point B were present in the latter volume, the switched domain would cover the point A by the time t. Thus, the probability that no nucleus emerges in the volume Ω_1 around A during the time interval $(\tau,\tau+\Delta\tau)$ equals $1 - R_1(\tau)\Omega_1(t,\tau)\Delta\tau$. The time is now discretized in short steps $\Delta\tau, 2\Delta\tau, \ldots i\Delta\tau, \ldots$ from zero until the time $t = N\Delta\tau$. The time of the domain appearance is indicated as $\tau = i\Delta\tau$ with the index i varying from zero to N. Then the probability that the point A is not covered by the switched area by the time t results as the product of such probabilities in all elapsed intervals:

$$q_1(t) = \prod_{i=0}^{N}[1 - R_1(i\Delta\tau)\Omega_1(N\Delta\tau, i\Delta\tau)\Delta\tau]. \tag{2}$$

The logarithm of Eq. (2) brings about the sum which transforms to the integral when $\Delta\tau \to 0$:

$$\begin{aligned}\ln q_1(t) &= -\sum_{i=0}^{N} R_1(i\Delta\tau)\Omega_1(N\Delta\tau, i\Delta\tau)\Delta\tau|_{\Delta\tau\to 0} \\ &\to -\int_0^t d\tau R_1(\tau)\Omega_1(t,\tau),\end{aligned} \tag{3}$$

so that

$$q_1(t) = \exp\left[-\int_0^t R_1(\tau)\Omega_1(t,\tau)d\tau\right]. \tag{4}$$

Now we consider a sequence of two switching events according to the first and then to the second 90° switching event. First let us evaluate a probability $p_1(t_1,\Delta t_1)$ of switching according to the first mechanism (first 90° switching event) within the interval $(t_1, t_1+\Delta t_1)$, which can be derived from the relation

$$q_1(t_1+\Delta t_1) = q_1(t_1)[1 - p_1(t_1,\Delta t_1)]. \tag{5}$$

By expansion of the left-hand side up to the first order in Δt_1 and assuming the time-independent R_1 one finds using Eq. (4),

$$\ln q_1(t_1+\Delta t_1) = \ln q_1(t_1) - R_1\Omega_1(t_1,0)\Delta t_1. \tag{6}$$

From comparison with Eq. (5) it is apparent that

$$p_1(t_1,\Delta t_1) = R_1\Omega_1(t_1,0)\Delta t_1. \tag{7}$$

For the probability not to switch according to the second mechanism (second 90° switching event) we obtain, similar

to (4),

$$q_2(t) = \exp\left[-\int_0^t R_2(\tau)\Omega_2(t,\tau)d\tau\right], \tag{8}$$

with

$$\Omega_2(t,\tau) = A_2[v_2(t-\tau)]^{n_2}, \tag{9}$$

where parameters A_2, v_2, and n_2 characterize the second switching process in analogy to the first one. The probability to switch once according to the first mechanism within the interval $(t_1, t_1 + \Delta t_1)$ and not to switch anymore until the time t is then

$$q_1(t_1)R_1\Omega_1(t_1,0)\Delta t_1 q_2(t-t_1). \tag{10}$$

Finally, the total probability to switch once according to the first mechanism and not to switch anymore until time t is obtained by summation over all possible intervals $(t_1, t_1 + \Delta t_1)$ as

$$L_1(t) = \int_0^t dt_1 q_1(t_1)R_1\Omega_1(t_1,0)q_2(t-t_1). \tag{11}$$

The total probability to switch firstly according to the first mechanism and secondly according to the second mechanism until time t reads apparently as

$$L_2(t) = \int_0^t dt_1 q_1(t_1)R_1\Omega_1(t_1,0)[1-q_2(t-t_1)]. \tag{12}$$

By substituting Eqs. (1), (4), (8) into Eqs. (11), (12), one finds general forms

$$L_1(t) = \frac{\alpha}{\tau_1}\int_0^t dt_1\left(\frac{t_1}{\tau_1}\right)^{\alpha-1}\exp\left[-\left(\frac{t_1}{\tau_1}\right)^{\alpha}-\left(\frac{t-t_1}{\tau_2}\right)^{\beta}\right]$$

$$L_2(t) = \frac{\alpha}{\tau_1}\int_0^t dt_1\left(\frac{t_1}{\tau_1}\right)^{\alpha-1} \times \exp\left[-\left(\frac{t_1}{\tau_1}\right)^{\alpha}\right]\left\{1-\exp\left[-\left(\frac{t-t_1}{\tau_2}\right)^{\beta}\right]\right\}, \tag{13}$$

where the switching times τ_1 and τ_2 for the first and the second processes are defined by the geometrical and kinetic characteristics of the growing domains, which can in principle be different. These parameters, as well as the exponents α and β, will be used to fit experimental data on the time-dependent polarization and strain.

Let us define a mean polarization variation due to all 90° reorientation events by P_{90}. Then the total polarization change all over the system due to the two sequential polarization variations by P_{90} amounts to

$$\Delta p(t) = P_{90}L_1(t) + 2P_{90}L_2(t), \tag{14}$$

or, equivalently,

$$\Delta p(t) = 2P_{90}\left\{1-\exp\left[-\left(\frac{t}{\tau_1}\right)^{\alpha}\right]\right\} - P_{90}L_1(t), \tag{15}$$

noting that

$$L_2(t) = 1-\exp\left[-\left(\frac{t}{\tau_1}\right)^{\alpha}\right] - L_1(t). \tag{16}$$

Unfortunately, the integrals in Eq. (13) cannot be generally solved in a closed form for arbitrary α and β. Their qualitative behavior can, however, be comprehended from a simple particular case $\alpha = \beta = 1$. For this choice

$$L_1(t) = \frac{\tau_2}{\tau_2-\tau_1}(e^{-t/\tau_2} - e^{-t/\tau_1}) \quad \text{and}$$

$$L_2(t) = 1 + \frac{\tau_1}{\tau_2-\tau_1}e^{-t/\tau_1} - \frac{\tau_2}{\tau_2-\tau_1}e^{-t/\tau_2}. \tag{17}$$

Considering a typical situation with $\tau_1 \ll \tau_2$ [37], $L_1(t) \cong 1 - e^{-t/\tau_1}$ for $0 < t < \tau_1$ and $L_1(t) \cong e^{-t/\tau_2}$ for $\tau_1 \ll t$. Similarly, for arbitrary indices α and β, the function $L_1(t)$ first increases on the timescale of τ_1 and then decreases on the timescale of τ_2, vanishing asymptotically.

B. Combination of consecutive 90°- and parallel 180° switching events

Analysis of the experimental data by many authors shows that the application of an external field can drive the motion of both 180° and non-180° domain walls [35,36,38,39]. As will be shown later, also in our case polarization and strain measurements can only be comprehended when introducing additionally simultaneous 180° switching events [Fig. 1(b)]. Thereby, the total switched polarization will be denoted $2P_s$ and can be directly determined from experiment. The contributions of both consecutive 90° switching events are assumed equal to $P_{90} = P_s\eta$ with a positive $\eta < 1$ presenting the fraction of 90° events and used further as a fitting parameter. The mean amplitude of the parallel 180° switching events is then given by $P_{180} = 2P_s(1-\eta)$ so that $P_{180} + 2P_{90} = 2P_s$. The temporal polarization variation is then presented by extension of Eq. (15) as

$$\Delta p(t) = 2P_s\eta\left\{1-\exp\left[-\left(\frac{t}{\tau_1}\right)^{\alpha}\right]\right\} - P_s\eta L_1(t) + 2P_s(1-\eta)\left\{1-\exp\left[-\left(\frac{t}{\tau_3}\right)^{\gamma}\right]\right\}, \tag{18}$$

where the first two terms represent the contributions from 90°- and the third term contributions from 180° switching events with the corresponding switching time τ_3 and the Avrami exponent γ. In addition to the aforementioned parameters, the latter two will also be used for fitting the time-dependent polarization reversal and strain data.

C. Relation between simultaneous polarization and strain in a system with stochastic consecutive 90°- and parallel 180° events

To prove the consistency of the theory advanced above, we derive here the contribution to the strain tensor S_{ij} directly from the variation of polarization p_n. To this end one can use a relation between the strain and the polarization derived from electrostriction, valid for any solid [40,41],

$$S_{ij} = Q_{ijmn}p_m p_n, \tag{19}$$

with the electrostriction tensor Q_{ijmn}, if no stress is applied to the system. For ferroelectrics with a cubic parent phase, the piezoelectric contribution results from Eq. (19) when the

spontaneous polarization **P** is singled out as

$$p_n \cong P_n + \varepsilon_0 \varepsilon_{nm} E_m, \tag{20}$$

with the permittivity of vacuum ε_0 and the relative permittivity of the ferroelectric ε_{nm}. By substitution of Eq. (20) into Eq. (19) and neglecting a small quadratic field contribution [42], one obtains

$$S_{ij} \cong Q_{ijmn} P_m P_n + d_{ijk} E_k, \tag{21}$$

whereby the general equation for the piezoelectric coefficient is used [41]:

$$d_{ijk} = 2\varepsilon_0 \varepsilon_{km} Q_{ijml} P_l. \tag{22}$$

Using the Voigt notations [43] these formulas can be specified for the direction z of the macroscopic strain measurements as

$$S_3 = Q_{11} P_3^2 + Q_{12}\left(P_1^2 + P_2^2\right) + 2\varepsilon_0 \varepsilon_{33} Q_{11} E_3 P_3. \tag{23}$$

Note that the P_3 component is changed by 180°, as well as 90° events, and thus the piezoelectric part contains contributions from the intrinsic lattice expansion and domain switching processes. The quantity measured in the experiment is the field-driven variation of the strain $\Delta S_3 = S_3 - S_3^0$, whereby S_3^0 is the remanent strain of a sample fully polarized downward. In the considered model, polarization components can only adopt values $P_n = \pm P_s$ or 0 at any time so that $P_1^2 + P_2^2 + P_3^2 = P_s^2$. Thus, in the initial state we assume $P_3 = -P_s$ everywhere and $S_3^0 = Q_{11} P_s^2$. Then the strain variation can be expressed as

$$\Delta S_3 = (Q_{12} - Q_{11})\left(P_1^2 + P_2^2\right) + 2\varepsilon_0 \varepsilon_{33} Q_{11} E_3 P_3. \tag{24}$$

The 180° switching processes fully contribute to the variation of polarization P_3 [see Fig. 1(a)] and thus only change the strain by the linear term in Eq. (24). In contrast, the first and second 90° switching events rotate the unit cell by 90°, thus contributing to the variation of the strain by both terms in Eq. (24). The squared transverse polarization $P_1^2 + P_2^2 = P_\perp^2$ adopts by the first 90° switching event a value P_s^2 resulting in the maximum possible spontaneous strain $\Delta S_{\max} = (Q_{12} - Q_{11}) P_s^2$. It is also important to note that the first 90° rotation of polarization contributes to the strain by $\Delta S_{\max}$ and the second 90° rotation changes it by $-\Delta S_{\max}$, so that two consequent 90° rotations are equivalent to one 180° switching and thus in sum cause no variation of the strain by the quadratic term, but by the linear term in Eq. (24). Using the switching probabilities derived in the Sec. II B, the averaged strain variation can now be expressed as

$$\Delta S_3(t) = \Delta S_{\max} \eta L_1(t) + 2\varepsilon_0 \varepsilon_{33} Q_{11} E_3 (\Delta p(t) - P_s), \tag{25}$$

with functions $L_1(t)$ and $\Delta p(t)$ given by Eqs. (13) and (18), respectively. Note that both formulas for polarization (18) and strain (25) present averaging over the whole system and neglect electric and elastic interactions [44] between different switching regions during the polarization reversal.

III. EXPERIMENTAL WORK

Bulk polycrystalline $Pb_{0.985}La_{0.01}(Zr_{0.475}Ti_{0.525})O_3$ ceramics were prepared by a mixed-oxide route [45]. The switched polarization and the macroscopic strain were measured simultaneously. The samples were poled in direction downward

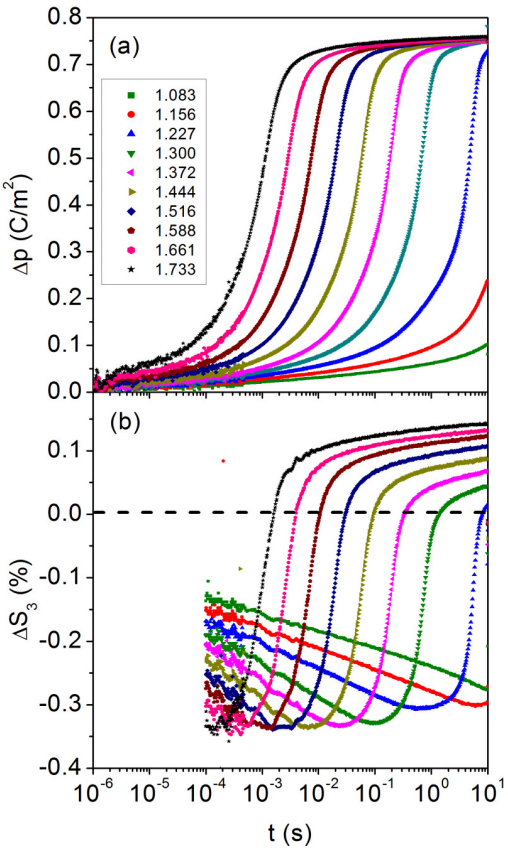

FIG. 3. Results of the simultaneous dynamic measurements of (a) switched polarization Δp, and (b) strain ΔS_3 of a polycrystalline PZT ceramic. The curves were measured at different applied fields E_{SW}, as indicated by the inset values in kV/mm. The dashed line represents the initial value $\Delta S_3 = 0$ for $E_{SW} = 0$, which is related to the remanent strain S_3^0.

with an electric field of 3 kV/mm for 20 s. After a wait time of 100 s, a 10-s pulse switching field E_{SW} was applied opposite to the poling direction. In order to realize a sharp high-voltage (HV) pulse rise of 115 ns (rise time up to 75% of the maximal voltage), a buffer capacitor, which was charged by a high-voltage source (Trek model 20/20C, Lockport, NY), was combined with a commercial fast HV transistor switch (HTS 41-06-GSM, Behlke GmbH, Kronberg, Germany) [46]. The charge was monitored by measuring the voltage drop across a reference capacitor (WIMA MKS4, Wima, Mannheim, Germany), while the macroscopic displacement of the sample was simultaneously measured by an optical displacement sensor (D63, Philtec Inc., Annapolis, MD) with a time resolution of 10^{-4} s.

Figure 3 displays the time-dependent data of polarization and strain for various switching fields E_{SW}. Note that the leakage current and the dielectric displacement were subtracted in the presented polarization data Δp. The variation of the strain, ΔS_3, starts in all measurements from zero which is not explicitly seen in the plot since the data below 10^{-4} s are not available.

Electrostrictive coefficient Q_{11} and large signal permittivity ε_{ls} were determined by fitting the high-field part of strain and

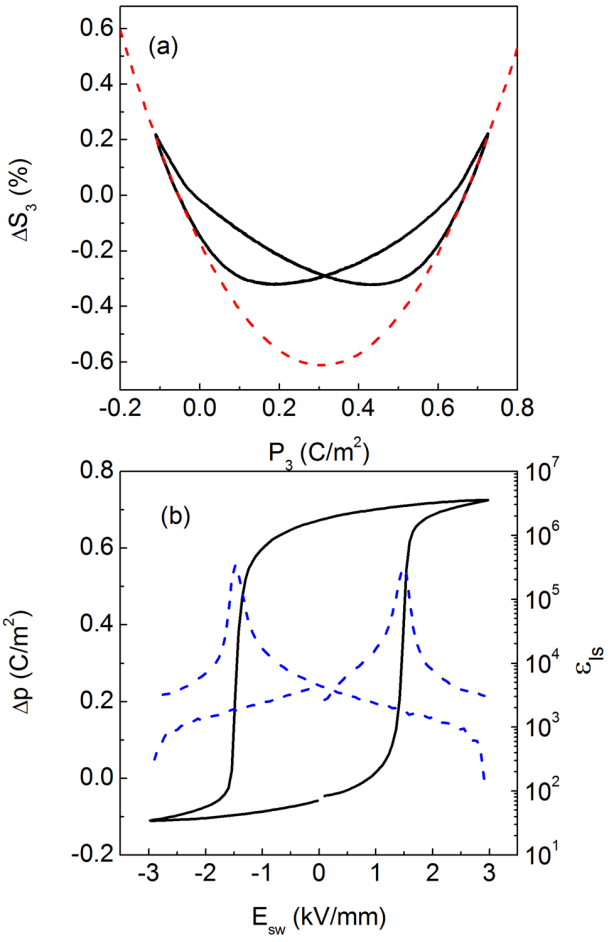

FIG. 4. Experimental determination of the (a) electrostrictive coefficient Q_{11}, and (b) large signal permittivity ε_{ls} from bipolar polarization and strain loops.

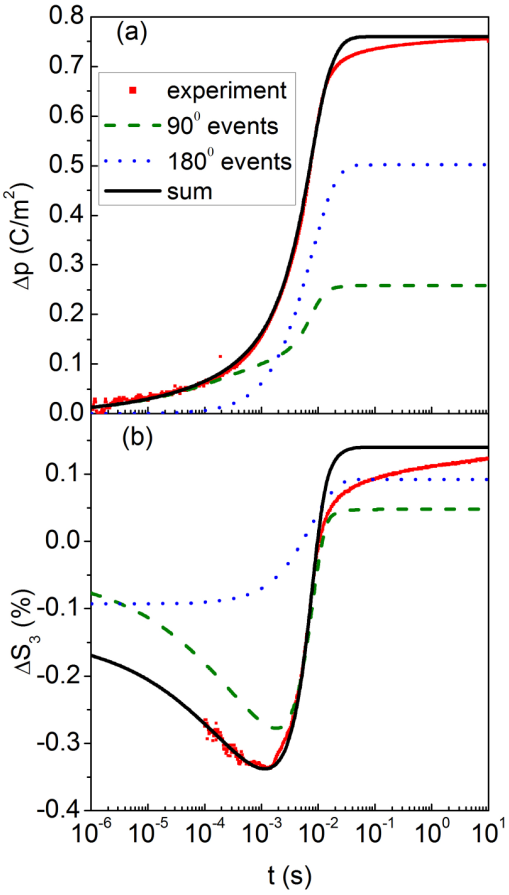

FIG. 5. Polarization (a) and strain (b) variation with time at the applied field of 1.588 kV/mm. Experimental curves are shown by symbols, separated theoretical contributions from 90° switching events by dashed lines, contributions from 180° switching events by dotted lines, and their sum by solid lines.

bipolar polarization measurements. For the former, Eq. (19) was fitted as $S_3 = Q_{11}P_3^2$ [47] to the data in Fig. 4(a) and Q_{11} was determined as $Q_{11} = 0.046\,\mathrm{m}^4/\mathrm{C}^2$, which is close to the value of $0.044\ \mathrm{m}^4/\mathrm{C}^2$ reported for piezoelectric transducer (PZT) ceramic at the tetragonal side of the morphotropic phase boundary [41,47]. The large field permittivity ε_{ls} was calculated by normalization of the derivative of the polarization with respect to the electric field: $\varepsilon_{ls} = (dP/dE)/\varepsilon_0$ [48]. As shown in Fig. 4(b) a saturated value of about $\varepsilon_{ls} = 3 \cdot 10^3$ was obtained.

IV. ANALYSIS AND DISCUSSION OF EXPERIMENTAL RESULTS

Since Eq. (18) contains a smaller number of fitting parameters than Eq. (25), the polarization-time curves [Fig. 3(a)] were fitted first. This fitting defines in the first iteration the parameters η, τ_1, τ_2, τ_3, α, β, and γ. These parameters were then kept constant while fitting the corresponding strain-time curves using $\Delta S_{\max}$ and ε_{33} in Eq. (25) as variable parameters. Although this procedure provided at once a satisfactory agreement with both polarization-time and strain-time experimental curves, a few further iteration steps were carried out because the description of the strain-time curve turned out to be more sensitive for the parameters τ_1, τ_2.

Having the set of parameters established enables us to describe the time dependency of the macroscopic strain and polarization, as shown in Fig. 5 for an applied field strength of 1.588 kV/mm.

The above-described fitting procedure was performed separately for all data sets obtained experimentally for each value of the electric field E_{Sw}, shown in Fig. 3. The materials characteristics P_s, Q_{11}, $\Delta S_{\max}$, ε_{33} were thereby kept constant all over the studied field region. The shares of 90 and 180° switching processes were found to be field independent with $\eta = 0.34$ within the considered field range 1.1–1.7 kV/mm. However, even though similar 180° and non-180° switching shares were previously reported [38,39], it should be noted that 180° switching can also happen strain-free by two statistically dependent, coherent 90° events (Fig. 6), as suggested by Arlt [49].

The results of fitting are exemplarily presented in Fig. 7 for representative field values. As is seen, Eqs. (18) and (25) well approximate both polarization-time and strain-time curves in the short and intermediate time regions, whereby the latter is identified by the maximum switching rate. Furthermore,

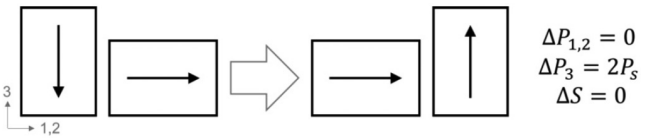

FIG. 6. Example of two coherent 90° switching events which do not change the overall strain but contribute to the P_3 polarization component, similar to a 180° switching event.

these formulas allow the prediction of polarization and strain dependences beyond the observed time interval if appropriate fitting was performed at shorter times, as is demonstrated in Figs. 7(a) and 7(b).

Nevertheless, theoretical curves (solid lines) notably deviate from experimental ones (symbols) at the later stages of switching, when approaching the saturated polarization. As compared to the experiment, the analytical calculations exhibit a sharper steplike behavior, typical for the classical KAI concept [5,7,9] and observed in single crystals [6,7]. In ceramics, however, a more dispersive behavior is typical at longer switching times [7–20]. Physical reasons of this behavior are still disputed and may be attributed to a creeplike domain wall movement of ferroelastic domains [50] related to a broad distribution of the switching times [8]. This could be explained by the inhomogeneous field mechanism model [15,16], which derives a wide statistical distribution of switching times from the nonuniformly distributed electrical field in random systems, such as polycrystalline ferroelectrics. Over and above, the statistical field distribution does not remain fixed in the course of polarization reversal and develops due to varying depolarization fields [21–26]. As was shown in a recent work [29], the field distribution is widening with the polarization increase and mostly affects the poling process at later stages approaching the saturation. This could explain the discrepancy between experimental and fitting curves. In the current model, however, we would like to focus on the statistical explanation of sequential 90° switching processes. Introduction of distributed switching times could improve fitting of the experiment data, but this would make a model more sophisticated, less transparent, and would exceed the scope of this work.

The neglected field and consequently time distributions are presumably also responsible for noninteger values of the Avrami exponents (see Fig. 8), which are well-known from publications trying to explain a dispersive polarization response within the KAI approach [11,51–54]. However, the variation of the Avrami exponents might also have a physical meaning. Thus, an abrupt variation of the dimensionality of growing reversed domains from 3D toward 2D toward 1D domain geometry was identified in polarization kinetics experiments on PZT thin films and simulations [55]. This can be related to the jump in the Avrami index β due to coalescence of numerous small domains to large stripelike ones at higher electric fields.

The values of characteristic switching times, extracted from the dynamic curves of Fig. 7, are shown in Fig. 9. The switching times τ_2 and τ_3 exhibit the Merz law behavior [56], $\tau = \tau_0 \exp(E_a/E_{SW})$. Activation field E_a values for these two events were calculated to be about 33 kV/mm. The field dependence of τ_1 could not be described by the Merz law with a single activation field value over the entire field range, as previously reported for some ceramics and temperature regimes [17,19]. However, it is obvious that the activation energy for the first

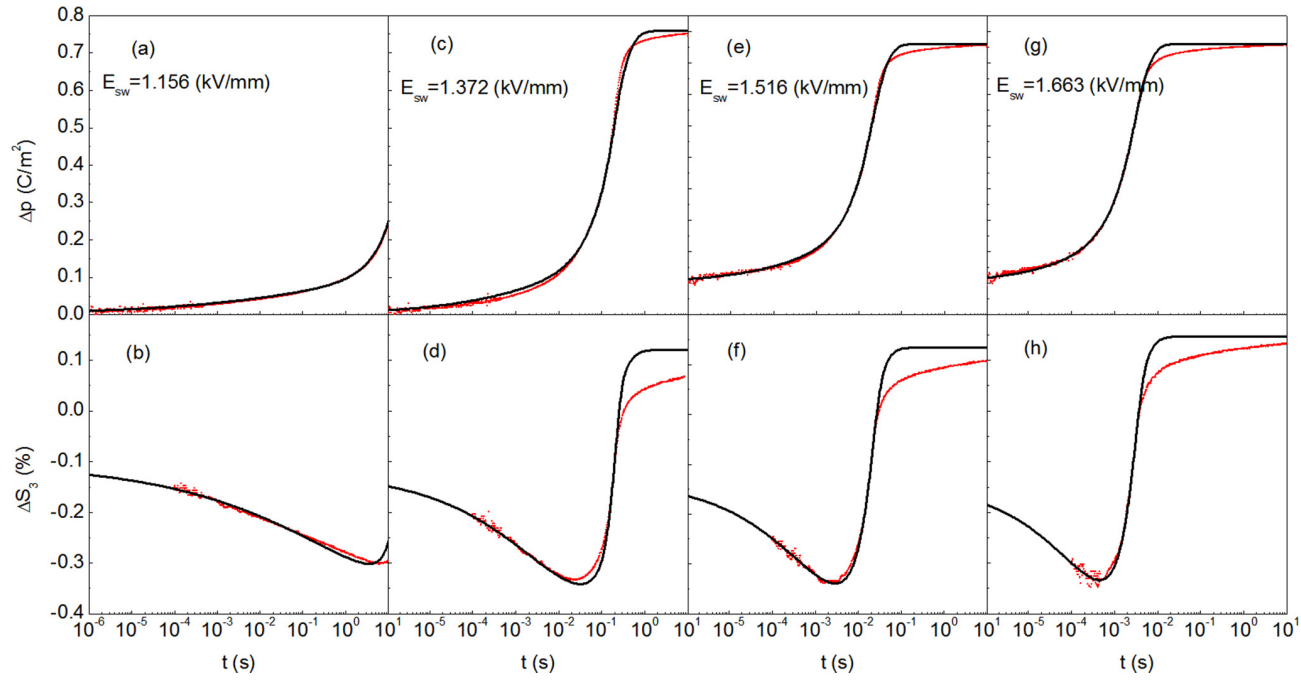

FIG. 7. Variation of the polarization (a), (c), (e), (g) and strain (b), (d), (f), (h) with time at different field values in kV/mm as indicated in the plots. Experimental curves are shown by symbols and fitting curves by solid lines.

90° switching event is the smallest among the three events and is near 27.7 kV/mm in the high-field region. The lower value of the activation field for the first switching may be assigned to the promoting effect of the residual stresses, suggested by x-ray diffraction studies [30,37].

The fitting has revealed a relative permittivity value of $2.85 \cdot 10^3$ being field independent as expected for this field range [57]. This value is comparable with the experimentally measured value of $3 \cdot 10^3$ evaluated as indicated above in Sec. III.

The maximum strain $\Delta S_{\max}$ was found to be about -1%, assuming that all switching occurs by 90°, as shown in the idealized model in Fig. 1(b).This parameter can, in principle, be estimated independently using data from mechanical loading (ferroelastic) experiments, whereby the poled sample is uniaxially compressed in the z direction. The value reported for the maximum strain in such conditions was around -0.68% [58]. Real materials deviate from the idealized model shown in Fig. 1(b), because the possible polarizations of grains are specified by their crystallographic orientations, which are randomly distributed. Additionally, in bulk polycrystals, domains can interact across grain boundaries leading to longer length-scale coupling of domain dynamics [30,31,59]. The c-axis directional distribution should be taken into account and the simplified formula for $\Delta S_{\max}$ has to be generalized to

$$\Delta S_{\max\_real} = (Q_{12} - Q_{11}) P_s^2 \langle(\sin^2\theta)\rangle_{\max}, \qquad (26)$$

where $\langle \sin^2\theta \rangle_{\max}$ defines a maximum possible value for $(P_x^2 + P_y^2)/P_s^2$ compatible with the tetragonal symmetry of grains when polarization tries to avoid the z direction. Thus, the parameter of the simplified model is related to the observed value by $\Delta S_{\max} = \Delta S_{\max\_real}/\langle(\sin^2\theta)\rangle_{\max}$. It is known that for tetragonal symmetry $\langle(\cos^2\theta)\rangle_{\max} = 0.701$, which defines a lower limit for $\langle \sin^2\theta \rangle$ as $1 - \langle(\cos^2\theta)\rangle_{\max} = 0.299$. The maximum limit $\langle \sin^2\theta \rangle_{\max}$ is expected to be close to $\langle(\cos^2\theta)\rangle_{\max}$. The fitting value $\Delta S_{\max}$ of -1% corresponds to $\langle(\sin^2\theta)\rangle_{\max} \approx 0.6$. From the maximum strain the other electrostriction coefficient can be evaluated as $Q_{12} = Q_{11} - \Delta S_{\max}/P_S^2 = 0.021$ (m^4/C^2).

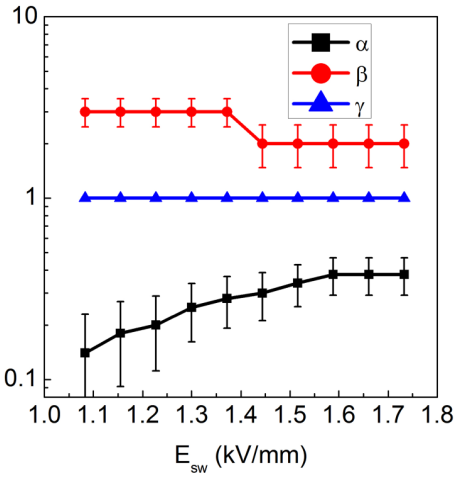

FIG. 8. Avrami exponents obtained by fitting at different field values. Symbols indicate the best-fit values and error bars their standard deviations.

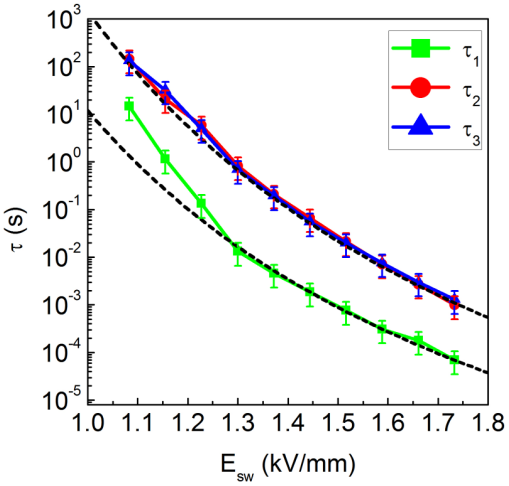

FIG. 9. Characteristic switching times, extracted by fitting and approximated by the Merz law, with $\tau_0 = 0.8 \cdot 10^{-11}$ s, and activation fields 33 and 27.7 kV/mm for the upper and lower curves, respectively.

V. CONCLUSIONS

We have developed a MSM model of the field-driven polarization reversal in ferroelectric ceramics. Similar to the classical KAI approach, this model assumes statistically independent, noncorrelated polarization switching region by region, neglecting both elastic and electric interaction between the switching regions. However, in contrast to the classical KAI consideration, the model includes two parallel channels of switching: a 180° polarization reversal and a sequential two-step 90° switching event. Application of the model to the experimental results of simultaneous macroscopic measurements of polarization and strain, over a wide time window performed at different applied fields, allowed determination of such characteristics of the switching processes as their field-dependent characteristic times and Avrami indices. Other parameters extracted from fitting of the experimental data, such as the maximum spontaneous strain and dielectric permittivity, are in agreement with independently measured values. A very important result of the analysis is the share of 90° switching events, which appears to be field independent in the used field region 1.1–1.7 kV/mm and equals $\eta = 0.34$. This value, however, should be treated with care because it counts only the statistically independent 90° switching events included in our stochastic model. For example, such statistically dependent, coherent 90° switching events that do not contribute to the strain (see Fig. 9) cannot be identified in this approach and thus they would appear as parallel 180° switching events.

ACKNOWLEDGMENTS

This work was supported by the Deutsche Forschungsgemeinschaft (DFG) Grants No. GE 1171/7-1 and No. KO 5100/1-1. J.E.D. acknowledges financial support from Australian Research Council Discovery Projects No. DP120103968 and No. DP130100415. M. Weber is acknowledged for the construction of the electrical HV setup. Dr. H. Kungl is acknowledged for the preparation of the sample.

[1] J. F. Scott, *Ferroelectric Memories* (Springer, Berlin, 2000).
[2] A. Kolmogoroff, Izv. Akad. Nauk SSSR, Ser. Mat. **1**, 355 (1937).
[3] M. Avrami, J. Chem. Phys. **8**, 212 (1940).
[4] Y. Isibashi and Y. Takagi, J. Phys. Soc. Jpn. **31**, 506 (1971).
[5] S. Hashimoto, H. Orihara, and Y. Ishibashi, J. Phys. Soc. Jpn. **63**, 1601 (1994).
[6] R. Z. Rogowski, K. Matyjasek, and R. Jakubas, Cryst. Res. Technol. **41**, 557 (2006).
[7] S. Zhukov, Y. A. Genenko, J. Koruza, J. Schultheiß, H. von Seggern, W. Sakamoto, H. Ichikawa, T. Murata, K. Hayashi, and T. Yogo, Appl. Phys. Lett. **108**, 012907 (2016).
[8] A. K. Tagantsev, I. Stolichnov, N. Setter, J. S. Cross, and M. Tsukada, Phys. Rev. B **66**, 214109 (2002).
[9] A. Gruverman, B. J. Rodriguez, C. Dehoff, J. D. Waldrep, A. I. Kingon, and R. J. Nemanich, Appl. Phys. Lett. **87**, 082902 (2005).
[10] O. Lohse, M. Grossmann, U. Boettger, D. Bolten, and R. Waser, J. Appl. Phys. **89**, 2332 (2001).
[11] D. Viehland and J.-F. Li, J. Appl. Phys. **90**, 2995 (2001).
[12] S. Zhukov, S. Fedosov, J. Glaum, T. Granzow, Y. A. Genenko, and H. von Seggern, J. Appl. Phys. **108**, 014105 (2010).
[13] J. Y. Jo, H. S. Han, J.-G. Yoon, T. K. Song, S.-H. Kim, and T. W. Noh, Phys. Rev. Lett. **99**, 267602 (2007).
[14] J. Y. Jo, S. M. Yang, H. S. Han, D. J. Kim, W. S. Choi, T. W. Noh, T. K. Song, J.-G. Yoon, C.-Y. Koo, J.-H. Cheon, and S.-H. Kim, Appl. Phys. Lett. **92**, 012917 (2008).
[15] S. Zhukov, Y. A. Genenko, O. Hirsch, J. Glaum, T. Granzow, and H. von Seggern, Phys. Rev. B **82**, 014109 (2010).
[16] Y. A. Genenko, S. Zhukov, S. V. Yampolskii, J. Schütrumpf, R. Dittmer, W. Jo, H. Kungl, M. J. Hoffmann, and H. von Seggern, Adv. Funct. Mater. **22**, 2058 (2012).
[17] D. C. Lupascu, S. Fedosov, C. Verdier, J. Rödel, and H. von Seggern, J. Appl. Phys. **95**, 1386 (2004).
[18] S. Zhukov, Y. A. Genenko, M. Acosta, H. Humburg, W. Jo, J. Rödel, and H. von Seggern, Appl. Phys. Lett. **103**, 152904 (2013).
[19] S. Zhukov, H. Kungl, Y. A. Genenko, and H. von Seggern, J. Appl. Phys. **115**, 014103 (2014).
[20] S. Zhukov, M. Acosta, Y. A. Genenko, and H. von Seggern, J. Appl. Phys. **118**, 134104 (2015).
[21] H. von Seggern and G. F. Leal Ferreira, Appl. Phys. Lett. **83**, 3353 (2003).
[22] S. N. Fedosov and H. von Seggern, J. Appl. Phys. **96**, 2173 (2004).
[23] X. J. Lou, J. Phys.: Condens. Matter **21**, 012207 (2009).
[24] Y. A. Genenko, J. Wehner, and H. von Seggern, J. Appl. Phys. **114**, 084101 (2013).
[25] G. Viola, K. B. Chong, F. Guiu, and M. J. Reece, J. Appl. Phys. **115**, 034106 (2014).
[26] K. Auluck and E. C. Kan, IEEE Trans. Electron Devices **63**, 631 (2016).
[27] J. E. Zhou, T.-L. Cheng, and Y. U. Wang, J. Appl. Phys. **111**, 024105 (2012).
[28] A. Leschhorn and H. Kliem, J. Appl. Phys. **121**, 014103 (2017).
[29] R. Khachaturyan, J. Wehner, and Y. A. Genenko, Phys. Rev. B **96**, 054113 (2017).
[30] J. E. Daniels, M. Majkut, Q. Cao, S. Schmidt, J. Wright, W. Jo, and J. Oddershede, Sci. Rep. **6**, 22820 (2016).
[31] M. Majkut, J. E. Daniels, J. P. Wright, S. Schmidt, and J. Oddershede, J. Am. Ceram. Soc. **100**, 393 (2016).
[32] I. Stolichnov, L. Malin, E. Colla, A. K. Tagantsev, and N. Setter, Appl. Phys. Lett. **86**, 012902 (2005).
[33] P. Bintachitt, S. Trolier-McKinstry, K. Seal, S. Jesse, and S. V. Kalinin, Appl. Phys. Lett. **94**, 042906 (2009).
[34] K. Seal, S. Jesse, M. P. Nikiforov, S. V. Kalinin, I. Fujii, P. Bintachitt, and S. Trolier-McKinstry, Phys. Rev. Lett. **103**, 057601 (2009).
[35] S. P. Li, A. S. Bhalla, R. E. Newnham, L. E. Cross, and C. Y. Huang, J. Mater. Sci. **29**, 1290 (1994).
[36] J. Yin and W. Cao, Appl. Phys. Lett. **79**, 4556 (2001).
[37] J. E. Daniels, C. Cozzan, S. Ukritnukun, G. Tutuncu, J. Andrieux, J. Glaum, C. Dosch, W. Jo, and J. L. Jones, J. Appl. Phys. **115**, 224104 (2014).
[38] C. M. Fancher, S. Brewer, C. C. Chung, S. Rohrig, T. Rojac, G. Esteves, M. Deluca, N. Bassiri-Gharb, and J. L. Jones, Acta Mater. **126**, 36 (2017).
[39] S. Gorfman, H. Simons, T. Iamsasri, S. Prasertpalichat, D. P. Cann, H. Choe, U. Pietsch, Y. Watier, and J. L. Jones, Sci. Rep. **6**, 20829 (2016).
[40] A. F. Devonshire, Adv. Phys. **3**, 85 (1954).
[41] A. L. Kholkin, E. K. Akdogan, A. Safari, P.-F. Chauvy, and N. Setter, J. Appl. Phys. **89**, 8066 (2001).
[42] N. Bassiri-Gharb, S. Trolier-Mckinstry, and D. Damjanovic, J. Appl. Phys. **110**, 124104 (2011).
[43] R. E. Newnham, *Properties of Materials. Anisotropy, Symmetry, Structure* (Oxford University Press Inc., New York, 2005).
[44] D. A. Hall, A. Steuwer, B. Cherdhirunkorn, T. Mori, and P. J. Withers, J. Appl. Phys. **96**, 4245 (2004).
[45] M. Hammer and M. J. Hoffmann, J. Am. Ceram. Soc. **81**, 3277 (1998).
[46] H. von Seggern and S. Fedosov, IEEE Trans. Dielectr. Electr. Insul. **7**, 543 (2000).
[47] M. J. Haun, Z. Q. Zhuang, E. Furman, S.-J. Jang, and L. E. Cross, J. Am. Ceram. Soc. **72**, 1140 (1989).
[48] J. Glaum, T. Granzow, L. A. Schmitt, H.-J. Kleebe, and J. Rödel, Acta Mater. **59**, 6083 (2011).
[49] G. Arlt, Integr. Ferroelectr. **16**, 229 (1997).
[50] D. Zhou and M. Kamlah, Acta Mater. **54**, 1389 (2006).
[51] C. Verdier, D. C. Lupascu, H. von Seggern, and J. Rodel, Appl. Phys. Lett. **85**, 3211 (2004).
[52] J. Li, Z. Liu, and B. W. Wessels, J. Appl. Phys. **107**, 124106 (2010).
[53] D. Pantel, Y.-H. Chu, L. W. Martin, R. Ramesh, D. Hesse, and M. Alexe, J. Appl. Phys. **107**, 084111 (2010).
[54] Y. Kim, X. Lu, S. Jesse, D. Hesse, M. Alexe, and S. V. Kalinin, Adv. Funct. Mater. **23**, 3971 (2013).
[55] V. Shur, E. Rumyantsev, and S. Makarov, J. Appl. Phys. **84**, 445 (1998).
[56] W. J. Merz, J. Appl. Phys. **27**, 938 (1956).
[57] S. Li, W. Cao, and L. E. Cross, J. Appl. Phys. **69**, 7219 (1991).
[58] K. G. Webber, E. Aulbach, T. Key, M. Marsilius, T. Granzow, and J. Rödel, Acta Mater. **57**, 4614 (2009).
[59] S. Mantri, J. Oddershede, D. Damjanovic, and J. E. Daniels, Acta Mater. **128**, 400 (2017).

6.2.4 PAPER IV

Correlated polarization-switching kinetics in bulk polycrystalline ferroelectrics. II: Impact of crystalline phase symmetries
R. Khachaturyan, Y.A. Genenko, *Physical Review B.*, **98(13)**, 134106 (2018).
DOI: 10.1103/PhysRevB.98.134106

Correlated polarization-switching kinetics in bulk polycrystalline ferroelectrics. II. Impact of crystalline phase symmetries

R. Khachaturyan* and Y. A. Genenko†
Institut für Materialwissenschaft, Technische Universität Darmstadt, 64287 Darmstadt, Germany

(Received 24 July 2018; published 15 October 2018)

Electric depolarization fields have a great impact on the polarization-switching kinetics in ferroelectrics although they are often neglected in statistical considerations. Analysis of statistical distributions and correlations of polarization and electric field during the field-driven polarization reversal in a bulk polycrystalline ferroelectric by means of the two-dimensional self-consistent mesoscopic switching (SMS) model has revealed that correlations, mediated by electrostatic fields, are mostly isotropic and short range at a typical scale of the mean grain size [Phys. Rev. B **96**, 054113 (2017)]. However, the magnitude of emerging depolarization fields remains substantial and strongly influences the switching kinetics. It is known, on the other hand, that the effect of inhomogeneities, such as a granular structure, on the electric field pattern and local field magnitudes is considerably overestimated in two-dimensional simulations. Three-dimensional extension of the SMS model in the current study allows a realistic evaluation of the impact of spatial correlations on the polarization switching in ferroelectric ceramics and opens a possibility to consider materials of different phase symmetries. It is shown that bound charges at grain boundaries due to mismatching grain polarizations as well as the subsequent depolarization fields are essentially dependent on the crystalline symmetry. This explains great differences in statistical field distributions and polarization kinetics observed in ceramics of different phase symmetries. Field correlations are anisotropic, depend on the material symmetry, but remain in all cases short range at the scale of a grain size. This sheds light on the success of models assuming statistically independent switching of different regions. Evolution of the statistical field distributions in the course of polarization reversal is also symmetry dependent but temporal changes in distributions are not substantial which clarifies a good performance of models neglecting the feedback via depolarization fields.

DOI: 10.1103/PhysRevB.98.134106

I. INTRODUCTION

The most characteristic property of ferroelectrics is their ability to switch the spontaneous polarization when a strong enough electric field is applied. This is a basic process in such ferroelectric applications as digital data storage (FERAM) [1]. Polarization reversal at some location generates a long-range depolarization field [2,3] which should affect the switching process at other locations. However, statistical concepts of polarization reversal typically neglect the feedback effect of depolarization fields and assume independent and uncorrelated nucleation and growth of reversed domains [4–13]. Nevertheless, the nucleation limited switching (NLS) model [7] and the inhomogeneous field mechanism (IFM) model [10,12], assuming a stable statistical distribution of switching times in polycrystalline systems, are able to describe with high accuracy the time-dependent response of ferroelectric ceramics of different chemical compositions and phase symmetries [7,8,12,14–20] as well as of organic ferroelectrics [21–27] and organic-inorganic ferroelectric composites [28,29]. Does it mean that the depolarization fields emerging during the switching process and the interaction of the switching regions can be neglected?

Experimental observations of polarization response by piezoelectric scanning probe microscopy and transmission electron microscopy revealed clustering ranging from a few grains [30] to agglomerations of 10^2–10^3 grains [31,32] in polycrystalline thin films. Similarly, the grain-resolved three-dimensional x-ray diffraction disclosed a collective dynamics in bulk ceramics correlated over approximately 10–20 grains [33–35], a characteristic scale resulting from the complicated and still not understood interplay between the electrostatic and elastic fields. The experimentally revealed characteristic lengths disagree with extremely long-range electrostatic correlations found in phase-field simulations [36] and microscopic modeling [37] of uniform ferroelectric media. Thus, the role of long-range depolarization fields in the switching dynamics of bulk ferroelectric ceramics still remains unclear.

Recent attempts to account for the feedback of depolarization fields in the statistical approach remained mostly within the mean-field approximation assuming the emergence of a time-dependent uniform electric field due to averaging of individual switching events [38–40]. Such an approach still misses the role of local correlations clearly observed in experiment [41–43].

A self-consistent mesoscopic switching (SMS) model [44,45] recently suggested by the authors accounts in a self-consistent way for the local depolarization fields emerging during the field-driven polarization reversal in individual grains of a random polycrystalline medium. This

*rubenftf@gmail.com
†genenko@mm.tu-darmstadt.de

two-dimensional model allowed tracing the evolution of statistical distributions of electric field and polarization as well as their auto- and cross correlations. It was established that both polarization and electric field are correlated at a short range of about the mean grain size. The depolarization fields appeared to be effectively screened by adapting bound charges at grain boundaries. This explains, on the one hand, why the classical statistical approach [6] neglecting correlations may satisfactorily describe total polarization switching at earlier and intermediate stages of polarization reversal in polycrystalline ferroelectrics. On the other hand, the continuously spreading statistical distribution of the local depolarization fields [45] might have a remarkable retarding impact on the later stage of polarization reversal observed in experiment [7,10,13,18,25,27] and modeling [38–40,44]. The question remains open, why the NLS and IFM models neglecting a feedback via depolarization fields are nevertheless able to describe polarization response over the time domain with high accuracy [8,12,14–17].

Two-dimensional (2D) simulations overestimate the effect of obstacles on the field-line pattern [20,46,47] and do not allow consideration of different crystalline symmetries typical of perovskite ferroelectrics which apparently have a great impact on the polarization-switching dynamics [15–17]. Therefore in the current study we extend the SMS model to a three-dimensional (3D) geometry. The paper is organized as follows. An analytical 3D model of a fully polarized uncorrelated ceramic is introduced in Sec. II and serves as a reference limiting case for the following simulations. Analytical calculations of the surface bound charges in uncorrelated ceramics of different symmetries are performed for comparison with the respective correlated cases. A numerical 3D-SMS model is introduced in Sec. III. Simulations within this model presented and discussed in Sec. IV show the time development of the total polarization, statistical field distributions, and spatial correlations of electric field and polarization components during their evolution in the course of the polarization reversal. The results are concluded in Sec. V.

II. ANALYTICAL MODEL OF A FULLY POLARIZED, UNCORRELATED BULK FERROELECTRIC CERAMIC

Ferroelectric ceramics are characterized by random shape of grains and random orientation of the crystal lattice inside the grains. In the current study we focus on the latter factor of randomness which allows one to capture the main reasons for emerging and development of depolarization fields. To this end we use an original model of a ferroelectric ceramic introduced in Ref. [48]. We imagine a sample consisting of a regular cubic lattice of equal tightly contacting single-crystalline cubic grains of size R much larger than the lattice constant of the material. The grain edges are supposed to be aligned along the axes of the Cartesian coordinate system x, y, z as is shown in Fig. 1. The sample of a macroscopic size $L \gg R$ is sandwiched between two plane electrodes located at $z = \pm L/2$. It is supposed to be polarized in a dc electric field substantially higher than the coercive field to the maximum possible spontaneous polarization in the z direction. After that the voltage at the electrodes is set back to zero so that the remanent polarization $\mathbf{P}_r$ in the z direction remains. This state

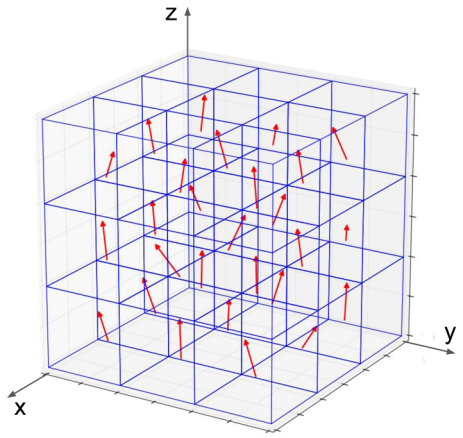

FIG. 1. Scheme of a three-dimensional distribution of polarization in a fully polarized ferroelectric ceramic represented by a regular array of cubic grains with arbitrary crystalline orientations.

will be considered as an initial one for the polarization reversal investigated in the next section.

Since the crystal structure of the grains is formed at temperatures far above the ferroelectric phase transition, the crystal axes orientation in different grains is supposed to be arbitrary and not correlated. In the high electric field the spontaneous polarization in each grain $\mathbf{P}_s$ takes on the direction of one of the pseudocubic symmetry axes closest to the direction of the applied field (see Fig. 1). Accordingly, an anisotropic dielectric permittivity tensor is arbitrarily oriented in the grains with its c axis along the local spontaneous polarization. The vectors $\mathbf{P}_s$, assumed to be uniform within each grain, have the same magnitude of P_s and are statistically distributed within the cone defined by the polar angle $\theta < \theta_{\max}$ with respect to the z axis. The angle $\theta_{\max}$ depends on the phase symmetry of the ferroelectric. For the cases of the tetragonal (T) and rhombohedral (R) symmetries the respective angles $\theta_{\max,t}$ and $\theta_{\max,r}$ were found by Uchida and Ikeda [49] to be equal to each other and amount to $\arcsin\sqrt{2/3}$. In the orthorhombic (O) phase this angle equals $\theta_{\max,o} = \pi/4$.

In the rest of this section, spatial fluctuations of the bound charges at the grain boundaries in the highly poled state of ceramics of different phase symmetries will be evaluated. For their calculation one needs a procedure of statistical averaging which is specified as follows.

A. Configurational averaging

Configurational averaging of local angle-dependent variables over the ensemble of all possible random configurations, which is equal to the averaging over the infinite sample volume, may be performed using the distribution function $f(\theta, \varphi)$ of a possible polarization directions compatible with the applied field direction. Derivation of this function presents a nontrivial task involving cumbersome calculations. For the case of tetragonal symmetry, the appropriate distribution function $f_t(\theta, \varphi)$ was derived in Ref. [48]:

$$f_t(\theta,\varphi) = \begin{cases} \frac{3}{2\pi}, & 0 \leqslant \theta \leqslant \frac{\pi}{4}, \\ \frac{6}{\pi^2}\left[\frac{\pi}{4} - \arccos\left(\cot\theta\right)\right], & \frac{\pi}{4} \leqslant \theta \leqslant \theta_{\max,t}, \end{cases} \tag{1}$$

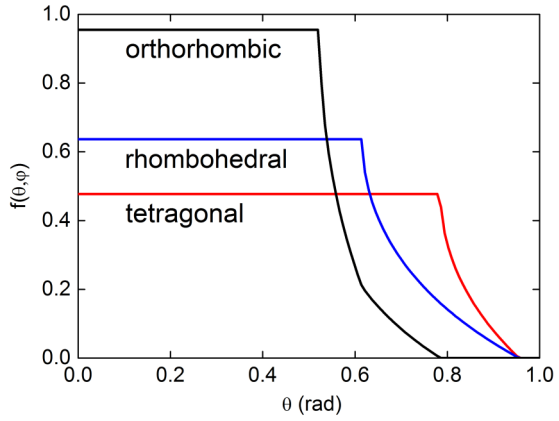

FIG. 2. Two-dimensional projection of statistical distributions $f(\theta, \varphi)$ of polarization directions on an arbitrary φ plane in fully polarized uncorrelated ferroelectric ceramics of different phase symmetries.

for $0 \leqslant \varphi < 2\pi$ where φ and θ are, respectively, the azimuthal and polar angle in spherical coordinates associated with the above introduced cartesian coordinates and centered in the center of the chosen grain. The distribution functions $f_r(\theta, \varphi)$ and $f_o(\theta, \varphi)$ for the cases of rhombohedral and orthorhombic symmetries are derived in Appendixes A and B and given by Eqs. (A5) and (B5), respectively. Since the considered poled polycrystalline ferroelectrics belong to the Curie symmetry group ∞m [50], the distribution functions are independent of the azimuthal angle and can be presented on a plane graph [51] as is shown in Fig. 2. It is seen that the orthorhombic phase, possessing twelve possible stable polarization directions, is described by the most concentrated polarization distribution $f_o(\theta, \varphi)$, followed by the wider rhombohedral distribution $f_r(\theta, \varphi)$, related to eight possible polarization directions, and the most spread tetragonal distribution $f_t(\theta, \varphi)$, related to six possible polarization directions.

Let us introduce as in Ref. [48] a three-dimensional numeration (integer coordinates) of grains $[n, k, m]$ associated with the Cartesian coordinates so that the centers of the grains take positions (nR, kR, mR). For evaluation of macroscopic mean values the sample will be considered as an infinite one so that the numbers $[n, k, m]$ run over all integers from $-\infty$ to $+\infty$. Assuming statistical independence of random angle variables in different grains the distribution function for polarization directions in all grains reads

$$F(\{\theta_i, \varphi_i\}) = \prod_{n,k,m} f(\theta_{n,k,m}, \varphi_{n,k,m}), \tag{2}$$

where $\{\theta_i, \varphi_i\}$ denotes the manifold of spherical angles in all grains, while $\theta_{n,k,m}$ and $\varphi_{n,k,m}$ denote the angles in the grain with numbers $[n, k, m]$. Calculating an ensemble average of a quantity $g(\{\theta_i, \varphi_i\})$,

$$\langle g \rangle = \prod_i \int \sin(\theta_i) d\theta_i \int d\varphi_i \, g(\{\theta_i, \varphi_i\}) F(\{\theta_i, \varphi_i\}), \tag{3}$$

one should take into account that all azimuthal and polar angle variables change in the same angle ranges, $0 \leqslant \varphi < 2\pi$, $0 \leqslant \theta \leqslant \theta_{\max}$. Thus, the ensemble average of the polarization along the z-axis $\langle P_z \rangle$ is reduced to

$$P_r = P_s \langle \cos(\theta_{n,k,m}) \rangle = P_s \int_0^{2\pi} d\varphi_{n,k,m} \times \int_0^{\theta_{\max}} f(\theta_{n,k,m}, \varphi_{n,k,m}) \sin(\theta_{n,k,m}) \times \cos(\theta_{n,k,m}) d\theta_{n,k,m}. \tag{4}$$

By applying the respective distribution functions for ceramics of different phase symmetries this formula brings about the maximum possible values of polarization $P_{\max}$ in nontextured ceramics of tetragonal, rhombohedral, and orthorhombic symmetries presented in Table I which coincide with the numbers known in literature [49,52,53]. The perpendicular x component of polarization in all cases vanishes,

$$\langle P_x \rangle = P_s \langle \cos(\theta_{n,k,m}) \cos(\varphi_{n,k,m}) \rangle = 0, \tag{5}$$

as well as $\langle P_y \rangle = 0$ for symmetry reasons. Finally, the local polarization can be conveniently decomposed in a sum of the mean and fluctuation polarizations as $\mathbf{P}_s = \mathbf{P}_r + \Delta\mathbf{P}_s$, where $\langle \mathbf{P}_r \rangle = (0, 0, P_{\max})$ with $\langle \Delta\mathbf{P}_s \rangle = 0$.

TABLE I. Mean polarization values and variances of bound charge densities at grain boundaries in uncorrelated tetragonal (T), rhombohedral (R), and orthorhombic (O) ceramics.

	T	R	O
$P_{\max}/P_s$	0.831	0.866	0.912
$\mathrm{SD}(\sigma^x)/P_s$	0.547	0.492	0.406
$\mathrm{SD}(\sigma^z)/P_s$	0.141	0.126	0.080

B. Variances of bound charges at grain boundaries

Surface bound charge densities at the faces of a cubic grain with the number $[n, k, m]$ located inside the bulk material are constant over the cubic faces and result from discontinuities of the respective normal components of the polarization $\Delta\mathbf{P}_s$ in the neighbor grains. Namely, the charge density at the bottom face perpendicular to the axis z equals

$$\sigma^z_{n,k,m} = P_s[\cos(\theta_{n,k,m-1}) - \cos(\theta_{n,k,m})], \tag{6}$$

the charge density at the left face perpendicular to the axis x equals

$$\sigma^x_{n,k,m} = P_s[\sin(\theta_{n-1,k,m}) \cos(\varphi_{n-1,k,m}) - \sin(\theta_{n,k,m}) \cos(\varphi_{n,k,m})], \tag{7}$$

and the charge density at the left face perpendicular to the axis y equals

$$\sigma^y_{n,k,m} = P_s[\sin(\theta_{n,k-1,m}) \sin(\varphi_{n,k-1,m}) - \sin(\theta_{n,k,m}) \sin(\varphi_{n,k,m})]. \tag{8}$$

Configurational averaging of the above charge densities for internal grains with the distribution functions $f(\theta_{n,k,m}, \varphi_{n,k,m})$, equal to the averaging over the sample volume, results in vanishing mean values $\langle \sigma^{x,y,z}_{n,k,m} \rangle = 0$, which does not preclude the fact that local values (6)–(8) in a certain random system are finite. For the top plane of a physical sample, Eq. (6) is not valid because there are no grains above

the top grain layer. For that reason the nonzero mean value $\langle\sigma^z_{n,k,m}\rangle = P_r$ produced by the mean polarization $\mathbf{P}_r$ prevails at the top plane of the sample $z = L/2$. Similarly, $\langle\sigma^z_{n,k,m}\rangle = -P_r$ at the bottom plane of the sample $z = -L/2$.

Typical magnitudes of the local charge densities at the internal grain faces (6)–(8) are characterized by the standard deviations (SD) of the respective charge densities,

$$\mathrm{SD}(\sigma^x) = \sqrt{\left\langle\left(\sigma^x_{n,k,m}\right)^2\right\rangle} = \mathrm{SD}(\sigma^y) \quad \text{and}$$
$$\mathrm{SD}(\sigma^z) = \sqrt{\left\langle\left(\sigma^z_{n,k,m}\right)^2\right\rangle}. \tag{9}$$

Table I shows their values normalized to P_s for ferroelectric ceramics of different phase symmetries. Details of calculations are presented in Appendix C. Substantial differences between $\mathrm{SD}(\sigma^z)$ and $\mathrm{SD}(\sigma^x)$ are explained by the fact that the polarization direction in the (x, y) plane and, hence, the variation of its azimuthal angle are not restricted while the polar angle is confined to the cone $\theta \leqslant \theta_{\max}$ around the positive z direction.

III. 3D SELF-CONSISTENT MODEL OF POLARIZATION-SWITCHING KINETICS IN A BULK FERROELECTRIC CERAMIC

The main task of the current study is to account for the electric interaction between different switching regions due to the emerging depolarization fields and finally to evaluate the feedback effect of these fields on the global polarization kinetics. To this end we advance here a three-dimensional self-consistent mesoscopic switching model (3D-SMS) of polarization reversal kinetics in a bulk ferroelectric ceramic which conceptually extends the previously developed 2D-SMS model [45]. Differently from the latter, the 3D-SMS model does not assume a random grain structure of the material but uses instead the regular cubic grain structure with randomized crystal lattice orientations delineated in Sec. II. Similarly to the previous 2D approach, the 3D-SMS model combines a numerical solution of the coarse-grained local equations for polarization development in individual grains with the global calculation of the electric field by the finite-element method (FEM), the whole algorithm being realized within a FlexPDE program (PDE Solutions Inc.). In the following, the description of ferroelectric ceramics and the evolution equations are presented in detail.

A. Creation of a random structure

We consider a polycrystalline bulk ferroelectric placed between two—top and bottom—plain electrodes. A cubic sample is assumed to consist of equal cubic single-crystalline grains as is schematically shown in Fig. 1. Each grain possesses the same phase symmetry—tetragonal, rhombohedral, or orthorhombic—and a random crystal orientation uncorrelated with neighbor grains. An initial polarization state is assumed to be created by a very strong electric field applied in positive z direction given by the vertical axis in Fig. 1. In this case, polarization directions in individual grains are arbitrarily chosen from an appropriate three-dimensional angle distribution function for a nontextured ferroelectric bulk ceramic of the respective symmetry using Eq. (1) or (A5) or (B5). According to the chosen polarization (c-axis) direction (and a random rotation around it), each grain is characterized by a dielectric tensor ε_{ij}, with principal values of the relative permittivity taken from Refs. [54–57] for exemplary materials of different symmetries.

In a coarse-grained consideration, polarization within each grain is characterized by a mean value $\mathbf{p}_i$ approximately presenting a multidomain state that entails discontinuities at grain boundaries where surface charge densities arise, equal to an abrupt variation of the normal component of the polarization when traversing the boundary. The electric field, in contrast, varies within the grains according to the Laplace equation and natural boundary conditions at the grain boundaries which comprise continuity of the tangential electric field and discontinuity of the normal component of the electric displacement equal to the surface charge density. To apply an external electric field of either sign in z direction, the top and the bottom surfaces of the computation box are held at constant potentials, whereas periodic boundary conditions are applied in x and y directions.

B. Evolution equations

The change in the polarization of individual grains will be considered in the spirit of the Kolmogorov-Avrami-Ishibashi (KAI) model of domain nucleation and growth [4–6] giving the total polarization reversal as

$$\Delta p(t) = 2P_s\{1 - \exp[-(t/\tau)^\beta]\}, \tag{10}$$

where P_s is the saturation polarization, β is the Avrami index depending on the reversal domain dimensionality, t is the time elapsed after the voltage application, and τ is the characteristic switching time. It is well known that τ is strongly dependent on the electric field value E, for example, according to the empiric Merz law [58] $\tau(E) = \tau_0 \exp(E_a/E)$, where E_a is the so called activation field and τ_0 is the switching time at very high fields.

In the original KAI approach the field E is assumed to be uniform in the whole system and constant in time. In ferroelectric ceramics the field is indeed distributed nonuniformly due to complying with the boundary conditions at the grain boundaries. In the spirit of the IFM model [10,12] we suppose that the local switching time $\tau(E)$ is determined by the local value of the electric field [59]. In accordance with our coarse-grained consideration, for the local field E the mean-field value over each grain will be taken. Over and above, we account for the fact that local switching time values are also time dependent together with the field E. To be able to capture this dependence we substitute the global time dependence of the polarization, Eq. (10), by the instantaneous rate of the polarization change derived by differentiation of Eq. (10) with respect to the time t:

$$\frac{dp}{dt} = \frac{P_s\,\mathrm{sgn}(E) - p}{\tau}\beta\left(\frac{t}{\tau}\right)^{\beta-1}. \tag{11}$$

Here the signum function $\mathrm{sgn}(\cdot)$ determines the direction to which the saturation of the polarization proceeds. This one-dimensional equation should be generalized to the actual 3D case. In the following we assume, as in the classical KAI approach [6], the polarization reversal to be dominated by

180°-switching events (which is generally not true [60–62]), so that the polarization only changes along the randomly chosen c direction within each grain given by a unit vector $\mathbf{n}_i$. This means that the local dielectric tensor remains unchanged during this process. Thus Eq. (11) can be generalized to the local vectorial form

$$\frac{d\mathbf{p}_i}{dt} = \frac{\mathbf{n}_i P_s \,\mathrm{sgn}(\langle\mathbf{E}\rangle_i \cdot \mathbf{n}_i) - \mathbf{p}_i}{\tau(|\langle\mathbf{E}\rangle_i \cdot \mathbf{n}_i|)} \beta \left[\frac{t}{\tau(|\langle\mathbf{E}\rangle_i \cdot \mathbf{n}_i|)}\right]^{\beta-1}, \quad (12)$$

where $\langle\mathbf{E}\rangle_i$ is the electric field averaged over the volume of the considered grain. Equation (12) takes into account that only the field projection on the local c axis promotes switching.

Calculated local values of the depolarization field ΔE_d scale with the magnitude of the saturation polarization P_s. Typical magnitudes of the field components, estimated exemplarily for lead zirconate titanate (PZT) [48], appear to be of the order of the thermodynamic coercive field which is known to exceed experimentally observed values of the coercive field by few orders of the magnitude [63]. In fact, local electric fields are strongly reduced by various physical mechanisms, first of all, by domain formation [63] and semiconductor properties of ferroelectric materials [64–66]. For low total polarizations, high local fields can be depressed by splitting in domains which leads to lower mean polarizations of grains and accordingly lower bound charges at grain boundaries. At higher polarizations, too high local fields may be depressed by screening of bound charges due to semiconductor effects including band bending and accumulation of charged defects in surface states at grain boundaries. Indeed, the fluctuation field ΔE_d provides a variation of the electrostatic potential across a grain about $\Delta\varphi \simeq \Delta E_d R$ that can reach several tens of volts [48]. Being much larger than a typical band gap in ferroelectric perovskites E_g of 3–4 eV such a potential sweep causes strong band bending and produces electron and/or hole spatial pockets which effectively reduce bound charges at grain boundaries. Due to this internal screening effect the local fields cannot exceed a typical value of $E_g/2qR$, with the elementary charge q, so that the potential sweep remains below $E_g/2q$ [65,66]. The local fields may be further reduced by accumulation of charge defects compensating bound charges at grain boundaries [67].

To account for the internal screening, an effective value of the local saturation polarization $P_s^* = 0.01$ C/m^2 was used for calculation of depolarization fields in the 2D-SMS model [45] that reduced local fluctuation fields to a typical magnitude of the coercive field in tetragonal PZTs. The drawback of this approach is that it uniformly depresses depolarization fields all over the system including locations where the field is already small. This might affect the statistical distribution of local electric fields and distort the true picture of field correlations. For that reason, in the actual 3D-SMS model we introduce another approach. Namely, each time after the FEM calculation of the electric field we apply a criterion testing the local field magnitude E and reducing it to the cutoff field $E_{\mathrm{cf}} < E_g/2qR$ if $E > E_{\mathrm{cf}}$. Thus the depolarization field is only depressed at locations where it is too large. Since the value E_{cf} may result from a sophisticated interplay of the above mentioned physical mechanisms it is used as a fitting parameter when comparing simulations with available data on polarization-switching kinetics.

C. Simulation procedure

Simulations include the following steps:

(1) Generation of a regular 3D array of $10\times10\times10$ cubic grains of size $R = 1$ μm and assigning to each grain a polarization direction (c axis) arbitrarily chosen from the statistical polarization distribution of the appropriate symmetry.

(2) Assignment of material parameters: saturation polarization, activation and cutoff fields, high-field switching time, Avrami index, eigenvalues of the permittivity tensor; assignment of the dielectric permittivity tensor in each grain by arbitrary rotation around its c axis.

(3) Evaluation of the spatial field distribution and average field magnitudes inside each grain using the finite element software FlexPDE.

(4) Evaluation of the polarization change in each grain during the time step Δt by integration of Eq. (12) over Δt using the software FlexPDE for the above calculated local average field values; consequent updating of the polarization in each grain.

(5) Calculation of the total polarization by adding up the local modified polarizations.

(6) Repetition of steps 3–5 until the total polarization reaches a saturated value.

For exemplary tetragonal and rhombohedral systems, lead zirconate titanate ceramics $Pb(Zr_xTi_{1-x})O_3$ with, respectively, $x = 0.515$ and $x = 0.6$ were chosen. The appropriate permittivity values were taken from Refs. [54,55], the other parameters were used as trial values and found by best fitting to the available polarization kinetics data for these compounds [16] as is shown below in Fig. 3. As an example of an orthorhombic ferroelectric at room temperature, potassium niobate $KNbO_3$ was chosen whose polarization and coercive field were taken from Ref. [68] and permittivity tensor from Refs. [56,57]. Sufficient polarization kinetics data for this material are not available, so that the respective kinetic parameters were exemplarily taken over from the solid solution $(1-x)Ba(Zr_{0.2}Ti_{0.8})O_3$-$x(Ba_{0.7}Ca_{0.3})TiO_3$ with $x = 0.5$, which possesses a comparable coercive field [17].

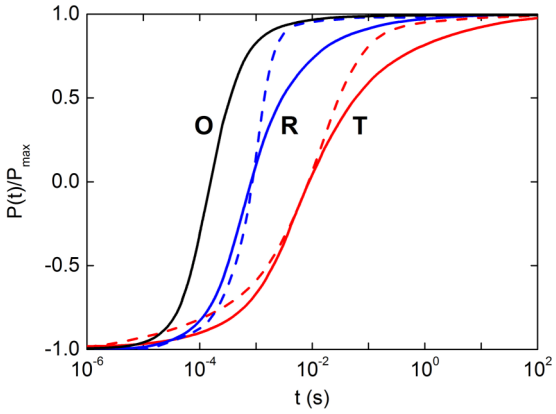

FIG. 3. Time evolution of the total polarization $P = \langle p_z \rangle$ normalized to its maximum value for materials of tetragonal (T), rhombohedral (R), and orthorhombic (O) symmetries, as indicated in the plot, at applied field values 1.8, 1.4, and 0.5 kV/mm, respectively. Solid and dashed lines show, respectively, simulated and experimental response. The other parameters used are gathered in Table II.

TABLE II. E_a, E_{cf}, β, and τ_0 values in tetragonal (T), rhombohedral (R), and orthorhombic (O) ceramics.

	T	R	O
E_a (kV/mm)	35	28	8
E_{cf} (kV/mm)	0.4	0.25	0.1
β	2	3	3
τ_0 (ps)	11.5	1.7	5
ε_{11}	1721	529	160
ε_{22}	1721	529	1000
ε_{33}	382	295	55

IV. SIMULATION RESULTS

A. Polarization-time dependencies

Polarization-time curves obtained from experimental measurements (dashed lines) and calculated ones (solid lines) are presented exemplarily in Fig. 3 for the above introduced materials of tetragonal, rhombohedral, and orthorhombic symmetries at different applied field values. They cannot be displayed on the same graph for the same applied field because the switching processes evolve at very different timescales. Note that the presented processes do not start from the initial highly polarized state described in Sec. II. This fully uncorrelated state includes, among others, unphysical local polarization configurations with highly charged grain boundaries. Due to resulting high local fields such places disappear after few polarization-switching cycles. After that polarization-switching curve becomes completely reproducible and weakly dependent on the applied field direction, a consequence of a finite size of the computation box.

Calculated polarization response demonstrates fair agreement with available experimental data for tetragonal and rhombohedral PZT ceramics using parameter values shown in Table II. The band gap E_g in PZT is known to be about 3.5 eV. The fitting value for the cutoff field E_{cf} is four times smaller than $E_g/2q$. This reveals that the band bending is not of crucial importance in the field suppression mechanism. Another physical reasons could be domain formation, inhomogeneous polarization distribution within domains, and possible non-180° rotations of polarization which are not taken into account in the actual model.

Non-180° rotations play an important role in polarization reversal [60–62] and seem to present a dominating mechanism at the beginning of this process because of much shorter switching times [13,60,69]. They also prevail with decreasing of the applied field value [13] that is supposed to explain the emerging deviation of simulated curves from experimental ones when the field is decreased, as is apparent in Fig. 4 presenting exemplary simulations for tetragonal symmetry. In the following we will use the parameters from Table II obtained by fitting of the kinetic polarization data in Fig. 3 for analysis of spatial fluctuations and correlations of polarization and field.

B. Charge and field spatial fluctuations

A rough insight into the coherence of polarization processes may be gained by studying grain boundary charges,

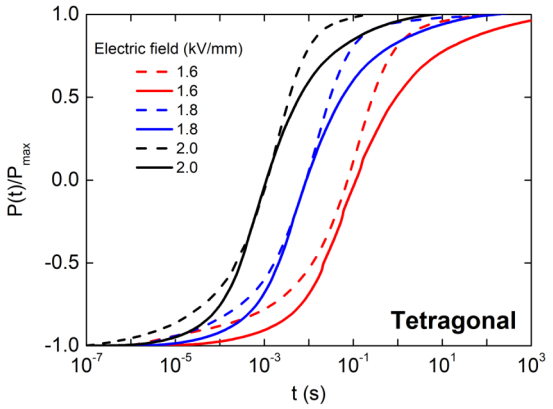

FIG. 4. Polarization-time curves for the tetragonal material at different applied field values as indicated in the plot. Dashed and solid lines show, respectively, experimental data from Ref. [16] and corresponding simulated response.

formed by polarization discontinuities between neighbor grains, in the course of the global polarization reversal. Their mean values averaged over the system volume remain, of course, equal to zero but their typical local magnitudes may be estimated from their variances. First a structure with maximum polarization in each grain is produced to compare standard deviations of simulated surface charges with analytical results of Sec. II B. A good agreement between the former and the latter for both x and z faces of cubic grains was found for all symmetries considered (cf. Tables I and III).

Surface charges vary with the evolution of the total polarization as is shown in Fig. 5. At the beginning of the displayed polarization reversal simulation the system is already somewhat aligned after a few polarization cycles, therefore initial levels of surface charges do not exactly coincide with those of fully uncorrelated systems.

For all phase symmetries, the initial and final polarization states are the most z aligned, exhibiting the lowest level of σ_z spatial fluctuations. At the same time the σ_x fluctuations are at the highest level in these states. Charge fluctuations interchange their intensities in the middle of polarization reversal, exhibiting the highest σ_z and the lowest σ_x spatial fluctuations for intermediate P values. For all phase symmetries the mean level of σ_x fluctuations during the polarization reversal is higher than of σ_z fluctuations, because of unbound polarization directions in (x, y) plane, with the highest difference between them in the most anisotropic tetragonal system [Fig. 5(a)]. Interestingly, the lowest level of charge fluctuations is observed not in the least anisotropic rhombohedral

TABLE III. Simulated maximum polarizations and standard deviations of surface charge densities (both evaluated with inaccuracy of 2%) in uncorrelated tetragonal (T), rhombohedral (R), and orthorhombic (O) ceramics.

	T	R	O
P_{max}/P_s	0.830	0.867	0.911
$SD(\sigma^x)/P_s$	0.541	0.515	0.437
$SD(\sigma^z)/P_s$	0.140	0.119	0.082

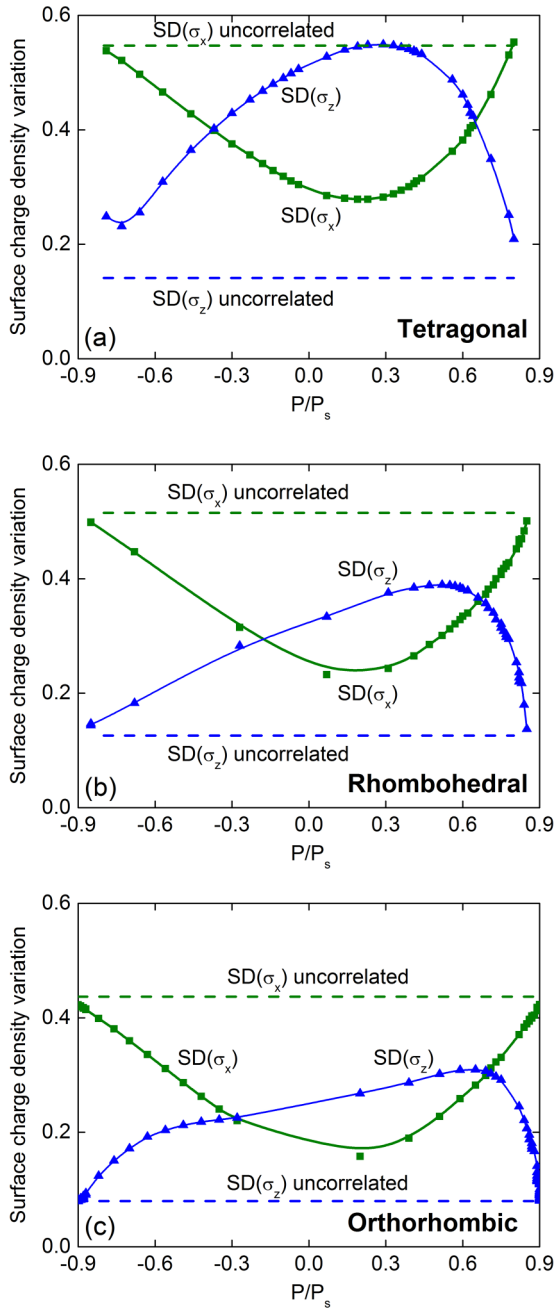

FIG. 5. Evolution of spatial charge fluctuations presented by standard deviations in units of P_s during the polarization reversal in (a) tetragonal, (b) rhombohedral, and (c) orthorhombic systems. Symbols show calculated quantities, solid lines are guide for the eye.

phase [Fig. 5(b)] but in the orthorhombic phase [Fig. 5(c)], obviously thanks to the most focused statistical distribution of polarization axes $f_o(\theta, \phi)$ in the latter phase (see Fig. 2).

Evolution of the field component fluctuations with the development of the total polarization is shown in Fig. 6 exhibiting the highest level of fluctuations in the most anisotropic tetragonal system and the lowest level of fluctuations again in the orthorhombic system. Since the local field components result to the same extent from both σ_x and σ_z charges and these vary with polarization in a complementary way (see Fig. 5) the field fluctuations do not vary much

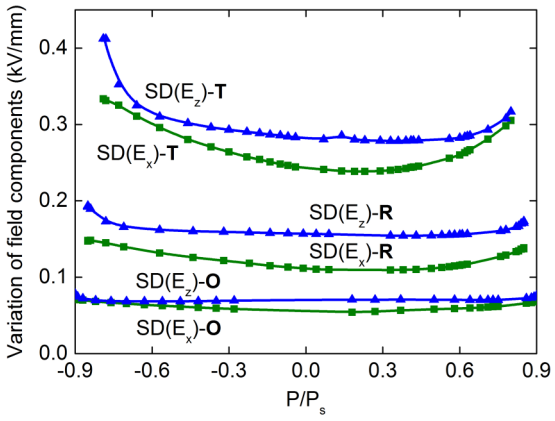

FIG. 6. Evolution of spatial field fluctuations presented by standard deviations of field components E_x and E_z in units of kV/mm during the polarization reversal in tetragonal (T), rhombohedral (R), and orthorhombic (O) systems.

when polarization changes. For all symmetries, variance of the E_z component exceeds that of the E_x component, the largest difference between them being observed in the initial polarization state ($-P_{\max}$) of the tetragonal ceramic.

C. Statistical field distributions

Evolution of the statistical field distributions during the polarization reversal exhibits nontrivial features which were not previously observed in 2D simulations [45]. As is seen in Fig. 7(a), the field distribution in the tetragonal ceramic is wide at the very beginning ($P/P_s = -0.81$). Then it rapidly becomes much narrower and higher when the total polarization changes up to $P/P_s = -0.662$ that takes a few tenth of millisecond on the timescale in Fig 3. After that the distribution height further slightly increases up to the polarization $P/P_s = -0.036$ and subsequently does not change up to $P/P_s = 0.634$. At the final stage, the distribution height decreases a little bit when the polarization grows to $P/P_s = 0.80$ virtually coinciding finally with that at $P/P_s = -0.662$.

Evolution of the field distribution in the rhombohedral ceramic exhibits partly similar but also some distinct features [Fig. 7(b)]. It transforms also rapidly from a wider to a narrower distribution when the polarization changes from $P/P_s = -0.851$ up to $P/P_s = -0.709$ that takes a few microseconds on the timescale in Fig 3. After that, however, it starts to decrease in height gradually changing its shape from a one-peak to a bimodal form when the polarization further changes to $P/P_s = -0.071$. Subsequently the distribution does not change essentially up to $P/P_s = 0.626$. At the final stage, the distribution height increases again when the polarization grows to $P/P_s = 0.848$ while the final distribution shape almost reproduces that in the state with $P/P_s = -0.709$.

The field distribution in the orthorhombic ceramic exhibits features similar to but not identical with the rhombohedral one. It transforms also rapidly from a wider initial one-peak distribution at $P/P_s = -0.902$ to a narrower distribution at $P/P_s = -0.704$ that takes a few microseconds on the timescale in Fig 3. After that it gradually decreases in

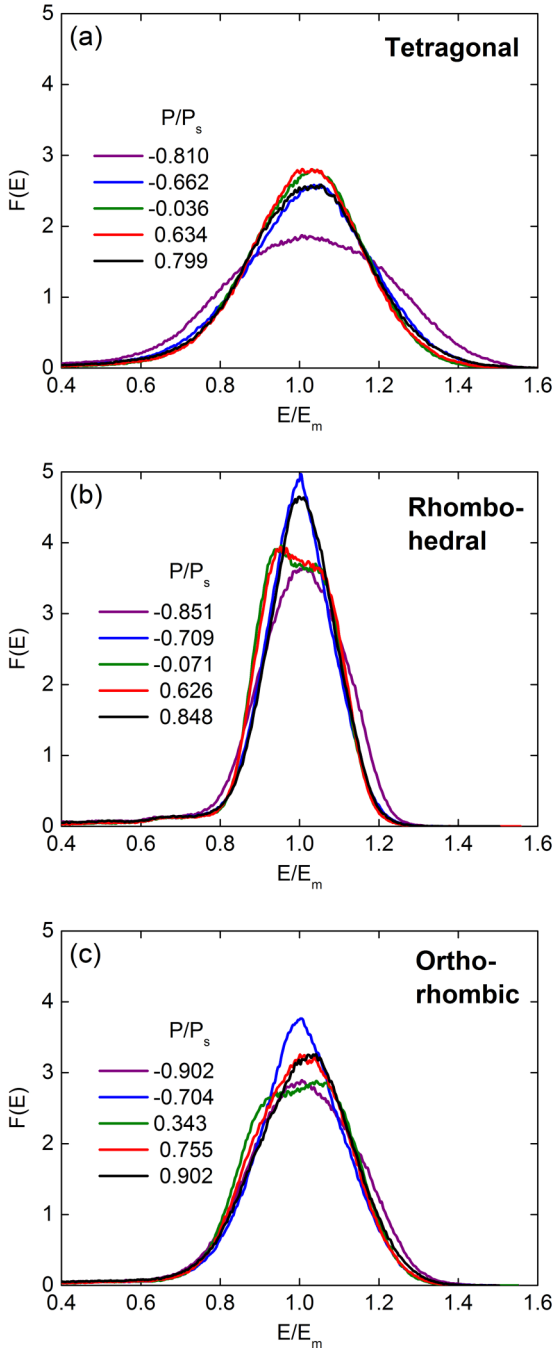

FIG. 7. Evolution of the statistical field distributions $F(E/E_m)$, where E_m is an applied field, in (a) tetragonal, (b) rhombohedral, and (c) orthorhombic ceramics for polarization variation from its negative to its positive maximum value. Representative polarization values are indicated in plots.

height changing its shape from a one-peak to a bimodal form when the polarization further changes to $P/P_s = 0.343$. Then the distribution height gradually increases again restoring a one-peak form when the polarization grows to $P/P_s = 0.755$ and remains stabilized until the end of the process at $P/P_s = 0.902$.

Notably, the saturated polarization values never reach the theoretical maximum magnitudes listed in Table I because the latter do not take into account possible disadvantageous local polarization configurations. Strong local depolarization fields appearing at such locations prevent reaching the maximum local polarizations thus limiting the total polarization value.

The evolution of the statistical distributions of fields seems to be more affected by statistical distributions of polarization directions $f(\theta, \varphi)$, which are narrower in the rhombohedral and orthorhombic ceramics, than by anisotropy of the permittivity tensor, which is substantially higher in the tetragonal and orthorhombic ceramics. This anisotropy, however, seems to be reflected by wider field distributions in the latter two systems. The absence of bimodal features in the field distribution of the tetragonal ceramic, Fig. 7(a), may also be due to the dominating role of the stray fields resulting from the highest anisotropy of this compound.

A general feature of evolution of statistical field distributions in all systems is that their shapes (particularly their widths) do not essentially change over the major part of the switching time (more than five decades). This behavior is in contrast to observations made in 2D simulations [45] where the statistical distribution was consistently broadening during the whole polarization reversal process. The difference to the simulation results of the 2D model [45] seems to stem from the stronger depression of the charge-induced depolarization fields by the assumed uniform reduction of polarization in the latter model, on the one hand, and from the overestimation of stray fields in 2D geometry, on the other hand.

The nonmonotonic variation of distributions with time may be rationalized as follows. In spite of the depolarization field reduction by different physical mechanisms in the actual model (see Sec. III B), the magnitude of these fields remains large and has a great impact on statistical field distributions in addition to the spatial fluctuations of the applied field due to the nonuniform granular structure of the system. On the one hand, the magnitude of spatial fluctuations of the depolarization fields generated by local bound charges roughly scales with the total polarization P. Thus, the variance of these fields is expected to be at maximum for the maximum values of polarization of either sign, the tendency observed in Fig. 6. On the other hand, the feedback through the depolarization fields provides an increasing synchronization of polarization switching in adjacent grains during the polarization reversal, which in turn leads to a continuous reduction of the variance of the depolarization fields with time. This makes the final distribution narrower than the initial one. Note, however, that, as soon as the voltage polarity is changed again, the distributions immediately transform back to the initial shapes as it should be in the completely symmetrical state. The difference in the behavior between tetragonal and rhombohedral ceramics might originate from much stronger anisotropy of the permittivity in the former. This means a stronger contribution of spatial field fluctuations of the applied field not related to the local charges. This dominating mechanism of the distribution broadening might hide in Fig. 7(a) the bimodal contribution from the depolarization fields which arises due to the cutoff of the high fields of the polarization charges. The behavior of field distributions in the orthorhombic ceramic bears features of both tetragonal and rhombohedral systems being in between them in anisotropy.

D. Spatial correlations

Two-point correlation functions of polarization and electric field components characterize how coherent the spatial fluctuations of these physical quantities are. The correlation coefficients are defined as

$$R_{E_\alpha,E_\beta}(\boldsymbol{\rho}) = \frac{\langle [E_\alpha(\mathbf{r}+\boldsymbol{\rho}) - \langle E_\alpha\rangle][E_\beta(\mathbf{r}) - \langle E_\beta\rangle]\rangle}{SD(E_\alpha)SD(E_\beta)}, \quad (13)$$

$$R_{p_\alpha,p_\beta}(\boldsymbol{\rho}) = \frac{\langle [p_\alpha(\mathbf{r}+\boldsymbol{\rho}) - \langle p_\alpha\rangle][p_\beta(\mathbf{r}) - \langle p_\beta\rangle]\rangle}{SD(p_\alpha)SD(p_\beta)}, \quad (14)$$

where α and β adopt values x, y, or z, and imply averaging over all pairs of points in the computational domain separated by a position vector $\boldsymbol{\rho}$. Due to cylindrical symmetry of the macroscopic system the correlation coefficients may only be dependent on the distance ρ and the angle the vector $\boldsymbol{\rho}$ makes with the field direction. For convenience, these coefficients will be displayed as polar diagrams in an arbitrary plain (ρ, ϕ) including the (vertical) field direction at $\phi = \pi/2$. A color legend from deep blue to deep red corresponds to the value variation from 0 to 1.

All cross correlations between the involved quantities including those between different polarization or field components were found to be negligible within the available accuracy. The autocorrelation coefficients of the polarization and field components exhibit nontrivial and distinct variations in compounds of different symmetries during the polarization reversal. This can only be captured when tracing a detailed evolution of the respective correlation functions. Since this analysis involves dozens of polar diagrams it is thoroughly presented in the Supplemental Material [70]. Here we merely show, for materials of different phase symmetries, exemplary plots of R_{E_z,E_z} and R_{p_z,p_z} coefficients in polarization states where correlations are most pronounced and anisotropic (Fig. 8). These demonstrate remarkable angle dependencies of correlations of both polarization and field components and an essential impact of the phase symmetry.

In all systems the correlations of the E_z component of the electric field are most pronounced in the x direction ($\phi = 0$ or $\phi = \pi$) as is seen in Figs. 8(a), 8(c) and 8(e) and in Figs. S1(f)–S1(j), S2(f)–S2(j), and S3(f)–S3(j) of the Supplemental Material [70]. Similarly, the correlations of the E_x component of the electric field are most pronounced in the z direction ($\phi = \pi/2$ or $\phi = 3\pi/2$) as is seen in Figs. S1(a)–S1(e), S2(a)–S2(e), and S3(a)–S3(e) of the Supplemental Material [70]. These correlations are apparently related to the continuity of the respective tangential field components across the cubic grain faces providing high field correlations at least in the neighbor grains. Beyond these features defined by the considered model geometry of the regular cubic grain array there are remarkable differences in the diagrams determined by the crystalline symmetries of different phases.

Differently from the field component correlations the correlation coefficient R_{p_x,p_x} reveals substantial variation between zero polarization state $P = 0$ and the maximum polarization states $P = \pm P_{\max}$ and also nontrivial anisotropic correlations in the intermediate states. In the tetragonal system, R_{p_x,p_x} is mostly of a fourfold symmetry with exception of the states around $P = 0$ where it becomes almost isotropic

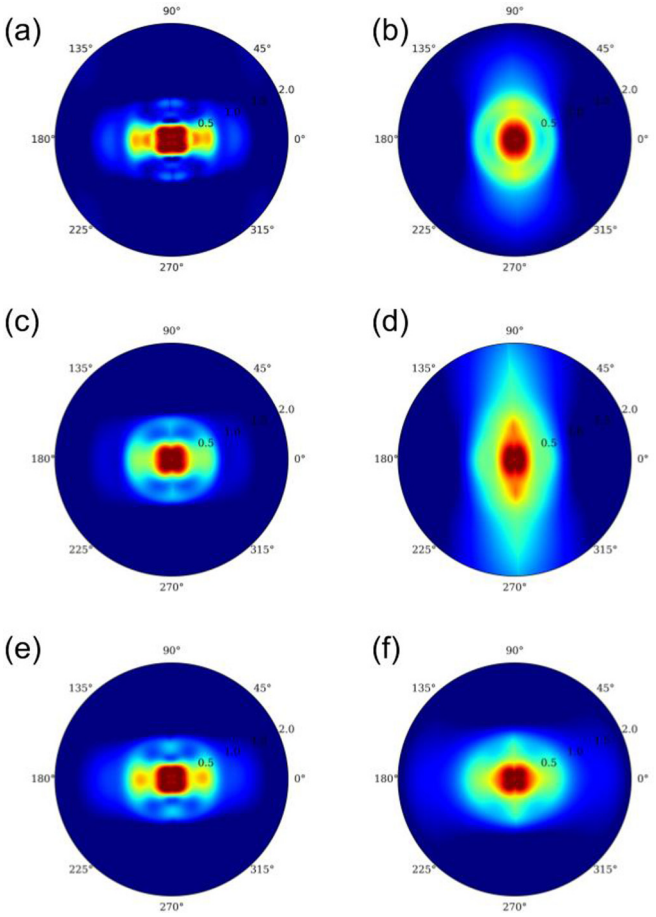

FIG. 8. Correlation coefficients R_{E_z,E_z} [(a), (c), and (e)] and R_{p_z,p_z} [(b), (d), and (f)] for tetragonal [at $P/P_s = 0.762$ (a) and -0.531 (b), respectively], rhombohedral [at $P/P_s = 0.853$ (c) and -0.299 (d), respectively], and orthorhombic [at $P/P_s = 0.895$ (e) and -0.548 (f), respectively] ceramics.

(Figs. S1(k)–S1(o) of the Supplemental Material [70]). In the rhombohedral system, R_{p_x,p_x} becomes additionally almost isotropic in the maximum polarization states $P = \pm P_{\max}$ revealing a twofold symmetry at intermediate polarization values (Figs. S2(k)–S2(o) of the Supplemental Material [70]). In the orthorhombic system, this coefficient retains a comparable fourfold symmetry at all polarization stages.

In contrast, the correlation coefficient R_{p_z,p_z} exhibits the strongest correlations along the z direction for the intermediate negative polarization values being otherwise virtually isotropic in the tetragonal system (Figs. S1(p)–S1(t) of the Supplemental Material [70]). These correlations along the poling direction are most strongly pronounced for intermediate negative to zero polarization values in the rhombohedral system (Figs. S2(p)–S2(t) of the Supplemental Material [70]). They are, however, only weakly visible in the orthorhombic system (Figs. S3(p)–S3(t) of the Supplemental Material [70]). The strongest z correlations in the rhombohedral ceramic result from the combination of the least anisotropic dielectric tensor of all systems considered and the relatively focused polarization axes distribution in this material (see Fig. 2).

With all anisotropic features and nonmonotonic behavior the correlations of both polarization and field remain short

range at the typical distance to the neighbor grain; a feature already observed in 2D simulations [45].

V. CONCLUSIONS

A long-standing question in the problem of polarization reversal kinetics was (i) why this process could be successfully described in statistical models [6–8] as statistically independent polarization-switching region by region as if the electric and elastic interactions of different regions were negligible. Furthermore, considering the evolution of depolarization fields in the course of polarization reversal [38–40,45], the question (ii) arises why the whole reversal process over many decades in time can be described as if the statistical distribution of the local fields does not change [10,12,15–17,25]. The presented simulations using the 3D-SMS model shed some light onto these problems.

Analysis of polarization and field correlations in Sec. IV D revealed that the depolarization field-mediated correlations remain short range at the typical scale of the grain size at all polarization stages for all phase symmetries considered. This means that, electrically, only nearest neighbors have effect on the polarization-switching process in a grain. Physical background of the short-range correlations is an effective screening of depolarization fields by adapting surface charges at grain boundaries [45]. This may answer the question (i) why statistical models [6–8] satisfactorily describe time dependence of the total polarization. On the other hand, the medium-range [33–35] correlations observed in ferroelectric ceramics and long-range [31,32] correlations observed in ferroelectric thin films seem rather to result from elastic interactions which cannot be screened as electrical ones.

The problem (ii) of emerging and varying depolarization field reveals different features in thin-film and bulk ferroelectrics. Being solely due to the presence of a very thin nonferroelectric layer below an electrode in the thin-film case [38,44,71] the depolarization field of this nature can hardly be significant in bulk ferroelectrics. In the latter case, a uniform depolarization field evolving together with the total polarization was conceived in Refs. [39,40]. From our point of view, in an experiment on the dc field-driven polarization reversal, such a field should be exactly compensated by charges at electrodes maintaining a constant voltage and thus would not play a role in polarization kinetics. On the other hand, spatial fluctuations of depolarization fields due to varying polarization of grains might be important. These fields arising due to mismatching polarizations in neighbor grains are typically much higher than coercive fields of ferroelectric materials. Therefore they are effectively reduced inside the grains by various physical mechanisms such as splitting in domains and semiconductor effects including band bending and possible accumulation of charged defects in surface states on grain boundaries. Since these mechanisms prevail during the whole polarization reversal process the statistical field distributions do not change much as was established in Sec. IV C. This explains why the NLS model [7,8,14,22] and the IFM model [12,15–17] neglecting the feedback due to depolarization fields are nevertheless able to describe the total polarization development in ferroelectric ceramics with high accuracy. We note that the statement on a stable statistical distribution of local electric fields resulting from the actual study using the 3D-SMS model revises the previous analysis based on the 2D-SMS model [45] where a broadening of the statistical field distribution during the polarization reversal was found. The physical reason of this discrepancy may be in overestimation of stray fields in 2D simulations as well as a simpler mechanism of the local field limitation assumed in the 2D-SMS model.

In conclusion, simulations using the 3D-SMS model helped to comprehend the paradoxically good performance of the statistical NLS and IFM models neglecting both the correlations between different switching regions and the feedback through the developing depolarization field. The 3D-SMS model itself, however, still provides only a fair agreement between the simulated time-dependent polarization reversal and available experimental data. Its most essential drawbacks are (i) the absence of possible polarization rotation in grains, which might strongly affect the switching kinetics, and (ii) the missing random shape of grains which could have a great effect on anisotropy of field and polarization correlations. Furthermore, since the local polarization development within grains is described by the statistical KAI approach, this model can hardly be applied to ceramics with a submicron grain size where a true single-domain state is expected to occur.

ACKNOWLEDGMENTS

Useful discussions with Jan Schultheiß , Jurij Koruza, and Andreas Klein are appreciated. R.K. gratefully acknowledges support of the research funded by Deutsche Forschungsgemeinschaft (GE 1171/7-1).

APPENDIX A: DIRECTIONAL STATISTICS OF POLARIZATIONS IN HIGHLY POLED UNCORRELATED FERROELECTRIC CERAMICS OF RHOMBOHEDRAL SYMMETRY

The distribution function of possible polarization directions in a polycrystalline ferroelectric of rhombohedral symmetry compatible with a given strong field direction can be derived in the spirit of the approach by Uchida and Ikeda [49], as was earlier done for the ceramics of tetragonal symmetry [48]. In their original work [49], Uchida and Ikeda avoided derivation of the distribution of polarization orientations around the applied field and used an alternative way to evaluate the mean directional cosine between the polarization and the applied field. To this end they fixed the polarization direction of a ferroelectric cell and averaged the directional cosine of the field over all possible field directions compatible with the chosen polarization direction. It was assumed that the crystal lattice orientation is arbitrary and completely decoupled from the form and orientation of grains.

Introducing the Cartesian coordinates aligned with a pseudocubic cell [see Fig. 9(a)] it is sufficient for the case of rhombohedral symmetry to consider a solid angle $0<\varphi<\pi/4$, $0<\vartheta<\pi/4$, in terms of a conventionally associated spherical coordinate system (r,φ,ϑ), comprising one of eight possible polarization directions with a Cartesian unit vector $\nu=(1,1,1)/\sqrt{3}$. Any field direction indicated by a unit vector $\mathbf{n}=(\sin\vartheta\cos\varphi,\sin\vartheta\sin\varphi,\cos\vartheta)$ from the considered

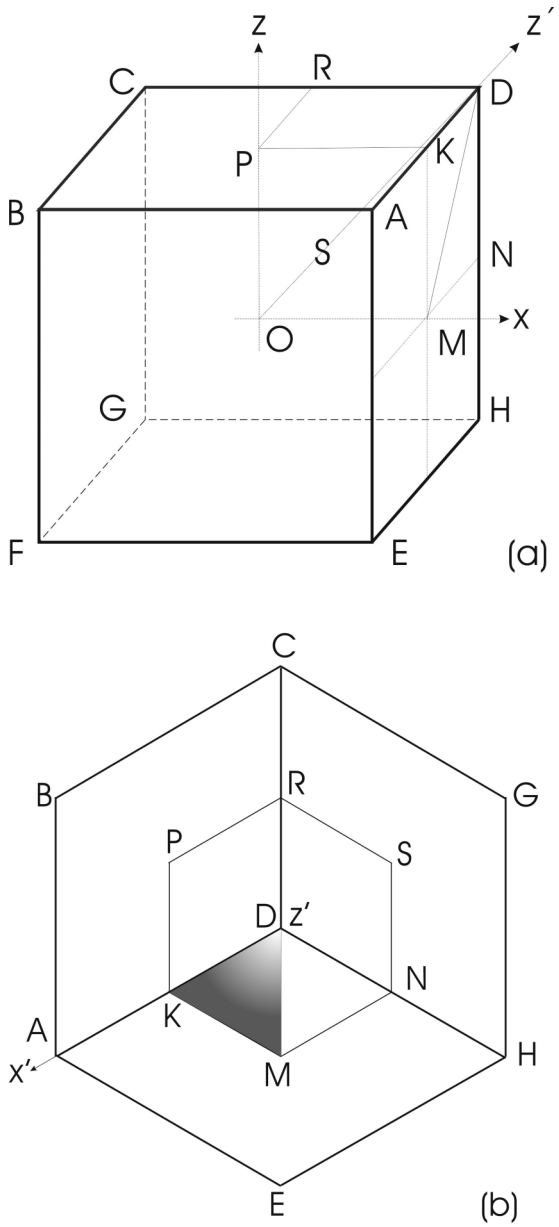

FIG. 9. (a) Scheme of a pseudocubic cell disclosing a polarization in the positive z' direction and a solid angle $OPRSNMK$ of strong electric field directions compatible with this polarization orientation. (b) Two-dimensional projection of the pseudocubic cell seen from a remote point at the axis z'. Shaded area DKM determines the considered solid angle with the center at origin.

solid angle, comprising directions crossing the origin O and the cube faces $DKPR$, $DRSN$, $DNMK$ in Fig. 9, equally favors the selected polarization direction ν. Crossing the border of the solid angle $PRSNMK$ by the field direction results in a 70.5°-polarization rotation to one of the neighboring stable polarization directions, OA, OC, OH.

The probability density for the field directions is uniform with a distribution function $p_r(\vartheta, \varphi) = 2/\pi$, the reciprocal value of the comprised solid angle of $4\pi/8 = \pi/2$, but it retains anisotropy through the choice of the considered solid angle. By averaging of a direction cosine $\cos\alpha = (\mathbf{n} \cdot \nu)$ with a tilt angle α over the chosen solid angle using the distribution function $p_r(\vartheta, \varphi)$ the mean projection of the field on the selected polarization direction can be evaluated:

$$\langle \cos\alpha \rangle = \int_0^{\pi/2} d\varphi \int_0^{\pi/2} d\vartheta \; p_r(\vartheta, \varphi) \sin\vartheta \cos\alpha = 0.866, \tag{A1}$$

which coincides with the result by Uchida and Ikeda [49] and also equals the mean polarization projection from the directions compatible with the fixed field direction.

To derive the distribution function of possible polarization directions compatible with a given field direction we chose the latter along the vector ν and rotate the Cartesian coordinate system (x, y, z) so that a new axis z' also coincides with ν (see Fig. 9). Basis unit vectors of the new Cartesian coordinate system (x', y', z') expressed in terms of the old one read $\mathbf{n}_{x'} = (1, -2, 1)/\sqrt{6}$, $\mathbf{n}_{y'} = (1, 0, 1)/\sqrt{2}$, and $\mathbf{n}_{z'} = (1, 1, 1)/\sqrt{3}$. Observed from a remote point at the axis z' the cubic cell looks like a figure of a sixfold rotational symmetry (being in fact threefold) where x' axis is hidden behind the line DA [Fig. 9(b)]. In terms of a spherical coordinate system (r, ϕ, θ) conventionally associated with the Cartesian system (x', y', z') it is sufficient to consider the azimuthal angle region between the directions $\phi = 0$ (hidden behind the line DA) and $\phi = \pi/3$ (hidden behind the line DE). The distribution function of interest $f_r(\theta, \phi)$ must be ϕ independent since due to arbitrary crystal orientation in different grains there is no selected direction in the (x', y') plane normal to the applied field. Therefore it can be derived by averaging over the azimuthal angle from the relation

$$2\pi \sin\theta \, d\theta \; f_r(\theta, \phi) = 6 \int_{\phi_0}^{\pi/3} d\phi' \; \sin\theta \, d\theta \; p_r(\theta, \phi'). \tag{A2}$$

The lower integration limit ϕ_0 is defined by the line KM bounding the solid angle $ODKM$. For any unit vector $\mathbf{n} = (\sin\theta\cos\phi, \sin\theta\sin\phi, \cos\theta)$ crossing this line a condition $\varphi = 0$ applies, therefore the relations

$$\begin{aligned} (\mathbf{n} \cdot \mathbf{n}_{z'}) &= \cos\theta = (\sin\vartheta + \cos\vartheta)/\sqrt{3}, \\ (\mathbf{n} \cdot \mathbf{n}_{x'}) &= \sin\theta\cos\phi = (\sin\vartheta + \cos\vartheta)/\sqrt{6} \end{aligned} \tag{A3}$$

are valid. By dividing the second equation by the first one a relation $\tan\theta\cos\phi = 1/\sqrt{2}$ results which can be alternatively resolved as

$$\theta_r(\phi) = \arctan\left(\frac{1}{\sqrt{2}\cos\phi}\right) \quad \text{or} \quad \phi_r(\theta) = \arccos\left(\frac{\cot\theta}{\sqrt{2}}\right). \tag{A4}$$

When ϕ varies from 0 to $\pi/3$ the function θ_r monotonically rises from $\theta_{r1} = \arctan(1/\sqrt{2})$ (corresponding to 35.2°) to $\theta_{r2} = \arctan\sqrt{2}$ (corresponding to 54.7°). As long as $\theta < \theta_{r1}$ integration in Eq. (A2) goes from $\phi_0 = 0$ to $\pi/3$ which results in a constant value of $f_r(\theta, \phi)$. When $\theta_{r1} < \theta < \theta_{r2}$ integration in Eq. (A2) goes from $\phi_0 = \phi_r$ to $\pi/3$ which results finally in a directional distribution

$$f_r(\theta, \phi) = \begin{cases} \frac{2}{\pi}, & 0 \leqslant \theta \leqslant \theta_{r1}, \\ \frac{6}{\pi^2}\left[\frac{\pi}{3} - \arccos\left(\frac{\cot\theta}{\sqrt{2}}\right)\right], & \theta_{r1} \leqslant \theta \leqslant \theta_{r2}, \end{cases} \tag{A5}$$

which is properly normalized to unity when integrating over the full solid angle. Averaging using Eq. (A5) brings about mean values $\langle\cos\theta\rangle = 0.866$ and $\langle\cos^2\theta\rangle = 0.758$ in agreement with Uchida and Ikeda [49].

APPENDIX B: DIRECTIONAL STATISTICS OF POLARIZATIONS IN HIGHLY POLED UNCORRELATED FERROELECTRIC CERAMICS OF ORTHORHOMBIC SYMMETRY

Orthorhombic symmetry allows twelve stable polarization directions, namely, four in-plane diagonal orientations in each of (x, y), (y, z), and (x, z) planes in the Cartesian coordinates (x, y, z) aligned with a pseudocubic cell [see Fig. 10(a)].

Similar to the case of rhombohedral symmetry we start with determination of a solid angle comprising possible strong field directions compatible with a certain polarization direction, in this case exemplarily given by a unit vector $\nu = (1, 1, 0)/\sqrt{2}$. This polarization is compatible with a strong electric field applied in any direction crossing the origin O and a rhombic area $ATBS$ (Fig. 10). Crossing the border of this area by the field direction would entail 60° switching of the polarization to one of the neighboring stable polarization directions given by vectors OL, OM, ON, OP [Fig. 10(a)]. The solid angle $OATBS$ has a fourfold symmetry so that it is sufficient to consider one quarter of it bounded by the triangle BKT. The lines KT and KB are defined, respectively, by conditions $0 < \varphi < \pi/4$, $\vartheta = \pi/2$ and $\varphi = \pi/4$, $\pi/2 < \vartheta < \pi/2 + \theta_o$ with $\theta_o = \arctan(1/\sqrt{2})$ in terms of a conventionally associated spherical coordinate system (r, φ, ϑ). The boundary BT is determined by a unit vector directed to this line from origin O, $\mathbf{n}_0 = (\sqrt{\sin^2\vartheta - \cos^2\vartheta}, -\cos\vartheta, \cos\vartheta)$, and obeys a relation $\tan\vartheta = -1/\sin\varphi$ or $\vartheta_0(\varphi) = \pi - \arctan(1/\sin\varphi)$.

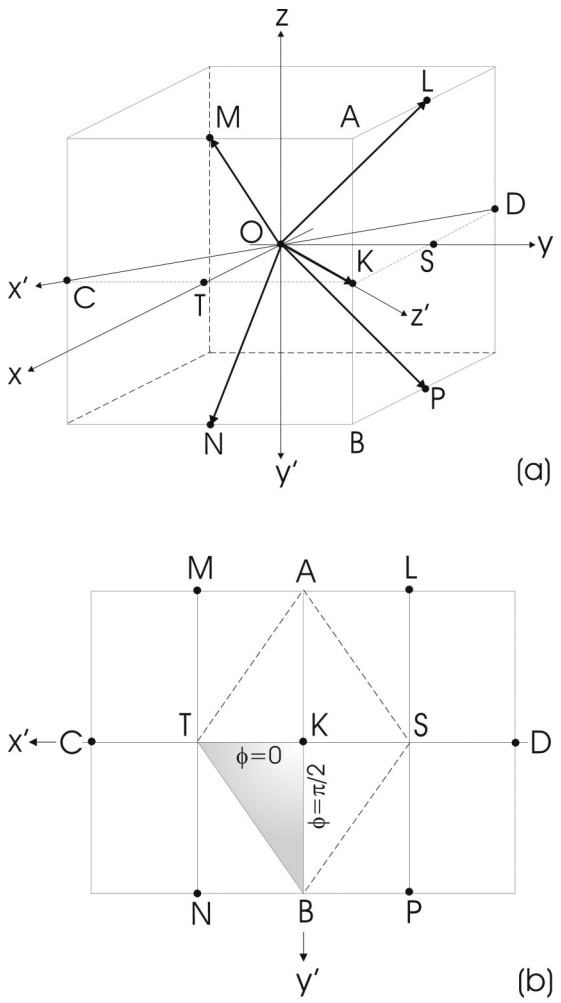

FIG. 10. (a) Scheme of a pseudocubic cell disclosing a polarization in the positive z' direction and a solid angle $OATBS$ of strong electric field directions compatible with this polarization orientation. (b) Two-dimensional projection of the pseudocubic cell seen from a remote point at the axis z'. Shaded area BKT determines the considered solid angle with the center at origin.

By integrating over the solid angle $OATBS$ its value is found to equal $\pi/3$ as it should be considering the 12 available polarization directions over the total solid angle. Since all field directions with the solid angle $OATBS$ are equally in favor of the polarization direction ν the probability density for the field directions is uniform with a distribution function $p_o(\vartheta, \varphi) = 3/\pi$, the reciprocal value of the comprised solid angle. By averaging of a direction cosine $\cos\alpha = (\mathbf{n}\cdot\nu)$ with a tilt angle α of an arbitrary field direction $\mathbf{n}$ over the chosen solid angle the mean projection of the field on the selected polarization direction can be evaluated using the distribution function $p_o(\vartheta, \varphi)$:

$$\langle\cos\alpha\rangle = 4\int_0^{\pi/4} d\varphi \int_{\pi/2}^{\vartheta_0(\varphi)} d\vartheta\; p_o(\vartheta,\varphi)\sin\vartheta\cos\alpha = 0.912, \tag{B1}$$

a value known from literature [52,53].

To derive the distribution function of possible polarization directions compatible with a given field direction we chose the latter along the vector ν and rotate the Cartesian coordinate system (x, y, z) so that a new axis z' also coincides with ν [see Fig. 10(a)]. Basis unit vectors of the new Cartesian coordinate system (x', y', z') expressed in terms of the old one read $\mathbf{n}_{x'} = (1, -1, 0)/\sqrt{2}$, $\mathbf{n}_{y'} = (0, 0, -1)$, and $\mathbf{n}_{z'} = (1, 1, 0)/\sqrt{2}$. Observed from a remote point at the axis z' the cubic cell looks like a rectangle with the rhombic boundary of the considered solid angle $ASBT$ [Fig. 10(b)]. In terms of a spherical coordinate system (r, ϕ, θ) conventionally associated with the Cartesian system (x', y', z') it is sufficient to consider a quarter of the above solid angle delineated by the triangle BKT [shadowed area in Fig. 10(b)] within the azimuthal angle region between $\phi = 0$ (line KT) and $\phi = \pi/2$ (line KB). An equation describing the last line bounding the solid angle BT can be derived from the relations

$$\begin{aligned}
(\mathbf{n}_0\cdot\mathbf{n}_{z'}) &= \cos\theta = \frac{\sqrt{\sin^2\vartheta - \cos^2\vartheta} - \cos\vartheta}{\sqrt{2}},\\
(\mathbf{n}_0\cdot\mathbf{n}_{x'}) &= \sin\theta\cos\phi = \frac{\sqrt{\sin^2\vartheta - \cos^2\vartheta} + \cos\vartheta}{\sqrt{2}},\\
(\mathbf{n}_0\cdot\mathbf{n}_{y'}) &= \sin\theta\sin\phi = -\cos\vartheta,
\end{aligned} \tag{B2}$$

from which an equation

$$\cos(\phi - \phi_0) = 1/\sqrt{3}\tan\theta \tag{B3}$$

with $\phi_0 = \arctan\sqrt{2}$ results.

The distribution function of possible polarization directions in a polycrystalline ferroelectric orthorhombic symmetry compatible with a given strong field direction $f_o(\theta, \phi)$ must be ϕ independent since due to arbitrary crystal orientation in different grains there is no selected direction in the (x', y') plane normal to the applied field. Therefore it can be derived by averaging over the azimuthal angle from the relation

$$2\pi \sin\theta\, d\theta\, f_o(\theta, \phi) = 4\int d\phi'\, \sin\theta\, d\theta\, p_o(\theta, \phi'), \tag{B4}$$

which looks similar to Eq. (A2) however covers a more complicated integration region. According to Eq. (B3), in the polar angle region $0 < \theta < \pi/6$ integration in Eq. (B4) goes over the azimuthal region $0 < \phi' < \pi/2$. In the polar angle region $\pi/6 < \theta < \theta_o$ integration over the azimuthal angle includes two regions $0 < \phi' < \phi_-$ and $\phi_+ < \phi' < \pi/2$ with $\phi_\pm = \phi_0 \pm \arccos(1/\sqrt{3}\tan\theta)$ being the solutions to Eq. (B3). And finally in the polar angle region $\theta_o < \theta < \pi/4$ integration over the azimuthal angle goes over the region $0 < \phi' < \phi_-$ only (the other region disappears). This leads to the directional distribution

$$f_o(\theta, \phi) = \begin{cases} \frac{3}{\pi}, & 0 \leqslant \theta \leqslant \pi/6, \\ \frac{6}{\pi^2}\left[\frac{\pi}{2} - 2\arccos\left(\frac{\cot\theta}{\sqrt{3}}\right)\right], & \pi/6 \leqslant \theta \leqslant \theta_o, \\ \frac{6}{\pi^2}\left[\phi_0 - \arccos\left(\frac{\cot\theta}{\sqrt{3}}\right)\right], & \theta_o \leqslant \theta \leqslant \pi/4, \end{cases} \tag{B5}$$

which is properly normalized to unity. Averaging using Eq. (B5) brings about mean values $\langle\cos\theta\rangle = 0.912$ and $\langle\cos^2\theta\rangle = 0.835$ confirming Refs. [52,53].

APPENDIX C: SPATIAL FLUCTUATIONS OF BOUND CHARGES IN HIGHLY POLED, UNCORRELATED FERROELECTRIC CERAMICS

Variances of the surface bound charge densities at the differently oriented grain boundaries are defined by coefficients

$$a = \langle\cos(\theta_{n,k,m})^2\rangle \quad \text{and} \quad b = \langle\cos(\theta_{n,k,m})\rangle^2. \tag{C1}$$

Using the distribution functions derived in Appendixes A and B and Ref. [48] they can be calculated to equal $a_t = 0.701$ and $b_t = 0.691$ for the tetragonal case, $a_r = 0.758$ and $b_r = 0.75$ for the rhombohedral case, and $a_o = 0.835$ and $b_o = 0.832$ for the orthorhombic case.

Thanks to statistical independence of the polarization directions in neighbor grains the variance of the charge density at the grain boundaries normal to the axis z [Eq. (6)] is reduced to

$$\left\langle\left(\sigma^z_{n,k,m}\right)^2\right\rangle = 2P_s^2(a - b). \tag{C2}$$

The variances of the charge densities at the grain boundaries perpendicular to the axes x [Eq. (7)] and y [Eq. (8)] are defined by

$$\left\langle\left(\sigma^x_{n,k,m}\right)^2\right\rangle = \left\langle\left(\sigma^y_{n,k,m}\right)^2\right\rangle = P_s^2(1 - a). \tag{C3}$$

These result in standard deviations of the respective charge densities [Eq. (9)] listed in Table I for different phase symmetries.

For calculation of various physical quantities, for example, of the field component variances [48], the knowledge of correlation functions of charge densities is needed. They appear to be diagonal in Cartesian indices β, β' and involve only the identical and the next neighbor indexes n, k, m:

$$\begin{aligned} \left\langle\sigma^x_{n,k,m}\sigma^x_{n',k',m'}\right\rangle &= \left(P_s^2/2\right)(1 - a)\delta_{k,k'}\delta_{m,m'} \\ &\quad \times (2\delta_{n,n'} - \delta_{n,n'-1} - \delta_{n,n'+1}), \\ \left\langle\sigma^y_{n,k,m}\sigma^y_{n',k',m'}\right\rangle &= \left(P_s^2/2\right)(1 - a)\delta_{n,n'}\delta_{m,m'} \\ &\quad \times (2\delta_{k,k'} - \delta_{k,k'-1} - \delta_{k,k'+1}), \\ \left\langle\sigma^z_{n,k,m}\sigma^z_{n',k',m'}\right\rangle &= P_s^2(a - b)\delta_{n,n'}\delta_{k,k'} \\ &\quad \times (2\delta_{m,m'} - \delta_{m,m'-1} - \delta_{m,m'+1}). \end{aligned} \tag{C4}$$

[1] J. F. Scott, *Ferroelectric Memories* (Springer, Berlin, 2000).
[2] R. Landauer, J. Appl. Phys. **28**, 227 (1957).
[3] R. C. Miller and G. Weinreich, Phys. Rev. **117**, 1460 (1960).
[4] A. Kolmogoroff, Izv. Akad. Nauk SSSR, Ser. Math. **1**, 355 (1937).
[5] M. Avrami, J. Chem. Phys. **8**, 212 (1940).
[6] Y. Ishibashi and Y. Takagi, J. Phys. Soc. Jpn. **31**, 506 (1971).
[7] A. K. Tagantsev, I. Stolichnov, N. Setter, J. S. Cross, and M. Tsukada, Phys. Rev. B **66**, 214109 (2002).
[8] J. Y. Jo, H. S. Han, J.-G. Yoon, T. K. Song, S.-H. Kim, and T. W. Noh, Phys. Rev. Lett. **99**, 267602 (2007).
[9] S. Zhukov, S. Fedosov, J. Glaum, T. Granzow, Y. A. Genenko, and H. von Seggern, J. Appl. Phys. **108**, 014105 (2010).
[10] S. Zhukov, Y. A. Genenko, O. Hirsch, J. Glaum, T. Granzow, and H. von Seggern, Phys. Rev. B **82**, 014109 (2010).
[11] D. Kedzierski, E. V. Kirichenko, and V. A. Stephanovich, Phys. Lett. A **375**, 685 (2011).
[12] Y. A. Genenko, S. Zhukov, S. V. Yampolskii, J. Schütrumpf, R. Dittmer, W. Jo, H. Kungl, M. J. Hoffmann, and H. von Seggern, Adv. Funct. Mater. **22**, 2058 (2012).
[13] Y. A. Genenko, R. Khachaturyan, J. Schultheiß, A. Ossipov, J. E. Daniels, and J. Koruza, Phys. Rev. B **97**, 144101 (2018).
[14] J. Y. Jo, S. M. Yang, H. S. Han, D. J. Kim, W. S. Choi, T. W. Noh, T. K. Song, J.-G. Yoon, C.-Y. Koo, J.-H. Cheon, and S.-H. Kim, Appl. Phys. Lett. **92**, 012917 (2008).
[15] S. Zhukov, Y. A. Genenko, M. Acosta, H. Humburg, W. Jo, J. Rödel, and H. von Seggern, Appl. Phys. Lett. **103**, 152904 (2013).
[16] S. Zhukov, H. Kungl, Y. A. Genenko, and H. von Seggern, J. Appl. Phys. **115**, 014103 (2014).

[17] S. Zhukov, M. Acosta, Y. A. Genenko, and H. von Seggern, J. Appl. Phys. **118**, 134104 (2015).

[18] S. Zhukov, Y. A. Genenko, J. Koruza, J. Schultheiß, H. von Seggern, W. Sakamoto, H. Ichikawa, T. Murata, K. Hayashi, and T. Yogo, Appl. Phys. Lett. **108**, 012907 (2016).

[19] S. Zhukov, J. Glaum, H. Kungl, E. Sapper, R. Dittmer, Y. A. Genenko, and H. von Seggern, J. Appl. Phys. **120**, 064103 (2016).

[20] R. Khachaturyan, S. Zhukov, J. Schultheiß, C. Galassi, C. Reimuth, J. Koruza, H. von Seggern, and Y. A. Genenko, J. Phys. D: Appl. Phys. **50**, 045303 (2017).

[21] J. Schütrumpf, S. Zhukov, Y. A. Genenko, and H. von Seggern, J. Phys. D: Appl. Phys. **45**, 165301 (2012).

[22] A. Nautiyal, K. C. Sekhar, N. P. Pathak, N. Dabra, J. S. Hundal, and R. Nath, Appl. Phys. A **99**, 941 (2010).

[23] N. Dabra, J. S. Hundal, A. Nautiyal, K. C. Sekhar, and R. Nath, J. Appl. Phys. **108**, 024108 (2010).

[24] D. Zhao, I. Katsouras, K. Asadi, P. W. M. Blom, and D. M. de Leeuw, Phys. Rev. B **92**, 214115 (2015).

[25] J. Lee, A. J. J. M. van Breemen, V. Khikhlovskyi, M. Kemerink, R. A. J. Janssen, and G. H. Gelinck, Sci. Rep. **6**, 24407 (2016).

[26] D. Zhao, I. Katsouras, K. Asadi, W. A. Groen, P. W. M. Blom, and D. M. de Leeuw, Appl. Phys. Lett. **108**, 232907 (2016).

[27] A. V. Gorbunov, T. Putzeys, I. Urbanavičiūtė, R. A. J. Janssen, M. Wübbenhorst, R. P. Sijbesma, and M. Kemerink, Phys. Chem. Chem. Phys. **18**, 23663 (2016).

[28] K. C. Sekhar, A. Nautiyal, and R. Nath, Appl. Phys. A **95**, 415 (2009).

[29] N. Mishra, N. Dabra, A. Nautiyal, J. S. Hundal, G. D. Varma, N. P. Pathak, and R. Nath, Ferroelectr. Lett. **42**, 75 (2015).

[30] I. Stolichnov, L. Malin, E. Colla, A. K. Tagantsev, and N. Setter, Appl. Phys. Lett. **86**, 012902 (2005).

[31] P. Bintachitt, S. Trolier-McKinstry, K. Seal, S. Jesse, and S. V. Kalinin, Appl. Phys. Lett. **94**, 042906 (2009).

[32] K. Seal, S. Jesse, M. P. Nikiforov, S. V. Kalinin, I. Fujii, P. Bintachitt, and S. Trolier-McKinstry, Phys. Rev. Lett. **103**, 057601 (2009).

[33] J. E. Daniels, M. Majkut, Q. Cao, S. Schmidt, J. Wright, W. Jo, and J. Oddershede, Sci. Rep. **6**, 22820 (2016).

[34] M. Majkut, J. E. Daniels, J. P. Wright, S. Schmidt, and J. Oddershede, J. Am. Ceram. Soc. **100**, 393 (2017).

[35] S. Mantri, J. Oddershede, D. Damjanovic, and J. E. Daniels, Acta Mater. **128**, 400 (2017).

[36] J. E. Zhou, T.-L. Cheng, and Y. U. Wang, J. Appl. Phys. **111**, 024105 (2012).

[37] A. Leschhorn and H. Kliem, J. Appl. Phys. **121**, 014103 (2017).

[38] X. J. Lou, J. Phys.: Condens. Matter **21**, 012207 (2009).

[39] G. Viola, K. B. Chong, F. Guiu, and M. J. Reece, J. Appl. Phys. **115**, 034106 (2014).

[40] K. Auluck and E. C. Kan, IEEE Trans. Electron Devices **63**, 631 (2016).

[41] D. M. Marincel, H. Zhang, A. Kumar, S. Jesse, S. V. Kalinin, W. M. Rainforth, I. M. Reaney, C. A. Randall, and S. Trolier-McKinstry, Adv. Funct. Mater. **24**, 1409 (2014).

[42] D. M. Marincel, H. R. Zhang, J. Britson, A. Belianinov, S. Jesse, S. V. Kalinin, L. Q. Chen, W. M. Rainforth, I. M. Reaney, C. A. Randall, and S. Trolier-McKinstry, Phys. Rev. B **91**, 134113 (2015).

[43] D. M. Marincel, H. Zhang, S. Jesse, A. Belianinov, M. B. Okatan, S. V. Kalinin, W. M. Rainforth, I. M. Reaney, C. A. Randall, and S. Trolier-McKinstry, J. Am. Ceram. Soc. **98**, 1848 (2015).

[44] Y. A. Genenko, J. Wehner, and H. von Seggern, J. Appl. Phys. **114**, 084101 (2013).

[45] R. Khachaturyan, J. Wehner, and Y. A. Genenko, Phys. Rev. B **96**, 054113 (2017).

[46] L. Padurariu, L. Curecheriu, C. Galassi, and L. Mitoseriu, Appl. Phys. Lett. **100**, 252905 (2012).

[47] L. Padurariu, L. Petronela Curecheriu, and L. Mitoseriu, Acta Mater. **103**, 724 (2016).

[48] Y. A. Genenko, J. Glaum, O. Hirsch, H. Kungl, M. J. Hoffmann, and T. Granzow, Phys. Rev. B **80**, 224109 (2009).

[49] N. Uchida and T. Ikeda, Jpn. J. Appl. Phys. **6**, 1079 (1967).

[50] R. E. Newnham, *Properties of Materials. Anisotropy, Symmetry, Structure* (Oxford University Press, Oxford, 2005).

[51] J. L. Jones, M. Hoffman, and K. J. Bowman, J. Appl. Phys. **98**, 024115 (2005).

[52] H. G. Baerwald, Phys. Rev. **105**, 480 (1957).

[53] B. Jaffe, W. R. Cook, Jr., and H. Jaffe, *Piezoelectric Ceramics* (Academic Press, New York, 1971).

[54] M. J. Haun, E. Furman, S. J. Jang, and L. E. Cross, Ferroelectrics **99**, 63 (1989).

[55] X.-H. Du, U. Belegundu, and K. Uchino, Jap. J. Appl. Phys. **36**, 5580 (1997).

[56] E. Wiesendanger, Ferroelectrics **6**, 263 (1974).

[57] L. Liang, Y. L. Li, L.-Q. Chen, S. Y. Hu, and G.-H. Lu, J. Appl. Phys. **106**, 104118 (2009).

[58] W. J. Merz, Phys. Rev. **95**, 690 (1954).

[59] D. C. Lupascu, S. Fedosov, C. Verdier, J. Rodel, and H. von Seggern, J. Appl. Phys. **95**, 1386 (2004).

[60] J. E. Daniels, C. Cozzan, S. Ukritnukun, G. Tutuncu, J. Andrieux, J. Glaum, C. Dosch, W. Jo, and J. L. Jones, J. Appl. Phys. **115**, 224104 (2014).

[61] S. Gorfman, H. Simons, T. Iamsasri, S. Prasertpalichat, D. P. Cann, H. Choe, U. Pietsch, Y. Watier, and J. L. Jones, Sci. Rep. **6**, 20829 (2016)

[62] C. M. Fancher, S. Brewer, C. C. Chung, S. Rohrig, T. Rojac, G. Esteves, M. Deluca, N. Bassiri-Gharb, and J. L. Jones, Acta Mater. **126**, 36 (2017).

[63] A. K. Tagantsev, L. E. Cross, and J. Fousek, *Domains in Ferroic Crystals and Thin Films* (Springer, Berlin, 2010).

[64] Y. Watanabe, Phys. Rev. B **57**, 789 (1998).

[65] M. Y. Gureev, A. K. Tagantsev, and N. Setter, Phys. Rev. B **83**, 184104 (2011).

[66] Y. A. Genenko, O. Hirsch, and P. Erhart, J. Appl. Phys. **115**, 104102 (2014).

[67] M. Blömker, E. Erdem, S. Li, S. Weber, A. Klein, J. Rödel, and T. Frömling, J. Am. Ceram. Soc. **99**, 543 (2016).

[68] J. H. Kim and C. S. Yoon, Appl. Phys. Lett. **81**, 3332 (2002).

[69] J. Schultheiß, L. Liu, H. Kungl, M. Weber, L. Kodumudi Venkataraman, S. Checchia, D. Damjanovic, J. E. Daniels, and J. Koruza, Acta Mater. **157**, 355 (2018).

[70] See Supplemental Material at http://link.aps.org/supplemental/10.1103/PhysRevB.98.134106 for polar diagrams of correlation coefficients for polarization and electric field components.

[71] A. K. Tagantsev and I. A. Stolichnov, Appl. Phys. Lett. **74**, 1326 (1999).

Supplementary Materials to the manuscript

"Correlated polarization-switching kinetics in bulk polycrystalline ferroelectrics. II: Impact of crystalline phase symmetries"

R. Khachaturyan[1, a)] and Y. A. Genenko[1, b)]

Institut für Materialwissenschaft, Technische Universität Darmstadt, 64287 Darmstadt, Germany

[a)]Electronic mail: rubenftf@gmail.com

[b)]Electronic mail: genenko@mm.tu-darmstadt.de

POLAR DIAGRAMS OF CORRELATION COEFFICIENTS

Two-point auto-correlation coefficients of polarization and electric field components are defined as

$$R_{E_x,E_x}(\boldsymbol{\rho}) = \frac{\langle E_x(\mathbf{r}+\boldsymbol{\rho})E_x(\mathbf{r})\rangle}{\langle E_x(\mathbf{r})^2\rangle} \tag{1}$$

$$R_{E_z,E_z}(\boldsymbol{\rho}) = \frac{\langle (E_z(\mathbf{r}+\boldsymbol{\rho}) - \langle E_z\rangle)\,(E_z(\mathbf{r}) - \langle E_z\rangle)\rangle}{\langle (E_z(\mathbf{r}) - \langle E_z\rangle)^2\rangle} \tag{2}$$

$$R_{p_x,p_x}(\boldsymbol{\rho}) = \frac{\langle p_x(\mathbf{r}+\boldsymbol{\rho})p_x(\mathbf{r})\rangle}{\langle p_x(\mathbf{r})^2\rangle} \tag{3}$$

$$R_{p_z,p_z}(\boldsymbol{\rho}) = \frac{\langle (p_z(\mathbf{r}+\boldsymbol{\rho}) - \langle p_z\rangle)\,(p_z(\mathbf{r}) - \langle p_z\rangle)\rangle}{\langle (p_z(\mathbf{r}) - \langle p_z\rangle)^2\rangle} \tag{4}$$

and result from averaging over all pairs of points in the computational domain separated by a position vector $\boldsymbol{\rho}$. Due to cylindrical symmetry of the macroscopic system the correlation coefficients may only be dependent on the distance ρ and the angle the vector $\boldsymbol{\rho}$ makes with the applied field direction. For convenience, these coefficients will be displayed as polar diagrams in an arbitrary plain (ρ, ϕ) including the (vertical) field direction at $\phi = \pi/2$. A color legend from deep blue to deep red corresponds to the value variation from 0 to 1. All cross-correlations between the involved quantities including those between different polarization or field components are negligible.

The correlation diagrams are shown below in three blocks related to tetragonal, rhombohedral and orthorhombic materials, respectively. The area of diagrams is limited by $\rho < 2\,\mu$m because outside this region correlations become negligible. Considering the assumed grain size of 1 μm the diagram radius reaches the next neighbor distance. Each row of five figures presents evolution of one correlation coefficient when polarization is changing from the maximum negative to the maximum positive value. Exemplary diagrams are shown for particular polarization values at which a correlation coefficient exhibits the most anisotropic features.

A. Tetragonal ceramic $\mathbf{Pb(Zr_{0.515}Ti_{0.485})O_3}$

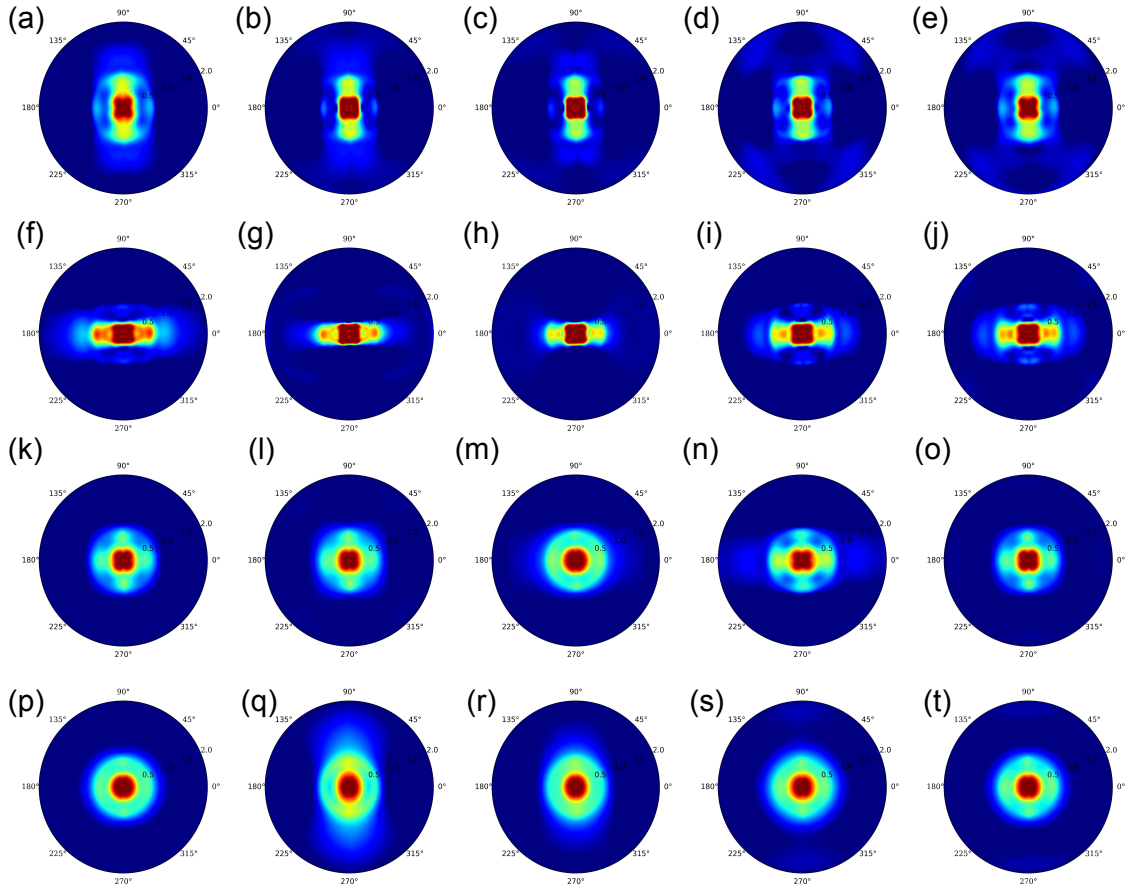

FIG. S1. Correlation coefficients for the tetragonal PZT ceramic. R_{E_x,E_x} is presented in plots (a-e) for the polarization values $P/P_s = -0.741$ (a), -0.531 (b), -0.03 (c), 0.664 (d) and 0.762 (e). R_{E_z,E_z} is presented in plots (f-j) for the polarization values $P/P_s = -0.741$ (f), -0.531 (g), -0.03 (h), 0.664 (i) and 0.762 (j). R_{p_x,p_x} is presented in plots (k-o) for the polarization values $P/P_s = -0.741$ (k), -0.249 (l), -0.03 (m), 0.372 (n) and 0.762 (o). R_{p_z,p_z} is presented in plots (p-t) for the polarization values $P/P_s = -0.741$ (p), -0.531 (q), -0.03 (r), 0.664 (s) and 0.762 (t).

B. Rhombohedral ceramic $Pb(Zr_{0.6}Ti_{0.4})O_3$

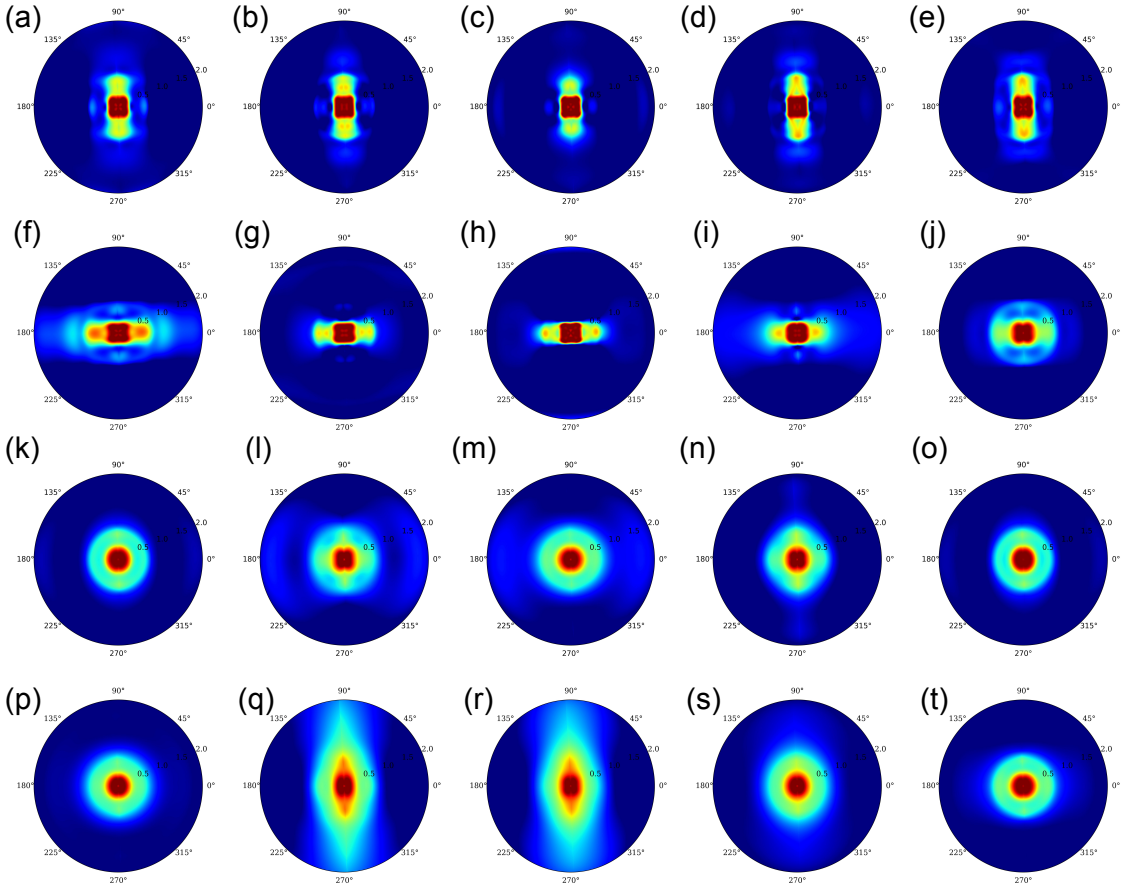

FIG. S2. Correlation coefficients for the rhombohedral PZT ceramic. R_{E_x,E_x} is presented in plots (a-e) for the polarization values $P/P_s = -0.850$ (a), -0.716 (b), 0.013 (c), 0.708 (d) and 0.853 (e). R_{E_z,E_z} is presented in plots (f-j) for the polarization values $P/P_s = -0.850$ (f), -0.716 (g), 0.013 (h), 0.708 (i) and 0.853 (j). R_{p_x,p_x} is presented in plots (k-o) for the polarization values $P/P_s = -0.850$ (k), -0.299 (l), 0.013 (m), 0.560 (n) and 0.853 (o). R_{p_z,p_z} is presented in plots (p-t) for the polarization values $P/P_s = -0.850$ (p), -0.299 (q), 0.013 (r), 0.560 (s) and 0.853 (t).

C. Orthorhombic ceramic $KNbO_3$

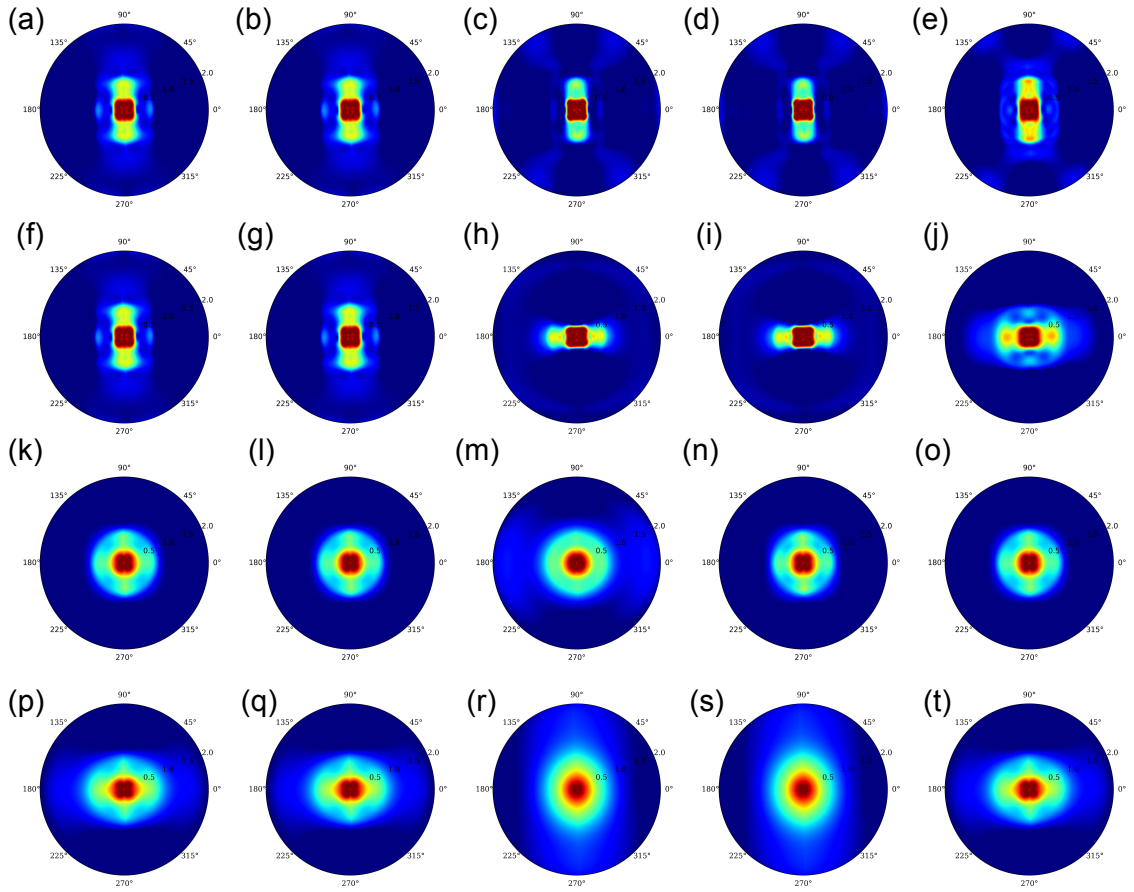

FIG. S3. Correlation coefficients for the orthorhombic KNBO ceramic. R_{E_x,E_x} is presented in plots (a-e) for the polarization values $P/P_s = -0.895$ (a), -0.548 (b), -0.197 (c), 0.398 (d) and 0.895 (e). R_{E_z,E_z} is presented in plots (f-j) for the polarization values $P/P_s = -0.895$ (f), -0.548 (g), -0.197 (h), 0.398 (i) and 0.895 (j). R_{p_x,p_x} is presented in plots (k-o) for the polarization values $P/P_s = -0.895$ (k), -0.548 (l), -0.197 (m), 0.398 (n) and 0.895 (o). R_{p_z,p_z} is presented in plots (p-t) for the polarization values $P/P_s = -0.895$ (p), -0.548 (q), -0.197 (r), 0.398 (s) and 0.895 (t).

References

[1] A. KOLMOGOROFF. **On the Statistical Theory of Crystallization of Metals**. Izvestia Akademii Nauk SSSR, Ser. Mat. 1, p. 355, 1937. ix, 41

[2] MELVIN AVRAMI. **Kinetics of Phase Change. II Transformation-Time Relations for Random Distribution of Nuclei**. The Journal of Chemical Physics, vol. 8(2), p. 212, 1940. 41, 43

[3] YOSHIHIRO ISHIBASHI AND YUTAKA TAKAGI. **Note on Ferroelectric Domain Switching**. Journal Physical Society of Japan, vol. 31(2), pp. 506-510, 1970. ix, 17, 41

[4] ALEXANDER K. TAGANTSEV, IGOR STOLICHNOV, NAVA SETTER, JEFFREY S. CROSS, AND MINEHARU TSUKADA. **Non-Kolmogorov-Avrami switching kinetics in ferroelectric thin films**. Physical Review B, vol. 66(21), 2002. ix, 41, 42, 43, 47

[5] DORU C. LUPASCU, SERGEI FEDOSOV, CYRIL VERDIER, JÜRGEN RÖDEL, AND HEINZ VON SEGGERN. **Stretched exponential relaxation in perovskite ferroelectrics after cyclic loading**. Journal of Applied Physics, vol. 95(3), p. 1386, 2004. ix, 42

[6] YURI A. GENENKO, SERGEY ZHUKOV, SERGEY V. YAMPOLSKII, JÖRG SCHÜTRUMPF, ROBERT DITTMER, WOOK JO, HANS KUNGL, MICHAEL J. HOFFMANN, AND HEINZ VON SEGGERN. **Universal Polarization Switching Behavior of Disordered Ferroelectrics**. Advanced Functional Materials, vol. 22(10), pp. 2058-2066, 2012. ix, xiv, 42, 43, 44, 45, 47, 53

[7] YU. A. GENENKO, HIRSCH J. GLAUM, H. KUNGL, M. J. HOFFMANN, AND T. GRANZOW1. **Aging of poled ferroelectric ceramics due to relaxation of random depolarization fields by space-charge accumulation near grain boundaries**. Physical Review B., vol. 80(22), p. 224109, 2009. ix, xiv, 24, 33, 34, 35, 36, 44, 52, 57, 61, 66

[8] SERGEY ZHUKOV, HANS KUNGL, YURI A. GENENKO, AND HEINZ VON SEGGERN. **Statistical electric field and switching time distributions in PZT 1Nb2Sr ceramics: Crystal- and microstructure effects**. Journal of Applied Physics, vol. 115(1), 2014. ix, 43, 44, 47, 61, 62

[9] JAN SCHULTHEISS, LISHA LIU, HANS KUNGL, MICHAEL WEBER, LALTIHA KODUMUDI VENKATARAMAN, STEFANO CHECCHIA, JOHN E.DANIELS DRAGAN DAMJANOVIC, AND JURIJ KORUZA. **Revealing the sequence of switching mechanisms in polycrystalline ferroelectric/ferroelastic materials**. Acta Materialia, vol. 157, pp. 355-363, 2018. ix, 62

[10] WENHUI HE, QIANG LI, QINGFENG YAN, NENGNENG LUO, YILING ZHANG, XIANGCHENG CHU, AND DEZHONG SHEN. **Temperature-Dependent Phase Transition in Orthorhombic $[011]_c$ $Pb(Mg_{\frac{1}{3}}Nb_{\frac{2}{3}})O_3 - 0.35PbTiO_3$ Single Crystal**. Crystals, vol. 4, pp. 262-272, 2014. xiii, 20

[11] SACHIO HORIUCHI AND YOSHINORI TOKURA. **Organic ferroelectrics**. Nature Materials, vol. 7, pp. 357-366, 2008. xiii, 17, 21

[12] P. MARTON, I. RYCHETSKY, AND J. HLINKA. **Domain walls of ferroelectric $BaTiO_3$ within the Ginzburg-Landau-Devonshire phenomenological model**. Physical Review B, vol. 81(14), p. 139906, 2011. xiii, 25, 26, 27

[13] WALTER J. MERZ. **Domain Formation and Domain Wall Motions in Ferroelectric BaTiO, Single Crystals**. Physical Review, vol. 95(3), p. 690, 1954. xiii, 17, 27, 28, 29, 31

[14] VLADIMIR SHUR, EVGENII RUMYANTSEV, AND SERGEI MAKAROV. **Kinetics of ferroelectric domain structure: Retardation effects**. Ferroelectrics, vol. 191, pp. 319-333, 1996. xiii, 28

[15] ROBERT C. MILLER AND ALBERT SAVAGE. **Velocity of Sidewise 180° Domain-Wall Motion in $BaTiO_3$ as a Function of the Applied Electric Field**. Physical Review, vol. 112(3), p. 755, 1958. xiii, 30

[16] ROBERT C. MILLER AND ALBERT SAVAGE. **Direct Observation of Antiparallel Domains During Polarization Reversal in Single-Crystal Barium Titanate**. Physical Review L., vol. 2, p. 294, 1959. 28

[17] ROBERT C. MILLER AND GABRIEL WEINREICH. **Mechanism for the Sidewise Motion of 180° Domain Walls in Barium Titanate**. Physical Review, vol. 117(6), p. 1460, 1960. xiii, 29, 31

[18] G.W. TAYLOR. **High Field Polarization Reversals in Liquid Electrodes Barium Titanate Crystals**. Australian Journal of physics, vol. 15(4), pp. 549 - 567, 1962. 28, 29

[19] M. E. DROUGARD AND R. LANDAUER. **Nucleation and Growth of Ferroelectric Domains in $BaTiO_3$ at Fields from 2 to 450 kV/cm**. Journal of Applied Physics, vol. 34(11), p. 3255, 1963. 28, 29, 31

[20] H.L. STADLER AND P. ZACHMAND. **Temperature Dependence of 180° Domain Wall Velocity in $BaTiO_3$**. Journal of Applied Physics, vol. 35(10), p. 2895, 1964.

[21] H.L. STADLER. **Forward Velocity of 180° Ferroelectric Domain Walls in $BaTiO_3$**. Journal of Applied Physics, vol. 37(5), p. 1947, 1966. xiii, 30

[22] JAN SCHULTHEISS. **Polarization reversal dynamics in polycrystalline ferroelectric/ferroelastic ceramic materials**. Ph.D. Thesis, Technische Universit at, Darmstadt, 2018. xiii, 30

[23] BING JIANG, YANG BAI, WUYANG CHU, YANJING SU, AND LIJIE QIAOB. **Direct observation of two 90° degrees steps of 180° degrees domain switching in $BaTiO_3$ single crystal under an antiparallel electric field**. Applied Physics Letters, vol. 93(15), p. 152905, 2008. xiii, 31, 32, 37, 47, 61

[24] P.C. KING, S.H. ZAHIRI, AND J. FRIEND M. JAHEDI. **COLD SPRAY ELECTRODING OF PIEZOELECTRIC CERAMIC**. Materials Forum, vol. 31, pp. 116-119, 2007. xiii, 33

[25] TALAL M.KAMEL AND G.DE WITH. **Grain size effect on the poling of soft $Pb(Zr,Ti)O_3$ ferroelectric ceramics**. Journal of the European Ceramic Society, vol. 28(4), pp. 851-861, 2008. xiv, 34, 35

[26] JOHN E. DANIELS, CLAYTON COZZAN, SUPPHATUCH UKRITNUKUN, GOKNUR TUTUNCU, JEROME ANDRIEUX, JULIA GLAUM, CHRIS DOSCH, WOOK JO, AND JACOB L. JONES. **Two-step polarization reversal in biased ferroelectrics**. Journal of Applied Physics, vol. 115(22), p. 224104, 2014. xiv, 36, 37, 53, 55

[27] YUANYUAN JING, JOHN E. BLENDELL, AND KEITH J. BOWMAN. **Three dimensional piezoresponse force microscopy polarization difference maps**. Journal of Applied Physics, vol. 109(7), p. 074110, 2011. xiv, 37, 38

[28] DRAGAN DAMJANOVIC. **Ferroelectric, dielectric and piezoelectric properties of ferroelectric thin films and ceramics**. Reports on Progress in Physics, vol. 61(9), pp. 1267-1324, 1998. xiv, 20, 24, 36, 39

[29] A. GRUVERMANA, B. J. RODRIGUEZ, C. DEHOFF, J. D. WALDREP, A. I. KINGON, R. J. NEMANICH, AND J. S. CROSS. **Direct studies of domain switching dynamics in thin film ferroelectric capacitors**. Applied Physics Letters, vol. 87(8), 2005. xiv, 41, 42, 43

[30] X. J. LOU. **Statistical switching kinetics of ferroelectrics**. Journal of Physics: Condensed Matter, Volume 21(1), 2008. xv, 47, 48, 49, 50, 51

[31] Y. A. GENENKO, J. WEHNER, AND H. VON SEGGERN. **Self-consistent model of polarization switching kinetics in disordered ferroelectrics**. Journal of Applied Physics, vol. 114(8), 2013. xv, 49, 50, 51, 52, 53, 54, 58, 60, 65

[32] J.J. BERNSTEIN, S.L. FINBERG, K. HOUSTON, L.C. NILES, H.D. CHEN, L.E. CROSS, K.K. LI, AND K. UDAYAKUMAR. **Micromachined high frequency ferroelectric sonar transducers**. IEEE Transactions on Ultrasonics, Ferroelectrics, and Frequency Control, vol. 44(5), 1997. 17

[33] E. A. MCLAUGHLIN AND H. C. ROBINSON. **Single-crystal ferroelectrics for sonar devices**. The Journal of the Acoustical Society of America, vol. 116(4), p. 2590, 2004. 17

[34] C.R. BOWEN, H.A. KIM, P.M. WEAVERB, AND S. DUNN. **Piezoelectric and ferroelectric materials and structures for energy harvesting applications**. Energy Environmental & Sciences, vol. 7, pp. 25-44, 2014. 17

[35] J. VALASEK. **Piezo-Electric and Allied Phenomena in Rochelle Salt**. Physical Review, vol. 17, p. 475, 19221. 17, 18

[36] ASHIM KUMAR BAIN AND PREM CHAND. **Pyroelectricity and Piezoelectricity**. WileyâĂŘVCH Verlag GmbH & Co. KGaA, Ferroelectrics, ISBN 9783527805310, 2017. 17

[37] M. ACOSTA, N. NOVAK, V. ROJAS1, R. VAISH S. PATEL, J. KORUZA, G.A. ROSSETTI JR., AND J. R ODEL. **$BaTiO_3$-based piezoelectrics: Fundamentals, current status, and perspectives**. Applied Physics Reviews, vol. 4(4), 2017. 17, 20, 27, 34

[38] **Materials with market value: Global ceramic and glass industry poised to reach $1 trilion**. American Ceramic Society Bulletin, vol. 96(3), pp. 27-37, 2017. 17

[39] ELIZABETH A. LITTLE. **Dynamic Behavior of Domain Walls in Barium Titanate**. Physical Review, vol. 98(4), p. 978, 1955. 17, 35

[40] J. F. SCOTT. **Applications of Modern Ferroelectrics**. Science, vol.315(5814), pp. 954-959, 2007. 17

[41] Y. FUJISAKI. **Current Status of Nonvolatile Semiconductor Memory Technology**. Japanese Journal of Applied Physics, vol. 49(10), p. 100001, 2010. 17

[42] R.E. NEWNHAM. **Properties of Materials. Anisotropy, Symmetry, Structure**. Oxford University Press, 2005. 18

[43] A. SAFARI. **Piezoelectric and acoustic materials for transducer applications**. Springer Science Business Media, p. 21, ISBN 0387765409, 2008. 18

[44] EUGENE A. ELISEEV, IVAN S. VOROTIAHIN, YEVHEN M. FOMICHOV, MAYA D. GLINCHUK, SERGEI V. KALININ, YURI A. GENENKO, AND ANNA N. MOROZOVSKA. **Defect-driven flexochemical coupling in thin ferroelectric films**. Physical Review B., vol. 97(2), 2018. 18

[45] A.K. TAGANTSEV. **Mechanisms of polarization switching in ferroelectric thin films**. Ferroelectrics, vol. 184(1), pp,79-88, 1996. 18

[46] SHAOPING LI, JEFFERY A. EASTMAN, JAMES M. VETRONE, CHRISTOPHER M. FOSTER, ROBERT E. NEWNHAM, AND L. ERIC CROSS. **Dimension and Size Effects in Ferroelectrics**. Japanese Journal of Applied Physics, vol. 36(8), part 1, 1997. 18

[47] M.E. LINES AND A.M. GLASS. **Principles and Applications of Ferroelectrics and Related Materials, Oxford Classic Texts In The Physical Sciences**. Oxford University Press, USA, ISBN-13 9780198507789, 2001. 18

[48] EUGENE A. ELISEEV, SERGEI V. KALININ, AND ANNA N. MOROZOVSKA. **Finite size effects in ferroelectric-semiconductor thin films under open-circuit electric boundary conditions**. Journal of Applied Physics, vol. 117(3), 2015. 18

[49] A. L. KHOLKIN, E. K. AKDOGAN, A. SAFARI, P.-F. CHAUVY, AND N. SETTER. **Characterization of the effective electrostriction coefficients in ferroelectric thin films**. Journal of Applied Physics, vol. 89(12), p. 8066, 2001. 18, 19

[50] Y. A. GENENKO, R. KHACHATURYAN, J.SCHULTHEISS, J. E. DANIELS A. OSSIPOV, AND J. KORUZA. **Stochastic multistep polarization switching in ferroelectrics**. Physical Review B, vol. 97(14), 2018. 19

[51] SUSAN TROLIER-MCKINSTRY AND NAZANIN BASSIRI GHARB. **Piezoelectric nonlinearity due to motion of 180° domain walls in ferroelectric materials at subcoercive fields: A dynamic poling model**. Applied Physics Letters, vol. 88(20), 2006. 20

[52] T. FURUKAWA, M. DATE, AND E. FUKADA. **Hysteresis phenomena in polyvinylidene fluoride under high electric field**. Journal of Applied Physics, vol. 51, p. 1135, 1980. 21

[53] J. W GOODBY. **Ferroelectric liquid crystals: Principles, properties and applications.** Advanced Materials vol. 5(3), pp.227-228, 1993. 21

[54] ASHIM KUMAR BAIN AND PREM CHAND. **Ferroelectrics: Principles and Applications**. WileyâĂŘVCH Verlag GmbH & Co. KGaA, Ferroelectrics, ISBN 9783527805310, 2017. 22

[55] S.K. SINGHA, R. PALAIB, K. MARUYAMAC, AND H. ISHIWARA. **Effects of Ni Substitution on Structural, Dielectrical, and Ferroelectric Properties of Chemical-Solution-Deposited Multiferroic $BiFeO_3$ Films**. Electrochemical and Solid-State Letters, vol. 11(7),2008. 22

[56] JENS KLING HARTMUT FUESS MICHAEL KNAPP HANS KUNGL MANUEL HINTERSTEIN, KRISTIN A. SCHOENAU AND MICHAEL J. HOFFMANN. **Influence of lanthanum doping on the morphotropic phase boundary of lead zirconate titanate**. Journal of Applied Physics, vol. 108(2), 2010.

[57] THI HINH DINH, HYUN-YOUNG LEE, CHANG-HO YOON, RIZWAN AHMED MALIK, YOUNG-MIN KONG, JAE-SHIN LEE, AND VU DIEM NGOC TRAN. **Effect of lanthanum doping on the structural, ferroelectric, and strain properties of $Bi_{\frac{1}{2}}(Na_{0.82}K_{0.18})_{\frac{1}{2}}TiO_3$ lead-free ceramics**. Journal of the Korean Physical Society, vol. 62, p. 1004, 2013. 22

[58] WEN-LI YAN, GUANG-HONG LUÂĂÄ, AND FENG LIU. **Effect of Chlorine Substitution on Lattice Distortion and Ferroelectricity of $CH_3NH_3PbI_3$**. Journal of Physical Chemistry C, vol. 120(32), pp. 17972-17977, 2016. 22

[59] M. ITOH, R. WANG, Y. INAGUMA, T. YAMAGUCHI, Y-J. SHAN, AND T. NAKAMURA. **Ferroelectricity Induced by Oxygen Isotope Exchange in Strontium Titanate Perovskite**. Physical Review Letters, vol. 82, p. 3540, 1999. 22

[60] E. MIKHEEV, I. STOLICHNOV, A.K. TAGANTSEV, AND N. SETTER. **Polarization screening in polymer ferroelectric films: Uncommon bulk mechanism**. Applied Physics Letters, vol. 101(13), 2012. 24

[61] SERGEI V KALININ, YUNSEOK KIM, DILLON D FONG, AND ANNA N MOROZOVSKA. **Surface-screening mechanisms in ferroelectric thin films and their effect on polarization dynamics and domain structures**. Reports on Progress in Physics, vol. 81(3), 2018. 24

[62] TOSHITO MITSUI AND JIRO FURUICHI. **Domain Structure of Rochelle Salt and KH_2PO_4**. Physical Review, vol. 90, p. 193, 1953. 24

[63] ALEXANDER K. TAGANTSEV, L. ERIC CROSS, AND JAN FOUSEK. **Domains in Ferroic Crystals and Thin Films**. Springer, ISBN 978-1-4419-1416-3, 2010. 24, 27

[64] P. BHARATHI AND K. B. R. VARMA. **Grain and the concomitant ferroelectric domain size dependent physical properties of $Ba_0.85Ca_0.15Zr_0.1Ti_0.9O_3$ ceramics fabricated using powders derived from oxalate precursor route**. Journal of Applied Physics, vol. 116(16), 2014. 24

[65] WENWU CAO AND CLIVE A.RANDALL. **Grain size and domain size relations in bulk ceramic ferroelectric materials**. Journal of Physics and Chemistry of Solids, vol. 57(10), pp. 1499-1505, 1996. 24, 35

[66] PENG GAO, JASON BRITSON, CHRISTOPHER T. NELSON, JACOB R. JOKISAARI, CHEN DUAN, MORGAN TRASSIN, SEUNG-HYUB BAEK, HUA GUO, LINZE LI, YIRAN WANG, YING-HAO CHU, ANDREW M. MINOR, CHANG-BEOM EOM, RAMAMOORTHY RAMESH, LONG-QING CHEN, AND XIAOQING PAN. **Ferroelastic domain switching dynamics under electrical and mechanical excitations**. Nature Communications vol. 5(3801), 2014. 25

[67] YURI A.GENENKO, JULIA GLAUM, MICHAEL J.HOFFMANN, AND KARSTEN ALBE. **Mechanisms of aging and fatigue in ferroelectrics**. Materials Science and Engineering: B., vol. 192, pp. 52-82, 2015. 27, 40

[68] A. SAVAGE AND R.C. MILLER. **Temperature Dependence of the Velocity of Sidewise 180° Domain-Wall Motion in $BaTiO_3$**. Journal of Applied Physics, vol. 31, p. 1546, 1960. 28

[69] HENERY L. STADLER. **Ferroelectric polarization reversal in single crystals**. Ferroelectrics, vol. 137(1), 1992. 28

[70] ROLF LANDAUER. **Electrostatic Considerations in $BaTiO_3$ Domain Formation during Polarization Reversal**. Journal of Applied Physics, vol. 28, p. 227, 1957. 28

[71] G. GERRA, A. K. TAGANTSEV, AND N. SETTER. **Surface-Stimulated Nucleation of Reverse Domains in Ferroelectrics**. Physical Review Letters, vol. 94(10), 2005. 28

[72] AN-QUAN JIANG, HYUN JU LEE, CHEOL SEONG HWANG, , AND TING-AO TANG. **Resolving the Landauer paradox in ferroelectric switching by high-field charge injection**. Physical Review B., vol. 80(2), 2009. 28

[73] WALTER J. MERZ. **Switching Time in Ferroelectric $BaTiO_3$ and Its Dependence on Crystal Thickness**. Journal of Applied Physics, vol. 27(8), p. 938, 1956. 28, 29, 31

[74] ENNIO FATUZZO. **Theoretical Considerations on the Switching Transient in Ferroelectrics**. Physical Review, vol. 127, 1962. 29

[75] M. E. DROUGARD AND R. LANDAUER. **On the Dependence of the Switching Time of Barium Titanate Crystals on Their Thickness**. Journal of Applied Physics, vol. 30(11), p. 1663, 1959. 29

[76] A. LESCHHORN AND H. KLIEM. **Influence of thermal vibrations on polarization switching in the model of local fields**. Journal of Applied Physics, vol. 121(1), 2017. 31, 40, 47

[77] ROBERT C. MILLER AND ALBERT SAVAGE. **Motion of 180° Domain Walls in $BaTi0_3$ under the Application of a Train of Voltage Pulses**. Journal of Applied Physics, vol. 32(4), p. 714, 1961. 31

[78] WUYI PAN, QIMING ZHANG, AMAR S. BHALLA, AND LESLIE E. CROSS. **Field-Induced Strain in Single-Crystal $BaTi0_3$**. Journal of the American Ceramic Society, vol. 71(6), pp. 302-305, 1998. 31, 32

[79] SHAOPING LI, A.S. BHALLA, R.E. NEWNHAM, L.E. CROSS, AND CHI-YUEN HUANG. **90° domain reversal in $Pb(Zr_xTi_{1x})O_3$ ceramics**. Journal of Materials Science, vol. 29(5), pp 1290-1294, 1994. 36, 55

[80] JIANHUA YIN AND WENWU CAO. **Polarization reversal study using ultrasound**. Applied Physics Letters, vol. 79(27), p. 4556, 2002. 31, 55

[81] B. JAFFE, W. R. COOK, AND H. JAFFE. **Piezoelectric Ceramics**. Academic Press, London, 1971. 33

[82] NAOYA UCHIDA AND TAKURO IKEDA. **Electrostriction in Perovskite-Type Ferroelectric Ceramics**. Japanese Journal of Applied Physics, Volume 6(9), 1967. 34, 36

[83] H. G. BAERWALD. **Thermodynamic Theory of Ferroelectric Ceramics**. Physical Review, vol. 105, p. 480, 1957. 34

[84] JURIJ KORUZA, PEDRO GROSZEWICZ, HERGEN BREITZKE, GERD BUNTKOWSKY, TADEJ ROJAC, AND BARBARA MALIĆ. **Grain-size-induced ferroelectricity in $NaNbO_3$**. Acta Materialia, vol. 126, pp. 77-85, 2017. 34

[85] M. H. FREY AND D. A. PAYNE. **Grain-size effect on structure and phase transformations for barium titanate**. Physical Review B., vol. 54, p. 3158, 1996. 34

[86] ZHE ZHAO, VINCENZO BUSCAGLIA, MASSIMO VIVIANI, MARIA TERESA BUSCAGLIA, LILIANA MITOSERIU, ANDREA TESTINO, MATS NYGREN, MATS JOHNSSON, AND PAOLO NANNI. **Grain-size effects on the ferroelectric behavior of dense nanocrystalline $BaTiO_3$ ceramics**. Physical Review B., vol. 70(2), 2004. 34

[87] J. HAO, W. BAI, W. LI, AND J. ZHAI. **Correlation Between the Microstructure and Electrical Properties in HighâĂŘPerformance $(Ba_{0.85}Ca_{0.15})(Zr_{0.1}Ti_{0.9})O_3$ Lead-Free Piezoelectric Ceramics**. Journal of the American Ceramic Society, vol. 95(6), pp. 1998-2006, 2012. 34

[88] YUNSEOK KIMA AND YOUNGSANG CHO. **Correlation between grain size and domain size distributions in ferroelectric media for probe storage applications**. Applied Physics Letters, vol. 89(16), 2006. 35

[89] C.A. RANDALL, N. KIM, W.W. CAO J.P. KUCERA, AND T.R. SHROUT. **Intrinsic and extrinsic size effects in fine-grained morphotropic-phase-boundary lead zirconate titanate ceramics**. Journal of American Ceramic Society, vol. 81(3), pp. 677-688, 1998. 35

[90] T. TAKEUCHI, M. TABUCHI, I. KONDOH, N. TAMARI, AND H. KAGEYAMA. **Synthesis of Dense Lead Titanate Ceramics with Submicrometer Grains by Spark Plasma Sintering**. Journal of American Ceramic Society, vol. 83(3), pp. 541-544, 2000. 35

[91] SANG-JOO KIM. **Polarization switching of ferroelectric ceramics with grain boundary effect: A simple continuum model**. Journal of Applied Physics, vol. 92, p. 2668, 2002. 35

[92] S.CHOUDHURYA, C. KRILL 3 Y.L.LIA, AND L.Q.CHENA. **Effect of grain orientation and grain size on ferroelectric domain switching and evolution: Phase field simulations**. Acta Materialia, vol. 55(4), pp. 1415-1426, 2007.

[93] W.ZHANG AND K.BHATTACHARYA. **A computational model of ferroelectric domains. Part II: grain boundaries and defect pinning**. Acta Materialia, vol. 53(1), pp. 199-209, 2005. 35

[94] X. SUN, Y.J.SU, K.W. GAO, L.Q. GUO, AND L.J. QIAO. **Charge accumulation in grain boundary promotes intergranular fracture of lead zirconate titanate piezoceramics under mechanical and electric load**. Scripta Materialia, vol. 66(5), pp. 292-295, 2016. 35

[95] R. W. CAHN. **Twinned Crystals**. Advances in Physics, vol. 3(12), pp. 363-445, 1954. 35

[96] W.R. BUSSESM, L.E. CROSS, AND A.K. GOSWAMI. **Phenomenological Theory of High Permittivity in Fine-Grained Barium Titanate**. Journal of the American Ceramic Society, vol. 49(1), pp. 200-206, 1996. 35

[97] R.C. DEVRIES AND J.E. BURKE. **Microstructure of Barium Titanate Ceramics**. Journal of the American Ceramic Society, vol. 40(6), pp. 200-206, 1957. 36

[98] MAXIM B. KELMAN AND PAUL C. MCINTYRE. **Effect of applied mechanical strain on the ferroelectric and dielectric properties of $Pb(Zr_{0.35}Ti_{0.65})O_3$ thin films**. Journal of Applied Physics, 93(11), p. 9231,2003. 36

[99] HIROFUMI TAKAHASHI, YOSHIKI NUMAMOTO, JUNJI TANI, AND SADAHIRO TSUREKAWA. **Domain Properties of High-Performance Barium Titanate Ceramics**. Japanese Journal of Applied Physics, vol. 46(10B), Part 1, 2007. 36

[100] A. GRUVERMAN, O. AUCIELLO, AND H. TOKUMOTO. **Nanoscale investigation of fatigue effects in $Pb(Zr,Ti)O_3$ films**. Applied Physics Letters, vol. 69, p. 3191, 1996. 36

[101] G. ARLT AND J. H. CALDERWOOD. **Coercive and switching fields in ferroelectric ceramics**. Applied Physics Letters, vol. 81(14), pp. 2605-2607, 2002. 36

[102] JAE-WUNG LEE, CHEE-SUNG PARK, MIYOUNG KIM, AND HYOUN-EE KIM. **Effects of Residual Stress on the Electrical Properties of PZT Films**. Journal of the American Ceramic Society, vol. 90(4), pp. 1077-1080, 2007. 36

[103] DON BERLINCOURT AND HELMUT H. A. KRUEGER. **Domain Processes in Lead Titanate Zirconate and Barium Titanate Ceramics**. Journal of Applied Physics, vol. 30(11), p. 1804, 1959. 36

[104] NAOYA UCHIDA AND TAKURO IKEDA. **Temperature and Bias Characteristics of $Pb(Zr\text{-}Ti)O_3$ Families Ceramics**. Japanese Journal of Applied Physics, vol. 4(11), 1965.

[105] TAKAAKI TSURUMI, YUTAKA KUMANO, NAOKI OHASHI, TADASHI TAKENAKA, AND OSAMU FUKUNAGA. 90° **Domain Reorientation and Electric-Field-Induced Strain of Tetragonal Lead Zirconate Titanate Ceramics**. Japanese Journal of Applied Physics, vol. (9B), Part 1, pp. 5970-5975, 1997. 36

[106] C.M.FANCHER, C.CHUNG BREWER, RÖHRIG, T.ROJAC, G.ESTEVES, M.DELUCAC, N.BASSIRI-GHARB, AND J.L.JONES. **The contribution of 180° domain wall motion to dielectric properties quantified from in situ X-ray diffraction**. cta Materialia 126(2017), pp. 36-43, 2017. 37, 55

[107] G. ARLT. **Switching and dielectric nonlinearity of ferroelectric ceramics**. Ferroelectrics, vol. 189(1), pp. 91-101, 1996. 37

[108] U. ROBELS, J.H. CALDERWOOD, AND G. ARLT. **Shift and deformation of the hysteresis curve of ferroelectrics by defects: An electrostatic model**. Journal of Applied Physics, vol. 77, p. 4002, 1995. 38

[109] E.M. ANTON, R.E. GARCIA, T.S. KEY, J.E. BLENDELL, AND K.J. BOWMAN. **Domain switching mechanisms in polycrystalline ferroelectrics with asymmetric hysteretic behavior**. Journal of Applied Physics, vol. 105(2), 2009.

[110] LI JIN, FEI LI, , AND SHUJUN ZHANG. **Decoding the Fingerprint of Ferroelectric Loops: Comprehension of the Material Properties and Structures**. ournal of the American Ceramic Society, vol. 97(1), pp. 1-27, 2014. 38

[111] J.J. LEE AND S.B. DESU. **The shifting of P-E hysteresis loop by the asymmetric contacts on ferroelectric PZT thin films**. Ferroelectrics Letters Section, vol. 20(1-2), pp. 27-34, 1995. 40

[112] I.B. MISIRLIOGLU1, M.B. OKATAN, AND S.P. ALPAY. **Asymmetric hysteresis loops and smearing of the dielectric anomaly at the transition temperature due to space charges in ferroelectric thin films**. Journal of Applied Physics, vol. 108(3), 2010. 40

[113] PAUL ERHART AND KARSTEN ALBE. **Modeling the electrical conductivity in BaTiO3 on the basis of first-principles calculations**. Journal of Applied Physics, vol. 104(4), 2008. 40

[114] SHI LIU, ILYA GRINBERG, AND ANDREW M. RAPPE. **Intrinsic ferroelectric switching from first principles**. Nature, vol. 534, pp. 360-363, 2016. 40

[115] ANDREAS LESCHHORN, STEPHANE DJOUMBOU, AND HERBERT KLIEM. **Microscopic model of domain wall motion**. Journal of Applied Physics, 115, 114106, 2014. 40

[116] YANG-BIN MA, KARSTEN ALBE, AND BAI-XIANG XU. **Lattice-based Monte Carlo simulations of the electrocaloric effect in ferroelectrics and relaxor ferroelectrics**. Physical Review B., vol. 91(18), 2015. 40

[117] YANG-BIN MA, ANNA GRÜNEBOHM, KAI-CHRISTIAN MEYER, KARSTEN ALBE, AND BAI-XIANG XU. **Positive and negative electrocaloric effect in $BaTiO_3$ in the presence of defect dipoles**. Physical Review B., vol. 994(9), 2016. 40

[118] A.F. DEVONSHIRE. **CIX. Theory of barium titanate – Part 2**. Philosophic Magazine, vol. 42(333), pp. 1065-1079, 1951. 40

[119] FUMIO NARITA AND TAKUYA KOBAYASHI & YASUHIDE SHINDO. **Evaluation of dielectric and piezoelectric behavior of unpoled and poled barium titanate polycrystals with oxygen vacancies using phase field method**. International Journal of Smart and Nano Materials, vol.7(4), pp. 265-275, 2016. 40

[120] O. LOHSE, M. GROSSMANN, U. BOETTGER, D. BOLTEN, AND R. WASER. **Relaxation mechanism of ferroelectric switching in $Pb(Zr,Ti)O_3$ thin films**. Journal of Applied Physics, vol. 89, p. 2332, 2001. 41

[121] D. VIEHLAND AND J.-F. LI. **Kinetics of polarization reversal in $0.7Pb(Mg_{\frac{1}{3}}Nb_{\frac{2}{3}})O3$-$0.3PbTiO_3$: Heterogeneous nucleation in the vicinity of quenched random fields**. Journal of Applied Physics, vol. 90, p. 2995, 2001. 42

[122] S. ZHUKOV, S. FEDOSOV, J. GLAUM, T. GRANZOW, Y. A. GENENKO, AND H. VON SEGGERN. **Effect of bipolar electric fatigue on polarization switching in lead-zirconate-titanate ceramics**. Journal of Applied Physics, vol. 108(1), 2010. 42

[123] J.Y. JO, H.S. HAN, J.-G. YOON, T.K. SONG, S.-H. KIM, AND T.W. NOH. **Domain Switching Kinetics in Disordered Ferroelectric Thin Films**. Physical Review Letters, vol. 99(26), 2007. 43, 47

[124] D.KEDZIERSKIA, E.V.KIRICHENKOB, AND V.A.STEPHANOVICH. **On the theory of domain switching kinetics in ferroelectrics**. Physics Letters A, vol. 375(3),2011. 43

[125] SERGEY ZHUKOVA, YURI A. GENENKO, MATIAS ACOSTA, HEIDE HUMBURG, WOOK JO, JÜRGEN RÖDEL, AND HEINZ VON SEGGERN. **Polarization dynamics across the morphotropic phase boundary in $Ba(Zr_{0.2}Ti_{0.8})O_{3-x}(Ba_{0.7}Ca_{0.3})TiO_3$ ferroelectrics**. Applied Physics Letters, vol. 103(15), 152904, 2013. 44, 47

[126] SERGEY ZHUKOV, MATIAS ACOSTA, YURI A. GENENKOA, AND HEINZ VON SEGGERN. **Polarization dynamics variation across the temperature- and composition-driven phase transitions in the lead-free $Ba(Zr_{0.2}Ti_{0.8})O_{3x}(Ba_{0.7}Ca_{0.3})TiO_3$ ferroelectrics**. Journal of Applied Physics, 118(13), 2015.

[127] SERGEY ZHUKOV, YURI A. GENENKO, JURIJ KORUZA, JAN SCHULTHEISS, HEINZ VON SEGGERN, WATARU SAKAMOTO, TATSURO MURATA HIROKI ICHIKAWA, KOICHIRO HAYASHI, AND TOSHINOBU YOGO. **Effect of texturing on polarization switching dynamics in ferroelectric ceramics**. Applied Physics Letters, vol. 108(1), 2016. 44

[128] S. ZHUKOV, J. GLAUM, H. KUNGL, E. SAPPER, Y. A. GENENKO R. DITTMER, AND H. VON SEGGERN. **Fatigue effect on polarization switching dynamics in polycrystalline bulk ferroelectrics**. Journal of Applied Physics, vol. 120(6), 2016. 44, 47

[129] J SCHÜTRUMPF, S ZHUKOV, Y A GENENKO, AND H VON SEGGERN. **Polarization switching dynamics by inhomogeneous field mechanism in ferroelectric polymers**. Journal of Physics D: Applied Physics, vol. 45(16), 2012. 44, 47

[130] M. J DAVIS. **Picturing the elephant: Giant piezoelectric activity and the monoclinic phases of relaxor-ferroelectric single crystals**. Journal of Electroceramics, vol. 19(1), pp. 25-47, 2007. 44

[131] B. NOHEDA AND D. E. COX. **Bridging phases at the morphotropic boundaries of lead oxide solid solutions**. Phase Transitions, vol. 79(1-2), pp. 5-20, 2006. 44

[132] J.E. ZHOU, Y. YAN, S. PRIYA, AND Y.U. WANG. **Computational study of textured ferroelectric polycrystals: Dielectric and piezoelectric properties of template-matrix composites**. Journal of Applied Physics, vol. 121(2), 2017. 44

[133] Y. SAITO, H. TAKAO, T. TANI, T. NONOYAMA, K. TAKATORI, T. HOMMA, T. NAGAYA, AND M. NAKAMURA. **Lead-free piezoceramics**. Nature, vol. 432(84), 2004. 44

[134] JACOB L. JONES BENJAMIN J. IVERSON KEITH J BOWMAN. **Texture and Anisotropy of Polycrystalline Piezoelectrics**. Journal of the American Ceramic Society, vol. 90(8), pp. 2297-2314, 2007. 44

[135] J. M. HERBERT A. J. MOULSON. **Electroceramics: Materials, Properties**. Applications. West Sussex: John Wiley&Sons, $2^{nd} edition, ISBN: 978-0-471-49748-6, 2003$. 46

[136] TOPOLOV, VITALY YURYEVICH, BOWEN, AND CHRISTOPHER RHYS. **Electromechanical Properties in Composites Based on Ferroelectrics**. Springer, ISBN 978-1-84882-000-5, 2009. 46

[137] AKDOGAN E K, ALLAHVERDI M, AND SAFARI A. **Piezoelectric composites for sensor and actuator applications**. IEEE Transactions on Ultrasonics, Ferroelectrics, and Frequency Control, vol. 52(5), 2005. 46

[138] RUI GUO, CHANG-AN WANG, AND ANKUN YANG. **Effects of pore size and orientation on dielectric and piezoelectric properties of 1-3 type porous PZT ceramics**. Journal of the European Ceramic Society, vol. 31(4), pp. 605-609, 2011. 46

[139] T.T. XU AND C.A. WANG. **Control of pore size and wall thickness of 3-1 type porous PZT ceramics during freeze-casting process**. Materials & Design, vol. 91, pp. 242-247, 2016. 46

[140] Y. ZHANG, Y.X. BAO, D. ZHANG, AND C.R. BOWEN. **Porous PZT Ceramics with Aligned Pore Channels for Energy Harvesting Applications**. Journal of the American Ceramic Society, vol. 98(10), pp. 2980-2983, 2015. 46

[141] L. STOLERIU, A. STANCU, L. MITOSERIU, D. PIAZZA, AND C. GALASSI. **Analysis of switching properties of porous ferroelectric ceramics by means of first-order reversal curve diagrams**. Physical Review B. vol. 74(17), 2006. 46

[142] L. STOLERIU, A. STANCU, L. MITOSERIU, D. PIAZZA, AND C. GALASSI. **Tailoring non-linear dielectric properties by local field engineering in anisotropic porous ferroelectric structures**. Applied Physics Letters, vol. 100(25), 2012. 46, 58

[143] R. STANCULESCU, C.E. CIOMAGA, L. PADURARIU, GALIZIA P, N. HORCHIDAN, C. CAPIANI, C. GALASSI, AND L. MITOSERIU. **Study of the role of porosity on the functional properties of (Ba,Sr)TiO_3 ceramics**. Journal of Alloys and Compounds, vol. 643, pp. 79-87, 2015. 46

[144] L. PADURARIU, L.P. CURECHERIU, AND L. MITOSERIU. **Nonlinear dielectric properties of paraelectric-dielectric composites described by a 3D Finite Element Method based on Landau-Devonshire theory**. Acta Materialia, vol. 103(724), pp. 724-734, 2016. 46, 58

[145] R. JAYENDIRAN AND A. AROCKIARAJAN. **Modeling of dielectric and piezoelectric response of 1-3 type piezocomposites**. Journal of Applied Physics, vol. 112(4), 2012. 46

[146] R. JAYENDIRAN AND A. AROCKIARAJAN. **Viscoelastic modeling and experimental characterization of thermo-electromechanical response of 1-3 piezocomposites**. Journal of Applied Physics, 116(2), 2014.

[147] R. JAYENDIRAN AND A. AROCKIARAJAN. **Effect of viscoelastic and dielectric relaxing matrix on ferroelastic behaviour of 1-3 piezocomposites**. AIP Advanced, vol. 5(2), 2015. 46

[148] W. WERSING, K. LUBITZ, AND J. MOHAUPT. **Dielectric, elastic and piezoelectric properties of porous PZT ceramics**. Ferroelectrics, vol. 68(1),1986. 46

[149] K.C. SEKHAR, ARVIND NAUTIYAL, AND R. NATH. **Analysis of ferroelectric switching in sodium nitrite:poly(vinyl alcohol) nanocomposite films**. Applied Physics A, vol. 95(2), pp. 415-421, 2009. 46, 47

[150] N. MISHRA, N. DABRA, A. NAUTIYAL, J.S. HUNDAL, G.D. VARMA, N.P. PATHAK, AND R. NATH. **Ferroelectric and Switching Properties of Spray Deposited $NaNO_2$: PVA Composite Films on Porous Silicon**. Ferroelectrics Letters, vol. 42(75), pp. 75-86, 2015. 46

[151] IGOR STOLICHNOVA, LISA MALIN, ENRICO COLLA, ALEXANDER K. TAGANTSEV, AND NAVA SETTER. **Microscopic aspects of the region-by-region polarization reversal kinetics of polycrystalline ferroelectric Pb(Zr,Ti)O_3 films**. Applied Physics Letters, vol. 86(1), 2005. 46, 47

[152] DANIEL M. MARINCEL, HUAIRUO ZHANG, AMIT KUMAR, STEPHEN JESSE, SERGEI V. KALININ, W. M. RAINFORTH, IAN M. REANEY, CLIVE A. RANDALL, AND SUSAN TROLIER-MCKINSTRY. **Influence of a Single Grain Boundary on Domain Wall Motion in Ferroelectrics**. Advanced Functional Materials, vol. 24(10),2013. 47

[153] D.M. MARINCEL, H.R. ZHANG, J. BRITSON, A. BELIANINOV, S. JESSE, S.V. KALININ, L.Q. CHEN, W.M. RAINFORTH, I.M. REANEY, C.A. RANDALL, AND S. TROLIER-MCKINSTRY. **Domain pinning near a single-grain boundary in tetragonal and rhombohedral lead zirconate titanate films**. Physical Review B, vol. 91(13), 2015.

[154] DANIEL M. MARINCEL, HUAIRUO ZHANG, STEPHEN JESSE, ALEX BELIANINOV, MAHMUT B. OKATAN, SERGEI V. KALININ, IAN M. REANEY W. MARK RAINFORTH, CLIVE A. RANDALL, AND SUSAN TROLIER-MCKINSTRY. **Domain Wall Motion Across Various Grain Boundaries in Ferroelectric Thin Films**. Journal of the American Ceramic Society, vol. 98(6),2015. 47

[155] PATAMAS BINTACHITT, SUSAN TROLIER-MCKINSTRY, KATYAYANI SEAL, STEPHEN JESSE, AND SERGEI V. KALININ. **Switching spectroscopy piezoresponse force microscopy of polycrystalline capacitor structures**. Applied Physics Letters, vol. 94(4), 2009. 47

[156] K. SEAL, M.P. NIKIFOROV S. JESSE, S.V. KALININ, I. FUJII, P. BINTACHITT, AND S. TROLIER-MCKINSTRY. **Spatially Resolved Spectroscopic Mapping of Polarization Reversal in Polycrystalline Ferroelectric Films: Crossing the**

Resolution Barrier. Physical Review Letters, vol. 103(5), 2009. 47

[157] J. E. ZHOU, T.-L. CHENG, AND Y. U. WANG. **Correlated nucleation and self-accommodating kinetic pathway of ferroelectric phase transformation**. Journal of Applied Physics, vol. 111(2), 2012. 47

[158] SERGEY ZHUKOV, YURI A. GENENKO, OFER HIRSCH, JULIA GLAUM, TORSTEN GRANZOW, AND HEINZ VON SEGGERN. **Dynamics of polarization reversal in virgin and fatigued ferroelectric ceramics by inhomogeneous field mechanism**. Physical Review B., vol. 82(1), 2010. 47

[159] A.V. GORBUNOV, T. PUTZEYS, R.A.J. JANSSEN I. URBANAVIIT, M. WÜBBENHORST, R.P. SIJBESMAD, AND M. KEMERINK. **True ferroelectric switching in thin films of trialkylbenzene-1,3,5-tricarboxamide (BTA)**. Physical Chemistry Chemical Physics, vol. 18, pp. 23663-23672, 2016. 47

[160] JIYOUL LEE, ALBERT J. J. M. VAN BREEMEN, VSEVOLOD KHIKHLOVSKYI, MARTIJN KEMERINK, RENE A. J. JANSSEN, AND GERWIN H. GELINCK. **Pulse-modulated multilevel data storage in an organic ferroelectric resistive memory diode**. Scientific Reports, vol. 6(24407), 2016.

[161] D. ZHAO, I. KATSOURAS, K. ASADI, P.W.M. BLOM, , AND D.M. DE LEEUW. **Switching dynamics in ferroelectric P(VDF-TrFE) thin films**. Physical Review, vol. 92(2), 2015.

[162] NAVNEET DABRA, JASBIR S. HUNDAL, A. NAUTIYAL, K. C. SEKHAR, AND R. NATH. **Analysis of ferroelectric polarization switching in $(NH_4)_{0.39}K_{0.61}NO_3$ films using nucleation limited switching model**. Journal of Applied Physics, vol. 108(2), 2010.

[163] A. NAUTIYAL, K.C. SEKHAR, N.P. PATHAK, N. DABRA, J.S. HUNDAL, AND R. NATH. **Polarization switching properties of spray deposited $CsNO_3$: PVA composite fielms**. Applied Physics A, vol. 99(4), pp. 941-946, 2010. 47

[164] N. MISHRA, N. DABRA, A. NAUTIYAL, J. S. HUNDAL, N. P. PATHAK G. D. VARMA, AND R. NATH. **Ferroelectric and Switching Properties of Spray Deposited $NaNO_2$: PVA Composite Films on Porous Silicon**. Ferroelectrics Letters Section, vol. 42(4-6), pp. 75-86, 2015. 47

[165] GIUSEPPE VIOLA, KOK BOON CHONG, FRANK GUIU, AND MICHAEL JOHN REECE. **Role of internal field and exhaustion in ferroelectric switching**. Journal of Applied Physics, vol. 115(3), 2013. 47, 50

[166] Y.-H. SHIN, I. GRINBERG, I.-W. CHEN, AND A. M. RAPPE. **Nucleation and growth mechanism of ferroelectric domain-wall motion**. Nature, vol. 449(881), 2007. 47

[167] JOSEPH M. BENEDETTO, RANDALL A. MOORE, AND F. BARRY MCLEAN. **Effects of operating conditions on the fast-decay component of the retained polarization in lead zirconate titanate thin films**. Journal of Applied Physics, vol. 75(1), p. 460, 1994. 47

[168] A. K. TAGANTSEV AND I. A. STOLICHNOV. **Injection-controlled size effect on switching of ferroelectric thin films**. Applied Physics Letters 74(9), p. 1326, 1999. 47

[169] X. J. LOU, M. ZHANG, S. A. T. REDFERN, AND J. F. SCOTT. **Fatigue as a local phase decomposition: A switching-induced charge-injection model**. Physical Review B., vol. 75(22), 2007. 48

[170] K. AULUCK AND E. C. KAN. **Circuit Models for Ferroelectrics-Part 1: Physics of Polarization Switching**. IEEE Transactions on Electron Devices, vol. 63(2), pp. 631-636, 2016. 50

[171] ZEKAI SEN. **Spatial Modeling Principles in Earth Sciences**. Springer, $2^{nd} edition, ISBN 978-3-319-41756-1, 2009$. 51

[172] M.J. HAUN, E. FURMAN, AND S.J. JANG & L.E. CROSS. **Thermodynamic theory of the lead zirconate-titanate solid solution system, part 5: Theoretical calculations**. Ferroelectrics, vol. 99(63), 1989. 51

[173] XIAO HONG DU, UMA BELEGUNDU, AND KENJI UCHINO. **Crystal Orientation Dependence of Piezoelectric Properties in Lead Zirconate Titanate: Theoretical Expectation for Thin Films**. Japanese Journal of Applied Physics, vol. 36(9A), Part 1, 1997. 51

[174] P. BINTACHITT, S. JESSE, D. DAMJANOVIC, Y. HAN, I. M. REANEY, S. TROLIER-MCKINSTRY, AND S.V. KALININ. **Collective dynamics underpins Rayleigh behavior in disordered polycrystalline ferroelectrics**. Proceeding of the National Academy of Sciences of the United States of America, vol. 107(16), pp. 7219-7224, 2010. 53

[175] F. GRIGGIO, S. JESSE, A. KUMAR, O. OVCHINNIKOV, T.N. JACKSON H. KIM, D. DAMJANOVIC, S. V. KALININ, AND S. TROLIER-MCKINSTRY. **Substrate Clamping Effects on Irreversible Domain Wall Dynamics in Lead Zirconate Titanate Thin Films**. Physical Review Letters, vol. 108(15), 2012. 53

[176] S. GORFMAN. **Sub-microsecond X-ray crystallography: techniques, challenges, and applications for materials science**. Crystallography Reviews, vol. 20(3),2014. 53

[177] GIOVANNI ESTEVES, CHRIS M. FANCHER, AND JACOB L. JONES. **In situ characterization of polycrystalline ferroelectrics using x-ray and neutron diffraction**. Journal of Materials Research, vol. 30(3), pp. 340-356, 2014. 53

[178] J.E. DANIELS, M. MAJKUT, S. SCHMIDT Q. CAO, J. WRIGHT, W. JO, AND J. ODDERSHEDE. **Heterogeneous grain-scale response in ferroic polycrystals under electric field**. Scientific Reports, vol. 6(22820), 2016. 53

[179] M. MAJKUT, J. E. DANIELS, J. P. WRIGHT, S. SCHMIDT, AND J. ODDERSHEDE. **Electromechanical Response of Polycrystalline Barium Titanate Resolved at the Grain Scale**. Journal of the America Ceramic Society, vol. 100(1), 2017. 53

[180] S. MANTRI, J. ODDERSHEDE, D. DAMJANOVIC, AND J. E. DANIELS. **Ferroelectric domain continuity over grain boundaries**. Acta Materialia, vol. 128, pp. 400-405, 2017. 53

[181] S. GORFMAN, H. SIMONS, T. IAMSASRI, S. PRASERTPALICHAT, D.P. CANN, H. CHOE, U.PIETSCH, Y.WATIER, AND J.L.JONES. **Simultaneous resonant x-ray diffraction measurement of polarization inversion and lattice strain in polycrystalline ferroelectrics**. Scientific Reports, vol. 6(20829), 2016. 55

[182] J. SCHULTHEISS, L. LIU, H. KUNGL, M. WEBER, L. KODUMUDI VENKATARAMAN, S. CHECCHIA, D. DAMJANOVIC, J.E. DANIELS, AND J. KORUZA. **Revealing the sequence of switching mechanisms in polycrystalline/ferroelectric/ferroelastic materials**. Acta Materialia, vol. 157, pp. 355-363, 2018. 57, 65

[183] JULIA GLAUM, YURI A. GENENKO, HANS KUNGL, LJUBOMIRA ANA SCHMITT, AND TORSTEN GRANZOW. **Deaging of Fe-doped lead-zirconate-titanate ceramics by electric field cycling: 180°- vs. non-180° domain wall processes**. Journal of Applied Physics, vol. 112(3), 2012. 58

[184] J.I. ROSCOW, R.W.C. LEWIS, J. TAYLOR, AND C.R. BOWEN. **Modelling and fabrication of porous sandwich layer barium titanate with improved piezoelectric energy harvesting figures of merit**. Acta Materialia, vol. 128, pp. 207-217, 2018. 63

[185] EVA-MARIA ANTON, R. EDWIN GARCIA, THOMAS S. KEY, JOHN E. BLENDELL, AND KEITH J. BOWMAN. **Domain switching mechanisms in polycrystalline ferroelectrics with asymmetric hysteretic behavior**. Journal of Applied Physics, vol 105(2), 2009. 64

Dr. RUBEN KHACHATURYAN

Simulation engineer / material scientist

PERSONAL

D.O.B. 06 April, 1991

Languages English – Fluent
German – Intermediate
Russian – Fluent
Armenian – Intermediate

CONTACT

Phone - (+49) 151 63420645

Email - dr.khachaturyan@gmail.com

Address - Ferdinand-Wallbrecht str. 35, 30163 Hannover, Germany

SKILLS

- Materials modeling
- Computer simulations
- FEA
- 3D CAD
- Material analysis
- Mechanics
- Physics
- Solid state physics
- Electrodynamics
- Programming

PROGRAMS

- Ansys multiphysics
- FlexPDE
- Comsol (basics)
- PTC Creo
- Python
- C++ (basics)
- LaTex and standard office software

ABOUT ME

BSEE and MSEE are obtained in micro- and nanoelectronics with a profound understanding of solid state physics, and PhD in materials science with a focus on materials modeling. 6 years experience in materials science: 3 years in synthesis and experimental investigations of magnetic nanocomposites in an AC magnetic field and 3+ years in modeling and simulation of polarization and stress/strain dynamics of ferroelectric ceramics under a DC electric field.

WORK EXPERIENCE

Simulation Engineer
2016 – 2018

Group of Materials Modeling, Technische Universität Darmstadt, Germany

Developed new models to describe polarization and strain (stress) kinetics in ferroelectrics. Simulations of fields and materials mechanics were performed by means of Maxwell FEA and original Python scripts.

Tutor
2016 – 2018

Department of Materials Science,Technische Universität, Darmstadt, Germany

Introduced to the main theoretical aspects of optical and electronic properties of solids with further supervision of a computational work and scientific reports verification.

Research assistant
2012 – 2015

Laboratory of solid state physics, Institute for Physical Researchers of Naonal Academy of Sciences, Armenia

Synthesized and experimentally investigated biocompatible magnetic nanocomposites.

EDUCATION

FEM and CAD courses
2019 – Present

FEA and CAD courses with Ansys and PTC Creo, INTEW, Institute für Technische Weiterbildung, Germany

PhD degree
2016 – 2018

Department of Materials Science, Technische Universität Darmstadt, Germany

Computational materials science
2016 – 2017

Department of Materials Science, Technische Universität Darmstadt, Germany

Master degree
2012 – 2014

Department of physics and nanotechnologies, Russian-Armenian (Slavonic) University, Armenia

Bachelor degree
2008 – 2012

Department of physics and microelectronics, Russian-Armenian (Slavonic) University, Armenia

Journal publications

- **R. Khachaturyan** and Y. A. Genenko, Correlated polarization-switching kinetics in bulk polycrystalline ferroelectrics. II: Impact of crystalline phase symmetries, Phys.Rev.B. 98, 134106 (2018)
- Y.A. Genenko, **R. Khachaturyan**, J. Schultheiß, A. Ossipov, J.E. Daniels, J. Koruza, Stochastic multi-step polarization switching in ferroelectrics, Phys. Rev. B. 97, 144101 (2018)
- **Ruben Khachaturyan**, Jens Wehner, and Yuri A. Genenko, Correlated polarization- switching kinetics in bulk polycrystalline ferroelectrics: A self-consistent mesoscopic switching model, Phys. Rev. B. 96, 054113 (2017)
- **R. Khachaturyan**, S. Zhukov, J. Schultheiß, C. Galassi, C. Reimuth, J. Koruza, H. von Seggern and Y. A. Genenko, Polarization-switching dynamics in bulk ferroelectric with isometric and oriented anisometric pores, J. Phys. D: Appl. Phys. 50, 045303 (2017)
- A. Manukyan, A. Mirzakhanyan, L. Sajti, **R. Khachaturyan**, E. Kaniukov, L. Lobanovsky, and E. Sharoyan, Nano, 10, Magnetic properties of carbon-coated Ni nanoparticles prepared by solid-phase pyrolysis of nickel-phthalocyanine (2015)
- A.S. ManukyanAS Manukyan, A.A. Mirzakhanyan, **R. Khachaturyan**, A.T. Gyulasaryan, A.N. Kocharian, Yu.I. Yuzyuk, E.G. Sharoyan, Journal of Contemporary Physics (Armenian Academy of Science) 2, Structure and magnetic properties of carbon microspheres prepared by solid state pyrolysis of organic compounds (2015)

Conferences

- **R. Khachaturyan** and Y.A. Genenko, 3D self-consistent mesoscopic model of polarization switching, Electroceramics XVI - Hasselt, Belgium (2018); poster
- **R. Khachaturyan**, Y.A. Genenko, J. Schultheiß, A. Ossipov, J.E. Daniels, J. Koruza, Sequential polarization switching in ferroelectrics, DPG-Frühjahrstagungen (2018); oral presentation
- **Ruben Khachaturyan**, Jens Wehner, and Yuri A. Genenko, Correlated polarization-switching kinetics in bulk polycrystalline ferroelectrics, IMF, USA, (2017); oral presentation
- Y.A. Genenko, **R. Khachaturyan**, J. Schultheiß, A. Ossipov, J.E. Daniels, J. Koruza, Sequential Polarization Switching in Ferroelectrics: Statistical Description of Experiment, 27 th IEEE International Symposium on the Application of Ferroelectrics, Hiroshima, Japan, (2018); oral presentation
- J. Schultheiß, Y.A. Genenko, **R. Khachaturyan**, L. Liu, J.E. Daniels, J. Koruza, Polarization and strain dynamics in polycrystalline ferroelectric/ferroelastic materials: An experimental approach and mechanistic description, Conference on Electronic and Advanced Materials, Orlando, USA (2018); oral presentation

- J. Schultheiß, S. Zhukov, **R. Khachaturyan**, Y.A. Genenko, J. Koruza, Experimental approach for investigating polarization and strain switching dynamics in ferroelectric/ferroelastic materials, International conference scanning probe microscopy, Yekaterinburg, Russia (2017); oral presentation
- J. Schultheiß, Y.A. Genenko, S. Zhukov, **R. Khachaturyan**, L. Liu, J.E. Daniels, J. Koruza, Simultaneous Time-Resolved Measurements of Polarization and Strain Dynamics to Explore Switching in Ferroelectric/Ferroelastic Materials, 26 th IEEE International Symposium on the Application of Ferroelectrics, Atlanta, GA, USA (2017); oral presentation
- J. Schultheiß, Y.A. Genenko, S. Zhukov, **R. Khachaturyan**, L. Liu, J.E. Daniels, J. Koruza, Simultaneous Time-Resolved Measurements of Polarization and Strain Dynamics to Explore Switching in Ferroelectric/Ferroelastic Materials, 26 th IEEE International Symposium on the Application of Ferroelectrics, Atlanta, GA, USA (2017); poster
- **R. Khachaturyan**, S. Zhukov, J. Schultheiß, C. Galassi, C. Reimuth, J. Koruza, H. von Seggern and Y. A. Genenko,Polarization-switching dynamics in bulk ferroelectric with isometric and oriented anisometric pores, 25 th IEEE International Symposium on the Application of Ferroelectrics, Darmstadt, Germany (2016); oral presentation
- **R. Khachaturyan**, S. Zhukov, J. Schultheiß, C. Galassi, C. Reimuth, J. Koruza, H. von Seggern and Y. A. Genenko, Polarization-switching dynamics in bulk ferroelectric with isometric and oriented anisometric pores, 25 th IEEE International Symposium on the Application of Ferroelectrics, Darmstadt, Germany (2016); poster
- **R. Khachaturyan** *et al.*, Nickel-carbon nanocomposite: a dependence of the morphology on temperature and time of the solid-state pyrolysis, NATO Advanced Research Workshop, FANEM, Belarus, (2015)
- A. Manukyan, **R. Khachaturyan** *et al.*, *Preparation and Investigation of Metal-Carbon Nanocomposites for Medical Applications*, CTCT - 2015, 1-3 June, Jena/German, Book of abstracts pp. 18, (2015)
- A.S. Manukyan, **R. Khachaturyan** *et al.*, *Structure and Magnetic properties of Nickel−Carbon Nanocomposites Prepared by Solid-Phase Pyrolysis of Nickel Phthalocyanine*, Proc. of the Nanomeeting, Minsk, Belarus, (2013)
- A. S. Manukyan, A.A. Mirzakhanyan, T.K. Khachatryan, **R. Khachaturyan** *et al.,*, *Structure and magnetic properties of nickel-carbon nanocomposites prepared by solid-phase pyrolysis of nickel phthalocyanine, Physics*, Chemistry and Applications of Nanostructures: Reviews and Short Notes, (2013)